5-2018

Probing Magnetic and Vibrational Properties of Molecular Compounds by Neutron Scattering

Shelby Elizabeth Stavretis
University of Tennessee, sstavret@vols.utk.edu

To the Graduate Council:

I am submitting herewith a dissertation written by Shelby Elizabeth Stavretis entitled "Probing Magnetic and Vibrational Properties of Molecular Compounds by Neutron Scattering." I have examined the final electronic copy of this dissertation for form and content and recommend that it be accepted in partial fulfillment of the requirements for the degree of Doctor of Philosophy, with a major in Chemistry.

Ziling Xue, Major Professor

We have read this dissertation and recommend its acceptance:

Michael D. Best, David M. Jenkins, David G. Mandrus

Accepted for the Council:
Dixie L. Thompson

Vice Provost and Dean of the Graduate School

(Original signatures are on file with official student records.)

Probing Magnetic and Vibrational Properties of Molecular Compounds by Neutron Scattering

A Dissertation Presented for the

Doctor of Philosophy

Degree

The University of Tennessee, Knoxville

Shelby Elizabeth Stavretis

May 2018

Dedication

To Sam and Chance

Acknowledgement

First, I would like to acknowledge my advisor, Dr. Zi-ling (Ben) Xue for his guidance and support during my time in graduate school. I thank him for always seeking out opportunities to make me a better scientist. I would also like to acknowledge my committee members: Dr. David Jenkins, Dr. Michael Best, Dr. David Mandrus for their time and helpful feedback during my Ph.D. studies.

I would like to thank the numerous scientists at Oak Ridge National Laboratory (ORNL) and NIST National Center for Neutron Research who played a critical role in my neutron scattering research: Drs. Andrey Podlesnyak, Eugene Mamontov, Yongqiang (YQ) Cheng, Luke Daemen, Christina Hoffmann, Xiaoping Wang, Antonio Moreira Dos Santos, Timmy AJ Ramirez-Cuesta and Craig Brown. I am especially appreciative of YQ for his hours spent teaching me phonon calculations and neutron data analysis.

I thank Seth Hunter, Tabitha Cook, Adam Lamb and Sam Rosolina for welcoming me into the Xue group and teaching me various synthesis and analysis skills. To Kendhl Seabright and Roberto Federico Perez, who joined the Xue group with me in 2013, I treasure our friendship throughout the years. I am especially thankful to have gone through the ups and downs of graduate school with Roberto, who always extended a listening ear. To the Xue group alumni that have stayed in Knoxville, I am so thankful for our gatherings over the years.

Thanks go to the members of the Xue group that joined after me: Duncan Moseley, Zhiming Liu, Clay Mings, Peter Pham and Chelsea Widener. I look forward to seeing where your research will take you.

I also would like to thank my parents and brothers for their support throughout my entire Ph.D. studies. I am so appreciative of them always reminding me why I began this journey in the first place.

I would like to thank the Shull Wollan Center Graduate Fellowship, Donors of the American Chemical Society Petroleum Research Fund and the National Science Foundation for the support of my research. In addition, ORNL and the Department of Energy are acknowledged for the use of Spallation Neutron Source for my neutron scattering work. Thanks also go to NIST National Center for Neutron Research for the use of the Disk Chopper Spectrometer beamline.

Abstract

The primary focus of this dissertation is using inelastic neutron scattering (INS) to probe magnetic excitations in paramagnetic complexes including single-molecule magnets (SMMs). Other related studies include the following: (1) Simulating vibrational frequencies to understand spin-phonon coupling (SPC) in a single-molecule magnet; (2) Using quasi-elastic neutron scattering (QENS) to study molecular dynamics of a paramagnet. Zero-field splitting (ZFS) parameters (axial: *D* and rhombic: *E*) of metalloporphryins Fe(TPP)X [X = F, Br, I; H_2TPP = tetraphenylporphyrin] have been directly determined by INS. These studies provide a complete determination of ZFS parameters for a metalloporphryin halide series demonstrating that *D* increases from F to I complexes. *Ab initio* methods were led to the understanding of the origin of the halide trend. INS has also been used to probe several Co(II) and an Er(III) SMMs. The magnetic excitations were determined by a variety of methods demonstrating that INS is a unique technique to determine the magnitude of these excitations. Most prominently, INS conducted under variable magnetic fields, reveals magnetic excitations in single crystals and powder samples in the energy region above 40 cm^{-1}. In addition, this work shows a unique strength of INS to show the origin of spin-phonon entangled peaks at 0 T. Vibrational frequencies and simulation of atomic displacements in Co(II) SMMs have been calculated via *ab intio* methods to study SPC. Raman spectroscopy of $Co(acac)_2(H_2O)_2$ (acac = acetylacetonate), $Co(acac)_2(D_2O)_2$ and Co(acac-d_7)$_2$(D_2O)$_2$ gives experimental SPC constants of different magnitudes. By probing the displacements in atoms in the SMMs, a correlation between the largest bond angle change in the first coordination sphere and largest SPC constant has been discovered.

This work leads to understanding of how the electron spins in the Co(II) complexes interact with phonons in the energy region near the magnetic excitation. QENS has been used to study methyl rotation in $Co(acac)_2(D_2O)_2$, which behaves as a paramagnet in the temperature range probed (80–100 K). The use of external magnetic fields leads to the observation of field-dependent methyl rotation. This field-dependent behavior sheds light on intermolecular interactions in the solid state.

Table of Contents

List of Tables

List of Figures

Figure **Page**

List of Schemes

List of Abbreviations

SMM	Single-molecule magnet
ZFS	Zero-field spitting
INS	Inelastic neutron scattering
QENS	Quasielastic neutron scattering
KD	Kramers Doublet
T	Tesla
K	Kelvin
meV	Millielectron-volt
μeV	Microelectron-volt
SH	Spin-Hamiltonian
D	Axial zero-field splitting parameter
E	Rhombic zero-field splitting parameter
U	Magnetic separation for Co(II), S = 3/2
$\boldsymbol{Q}$	Momentum transfer vector
$E_{i(f)}$	Incident (final) energy
$\boldsymbol{k}_{i(f)}$	Incident (final) wavevector
CNCS	Cold Neutron Chopper Spectrometer
DCS	Disk Chopper Spectrometer
CNCS	Cold Neutron Chopper Spectrometer
VISION	Vibrational Spectrometer
TOPAZ	Single Crystal Diffractometer
SNS	Spallation Neutron Source

ORNL	Oak Ridge National Laboratory
NIST	National Institute of Standards and Technology
DC	Direct Current
AC	Alternating Current
DAVE	Data Analysis and Visualization Environment
VASP	*Vienna Ab Initio Simulation Package*
$\lvert\Lambda\rvert$	Spin-phonon coupling constant
FWHM	Full width at half maximum

Numbering Scheme for the Compounds

1	$Fe(TPP)F$ (H_2TPP = tetraphenylporpyrin)
2	$Fe(TPP)Br$
3	$Fe(TPP)I$
4	$(PPh_4)_2[Co(NO_3)_4]\cdot CH_2Cl_2$
5	$(MePPh_3)_2[Co(NO_3)_4]$
6	$(AsPh_4)_2[Co(NO_3)_4]$
7	$[Co(12C4)_2](I_3)_2(12C4)$ (12C4 = 12-crown-4)]
8	$Co(acac)_2(H_2O)_2$ (acac = acetylacetonate)
8-*d*$_4$	$Co(acac)_2(D_2O)_2$
8-*d*$_{18}$	$Co(acac\text{-}d_7)_2(D_2O)_2$
9-*d*$_4$	$Zn(acac)_2(D_2O)_2$
10	$Er[N(SiMe_3)_2]_3$

List of Attachments

File 1 Animation of phonon C in **8-*d*$_4$** (126.0 cm^{-1})…….8-d4_126.0_C.gif

File 2 Animation of phonon D in **8-*d*$_4$** (129.3 cm^{-1})…….8-d4_129.3_D.gif

File 3 Animation of phonon E in **8-*d*$_4$** (142.7 cm^{-1})…….8-d4_142.7_E.gif

File 4 Animation of phonon A in **8-*d*$_{18}$** (116.3 cm^{-1})…….8-d18_116.3_A.gif

Chapter 1

Introduction

1.1. Molecular Magnetism

Conventionally, intermetallic alloys such as $Nd_2Fe_{14}B$ are used as magnetic materials for many technological applications.[1] However, with the desire to miniaturize technology it is essential to find new magnetic materials for data storage and quantum computing that can represent the smallest possible unit as spin-based devices. Single-molecule magnets (SMMs) have been proposed to fit this criterion, with magnetism stemming from the intrinsic electronic structure (magnetic anisotropy) of the individual molecules.[1-2] Many metal complexes have unpaired electrons, making them paramagnetic. In transition metal complexes with quenched orbital contribution in the ground state, their magnetic anisotropy stems from zero-field splitting (ZFS).[3]

Initially, ZFS in paramagnetic complexes such as metalloporphyrins, was studied to gain a fundamental understanding of their magnetic properties.[4] Renewed interest in ZFS came about from the field of molecular magnetism which began with the first SMM, $[Mn_{12}O_{12}(OAc)_{16}(H_2O)_4]\cdot 2HOAc\cdot 4H_2O$ or known as $Mn_{12}Ac$, in the 1990s.[5] Today, ZFS remains central to interest in molecular magnetism of transition metals.

ZFS parameters are the terms in the spin-Hamiltonian (SH) for transition metal complexes to describe the magnetic anisotropy in systems with quenched angular momentum:[6-7]

$$H = D(\hat{S}_z^{\,2} - S(S+1)/3) + E(\hat{S}_x^{\,2} - \hat{S}_y^{\,2}) + \mu_B g\, \hat{S}\cdot\hat{H} \qquad \text{(Eq. 1.1)}$$

where μ_B is the Bohr magneton, D and E represent the axial and rhombic ZFS, respectively, $\hat{S}$ is the spin operator, $\hat{H}$ is the magnetic field vectors.

D and *E* serve to lift the degeneracy of the $2S + 1$ ($S > ½$) microstates, M_S, in the absence of magnetic field.[8] Eq. 1.1 is widely used in the SMM field to describe experimental data from magnetometry measurements. ZFS is caused by the second-order spin-orbital coupling (SOC) when angular orbital momentum is quenched for the complex.[1-2] First-order SOC describes mixing of the spin and orbital component of the *electronic ground state* whereas second-order SOC describes mixing the *ground* into the *excited states* which possess an orbital component.[1] Complexes with first-order SOC include low-coordinate transition metal and f-elements ions and are represented with m_J states.[2,9]

SMMs behave as superparamagnets which display magnetic hysteresis or slow magnetic relaxation of *molecular origin* below their blocking temperature (T_B).[1] This magnetic bi-stability leads to an energy barrier to spin reversal giving stable magnetic moments. Magnetic anisotropy stems from the preferential alignment of the magnetic moment, which will occur in the most energetically favorable direction, the easy–axis (*z* direction) or –plane (*xy* direction).[1] It is desirable to maintain magnetic stability for as long as possible in zero external field.

D can be positive or negative. However, SMM behavior is *typically* observed only when $D < 0$. In the positive *D* case, the smallest M_S levels are the lowest in energy, making the transition allowed between the ground magnetic levels.[1] However, in the negative *D* case, this transition is forbidden because the largest M_S levels are lower in energy. This forbidden transition provides the ideal SMM properties. Nevertheless, there are some well-known exceptions to this rule where positive *D* SMMs can give slow magnetic relaxation.[6,10-11]

Not only is the magnetic anisotropy in SMMs critical, but also are the phonons at a relevant energy range to interact with the magnetic moment.[12-15] The phonons provide an outlet for spin reversal at energies lower than the separation of the magnetic levels *U*.[14] This under barrier relaxation U_{eff} is promoted by spin-phonon coupling (SPC) (Figure 1.1). There are three relaxation processes as described by Eq. 1.2:[1-2] (1) Direct mechanism which involves relaxation of the ground state ($\pm M_S$ for quenched orbital angular momentum) with an emission of a phonon of the same energy; (2) Orbach mechanism which is an absorption of a phonon of energy *U* and subsequent relaxation from an excited state; (3) Raman mechanism which is similar to the Orbach mechanism expect that the relaxation occurs through a virtual instead of a real state. The magnitudes of these mechanisms are determined from a multi-parameter fit of the temperature vs. relaxation times obtained from AC susceptibility (Eq. 1.2).

$$\tau^{-1} = AH^{n_1}T + CT^{n_2} + {\tau_0}^{-1}\exp\left(\frac{-U_{eff}}{k_B T}\right) \qquad \text{(Eq. 1.2)}$$

Direct Raman Orbach

where *A*, *C* and τ_0 are parameters that contain the spin-phonon coupling matrix element and the speed of sound, *T* is temperature, and k_B is the Boltzmann constant.

Recent advances in the field of SMMs have revealed the importance of understanding the phonons interactions. Conventionally it was assumed that phonons in SMMs follow the Debye model.[14,16] This model predicts the phonon density of states to be relevant up to the Debye frequency. This model, however, only accounts for acoustic

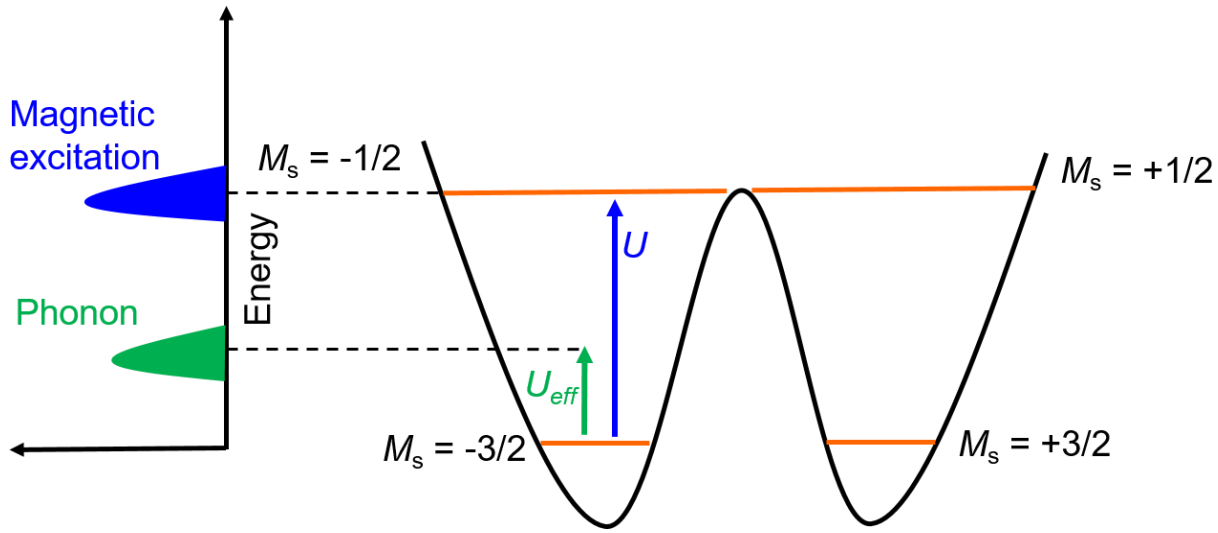

Figure 1.1. Representation of under barrier spin relaxation for an $S = 3/2$ ($D < 0$) SMM, where ZFS is the spectroscopically observed excitation (U) and $\hbar\omega$ is a lower energy phonon which contributes to faster reversal of the magnetic moment giving an effective barrier to relaxation U_{eff}.

phonon frequencies.[12,14] The problem with this assumption is optical phonons also play a role in the aforementioned relaxation processes. Therefore, SPC is not well understood in part because previous efforts have focused on tuning the *static* spin properties to reach higher U_{eff}, but neglected how to improve spin *dynamics* considering the unique phonon structure in each SMM and the strength of SPC.[12,14] Indeed, it has been theoretically proposed that low-frequency off-resonance phonon modes play a role in the barrier to relaxation.[12] Experimentally, this can be observed by comparing U_{eff} obtained from AC susceptibility to the spectroscopically obtained barrier U. As the T_B of SMMs is increased, it will become important to understand the vibrations that are activated at higher temperatures.

1.2. Experimental Studies

In order to classify the properties of molecular magnets many techniques have been developed to extract important information on the magnetic level separation.[3] Indeed determination of magnetic excitations is vital to understanding anisotropy and improving SMM properties. Magnetic excitations amongst M_S or m_J levels can reach well over 100 cm^{-1}. To gain a complete understanding of SMM properties it is necessary to accurately quantify these splittings. Spectroscopic measurements such as inelastic neutron scattering (INS) serve to explicitly determine magnetic excitations.

The most prominent method to characterize SMMs has been the use of magnetometry.[3] Firstly, the temperature dependence of the product of magnetic susceptibility and temperature ($\chi_M T$) can be measured typically showing a sharp decrease at low T. The behavior can be modelled with the SH to determine D and E. In

addition, magnetization data as a function of field (typically performed at variable temperatures) is a secondary method to extract these SH parameters. However, there are several shortcomings associated with *solely* using magnetometry methods to determine the SH parameters including: (1) Intermolecular effects at low temperatures from impurities could cause ferro- or anti-ferromagnetic ordering in the bulk sample; (2) Sign of D is unpredictable since the data can often be modelled equally well using both $D > 0$ and $D < 0$; (3) Accuracy of ZFS parameters from a multi-parameter fit of Eq. 1.1.

Resonance techniques such as electron paramagnetic resonance (EPR) have been used to study SMMs.[3,6] EPR is an accurate way to extract ZFS values. However, this method is limited by frequencies of conventional X- or Q-band EPR up to 1 cm^{-1}. ZFS of SMMs exceeding 1 cm^{-1} requires the use of higher frequency and field EPR (HF-EPR).[3] HF-EPR can only be used to *accurately* measure magnetic excitations up to ~33 cm^{-1} (1 THz).[3] HF-EPR is, nevertheless, successful at the determination of the sign of D.[17]

Frequency-domain magnetic resonance (FDMR) spectroscopy has also been developed to sweep the microwave (sub-THz or THz) frequencies in zero field (vs. sweeping the field in EPR experiments). This technique is limited to measuring separations <40 cm^{-1}.[3] Far-infrared techniques can be used to measure higher frequencies not accessible by FDMR.[3]

Inelastic neutron scattering (INS) has been used to determine magnetic excitations.[6,8] INS is beneficial because it does not have the lower and upper energies limitation of other techniques. This method will be discussed in detail in Section 1.3.

Spectroscopic methods like FDMR, far-IR and INS, as techniques that sweep the frequency, require differentiating magnetic peaks from those of phonons in the spectra. This will be further discussed in Chapters 2-3.

1.3. Neutron Scattering

1.3.1. Basics of Neutron Scattering

When neutrons of kinetic energy E_i interact with a sample, they are scattered, altering both momentum $\boldsymbol{Q}$ and energy E of the neutrons and the sample.[18] During the collision, the energy lost by the neutron will be gained by the sample. The probability that incident neutrons will be scattered from a sample is a function of the final wave vector $\boldsymbol{k}_f$ given its initial wave vector $\boldsymbol{k}_i$. The scattering triangle (Scheme 1.1) shows the kinematical conditions $\boldsymbol{k}_i$ and $\boldsymbol{k}_f$ that must be fulfilled to obtain a desired energy and momentum transfer; $\boldsymbol{Q} = \boldsymbol{k}_i - \boldsymbol{k}_f$. $\boldsymbol{Q}$ corresponds to the reciprocal space wavevectors for excitations.

1.3.2. INS to Probe Magnetic Excitations

Neutrons have spin and therefore carry a magnetic moment. There is a strong interaction between the magnetic field (magnetization density) created by unpaired electrons in the sample and magnetic moment of the neutrons. This interaction causes the incident neutrons to be scattered from the magnetization density of the paramagnetic ions. The resulting INS spectrum exhibits allowed transitions between M_S or m_J sublevels, thereby giving a direct measurement of the excitations. The cross-section for magnetic scattering corresponds to the number of neutrons scattered per

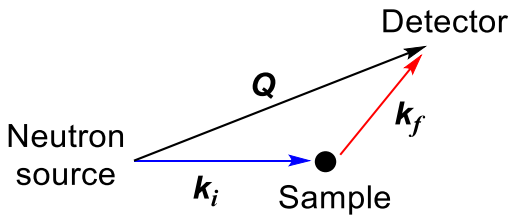

Scheme 1.1. Schematic of the INS process, $\boldsymbol{Q} = \boldsymbol{k_i} - \boldsymbol{k_f}$ is the scattering vector of the momentum transfer where $\boldsymbol{k_i}$ and $\boldsymbol{k_f}$ refer to the wavevector of the incoming and outgoing neutrons, respectively.

second, due to the magnetic interactions described above.[8] Scattering from unpaired electrons gives a distribution of the spin and orbital magnetization in the ***Q*** space. This dependence of the intensity on ***Q*** is a major difference between INS and optical spectroscopies, where the modes are observed at ***Q*** = 0.[19-20]

Neutron magnetic scattering cross-section is described as neutrons scattered into a solid angle $d\Omega$ with energy transfer between $\hbar\boldsymbol{\omega}$ and $\hbar(\boldsymbol{\omega} + \boldsymbol{d\omega})$, divided by the flux of the incident neutrons.[8] For unpolarized neutrons, identical magnetic ions with localized electrons, and spin-only scattering, the magnetic scattering cross-section is expressed by Eq. 1.3:[8,18,21]

$$\frac{d^2\sigma}{d\Omega d\omega} = (\gamma r_0)^2 \frac{k_f}{k_i}\left[\frac{1}{2} g\ F(\boldsymbol{Q})\right]^2 e^{-2W(\boldsymbol{Q})} \sum_{\alpha,\beta}\left(\delta_{\alpha\beta} - \frac{\boldsymbol{Q}_\alpha \cdot \boldsymbol{Q}_\beta}{Q^2}\right) S^{\alpha\beta}(\boldsymbol{Q},\omega) \qquad \text{(Eq. 1.3)}$$

where σ is the neutron cross section, γ is the gyromagnetic ratio, r_0 is the classical radius of an electron, *g* is the Landé *g*- factor, *F*(***Q***) is the dimensionless magnetic form factor defined as the Fourier transform of the normalized spin density associated with magnetic ions, $e^{-2W(\boldsymbol{Q})}$ is the Debye-Waller factor caused by thermal motion, $S^{\alpha\beta}(\boldsymbol{Q},\omega)$ is the magnetic scattering function, $\left(\delta_{\alpha\beta} - \frac{\boldsymbol{Q}_\alpha \boldsymbol{Q}_\beta}{Q^2}\right)$ is the polarization factor which implies neutrons can only couple to magnetic moments or spin fluctuations perpendicular to ***Q***, ***Q*** is the scattering vector of the momentum transfer (Scheme 1.1), $\hbar\omega$ is the energy change experienced by the sample, and ω is the angular frequency of neutron.

In Eq. 1.3, the magnetic form factor $F(\boldsymbol{Q})$ reveals the distribution of spin and orbital magnetization from unpaired electrons. It falls off with increased scattering vector $\boldsymbol{Q}$.[8] Therefore, peaks of magnetic origin decrease in intensity with increased $\boldsymbol{Q}$. In contrast, peaks of vibrational origin increase with increased $\boldsymbol{Q}$. However, strong incoherent scattering from samples containing hydrogen atoms may smear out $\boldsymbol{Q}$ dependence of the magnetic peaks and instrumentation constraints might limit the accessible $\boldsymbol{Q}$ range, leading to roughly constant intensities of the magnetic peaks throughout the observable $\boldsymbol{Q}$ range in the samples.[8,22-23]

1.3.3. Scattering from Nuclei and Phonons

Neutrons also can interact with nuclei of atoms. The probability of neutron-nuclear interaction is measured by the cross section of atoms, the operative area that the nucleus presents to an incident neutron.[19] For example, H-atoms have a large incoherent scattering cross section, leading to a dominating contribution of unstructured scattering in $\boldsymbol{Q}$-space from H-atoms in the neutron scattering spectrum ($\sigma_H = 80.27$ and $\sigma_D = 2.05$ barns; 1 barn = 10^{-28} square meter).[19,21] Using a different isotope as an alternative, deuteration is often a technique used in INS to decrease the incoherent scattering background contribution of H-atoms in the spectrum.

In addition to the background incoherent scattering from H-atoms, neutrons are simultaneously scattered in coherent ways, revealing phonon excitations in the INS spectrum.[21] Phonons are produced by oscillations of nuclei in a harmonized fashion about their equilibrium position in the lattice.[24] When interacting with crystalline solids, neutrons can absorb or emit energy equal to a quantum of phonon energy, $h\nu$.

There are no symmetry-based vibrational selection rules in INS spectroscopy.[19] Thus, in principle, all modes are observable in INS. This arises because neutrons are scattered by atomic nuclei via the strong interaction, in contrast to infrared and Raman spectroscopies where photons are scattered by electrons.

In molecular solids, modes in which the molecules vibrate primarily as a whole with little internal distortion, *i.e.*, lattice vibrations, are often characterized as external (intermolecular) modes, whereas significant distortions of atoms that comprise a part of the molecule with a small displacement of the molecular center-of-mass are often characterized as internal modes (intramolecular).[24] In other words, if the primary features of the mode involve significant distortions of atoms in the molecule, it is called an internal mode. The internal modes are also known as molecular vibrations, and they typically have much higher frequencies than the external modes. The external modes include translational and librational modes.[19] However, the internal and external modes often couple. In other words, all modes are essentially mixed. From the perspectives of solid-state physics, the internal and external modes originate from the same governing equations, and have the same mathematical representations.

For molecular crystal containing n atoms in m molecules per unit cell, there are $3n$-$6m$ internal modes and $6m$-3 external modes, in addition to 3 acoustic modes.[24] Both internal and external modes as well as acoustic modes in molecular crystals are called phonons.[19] The internal and external modes are also named optical phonons. This dissertation, in general, does not distinguish internal and external modes.

1.4. Current Dissertation

This dissertation serves to address three major current central points of debate in the field of molecular magnetism: (1) Use of only magnetometry to characterize magnetic excitations; (2) Neglect of the phonon spectrum and how it promotes spin-phonon coupling; (3) Inattention to interactions that exist between paramagnetic molecules in the solid state.

1.4.1. Chapter 2

The zero-field splitting (ZFS) parameters of nondeuterated metalloporphyrins Fe(TPP)X [X = F (**1**), Br (**2**), and I (**3**); H_2TPP = tetraphenylporphyrin] have been determined by inelastic neutron scattering (INS). This work provides a rare, complete determination of ZFS values for a metalloporphyrin halide series in which *D* is found to increase from F to I. *Ab initio* calculations confirm the trend in *D* values and reveal that it is correlated in part to increased covalency of the Fe-X bond.

1.4.2. Chapter 3

INS is a unique technique to directly probe the magnetic excitations in several SMMs. The magnetic separations of Co(II) and Er(III) SMMs have been detected using several methods to determine peaks of magnetic origin in INS including the following: (1) Temperature dependence; (2) $|Q|$ dependence; (3) Diamagnetic control; (4) Application of an external magnetic field. This body of work collectively shows how to best study SMMs with INS and to overcome technical challenges typically associated with using neutrons, such as sample size and increased background from strong

incoherent scattering from H-atoms leading to a decrease in sensitivity.

1.4.3. Chapter 4

Interaction of a magnetic moment with lattice vibrations (spin-phonon coupling) is a detrimental relaxation pathway in single-molecule magnets. However, there is little understanding how lattice vibrations lead to relaxation of the magnetic moment. This chapter examine Co(II) SMMs to understand how the unpaired electron spin interacts with phonon near the magnetic excitation.

1.4.4. Chapter 5

Molecular dynamics is a fundamental property of metal complexes. These dynamical processes are not well understood for paramagnetic complexes under external magnetic fields. Quasi-elastic neutron scattering (QENS) has been used to study the dynamics of $Co(acac)_2(D_2O)_2$ (**8-*d*$_4$**). The dominant dynamical process is methyl group rotation which is found to have a field-dependent rotation times. This field-dependent behavior is indicative of interactions between $Co(acac)_2(D_2O)_2$ molecules. We speculate these interactions may originate from the presence of unpaired electron spins dispersed on peripheral hydrogen atoms or from a structure change in the molecules stemming from a magnetic field effect on the paramagnetic Co(II) ions.

Chapter 2

Magnetic Transitions in Iron Porphyrin Halides by Inelastic Neutron Scattering and *Ab Initio* Studies of Zero-Field Splittings

Reproduced in part with permission from:

Stavretis, S.E.; Atanasov, M.; Podlesnyak, A. A.; Hunter, S.C.; Neese, F.; Xue, Z.-L., Magnetic Transitions in Iron Porphyrin Halides by Inelastic Neutron Scattering and *Ab Initio* Studies of Zero-Field Splittings. *Inorganic Chemistry* **2015**, *54*, 9790.

https://pubs.acs.org/doi/abs/10.1021/acs.inorgchem.5b01505

Publication Policy: https://pubs.acs.org/pb-assets/acspubs/Migrated/dissertation.pdf

The a*b initio* studies of zero-field splittings in the work were conducted by M. Atanasov and F. Neese. This author conducted the synthesis and characterization of Fe(TPP)X [X = F (**1**), Br (**2**), and I (**3**)] as well as interpretation and simulation of their INS data. The a*b initio* studies of zero-field splittings are included in the chapter to provide a comprehensive understanding of the chemistry.

2.1. Abstract

Zero-field splitting (ZFS) parameters of nondeuterated metalloporphyrins Fe(TPP)X [X = F, Br, I; H_2TPP = tetraphenylporphyrin] have been directly determined by inelastic neutron scattering (INS). The ZFS values are D = 4.49(9) cm^{-1} for tetragonal polycrystalline Fe(TPP)F (**1**), and D = 8.8(2) cm^{-1}, E = 0.1(2) cm^{-1} and D = 13.4(6) cm^{-1}, E = 0.3(6) cm^{-1} for monoclinic polycrystalline Fe(TPP)Br (**2**) and Fe(TPP)I (**3**), respectively. Along with our recent report of the ZFS value of D = 6.33(8) cm^{-1} for tetragonal polycrystalline Fe(TPP)Cl, these data provide a rare, complete determination of ZFS parameters in a metalloporphyrin halide series. The electronic structure of Fe(TPP)X (X = F, Cl, Br, I) has been studied by multireference *ab initio* methods: the complete active space self-consistent field (CASSCF) and the N-electron valence perturbation theory (NEVPT2) with the aim of exploring the origin of the large and positive zero-field splitting D of the $^6A_1$ ground state. D was calculated from wave functions of the electronic multiplets spanned by the d^5 configuration of Fe(III) along with spin−orbit coupling accounted for by quasi degenerate perturbation theory. Results reproduce trends of D from inelastic neutron scattering data increasing in the order from F, Cl, Br, to I. A mapping of energy eigenvalues and eigenfunctions of the S = 3/2 excited states on ligand field theory was used to characterize the σ- and π-antibonding effects decreasing from F to I. This is in agreement with both similar results deduced from *ab initio* calculations on CrX_6^{3-} complexes and the spectrochemical series showing a decrease of the ligand field in the same directions. A correlation is found between the increase of D and decrease of the π- and σ-antibonding energies e_λ^X ($\lambda = \sigma, \pi$) in the series from X = F to I. Analysis of this correlation using second-order perturbation theory

expressions in terms of angular overlap parameters rationalizes the experimentally deduced trend. *D* parameters from CASSCF and NEVPT2 results have been calibrated against those from the INS data, yielding a predictive power of these approaches. Methods to improve the quantitative agreement between *ab initio* calculated and experimental *D* and spectroscopic transitions for high-spin Fe(III) complexes are proposed.

2.2. Introduction

The chemistry of metalloporphyrins has the potential to impact our understanding of biological and geological roles that the naturally occurring systems play.[25-29] The diverse biological functions of heme proteins are often attributed to the varying degree of changes in the local heme environment as shown in Table 2.1 which is discussed below. Many metalloporphyrins often have unpaired electrons, making the compounds paramagnetic. One intrinsic property in paramagnetic compounds is the zero-field splitting (ZFS). For compounds with spin $S \geq 1$, the interaction of the electron spins mediated by spin orbital coupling leads to a splitting of the spin states of otherwise degenerate states.[7,30-31]

As introduced in Chapter 1, ZFS manifests as differences among energy levels in the absence of an external magnetic field. For d^5 Fe(III) porphyrin complexes here, the electronic ground states of $S = 5/2$ complexes are split as shown in Scheme 2.1. The resulting energy spectrum exhibits 2*D* and 4*D* peaks that are associated with transitions in ZFS. The rhombic ZFS, *E*, mixes $\Delta M_S = \pm 2$ states. Thus, $M_S = \pm 1/2$ states interact with either $M_S = \pm 5/2$ or $\mp 3/2$, leading to the shift of the energy levels in Scheme 2.1d.

Table 2.1. Comparison of D (cm^{-1}) values of different Fe(III) porphyrin halides determined by different methods

X =	**Fe(TPP)X by other methods**	**Fe(TPP)X by INS including the current work**	**Fe(III) protoporphyrin (IX) dimethyl ester halides by far-IR**	**Fe(III) deuteroporphyrin (IX) dimethyl ester halides by far-IR**
F	-	4.49(9)	5.0(1)[32]	5.55(11)[32]
Cl	6.5 (far-IR),[33] D = 3.2-11.9 determined by other methods[34]	6.33(8)[34]	6.95(14)[32]	8.95(18)[32]
Br	4.9 (magnetic susceptibility)[35] 9.15 (far-IR)[33] 12.5(5) (magnetic susceptibility)[36-37]	8.8(2)	9.75[33]	11.80(23)[32]
I	13.5(5)[37]	13.4(6)	14.5[33]	16.40(15)[32]

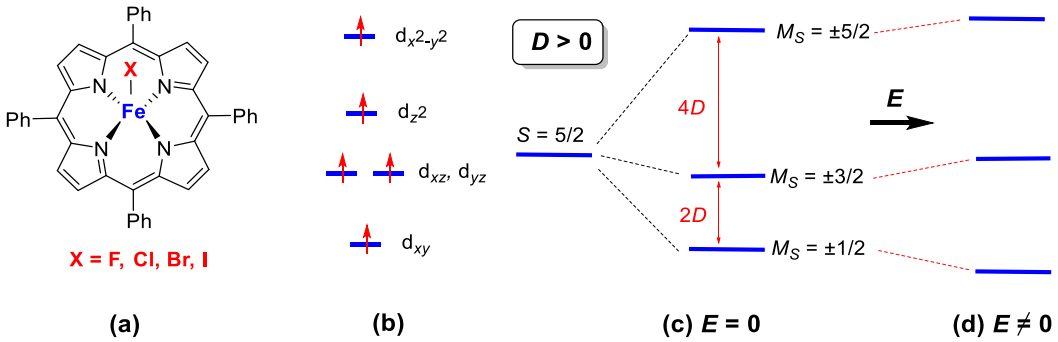

Scheme 2.1. (a) Structures of metalloporphyrins in the current studies. (b) d orbital splitting and ZFS in compounds with $S = 5/2$ with $D > 0$. (c) $E = 0$ (for $D < 0$ energy levels will be inverted). (d) $E \neq 0$, mixing of pure doublet states. (Pure states are only retained if $E << D$.[7])

ZFS is of fundamental importance to understanding molecular magnetism. While ZFS parameters have been actively studied, there is still a limited understanding on how ZFS parameters relate to the geometric and electronic structures of transition metals compounds, including how metal-ligand bonding affects ZFS.[7,30] Knowledge of the effects of metal-ligand bonding on ZFS also helps design better single molecule magnets (SMMs) as data storage and quantum computing materials.[38]

ZFS, including that of metalloporphyrins, has been investigated by several techniques, including electron paramagnetic resonance (EPR), magnetic susceptibility measurement, nuclear magnetic resonance (NMR), far-infrared (far-IR), Mössbauer spectroscopy, magnetic circular dichroism (MCD), and inelastic neutron scattering (INS).[25,31,39-41] The effect of ZFS on a transition metal ion is to partially or totally remove the $(2S + 1)$-fold degeneracy of the ground-state multiplet. In the case of d^5 Fe(III) compounds the ZFS in Scheme 2.1, the magnetization density that interacts with the spin of neutrons is the spin dipole moment from 5 unpaired d electrons, as the orbital angular momentum of the d electrons in the complexes is quenched. The resulting energy spectrum exhibits peaks associated with transitions from $M_S = \pm 1/2$ to $\pm 3/2$ ($2D$) and from $M_S = \pm 3/2$ to $\pm 5/2$ ($4D$) in Scheme 2.1.

To our knowledge, few bioinorganic complexes have been studied by INS. We recently reported direct determination of ZFS parameters of several non-deuterated metalloporphyrins M(TPP)Cl (M = Fe, Mn, Cr) and Mn(TPP) (H_2TPP = tetraphenylporphyrin).[34] With the nature of how ligands affect ZFS relatively unknown, the current study focuses on iron(III) porphyrin halides, which are common inorganic ligands, with two-fold interest: (a) The first is determination of ZFS parameters for

Fe(TPP)X [X = F (**1**), Br (**2**), and I (**3**)] by INS. Thus, along with Fe(TPP)Cl, a compound we recently studied,[34] this is a rare complete series of biomimetic halide compounds with the ZFS values determined.[32] (b) The second is the *ab initio* study of the electronic structure and magnetic anisotropy of the metalloporphyrins to explore the origin of the large and positive zero-field splitting of the $^6A_1$ ground state.

There have been many previous studies of the ZFS of Fe(III) compounds with a $^6A_1$ ground state. Solomon and co-workers have investigated the origin of the $^6A_1$ ground state zero-field splitting in axially distorted high-spin d^5 $[FeCl_4]^-$.[30] Brackett and co-workers have reported *D* values of four Fe(III) deuteroporphyrin IX dimethyl ester halides (Chart 2.1) that were determined by far-IR (Table 2.1).[32] Goff and co-workers have reported correlations of axial ligand field strength and zero-field splittings in the C-13 NMR spectra of 5- and 6-coordinate high-spin Fe(III) porphyrin complexes.[42] Ohya and Sato conducted a comparative study of Mössbauer spectra of three halides Fe(TPP)X (X = Cl, Br, I) to probe electronic effects of substituents and axial ligands.[43] In addition, *D* parameters of Fe(TPP)Br and Fe(TPP)I have been determined by magnetic susceptibility measurements.[35-37] For Fe(TPP)Br, $D = 13.0(5)$ cm^{-1} was reported intially[36] and later revised to 12.5(5) cm^{-1} based on reanalysis of the data. For Fe(TPP)I, the reported *D* = 13.5(5) cm-1.[37] Far-IR studies by Uenoyama gave $D = 9.15$ cm^{-1} for Fe(TPP)Br (Table 2.1).[33] To our knowledge, ZFS of Fe(TPP)F has not been studied. Although both molecules of Fe(TPP)Br (**2**) and Fe(TPP)I (**3**) have 4-fold symmetry, their crystals are in the monoclinic system. Thus the rhombic parameter *E* in Eq. 1.1 is required to explain ZFS properties of their crystalline samples. However, the earlier determination of ZFS parameters by magnetic susceptibility measurements and far-IR

Chart 2.1

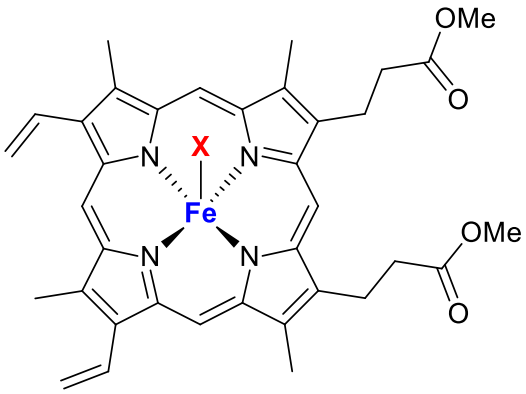

X = F, Cl, Br, I

Fe(III) protoporphyrin (IX) dimethyl ester halide

did not determine the *E* values.[35-37]Several experimental measurements, such as magnetic susceptibility and HFEPR, that allow for the determination of the *g*-factor require the use of a magnetic field, which prevents the direct measurement of zero-field splitting (ZFS).

INS has been used to probe the magnetic properties of metal complexes, especially excitations among low-lying energy levels.[22-23,44-47] For example, the low-lying energy levels of magnetic clusters have been characterized by INS.[7,22,44-48] *D* for single-molecule magnets $Mn_4O_3X(OAc)_3(dbm)_3$ [X = Br, Cl, OAc, and F] have been studied by Güdel and coworkers to see how the *D* values change with the axial X^- ligands.[22] The state-of-the-art facilities at Spallation Neutron Source (SNS) at Oak Ridge National Laboratory (USA) have made it possible to probe magnetic properties of nondeuterated metal complexes in detail.[46] We have used the Cold Neutron Chopper Spectrometer (CNCS)[49] at SNS to determine both the size and the sign of ZFS parameters *D* for nondeuterated metalloporphyrins Fe(TPP)X [X = F (**1**), Br (**2**), and I (**3**)] as well as the best fit *E* values for Fe(TPP)X [X = F (**1**), Br (**2**), and I (**3**)]. In addition, we have calculated the electronic structure of Fe(TPP)X [X = F (**1**), Br (**2**), and I (**3**)] by multi-reference *ab initio* methods to explore the origin of their *D* values of the $^6A_1$ ground state. A correlation is found between the increase of *D* and the decrease of the π- and σ-antibonding energies e_λ^X ($\lambda = \sigma, \pi$) in the series from X = F to I. Analysis of this correlation using second-order perturbation theory expressions in terms of angular overlap parameters allows us to rationalize the experimentally deduced trends.

2.3. Results and Discussion

2.3.1. INS Studies

Peak position in INS spectra gives a direct measurement of the eigenvalues of the spin Hamiltonian. When there is no external magnetic field and the compound is in the tetragonal environment, the spin Hamiltonian is defined by a single anisotropy parameter *D* and depends on the spin projection along *z*. The *E* parameter provides a distortion which removes the axial symmetry, and introduces anisotropy in the *xy* plane. For Fe(TPP)X, two magnetic INS peaks are observed, as discussed below. The *D* and *E* parameters were then determined from the spin Hamiltonian in Eq. 1.1 using INS data, as described below.

Simulated INS spectra were obtained by calculating the energies and corresponding wave functions via exact diagonalization of the spin Hamiltonian expressed in Eq. 1.1. These calculations can be used to get the INS intensity which is proportional to the scattering function $S^{\alpha\beta}(\boldsymbol{Q}, \omega)$. The experimental and simulated INS spectra are given for comparison.

In Fe(TPP)F (**1)**, the Fe(III) ion has a high spin (S = 5/2) configuration, and its electronic ground state is split into three Kramers doublets: M_S = ±1/2, ±3/2, and ±5/2 (Scheme 2.1). The spacings among the three doublets are 2*D* and 4*D*, respectively. In the INS spectra of **1**, a peak at 8.99 cm^{-1} was observed (Figure 2.1) at 1.6, 10, 50, and 100 K. This peak corresponds to the first excitation from the M_S = ±1/2 to the M_S = ±3/2 states. Magnetic intensities are based on Boltzmann statistics. Therefore, as the temperature is increased, the 2*D* peak decreases in intensity, as shown in Figure 2.1. In addition, the first-excited states are populated with the temperature increase. The

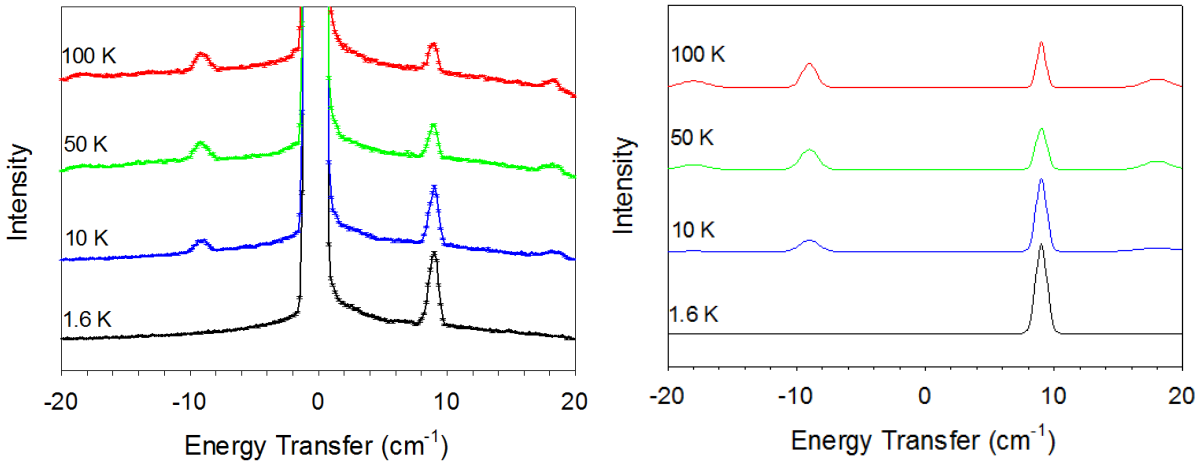

Figure 2.1. (Left) INS spectra of Fe(TPP)F (**1**) with incident neutron energy E_i = 24.20 cm^{-1}, Q = 0.5-1.3 $Å^{-1}$ and a step size of 0.024 cm^{-1}. (Right) Theoretical INS spectra of an S = 5/2 spin system with D = 4.49 cm^{-1}.

excitation from the first excited, M_S = ±3/2 states to the second excited, M_S = ±5/2 states produced the second, 4*D* peak. This peak is observed at 18.05 cm^{-1}, which is approximately twice the energy (8.99 cm^{-1}) of the 2*D* peak. The intensity of the 4*D* peak increases with temperature, indicating its magnetic origin. Analyses of the temperature dependence of experimental and calculated intensities are given in Figures A.6-A.8).

INS may also give the sign of *D* for these *S* = 5/2 systems. Because the 2*D* peak was observed at a low temperature before the 4*D* peak, the axial *D* parameters of these complexes (X = F, Br, I) are positive. If *D* < 0, the ground state would be M_S = ±5/2 and the first peak observed at 1.6 K would be 4*D* (Scheme 2.1c).

In addition, peaks with negative energy transfers were also observed in INS. When the temperature was raised to 10 K, a peak at -8.99 cm^{-1} appeared, indicating that the incident neutrons *gained* energy from the sample in the INS process. In other words, molecules at the ±3/2 states in Scheme 2.1 returned to the ground ±1/2 states, transferring the energy to the neutrons. Thus, the ZFS parameters are *D* = 4.49(9) cm^{-1} and *E* = 0 cm^{-1}. The error analysis is given in Figures A.5 and Tables A.1-A.2.

The *E* parameter in the monoclinic crystals of Fe(TPP)Br (**2**) leads to a change of the energy levels in Scheme 2.1d. The transitions from M_S = ±1/2 to ±3/2 and from M_S = ±3/2 to ±5/2 (*E* << *D*) are no longer 2*D* and 4*D*, respectively.[7] There is now an *E* component inside these transitions that is not independent of *D*. Experimentally, the energy of the 4*D* peak is very close to twice the energy of the 2*D* peak, demonstrating this compound is close to the axial symmetry with a small *E* value (see Figure 2.4 to view how *E* affects the energy levels of *S* = 5/2 compounds). The INS spectra of **2** are given in Figure 2.2. The first and second magnetic peaks are located at ±17.5 and 35.04

cm^{-1}, respectively. Thus, the ZSF parameters are D = 8.8(2) and E = 0.1(2) cm^{-1}.A comparison of the temperature dependence of experimental and calculated intensities, given in Figures A.11-A.13 in Appendix A, confirms the magnetic nature of the peaks. Other peaks (~11.5 and 26 cm^{-1}) in the spectra have different linewidths. In comparison to the magnetic peaks, they are broader and not well shaped. The differences suggest that the peaks are not due to transitions from well determined energy levels but rather from phonon density of states. This argument is confirmed by comparing how the intensities of the peaks change with different Q ranges with low to high Q values. The peaks at 11.5 and 26 cm^{-1} were identified as phonons as they have the greatest intensities at high Q as shown in Figure A.14. It should be noted that, in addition to a magnetic peak at 18.3 cm^{-1} (Table 2.1), Uenoyama also observed the 11.5 cm^{-1} peak, which was not identified in the far-IR spectrum of **2**.[33] The error analysis is given Figures A.9-A.13 and Table A.3.

Two incident energies had to be used to observe two magnetic transitions in the INS spectra. An incident neutron energy of E_i = 40.89 cm^{-1} only displayed the first magnetic peak at 26.8 cm^{-1} (Figure 2.3a). At a higher incident energy E_i = 97.35 cm^{-1}, the second magnetic peak at 53.3 cm^{-1} appeared (Figure 2.3b). Analysis of the INS spectra for Fe(TPP)I (**3**) and the determination of ZFS parameters were analogous to those for **2**. The temperature dependence of experimental and calculated intensities is shown in Figure A.17 in Appendix A. The second magnetic peak is broad and almost overlaps with a phonon peak, meaning this magnetic peak is not as resolved as the first due to the proximity of a phonon peak. Therefore, there is a larger error associated with the use of this peak to calculate the D and E parameters. Eq. 1.1 gave the ZFS

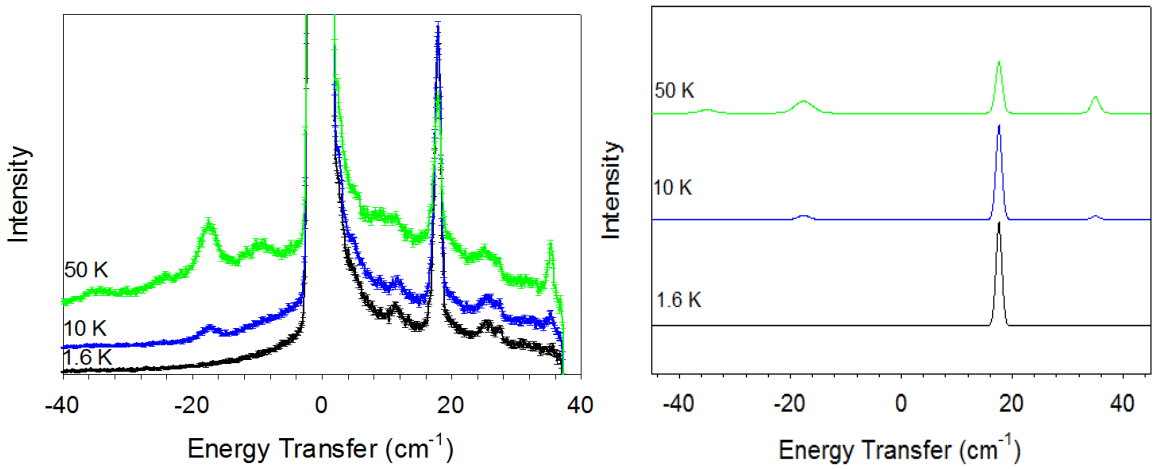

Figure 2.2. (Left) INS spectra of Fe(TPP)Br (**2**) with E_i = 40.89 cm^{-1}, Q = 0.48-1.8 Å^{-1} and a step size of 0.016 cm^{-1}. (Right) Theoretical INS spectra of an S = 5/2 spin system with D = 8.8 cm^{-1} and E = 0.1 cm^{-1}.

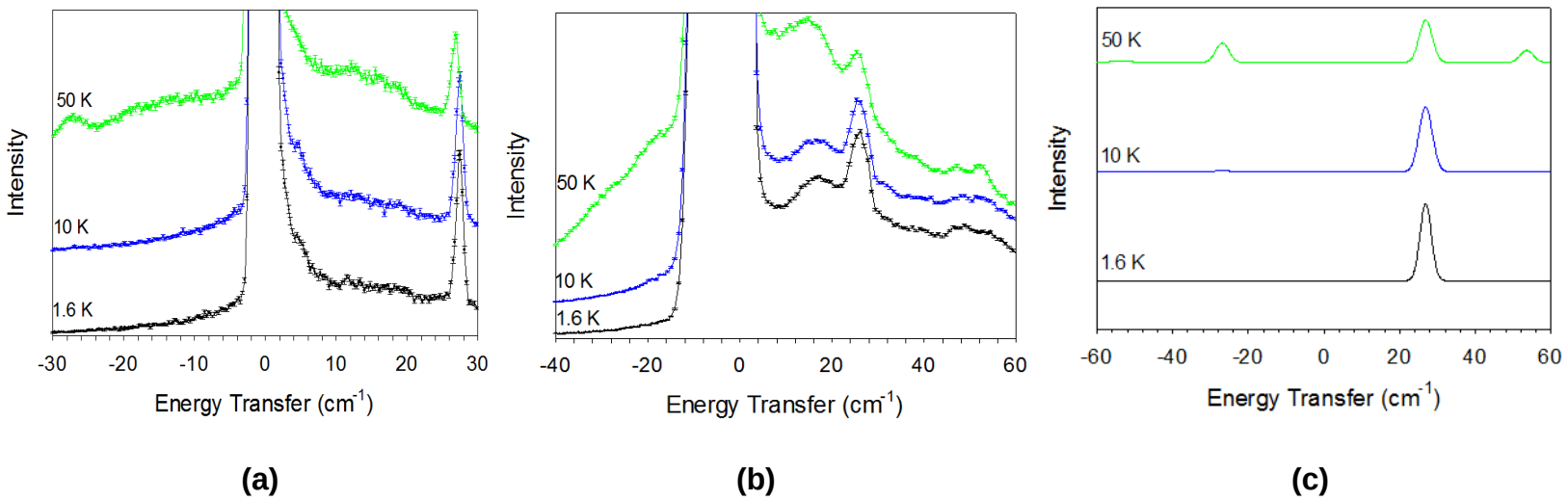

Figure 2.3. (a) INS spectra of Fe(TPP)I (**3**) with E_i = 40.89 cm^{-1}, Q = 0.5-1.0 Å^{-1} and a step size of 0.024 cm^{-1}. (b) INS spectra with E_i = 97.35 cm^{-1}, Q = 0.48-1.8 Å^{-1} and a step size of 0.024 cm^{-1}. (c) Theoretical INS spectra of an S = 5/2 spin system with D = 13.4 cm^{-1} and E = 0.3 cm^{-1}.

parameters D = 13.4(6) cm^{-1} and E = 0.3(6) cm^{-1}. As with **2**, the spectra for **3** also have additional peaks with broad linewidths which were determined to be from phonon density states. The presence of phonon peaks is confirmed by examining the Q dependence of the peaks in Figures A.18-A.19. As expected, the phonon peaks are more pronounced at high Q, while the magnetic peaks stay constant or decrease in intensity. The error analysis is given Figures A.15-A.17 and Table A.4.

Both **2** and **3** have a small E value. This in turn translates into small variations of the 2D and 4D peak positions. When the E parameter is small, there is little mixing of the energy levels until E > 2 cm^{-1} as observed in Figure 2.4. For example, in **3** with D = 13. 4 cm^{-1}, changing from E = 0 to 0.3 cm^{-1} leads to 0.58% increase and 0.11% decrease in the positions of 2D and 4D peaks, respectively.

The D values for Fe(TPP)X [X = F (**1**), Br (**2**), Cl[34] and I (**3**)] from the INS studies are listed in Table 2.1. D values of Fe(TPP)X, determined by other methods, and Fe(III) protoporphyrin/deuteroporphyrin IX dimethyl ester halides are also summarized there. Several methods gave D = 3.2-11.9 cm^{-1} for Fe(TPP)Cl and 4.9-12.5(5) cm^{-1} for **2**. Our INS studies[34] gave accurate values for the complexes. It is also interesting to note that the D values for Fe(TPP)X are similar to those of corresponding Fe(III) protoporphyrin IX dimethyl ester halides (Table 2.1).

2.3.2. Calculated Coordination Geometries

The geometries of the first-coordination spheres of the four Fe(TPP)X complexes are square pyramidal (Figure 2.5) with four equatorial Fe-N and one axial Fe-X bond. Structural parameters from X-ray data are well reproduced by the DFT geometry

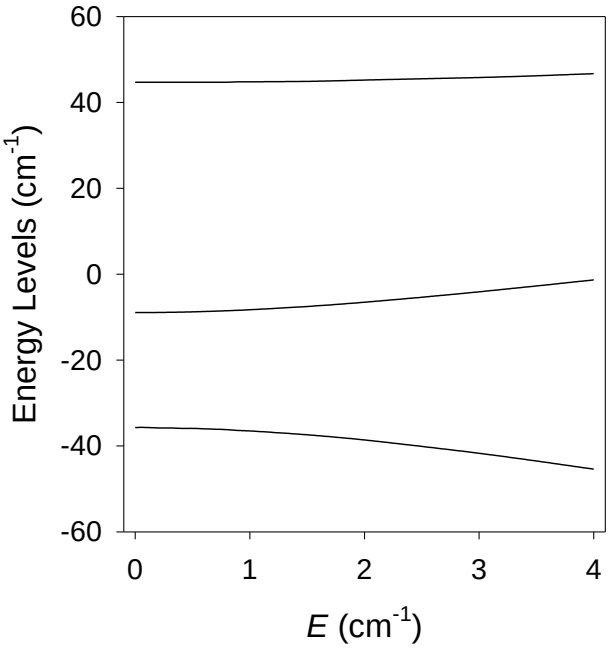

Figure 2.4. Effect of the *E* parameter on the energy levels of an *S* = 5/2 system with ZFS parameters of *D* = 13.4 and *E* = 0.3 cm^{-1} (in **3**).

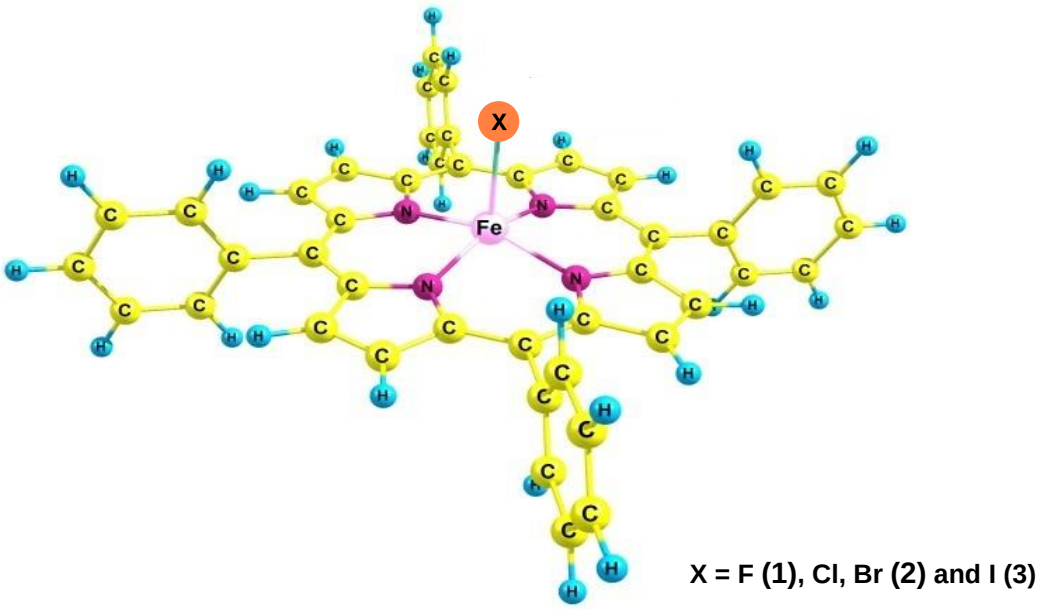

Figure 2.5. Structural view of the series of complexes as revealed by X-ray and neutron diffraction studies and DFT geometry optimizations.

optimization (Table 2.2). The set of Cartesian coordinates for each DFT optimized structure are listed in Appendix A.

2.3.3. Multiplet Energies and the Zero-Field Splitting (*D*)

From CASSCF and NEVPT2 calculations for Fe(TPP)X at DFT-optimized geometries we can conclude that all four complexes are in a $^6A_1$ ground state. Quartet (S = 3/2) excited states originate from the ^4G, ^4D, ^4F and ^4P states of the free Fe(III) ion split by the C_{4v} ligand field in the complex. Energies of CASSCF and NEVPT2 of these terms in the energy range below 50000 cm^{-1} are included in Tables A.5 and A.6. From all these, the states with the $^4T_1$ cubic parentage split into ^4E and $^4A_2$ terms. Their mixing with the $^6A_1$ ground state via spin-orbit coupling leads to splitting of its M_S = ±5/2, ±3/2 and ±1/2 sublevels thus governing the sign and magnitude of the zero-field splitting terms. From the three $^4T_1$ cubic terms, only two yield essential contributions to D. Their energies and calculated D values are depicted in Figure 2.6. Second-order perturbation theory yields the following $^6A_1$ ground state expression for D:

$$D(^4T_1) = \frac{\zeta_{eff}^2}{5}\left[\frac{1}{\Delta(^4A_2)} - \frac{1}{\Delta(^4E)}\right] \qquad \text{(Eq. 2.1)}$$

with ζ_{eff} is the effective SOC constant and $\Delta(^4A_2)$ and $\Delta(^4E)$ are the energies of the ^4E and $^4A_2$ C_{4v} sublevels of each $^4T_1$ term.

Table 2.2. Experimental (X-ray diffraction, X = F, Cl, Br, I; neutron diffraction, X = Cl) vs. DFT structural parameters of the Fe(TPP)X [X = F (**1**), Br (**2**), Cl and I (**3**)] complex series

X	**F (1)**		**Cl**		**Br (2)**		**I (3)**	
	X-ray	DFT	X-ray[50]/ neutron	DFT	X-ray[51]	DFT	X-ray[52]	DFT
Fe-X (Å)	-	1.815	2.194/ 2.200	2.210	2.348	2.360	2.554	2.566
Fe-N (Å)	-	2.063	2.052/ 2.067	2.061	2.069 2.074 2.057 2.078	2.057	2.061 2.076 2.055 2.074	2.054
∠XFeN (º)	-	102.78	100.99/ 101.96	102.89	104.10 103.89 103.67 103.04	102.37	102.94 103.38 103.26 101.83	101.86

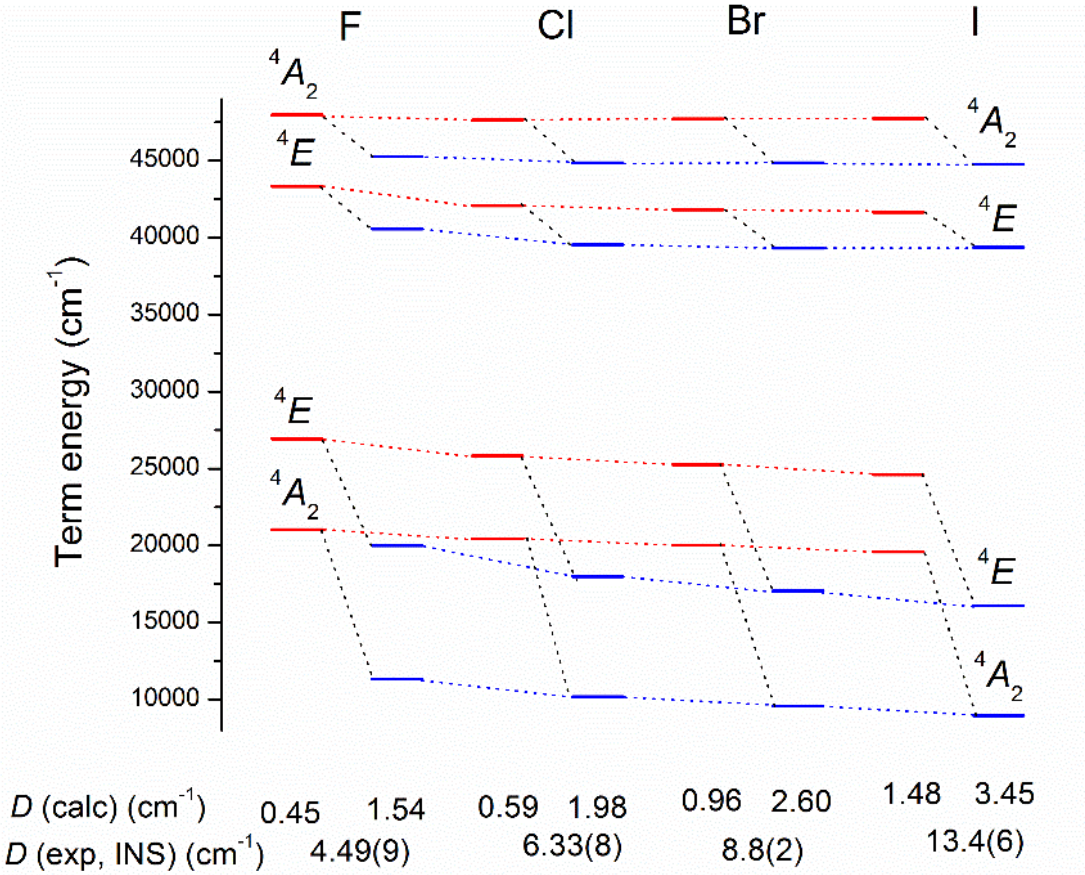

Figure 2.6. Term energies from CASSCF and NEVPT2 calculations governing the sign and magnitude of the $^6A_1$ ground state *D* value of the series of Fe(TPP)X [X = F (**1**), Cl, Br (**2**), I (**3**)] complexes; Color code: red-CASSCF, blue–NEVPT2.

From Eq. 2.1, it is evident that when the energy of the ^4E excited state is greater than the $^4A_2$ excited state (Figure 2.6) from the lowest cubic $^4T_1$ term, a positive D value results, while if the energy of the excited states is reversed ($^4E < {}^4A_2$) a negative D value results. Because of the larger $^4T_1$-$^6A_1$ energy separation for the second excited $^4T_1$ state, the positive term dominates and determines the positive sign of D for the entire complex. Qualitative predictions of the positive sign of D for such coordination geometries of Fe(III) using angular overlap model consideration have been published.[53]

In Figure 2.7 and Table 2.3, we compare calculated and experimental values of D. While the experimental trend D(F) < D(Cl) < D(Br) < D(I) is well reproduced, computed CASSCF values of D are about one order of magnitude (8-10) smaller than the experimental values. This can be attributed to the ionic nature of the CASSCF wave functions where metal-ligand covalence is largely underestimated. In agreement with these results, dynamical correlation accounted for by NEVPT2 improves the quantitative agreement with the experimental data, now D(NEVPT2) values differing by a factor of 3-4 compared with the experimental ones. This will be thoroughly discussed in a separate section below. The changes from the CASSCF to NEVPT2 results are reflected by the drop down in energy of the $^4A_2$ and ^4E lowest excited states by as much as 10000 cm^{-1} and by about half this amount for the second excited state of the same C_{4v} symmetry. The trends in D across the series are nicely reflected by the concerted lowering of the transitions energies from F to I in the series. The contributions to D from the two $^4T_1$ states (Tables A.5 and A.6 in comparison with Eq. 2.1) show that the improvement of the D parameters upon NEVPT2 corrections is largely dominated by the lowest $^4T_1$ term and the lowering of the excitation energy to $^4A_2$ (by about 10250 cm^{-1}) which exceeds

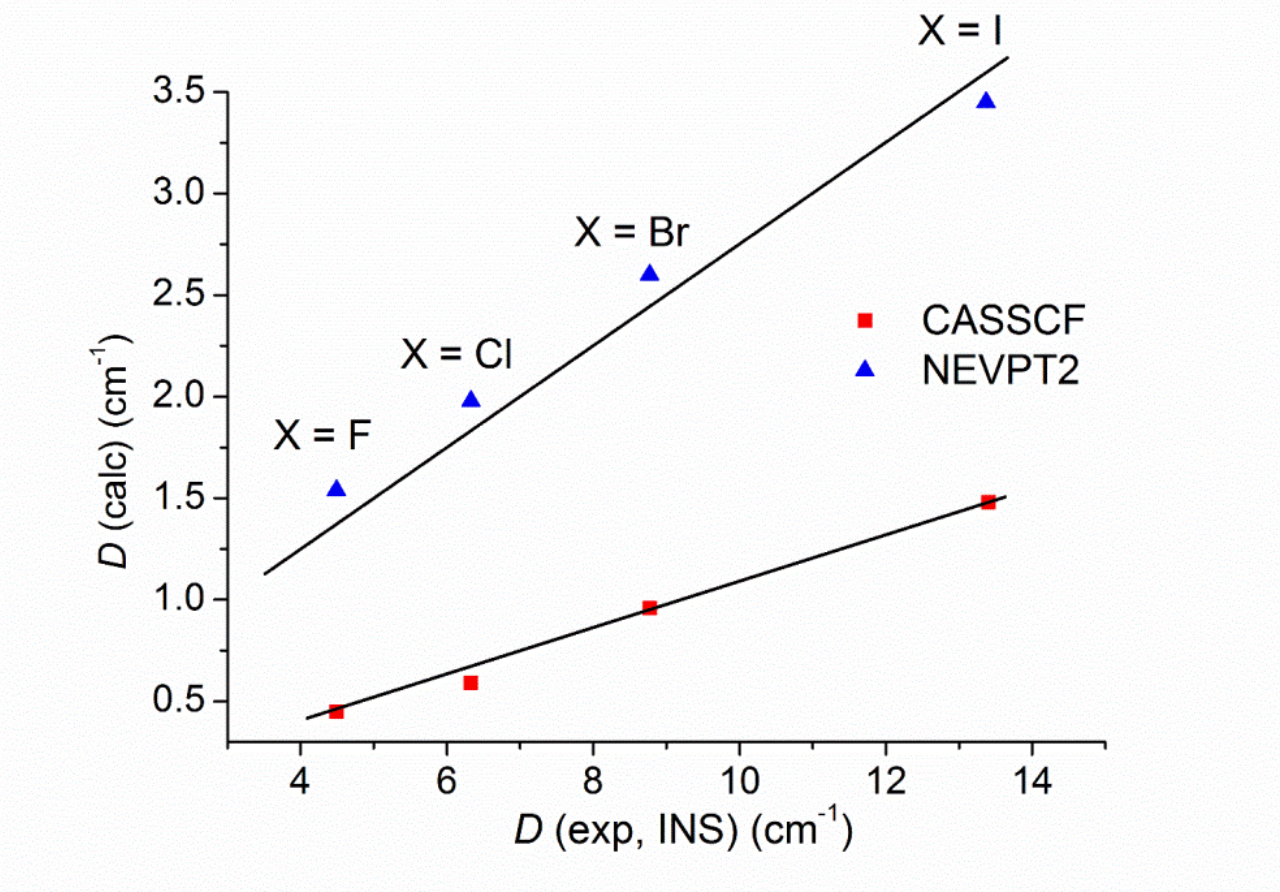

Figure 2.7. Calibration between experimental and CASSCF/NEVPT2 calculated values of the zero-field splitting parameter *D* for the Fe(TPP)X series; *D* (exp, INS) = 8.326 *D*(CASSCF) + 0.997, standard deviation = 0.18 cm^{-1}; *D* (exp, INS) = 4.625 *D*(NEVPT2).

Table 2.3. Metal-ligand bonding and electron repulsion parameters for the Fe(TPP)X [X = F (**1**), Cl, Br (**2**), I (**3**), DFT optimized structures] series (cm^{-1}) from *ab initio* ligand field analysis and a best fit of the angular overlap model to the CASSCF/NEVPT2 (CAS(5,5) active space) quartet excited state energies; For the sake of comparison values of the calculated and experimental (in parenthesis) ZFS parameter *D* (cm^{-1}) are listed

X	**F** (**1**)		**Cl**		**Br** (**2**)		**I** (**3**)	
Ligand field parameters	CASSCF	NEVPT2 (C%)[b]	CASSCF	NEVPT2	CASSCF	NEVPT2	CASSCF	NEVPT2
e_{σ}^{X}	6260	7355 (15)	4200	5348 (21)	3358	4501 (25)	2798	4055 (31)
e_{π}^{X}	2340	2625 (11)	1177	1287 (8)	843	873 (3)	523	474 (-10)
e_{σ}^{N}	5650	6058 (7)	5784	6266 (8)	5862	6372 (8)	5930	6467 (8)
B **(*B*/*B*$_o$)**	1145 0.88	1032 0.83	1127 0.87	1023 0.82	1122 0.86	1022 0.82	1114 0.85	1018 0.82
C **(*C*/*C*$_o$)**	4297 0.89	4698 1.05	4231 0.87	4735 1.05	4219 0.87	4761 1.06	4197 0.87	4800 1.07

Table 2.3. Continued

X	**F** (**1**)		**Cl**		**Br** (**2**)		**I** (**3**)	
Ligand field parameters	CASSCF	NEVPT2 (C%)[b]	CASSCF	NEVPT2	CASSCF	NEVPT2	CASSCF	NEVPT2
ζ (ζ/ζ_0)	436 0.92	436 0.92	429 0.91	429 0.91	415 0.88	415 0.88	392 0.83	392 0.83
D (calc)	0.45	1.54	0.59	1.98	0.96	2.60	1.48	3.45
D (exp, INS)	4.49(9)		6.33(8)		8.8(2)		13.4(6)	

[a] Parameterization was done under the following simplifying assumptions: $e^N_{\pi s} = e^N_{\pi c} = 0$.

[b] Percentage covalence C%, defined as {[e_λ(NEVPT2) - e_λ(CASSCF)]/e_λ(NEVPT2)} × 100 ($\lambda = \sigma, \pi$), is listed in brackets. (See Ref. 80, p. 187 for details.)

[c] Nephelauxetic ratios of the Racah parameters *B*, *C* and the spin-orbit coupling parameter ζ in the complex with respect to the computed values B_0, C_0, and ζ_0 for the free Fe(III) ion: 1301,4844, 472 (CASSCF) and 1240, 4490, 472 cm^{-1} (NEVPT2), respectively.

the energy lowering of the higher, excited ^4E state (by about 7800 cm^{-1}). This is a differential correlation effect which increases with Fe-X covalence increasing in the series F, Cl, Br, and I.

A calibration of the CASSCF and NEVPT2 values of *D* allows one to predict the experimental *D* starting from the computed ones. The latter are compared with the experimental *D* values in Figure 2.7. A least-square fit between the experimental and the theoretical *D* values leads to the following expressions:

$$D\ (\text{exp, INS}) = 8.326\ D(\text{CASSCF}) + 0.997\ (cm^{-1}) \qquad \text{(Eq. 2.2)}$$

$$D\ (\text{exp, INS}) = 4.625\ D(\text{NEVPT2}) - 2.8255\ (cm^{-1}) \qquad \text{(Eq. 2.3)}$$

with a standard deviation of 0.18 cm^{-1} between the two data sets.

2.3.4. Metal-Ligand Bonding of the CASSCF and NEVPT2 Many-Electron States and the Correlation with *D*

Bonding in Fe(TPP)X is governed by two types of donors – The equatorial nitrogen of the TPP and axial X ligands. Angular overlap expressions (Angular Overlap Ligand Field Analysis) for the energies of 3d-type MOs in the simple case of square-pyramidal FeN_4X with ligands at the *x,y* and *z* axes are given by:

$$e(b_1, d_{x2-y2}) = 3e_\sigma^N$$

$$e(a_1, d_{z2}) = e_\sigma^X + e_\sigma^N - 4e_{sd}^N - e_{sd}^X + 4(e_{sd}^X e_{sd}^N)^{1/2} \qquad \text{(Eq. 2.4)}$$

$$e(e, d_{xz,yz}) = e_\pi^X + 2e_{\pi\perp}^N$$

$$e(b_2, d_{xy}) = 4e^N_{\pi\|}$$

Two sets of parameters e^N_σ , e^X_σ and e^N_π , e^X_π are introduced to account for σ and π-antibonding, with $e^N_{\pi\|}$ and $e^N_{\pi\perp}$ describing iron-nitrogen in- and out-of-plane π-interactions, respectively. The parameters e^N_{sd} and e^X_{sd} account for the stabilization of the d_{z^2} orbital due to partial hybridization with the 4s one. The mixing of these two orbitals is induced by the fourfold symmetry where both orbitals are of the a_1 type. Since the N atoms of the porphyrin ligand do not possess electrons for in-plane π-bonding, $e^N_{\pi\|}$ can be safely set to zero. Even so, one is left with six parameters from which only three are independent in the given point group. To achieve further realistic approximation to reduce the number of parameters we considered a $Fe(TPP)^+$ complex without the X atom. For such a complex (D_{4h} symmetry), Eq. 2.4 is simplified to:

$$e(b_1, d_{x2-y2}) = 3e^N_\sigma$$

$$e(a_1, d_{z2}) = e^N_\sigma - 4e^N_{sd} \qquad \text{(Eq. 2.5)}$$

$$e(e, d_{xz,yz}) = 2e^N_{\pi\perp}$$

$$e(b_2, d_{xy}) = 0$$

A best fit of e^N_σ , $e^N_{\pi\perp}$ and e^N_{sd} and *B* to energy eigenvalues from CASSCF calculations of a $Fe(TPP)^+$ model complex resulted, respectively in values 5725, 99, 1289 and 990 cm^{-1}. These results show that while keeping to an approximate CASSCF

wavefunction $e_{\pi\perp}^{N}$ can be safely neglected. We thus arrive at a model with three parameters e_{σ}^{N}, e_{σ}^{X} and e_{π}^{N}, where e_{sd}^{N} and e_{sd}^{X} have been neglected. Parameters e_{σ}^{N}, e_{σ}^{X} and e_{π}^{N} and *B* have been obtained from a best fit to energies from CASSCF and NEVPT2 calculations for transitions from the $^6A_1$ ground into the *S* = 3/2 excited states (Table 2.3). In this procedure, the detailed angular geometry as given by the DFT structure optimizations was taken into account. While the energy of the Fe-N antibonding e_{σ}^{N} is almost constant between the various members, e_{σ}^{X} and e_{π}^{X} decrease across the series from F to I and thus correlate with the increase of *D* in the same direction (Figure 2.8). The bonding parameters from Table 2.3 have been used to deduce the ligand field splitting pattern of the 3d-MOs (Figure 2.8) which we in turn employ to rationalize *D* vs e_{π}^{X} and e_{σ}^{X} correlation. According to Eq. 2.1, the value of *D* is dominated by contributions from ^4E and $^4A_2$ terms for the lower and the upper $^4T_1$ states. All four transitions are governed by increase of interelectronic repulsion when going from the $^6A_1$ ground state (five unpaired electrons on each 3d MO) into excited states with electronic configurations, where one orbital becomes doubly occupied (an energy which equals roughly 10*B* + 6*C* for both $^4T_1$ states). Excitations from the $^6A_1$ ground state into the lower ^4E and $^4A_2$ pair correspond to $e \rightarrow t_2$ transitions with a gain of ligand field energy (ligand field de-excitation). As illustrated in Figure 2.9 (middle left), this gain is larger for the $^4A_2$ state than for the ^4E state, leading to an energy ordering $\Delta(^4E) > \Delta(^4A_2)$ and, according to Eq. 2.1, a positive contribution to *D*. Transitions to the upper $^4T_1$ state are of the $t_2 \rightarrow e$ type. Therefore, when exciting from $^6A_1$, they are adding energy to the 10*B* + 6*C* term. According to Figure 2.9 (middle, right), a $\Delta(^4E) <$

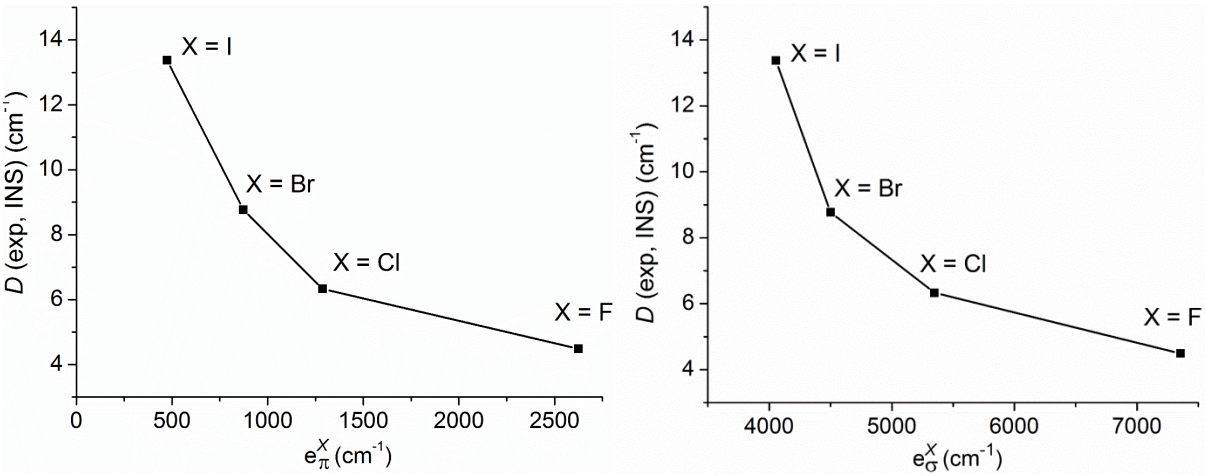

Figure 2.8. Magneto-structural correlation between the experimental *D* values and the Fe-X π (Left) and σ (Right) antibonding energies as given by a best fit of the angular overlap plus repulsion ligand field model to NEVPT2 eigenvalues.

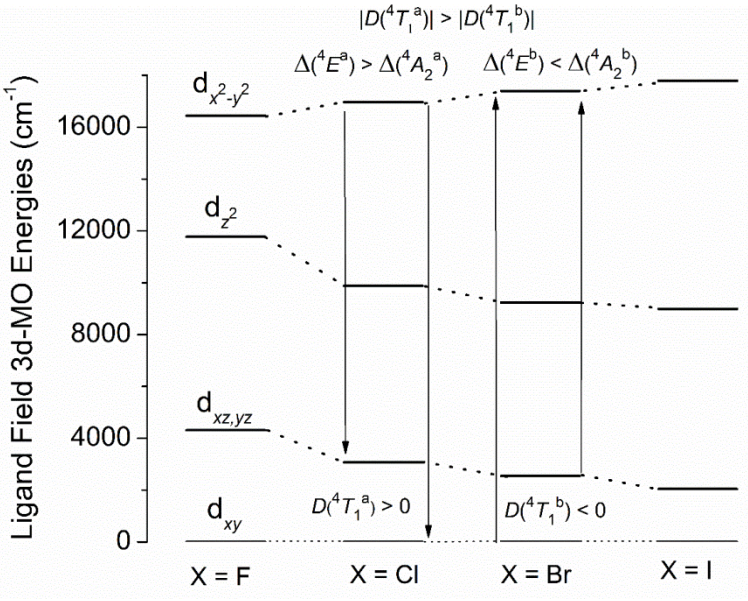

Figure 2.9. Ligand field 3d-MO energies from *ab initio* (NEVPT2) calculations of the Fe(TPP)X series.

$\Delta(^4A_2)$ term sequence for the upper $^4T_1$ state leads to a negative contribution to *D*. Coming from a lower lying transition, positive contributions to *D* clearly dominate and determine the overall sign of *D*. With e_σ^X and e_π^X decreasing across the series X = F to I, Both $^4A_2$, the lowest excited state, and ^4E, the second excited state, become lower in energy. However (Table A.5), the changes of the energy of $^4A_2$ dominate over those of ^4E and are mainly responsible for the observed increase in *D*. As shown in a comparison between the CASSCF and NEVPT2 results in Tables A.5 and A.6, the effect is enhanced when taking dynamical correlation into account.

2.3.5. Magnetic Anisotropy (*D*) and Metal-Ligand Covalence in the Fe(TPP)X Series

Changes in covalence in 3d complexes affect *D*: (1) Decrease in the spin-orbit coupling (SOC, quantified by ζ) reduces *D* (Eq. 2.1); (2) Reduction the interelectronic repulsion (quantified by the Racah parameters *B* and *C*) with respect to the free ions (non-relativistic and relativistic nephelauxetic effects, respectively) increases *D*. *Ab initio* ligand field analyses clearly manifest a decrease of *B* and ζ across the series (Table 2.3, CASSCF/NEVPT2 results) reflecting the expected increase of metal-ligand covalence from F to I, as shown in Figures A.20. It is worth considering these two effects on *D* separately.

2.3.6. Effect of Spin-Orbit Coupling (SOC) on *D*

Desrochers and coworkers studied ZFS in 4-coordinate C_{3v} Ni(II) complexes Tp*NiX [Tp*$^-$ = hydrotris(3,5-dimethylpyrazole)borate; X = Cl, Br, I] by HFEPR, reporting

D = +3.93(2), −11.43(3), −22.81(1) cm^{-1}, for X = Cl, Br, I, respectively, for the d^8 S = 1 complexes.[54] Studies by the Angular Overlap Model (AOM)[54] and wave-function-based *ab initio* methods[55] show that the final signs and magnitudes of D parameters here are mostly determined by the metal−ligand covalency and low symmetry in the scorpionate complexes. These 4-coordinate, d^8 Ni(II) complexes are more covalent than the 5-coordinate, high spin d^5 Fe(TPP)X in the current work. Theoretical studies of $[NiX_4]^{2-}$ (X = F, Cl, Br, I) also showed the increasing contribution of intra-ligand spin-orbit coupling to ZFS from F, Cl, Br to I in $[NiX_4]^{2-}$, leading to a sign reversal, between Br and I, of the spin-orbit splitting within the t_2-orbitals of Ni^{2+} ions.[56] Being relatively more ionic, the effect of the intrinsic spin-orbit couplings of the heavier ligands on D in the Fe(TPP)X series is not as strong as the one in the Tp*NiX or $[NiX_4]^{2-}$ complexes. In other words, the $\{Fe^{III}\text{-}X^-\}^7 \rightarrow \{Fe^{II}\text{-}X^\bullet\}^7$ charge transfer is much higher in energy than $\{Ni^{II}\text{-}X^-\}^{10} \rightarrow \{Ni^{I}\text{-}X^\bullet\}^{10}$ so that the large SOC of I^- cannot affect D considerably. Although the N atoms (on the porphyrin ligand) and halides X in Fe(TPP)X are involved in strong σ bonding with Fe(III) (as quantified by the parameters e_σ^N and e_σ^X in Eq. 2.4), there is no first-order spin-orbit coupling in the ground state $^6A_1$. Thus the impact of all these factors on the ZFS of the Fe(TPP)X series is not as large as in the Ni(II) complexes.

2.3.7. Effect of the Nephelauxetic Reduction of *B* and *C* on *D*

D values of axial Fe^{III} complexes are generally underestimated by both CASSCF and NEVPT2 methods. Correlation effects in the S = 5/2 ground state and S = 3/2 excited state are quite different. Dynamical correlation in the latter states is much more pronounced and is largely underestimated at both the CASSCF and NEVPT2 level of

theories. This differential correlation effect results in inter-electronic repulsion parameters *B* and *C* distinctly larger than ones deduced from experiment. This leads to: (a) A larger gap between the $^6A_1$ ground state and the $^4A_2$/^4E excited states; (b) Small values of *D* according to Eq. 2.1. To quantify the effect we have adapted the angular overlap model with parameters from Table 2.3 and studied the dependence of *D* on *B*, while keeping the ratio *C*/*B* unchanged. A model calculation for Fe(TPP)Cl as an example shows a dramatic increase of *D* when lowering *B* (Figure 2.10). Such (nephelauxetic) reduction of *B* is a measure of metal-ligand covalence. The rather large values of *B* deduced from the multireference *ab initio* calculations (1000-1100 cm^{-1}) reflect the rather ionic CASSCF wavefunctions. Due to this ionicity, the nephelauxetic reduction of *B* is largely underestimated at the *ab initio* level. The effect can be quantified by getting *B* that reproduces *D* from the INS work. Adapting again the angular overlap model with same values of the parameters for the complexes (Table 2.3, NEVPT2 set), we obtain *B* = 579 (F), 557 (Cl), 540 (Br), and 518 (I) cm^{-1}. In other words, they are twice as small as their *ab initio* counterparts (both CASSCF and NEVPT2, Table 2.3). Taking this result with precaution (owing to the model character of the given considerations), we can conclude that the reduction of *B* is largely governed by the TPP ligand and further modified by the covalence of the Fe-X bond increasing from F to I. Finally, the large reduction of the parameters *B* deduced from the INS data implies a shift of the electronic transitions $^6A_1 \rightarrow {}^4A_2$ ($^4T_1$) and $^6A_1 \rightarrow {}^4E$ ($^4T_1$) from their *ab initio* values [NEVPT2: 11135 and 20006 (F) to 8960 and 16089 cm^{-1} (I), Table A.6] to the near-IR and IR regions [explicitly: 4738/8878 (F), 3685/9035 (Cl), 2738/7652 (Br), and 1719/6135 (I)]. Thus these transitions are falling down in energy below the Soret

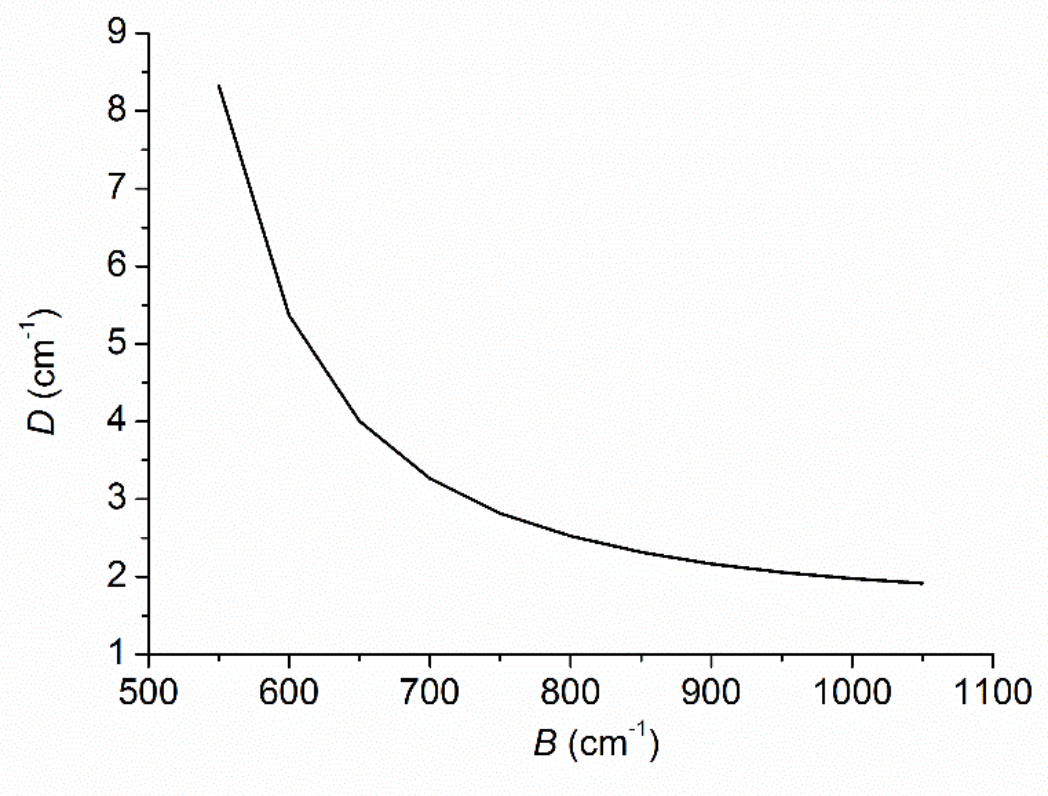

Figure 2.10. Variation of *D* with *B* for Fe(TPP)Cl taken as a model example. The figure has been constructed using the AOMX program package with model parameters set (NEVPT2) from Table 2.3. A *C*/*B* ratio of 4.63 has been adapted using the same data.

(≈ 24000 cm^{-1}) and Q-bands (16000-20000 cm^{-1})[57] π-π* absorption region. This opens an interesting perspective for their spectroscopic characterization.

2.4. Conclusions

Zero-field splittings in Fe(TPP)X [X = F (**1**), Br (**2**), I (**3**)]have been studied by inelastic neutron scattering, providing a rare, complete determination of ZFS parameters in a metalloporphyrin halide series. Ligand field analysis of the *ab initio* data show that the relatively large *D* values for these complexes is due delocalization of the σ d-electrons on the TPP ligand, which lowers the parameter *B* and reduces the energy gap between the ground $^6A_1$ ground and the $^4A_2$ excited state. The trend of the increase in *D*, from X = F, Cl, Br, to I, is further correlated with the increase in the covalency of the Fe-X bond in the same order. *Ab initio* multireference electronic structure calculations and their ligand field analysis allow one to relate the increase in the *D* values with the lowering of the energy gap between the $^6A_1$ ground state and the $^4T_1$ lowest excited state. This lowering is attributed to the weakening of both the σ and the π antibonding interactions between the Fe(III) ion and the axial halide ligand. Quantitative magnetostructural correlation were derived between *D* and the angular overlap model parameters e_σ and e_π, characterizing the bonds of iron(III) ion to the axial ligands.

Single-ion magnets (SIMs) are of intense current interest. There is a significant debate regarding the strategy for the design and synthesis of SIMs. To rationally design SIMs, key factors dictating the sign and magnitude of *D* values in metal complexes need to be identified. The current work not only reports ZFS parameters by inelastic neutron scattering for the 5-coordinate halide complexes but also identifies key factors that

determine the sign and magnitude of *D* values in these Fe^{III} single ion complexes.

An important point we learn from the current study is that, for square pyramidal 5-coordinate high-spin d^5 complexes, *D* may become negative if the equatorial ligand donors are weaker than the axial one.

2.5. Experimental

2.5.1. Synthesis of Fe(TPP)X

Fe(TPP)X [X = F (**1**), Br (**2**), I (**3**)] were prepared by following a literature method[58] with modifications. Since only general procedure for the synthesis of several metalloporphyrins is available in the literature,[35,42,58] details of our syntheses of Fe(TPP)X [X = F, Br, I] are given in Appendix A. The overall synthesis is shown in Scheme 2.2.

Air-stable solid products of Fe(TPP)X [X = F, Br, I] were characterized by UV–visible spectroscopy (Figure A.1) and powder X-ray diffraction (Figures A.2-A.4). Powder diffraction patterns were obtained on the PANalytical Empyrean diffractometer using Cu *K*α radiation (λ = 1.5418 Å) with samples of **1-3** on a zero-background plate holder. Powder X-ray diffraction of **1** is consistent with the simulated pattern predicted from the single-crystal X-ray diffraction data of Fe(TPP)Cl (Figure A.2).[50] We could not use the reported single-crystal X-ray structure of **1**, as some key data are not available.[59] The reported crystal structure does, however, indicate that the solid sample is in the tetragonal system,[59] as the crystal structure of Fe(TPP)Cl.[50] Indexing of our powder X-ray diffraction data from **1** sample by the McMaille method also yielded the same tetragonal cell.[60]

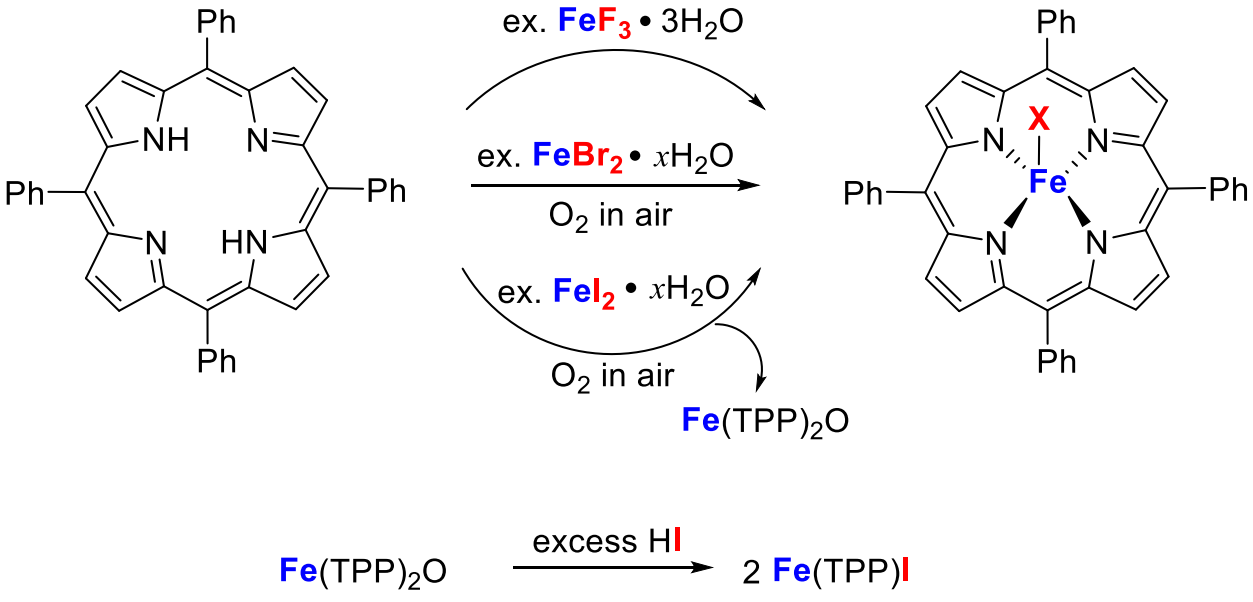

Scheme 2.2. Synthesis of Fe(TPP)X [X = F (**1**), Br (**2**), I (**3**)].

The powder X-ray diffraction of the Fe(TPP)Br (**2**) sample is consistent with the simulated pattern from the single-crystal X-ray diffraction data of **2**,[51,61] indicating that the solid sample is in the monoclinic crystal system. It should be noted that Skelton and White originally reported the structure in $P2_1/c$ [a =10.191(2), b = 16.121(5), c = 23.223(4) Å, β = 115.34(1)°].[51] This space group could be converted to $P2_1/n$.[61] Conversion by the matrix and software at http://www.cryst.ehu.es/cryst/celltran.html (using a primitive P cell) yields $P2_1/n$, a = 10.191(2), b = 16.121(5), c = 20.990(4) Å, β = 90.69(1)°. The powder X-ray diffraction of the **3** sample is consistent with the simulated pattern predicted from the single-crystal X-ray diffraction data of **3** [$P2_1/n$, a = 10.118(3), b = 16.352(4), c = 21.211(7) Å, β = 89.56(2)°],[52] indicating that the sample is also in the monoclinic crystal system. Because INS peaks other than the two expected magnetic transitions were observed for **2** and **3** as discussed below, elemental analyses of the two samples were performed (Appendix A), confirming the purity of the samples. Attempts to obtain mass spectra of Fe(TPP)X [X = F, Br, I] by MALDI/TOF (matrix-assisted laser desorption ionization time-of-flight) led to the observation of $Fe(TPP)^+$, indicating dissociation of the Fe−X bonds during the mass spectroscopic process (Appendix A).

2.5.2. INS Studies of Fe(TPP)X [X = F (1), Br (2), I (3)]

The INS measurements were carried out on the CNCS which is a direct geometry, time-of-flight spectrometer that receives a beam from a coupled cryogenic H_2 moderator.[49] For energy selection, the CNCS employs four chopper assemblies. The speeds and slit widths of the choppers can be varied, allowing adjustments in the

instrumental resolution and intensity of the incident beam. Approximately 500 mg of each sample was loaded into a ½-inch-thick aluminum tube. The three tubes, containing Fe(TPP)X [X = F (**1**), Br (**2**), I (**3**)] each, were placed in a sample holder. The sample holder was mounted in a standard liquid helium cryostat with a base temperature of T = 1.6 K. An oscillating radial collimator was used to reduce background scattering form the tail of the cryostat. Vanadium was used as a standard for the detector efficiency correction.

The incident neutron energy for every measurement was chosen to cover the anticipated region of interest in both the energy *E* and scattering-vector *Q* space.[18, 21] The small incident energy is especially important to observe excitations near the elastic peak (at energy transfer close to 0 cm^{-1}) as the full-width-at-half-maximum (FWHM) of the elastic peak, which is typically 1.5-2% of the incident energy, would be narrow, giving better energy resolution.

For **1**, measurements were performed at 1.6, 10, 50, and 100 K with incident neutron beam energies E_i = 24.20, 40.89, and 97.35 cm^{-1}. For **2** and **3**, measurements were performed at 1.6, 10, and 50 K with E_i = 24.20, 40.89, and 97.35 cm^{-1}. It took approximately 24 h to run the 3 samples at various temperatures and incident neutron energies. Data were then reduced and analyzed using the DAVE (Data Analysis and Visualization Environment) program package.[62]

2.5.3. Computational Details

Although the crystal structures of Fe(TPP)X [X = F (**1**),[59] Cl,[50] Br (**2**),[51] and I (**3**)[52]] complexes have been reported, only atomic coordinates for the structures of X = Cl, Br,

and I are available. In addition, the structure of X = Cl is disordered.[52] Therefore, for the sake of our analysis, we have used DFT geometries for all four complexes. Calculations for the available experimental structures show no major differences (Table A.7). DFT geometry optimization of all four complexes Fe(TPP)X [X = F (**1**), Cl, Br (**2**), I (**3**)] complexes was done with the BP86 functional and def2-TZVP basis sets. van der Waals correction for non-bonding interactions were included following Grimme.[63-64] Because of the participation of heavy ligands to the coordination sphere of Fe^{3+} scalar relativistic corrections were included with the Douglas-Kroll-Hess method along with appropriate basis sets.[65] Structural parameters from these computations are compared with X-ray data in Table 2.2.

The d^5 configuration of Fe^{III} gives rise to one S = 5/2 ground (6 microstates) and to 24 S = 3/2 (96 microstates) and 75 S = 1/2 (150 microstates) electronically excited states. Because the SOC operator connects only $\Delta S = 0, \pm 1$ and $\Delta L = 0, \pm 1$ states, the spin-components of the S = ½ states do not couple to the S = 5/2 ground state and have been neglected. Non-relativistic energy levels and wave functions have been computed using the Complete-Active-Space-Self-Consistent Field (CASSCF) method,[66] averaging over the electron densities of all considered states and taking an active space with 5 electrons distributed over the 5 3d-MOs (CAS(5,5)). Dynamical (short range) correlation effects were accounted for by using N-Electron Valence Perturbation Theory to Second order (NEVPT2).[67-71] The effect of NEVPT2 on the energy levels is to replace the diagonal matrix elements of the configuration interaction (CI) matrix given by CASSCF by improved diagonal energies. Such a replacement provides more accurate (but still approximate) energetics while keeping to the same (zeroth order) CASSCF

wave functions. CASSCF and NEVPT2 methods have been efficiently implemented in the program package ORCA[72] and allow computations on real systems (without necessity of model truncations) with unprecedented size (up to 100-200 atoms, 2000 contracted basis functions). From the resulting energies of many-electron states spin-Hamiltonian parameters were computed applying a computational protocol described elsewhere.[73] To this end, spin-orbit coupling (SOC) was taken into account using a mean-field spin-orbit coupling operator.[74-75] Spin-orbit mixing of non-relativistic CI eigenfunctions and splitting of the corresponding eigenvalues are accounted for by Quasi Degenerate Perturbation Theory (QDPT).[75] In these, as well as in the correlated calculations triple-ζ valence quality basis sets (def2-TZVP)[76-77] were used. Ground state ZFS parameters have been computed by diagonalizing the state interaction SOC matrix non-perturbatively using effective Hamiltonian theory. CASSCF and NEVPT2 energies for the lowest 17 excited states are listed in Tables A.5 and A.6.

Metal ligand antibonding energies have been derived using the angular overlap model (AOM)[78-79] of the ligand field with parameters which have been obtained from a least squares fit to 5x5 ligand field matrices resulting from the *ab initio* ligand field theory (AILFT) method.[80-81] Inter-electronic repulsion between the 3d-electrons has been modelled in terms of two Racah parameters *B* and *C*. AOM calculations were carried out with the AOMX program.[82]

Chapter 3

Direct Determination of Magnetic Excitations in SMMs by Inelastic Neutron Scattering

Reproduced in part with permission from:

Chen, L.; Cui, H.-H.; Stavretis, S.E.; Hunter, S.C.; Zhang, Y.-Q.; Chen, X.-T.; Sun, Y.-C.; Wang, Z.; Song, Y.; Podlesnyak A. A.; Ouyang, Z.-W., Xue, Z.-L., Slow Magnetic Relaxations in Cobalt(II) Tetranitrate Complexes. Studies of Magnetic Anisotropy by Inelastic Neutron Scattering and High-Frequency and -Field EPR Spectroscopy. *Inorganic Chemistry* **2016**, *55*, 12603.

https://pubs.acs.org/doi/abs/10.1021/acs.inorgchem.6b01544

This author helped collect the INS data on $(A)_2[Co(NO_3)_4]$ [A = Ph_4P^+ (**4**), $MePh_3P^+$ (**5**) and Ph_4As^+ (**6**)] at CNCS and conducted the analysis of the INS data. In addition, she compared the INS results with other data (HF-EPR and magnetometry measurements). This author interpreted the differences in relaxation processes in $(PPh_4)_2[Co(NO_3)_4]\cdot CH_2Cl_2$ (**4**) and $(MePPh_3)_2[Co(NO_3)_4]$ (**5**) using the AC susceptibility measurements and INS data. The magnetometry and HF-EPR studies, conducted by the co-authors, are included in this Chapter to fully understand the project and add context to the INS work presented here.

3.1. Abstract

Inelastic neutron scattering (INS) has been used to probe magnetic excitations in several mononuclear complexes: (1) SMMs $(A)_2[Co(NO_3)_4]$ (A = Ph_4P^+, **4**; $MePh_3P^+$, **5**) and non-SMM $(Ph_4As)_2[Co(NO_3)_4]$ (**6**); (2) SMM $[Co(12C4)_2](I_3)_2(12C4)$ (12C4 = 12-crown-4)] (**7**); (3) SMMs $Co(acac)_2(D_2O)_2$ (**8-*d*$_4$**) and $Co(acac\text{-}d_7)_2(D_2O)_2$ (**8-*d*$_{18}$**); (4) SMM $Er[N(SiMe_3)_2]_3$ (**10**). The magnetic excitations $U = 2(D^2 + 3E^2)^{1/2}$ for **4-6**, **7**, **8-*d*$_4$** and **8-*d*$_{18}$** and m_J (KD_{ground} to $KD_{excited}$; KD = Kramers doublet) for **10** have been determined by INS through the following methods: (1) Temperature dependence; (2) $|Q|$ dependence; (3) Diamagnetic control; (4) Application of an external magnetic field. The $|Q|$ dependence to determine magnetic excitation is unique to INS. These studies represent the first in the United States to determine magnetic excitations in SMMs by a variety of neutron instruments such as the Disk Neutron Chopper Spectrometer (DCS) at the NIST Center for Neutron Research and Cold Neutron Chopper Spectrometer (CNCS) and Vibrational Spectrometer (VISION) at Oak Ridge National Laboratory (ORNL). The main findings of this work include the following: (1) Use of magnetic fields to determine large magnetic separations (>40 cm^{-1}). (2) Direct determination of separations in protonated SMMs such as single crystals of **7**. The use of the single crystals improves the data quality by reducing broadening of the magnetic peak typically observed in powder samples as a result of different orientations of the powders inside the magnetic fields. (3) Probe of the origin of spin-phonon entangled peaks with $|Q|$ dependence. INS has been underutilized to determine magnetic separations in SMMs. Studies of several different SMMs with varying magnitudes of magnetic separations here demonstrate how to best study these compounds with INS.

3.2. Introduction

3.2.1. Methods to Probe SMMs with INS

There exist many challenges in identifying magnetic excitations with spectroscopic methods, including the overall weakness of expected magnetic contribution and identifying the magnetic peak amongst many phonon peaks. Inelastic neutron scattering (INS) is a unique, direct probe to study magnetic excitations in complexes of both d-[6,22,45,83-91] and f-metals.[92-98] In INS, magnetic excitations can be determined by a variety of methods: (1) Temperature dependence; (2) $|Q|$ dependence; (3) Diamagnetic control; (4) Application of an external magnetic field. One challenge that is relevant solely to INS is the strong incoherent scattering from H atoms in ligands of metal complexes. However, with a combination of the aforementioned techniques INS can reveal the magnetic excitations in the complexes. The observation of the magnetic excitations in SMMs is particularly significant.

The use of temperature dependence and diamagnetic controls has been previously utilized as a method to distinguish magnetic excitations in INS. For example, deuterated carbonate-bridged lanthanide (Ho and Er) triangles were synthesized along with the diamagnetic Y analogue (for comparison of phonon background) to find the magnetic excitation with variable temperatures.[92] These excitations were found to be <24 cm^{-1} (3 meV). Magnetic and phonon peaks exhibit different temperature dependences. The Bose correction has been used to reveal the magnetic excitation by INS of a Co^{II}-Y^{III} dinuclear SMM.[88] A peak at ~95.2 cm^{-1} was determined to show the greatest intensity drop between 4 and 100 K and therefore assigned to be a magnetic excitation.

Upon increasing the temperature, the intensity of the magnetic excitation will decrease according to Boltzmann statistics whereas phonon peaks *should* remain consistent with temperature. Often the Bose-correction ($f_{corrected}(E)$, Eq. 3.1) is used to eliminate any temperature dependence of the phonon peaks.

$$f_{corrected}(E) = \frac{1-\exp\left(\frac{-2E}{k_b T}\right)}{1+\exp\left(\frac{-2E}{k_b T}\right)} \times f(E) \qquad \text{(Eq. 3.1)}$$

where E is the energy, k_b is the Boltzmann constant (= 0.6950476 cm^{-1}/K), T is the temperature, and $f(E)$ is the uncorrected intensity of the INS data.

|*Q*| dependence has been used to probe a deuterated sample of a Tb-Cu di-nuclear SMM.[93] Magnetic intensity falls off with increased *Q* as scattering of the unpaired electrons in the outermost electronic orbitals in reciprocal space decreases. Therefore, peaks of magnetic origin decrease in intensity with increased *Q*. In contrast, peaks of vibrational origin increase in intensity with increased *Q*. However, strong incoherent scattering from samples containing non-deuterated complexes *may* smear out *Q* dependence of the magnetic peaks and instrumentation constraints might limit the accessible *Q* range, leading to roughly constant intensities of the magnetic peaks throughout the observable *Q* range in the samples.

There are few examples of using INS to determine magnetic excitations in mononuclear SMMs.[6,95,97] The current methods based on diamagnetic controls and temperature dependence, to probe magnetic excitations by INS, are not always

successful. For example, INS was unsuccessful at determining the magnetic excitation of an Yb^{3+} SMM.[16] The authors attributed this to overall weakness of the expected magnetic contribution and background contributions from H atoms.[16] Often *Q* dependence studies require deuteration of the SMMs, especially >50 cm^{-1} where phonons are prominent.

One unexplored area is combining magnetic fields with INS to study SMMs. While magnetic transition would be subjected to the Zeeman effect and therefore will shift in energy with field, phonons for the most part will remain unchanged (if there are no spin-phonon coupled peaks). INS with field is still not a routine measurement as, to our knowledge; no example of measurements on a mononuclear SMM has been reported. Early work includes the archetypical polynuclear $Mn_{12}Ac$ SMM which has a magnetic excitation <11.3 cm^{-1}.[99] It is often challenging to determine magnetic peaks at higher energies due to the prevalent phonons. These measurements are needed, as they are a critical part to understanding the properties of SMMs.

A variety of mononuclear SMMs including (1) $(A)_2[Co(NO_3)_4]$ [A = Ph_4P^+ (**4**), $MePh_3P^+$ (**5**) and Ph_4As^+ (**6**)]; (2) $[Co(12C4)_2](I_3)_2(12C4)$ (12C4 = 12-crown-4, **7**); (3) $Co(acac)_2(D_2O)_2$ (**8-*d*$_4$**) and $Co(acac\text{-}d_7)_2(D_2O)_2$ (**8-*d*$_{18}$**) and (4) $Er[N(SiMe_3)_2]_3$ (**10**) have been probed to examine how INS can be used to study SMMs with magnetic excitations at a variety of energy ranges. Different neutron spectrometers and sample environments have been explored to address the current challenges of using INS to magnetic excitations. Non-deuterated and deuterated samples as well as powder and single crystals have been studied to reveal the full potential of neutron scattering, as, at current, INS measurements are not routine.

3.2.2. Instrumentation in INS

There are two types of time-of-flight inelastic scattering instruments for INS, direct and indirect geometry spectrometers (Scheme 3.1). Cold Neutron Chopper Spectrometer (CNCS, Oak Ridge National Laboratory,[49] Oak Ridge, TN) and Disk Chopper Spectrometer (DCS,[100] NIST National Center for Neutron Research, Gaithersburg, MD) are examples of direct geometry instruments in the United States. Vibrational Spectrometer (VISION,[101] ORNL) is an example of an indirect geometry instrument. Each type of the spectrometers has advantages and disadvantages as summarized below.

A direct geometry spectrometer has a fixed incident energy E_i and the energy transfer between the neutrons and the sample is obtained by measuring scattered intensity as a function of E_f.[21] E_i is defined by a chopper that selects a single energy from an incident white beam and E_f is measured by time-of-flight.[102] There are a large number of detectors (array) at different scattering angles enabling a wide range of (Q,ω) space to be measured.

As an example, CNCS routinely accesses E_i between 8 and 400 cm^{-1} (1 and 50 meV) with an energy resolution between 2 and 3% of E_i at the elastic line.[103] In addition, the Q range between 0.05 and 10 $Å^{-1}$ gives access to smaller Q.

Direct geometry instruments can also be paired with external magnetic field in the sample environment. For example, CNCS can reach fields up to 8 T,[104] while DCS up to 10 T.

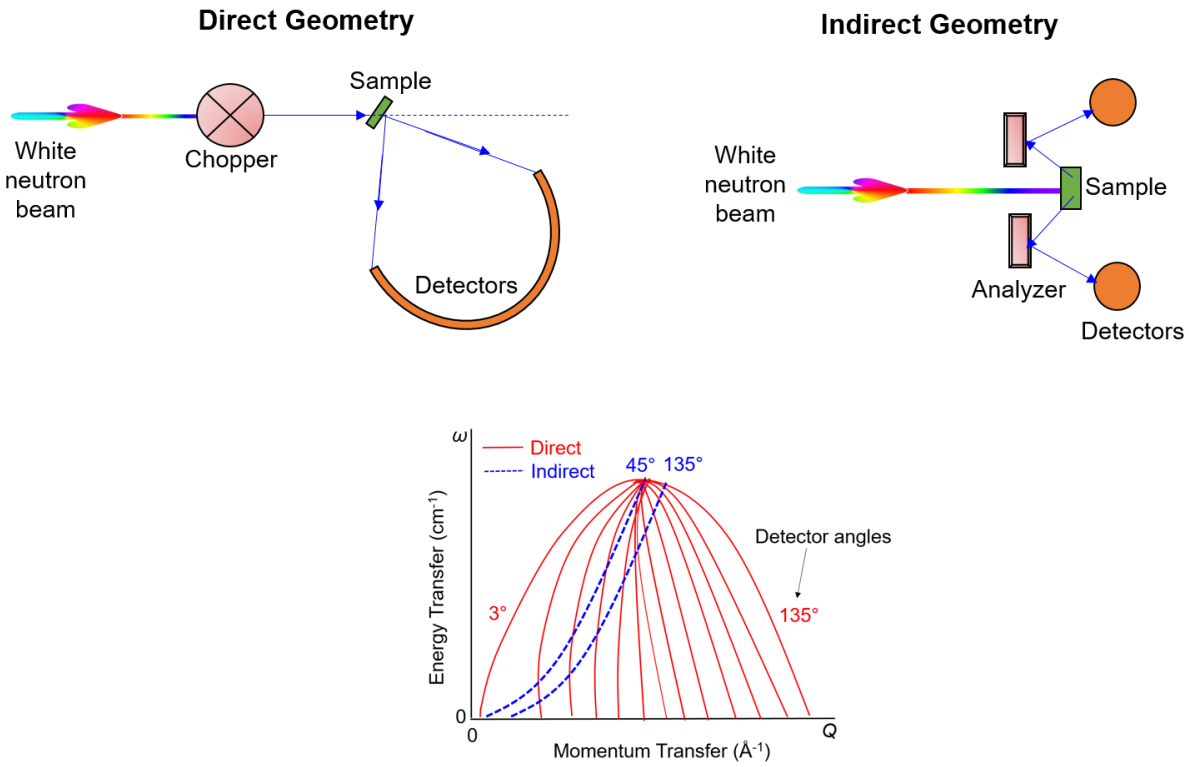

Scheme 3.1. (Top) Depiction of direct (left panel) and indirect geometry (right panel) instrumentation. (Bottom) Representation of trajectories in (Q, ω) space for a direct geometry spectrometer with detectors at angles between 3° and 135° (red lines). Indirect geometry spectrometer with scattering angles of 45° and 135°, forward scattering and backscattering, respectively (blue dashed lines).

Indirect geometry spectrometers rely on a fixed E_f by a crystal or filter while E_i is measured by time-of-flight of neutrons arriving on a small detector area.[19] E_f is usually specified to be small in energy (~28.2 cm^{-1} for VISION). Neutrons spread out in time traveling from the source to the sample arriving at times that relate to the incident wavelengths. This technique gives energy of 0-4000 cm^{-1} and Q ~2-13 $Å^{-1}$ (0.48-3.1 Å). The energy resolution of <1.5% $\Delta E/E$ is not determined by E_i as is the case with direct geometry instruments.[20,101] While these instruments have good energy resolution, the exchange is a fixed trajectory through $\boldsymbol{Q}$ space.[19] For most energy transfers, E_i is much larger than E_f. Thus, the momentum transfer $\boldsymbol{Q}$ is almost equal to $\boldsymbol{k_i}$ irrespective of the scattering angle. Therefore, the $\boldsymbol{Q}$ value is dependent on E giving the relationship: $E = 16.7Q^2$.[19] VISION has two banks of analyzers with two different scattering angles, one at 45° (forward scattering) and another at 135° (backscattering) giving two spectra per run.

3.2.3. $(A)_2[Co(NO_3)_4]$ [A = Ph_4P^+ (4), $MePh_3P^+$ (5) and Ph_4As^+ (6)]

Three mononuclear Co(II) nitrate complexes $(A)_2[Co(NO_3)_4]$ (Figure 3.1) with different counter-cations, Ph_4P^+ (**4**), $MePh_3P^+$ (**5**) and Ph_4As^+ (**6**) have been studied by X-ray crystallography, magnetic measurements, INS and HF-EPR. The X-ray diffraction studies showed that the structure of tetranitrate cobalt anion varies with the counter-cation. **4** and **5** have highly irregular seven-coordinate geometries while the central Co(II) ion of **6** is in a distorted dodecahedral configuration. These complexes are $S = 3/2$ systems with a magnetic separation equal of $U = 2(D^2 + 3E^2)^{1/2}$ (Scheme 3.2). Several seven-coordinate Co(II)-SIMs in the distorted pentagonal bipyramid geometry have

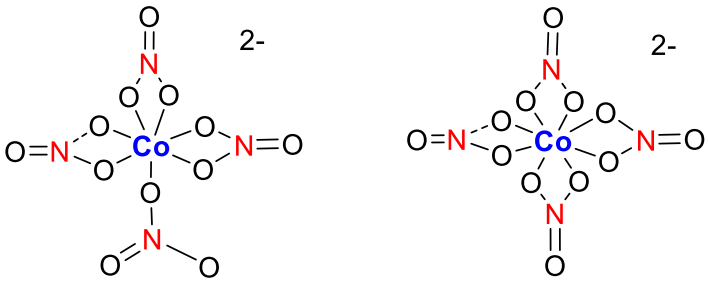

Figure 3.1. Structures of the anions $(A)_2[Co(NO_3)_4]$ (left) **4/5** and (right) **6**.

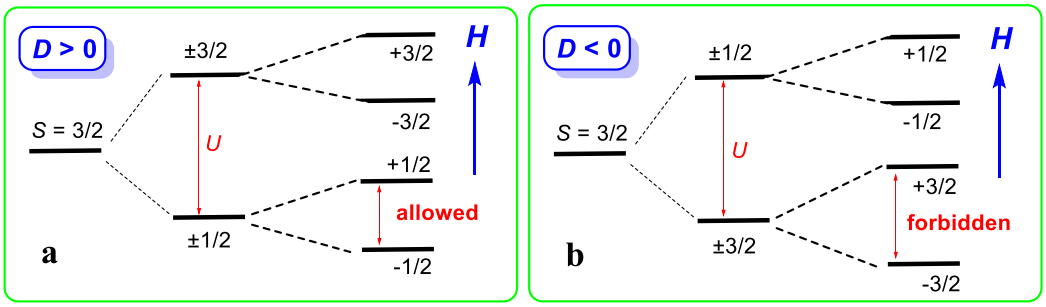

Scheme 3.2. (a) ZFS energy diagram, $D > 0$ with the application of a magnetic field. (b) ZFS energy diagram, $D < 0$ with the application of a magnetic field. $U = 2(D^2 + 3E^2)^{1/2}$.

been reported to exhibit large positive anisotropy.[105] Due to the limited number of known high-coordinate SMMs based on d-block ions, it is highly desirable to have more examples of high-coordinate SMMs in order to get an insight into the relationships between the coordination environment, local symmetry, magnetic anisotropy, and dynamic magnetic properties of SMMs.

Inelastic neutron scattering (INS) has been used to probe the magnetic properties of metal complexes, especially excitations among low-lying energy levels.[44,106-107] Most of the INS studies were limited to paramagnetic metal clusters,[18,22,44,106-107] and few reports have been published on mononuclear metal complexes[8,47-48,108] including one Co(II)-[88] and Re(IV)[109]-based SIM. INS has been conducted here to directly measure $U = 2(D^2 + 3E^2)^{1/2}$, determine the sign of D, and study the phonons near the ZFS peak.

3.2.4. $[Co(12C4)_2](I_3)_2(12C4)$ (12C4 = 12-crown-4) (7)

$[Co(12C4)_2](I_3)_2(12C4)$ (12C4 = 12-crown-4) (**7**), an eight-coordinate Co(II) SMM ($D < 0$), was previously reported to exhibit slow magnetic relaxation (Figure 3.2).[17] This compound was the first eight-coordinate 3d mononuclear complex classified as an SMM (with applied DC field of 500 Oe).[17] Typically, low-coordinate SMMs are more desirable because the d orbitals have a small separation between electronic ground and excited states allowing SOC to take place.[1,81,110] The ZFS diagram, for this $S = 3/2$ system under the perturbation of field is shown in Scheme 3.2b.

Previously, the DC magnetic susceptibility measurements was fit using the spin-Hamiltonian (Eq. 1.1) to yield $D = -37.6$ and $E = 0.1$ cm^{-1}.[17] In addition, field-dependent

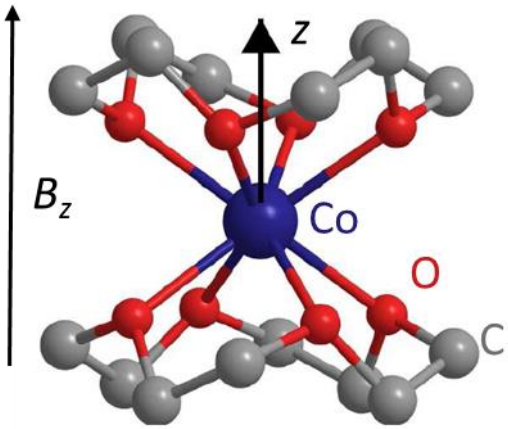

Figure 3.2. Structure of the cation, $[Co(12\text{-crown-}4)_2]^{2+}$, showing the local C_4 axis indicated by the black arrow.

magnetization was performed at applied magnetic fields of 1-7 T and temperatures between 1.8 and 5.0 K. Modeling the data with Eq. 1.1 gave D = -38.0 cm^{-1} and E= -0.75 cm^{-1}. To determine the sign of D, HF-EPR of **7** was collected between 100 and 700 GHz (3.3 and 23.3 cm^{-1}) with magnetic fields from 0 to 25 T.[17] These results were consistent with a large negative D (transition between the ±3/2 is forbidden since ΔM_S = 3; Scheme 3.2b). The ZFS parameters were also calculated using the CASPT2 method to yield values of D = -70.1 and E = 1.05 cm^{-1}. AC magnetic susceptibility measurements provided an effective barrier U_{eff} = 17.0 cm^{-1}.

As discussed in Chapter 1, determining the ZFS by magnetometry measurements is often inaccurate due to a multi-parameter fit of Eq. 1.1. Therefore, INS with the application of an external magnetic field has been utilized to *directly* determine U on oriented single crystals of **7**. Figure 3.2 shows the orientation of the magnetic axis which the crystals were aligned parallel to observe a discrete U peak shift. This compound possesses a challenge to study by INS as each molecule of **7** has 48 H atoms.

3.2.5. $Co(acac)_2(D_2O)_2$ (8-d_4) and $Co(acac\text{-}d_7)_2(D_2O)_2$ (8-d_{18})

$Co(acac)_2(H_2O)_2$ (**8**) is a prototypical example of an SMM with a positive D and large U.[10] Typically complexes with $D > 0$ are not considered to be SMMs due to the spin-allowed intra-Kramer transition (M_S = -1/2 $\rightarrow$ +1/2).[1] **8** is a high-spin, d^7 hexa-coordinated complex with a pseudo-tetragonal structure (Figure 3.3a). X-ray diffraction at 100 K, shows C_{2h} molecular symmetry. If the local symmetry around the Co(II) ion is approximated to D_{4h}, the ground electronic state is $^4A_{2g}$ (^4A_g for C_{2h}).[111] For high-spin, d^7

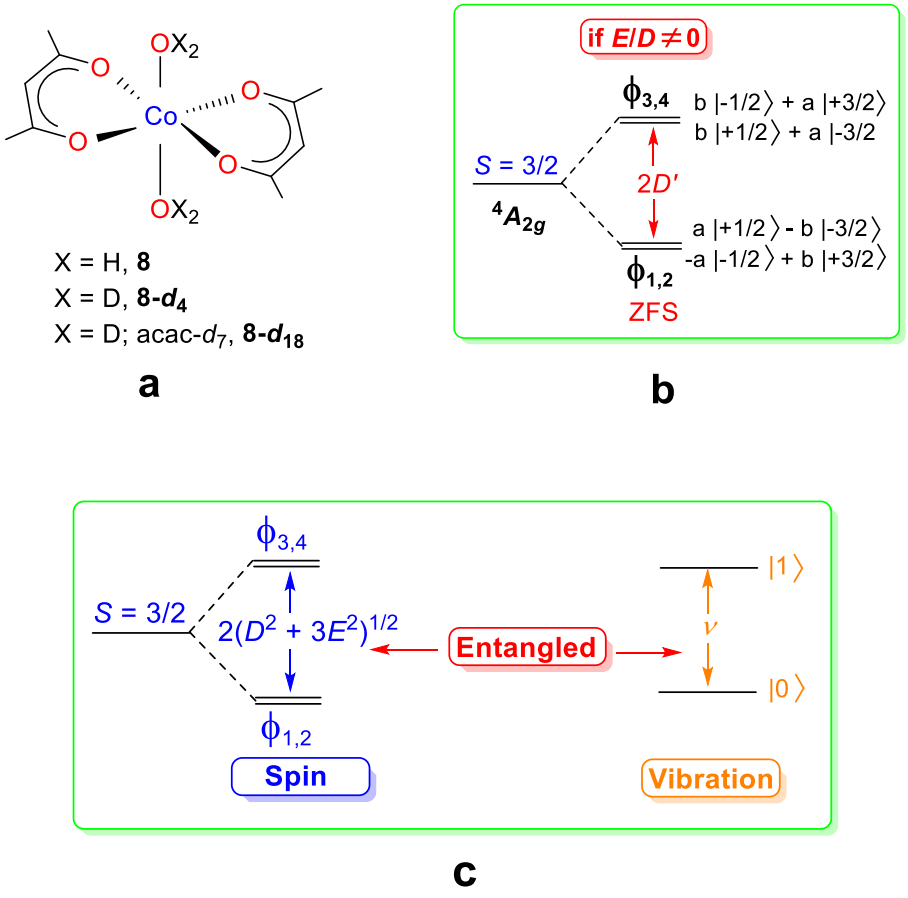

Figure 3.3. (a) Structures of **8**, **8-*d*$_4$** and **8-*d*$_{18}$**. (b) The quartet levels in **8** with lower symmetry [$E/D \neq 0$, $D > 0$, $U = 2(D^2 + 3E^2)^{1/2}$], where the mixing coefficients a = cos β and b = sin β are described by the mixing angle β obtained from the spin Hamiltonian (S = 3/2) with large D in the absence of field.[112-113] Mixing depends on the rhombicity as $\tan 2\beta = \sqrt{3}\,(E/D)$ (SI of ref. 10). (c) Representation of spin-phonon coupled excitations present in **8**, **8-*d*$_4$** and **8-*d*$_{18}$**.

complexes in D_{4h} symmetry, ZFS leads to two Kramers doublets (KDs) that, in the absence of rhombicity in zero field, can be labelled by $M_S = \pm 1/2$ and $\pm 3/2$. When $D < 0$, $E/D \approx 0$, the $M_S = \pm 3/2$ KD is the ground state (Scheme 3.1b) with an easy axis of magnetization along the *z*-direction. For sufficiently large $|D|$, fields up to a few Tesla cannot mix the two KDs and induce any measurable magnetization in the *x*- or *y*-directions. In contrast, for $D > 0$ and $E/D \approx 0$ complexes (Figure 3.3c), the ground state KD $M_S = \pm 1/2$ is split into $M_S = -1/2$ and $+1/2$ states by Zeeman splitting which is strongly direction-dependent. SMM behaviors in such complexes are not expected because transitions between these two states are spin-allowed.

Gómez-Coca and coworkers showed that **8** behaves as an SMM (in external DC fields) despite its low symmetry and dominating large rhombicity observed in EPR.[10] Magnetic susceptibility fittings revealed large $D \approx 57$ cm^{-1}. EPR spectra showed typical rhombic effective g'-values (2.65, 6.95, 1.83), rendering an easy axis of magnetization (along *y*), but this is far from the usual axial situation encountered for $D < 0$, $E/D \approx 0$, namely $g' = (0, 0, g'_z)$. The best global parametrization for EPR and susceptibility data was favored to have large rhombicity, $E/D = 0.31$, and moderate *g* anisotropy [for $S = 3/2$, $g = (2.50, 2.57, 2.40)$]. But in principle almost any value of E/D could be adopted, if the anisotropy of *g* is increased. The effects are covariant, because both rhombicity and *g* anisotropy are mixing M_S functions, at least for finite fields, as visualized in Figure 3.3b. SH parameters cannot be deduced experimentally because no EPR spectrum is feasible for such highly excited "$M_S = \pm 3/2$" KD in **1**. *Ab initio* calculations yielded different values: $D = 91.2$, $E = 10.1$ cm^{-1} (CASSCF) and $D = 63.3$, $E = 9.3$ cm^{-1} (CASPT2).

Their ZFS transitions have been probed by a combination of Raman, far-IR and

INS spectroscopies. (Only INS will be discussed in this dissertation.) Nearly degenerate ZFS and phonon peaks undergo spin-phonon couplings at 0 T, as revealed by these spectroscopies (Figure 3.3c). In magneto-Raman spectra, the magnetic features of these coupled peaks move and interact with other phonons of *g* symmetry as avoided crossings (coupling constants ≈ 1-2 cm^{-1}). Phonon features of the coupled peaks are directly observed with applied magnetic fields. Far-IR spectra reveal magnetic features of these spin-phonon-coupled peaks, while INS exhibits both the magnetic and phonon features of the coupled peaks.

3.2.6. $Er[N(SiMe_3)_2]_3$ (10)

$Er[N(SiMe_3)_2]_3$ (**10**) was the first equatorial, Er-based SMM.[114] Lanthanide-based SMMs are attractive based on their innate spin-orbital coupling.[115] For Er(III) ions it is desirable to have prolate shaped electron densities.[115] This prolate geometry minimizes charge contact with the axially located f-element electron density, stabilizing the m_J states. Low-coordinate SMMs give highly axial equatorially coordinate geometries yielding large magnetic anisotropies.[81,114] $Er[N(SiMe_3)_2]_3$ (**10**) (Figure 3.4) has trigonal geometry with a C_3 axis with a magnetic ground state of $m_J = \pm 15/2$.[114] This low geometry enhances the uniaxial anisotropy by the crystal field only in equatorial positions.

The crystal field splitting pattern was previously simulated by the crystal field Hamiltonian for C_{3v} Er(III).[116] The magnetic ground to first excited state ($m_J = \pm 15/2 \rightarrow \pm 13/2$) was computed to be 82 cm^{-1} (Figure 3.5). Alternatively, the first excited state was found to be at 85 cm^{-1} from fitting of the ln(τ) vs T^{-1} data (τ = relaxation time in the AC

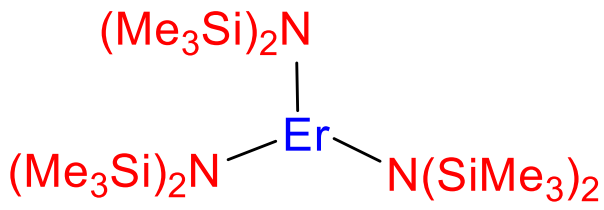

Figure 3.4. Structure of $Er[N(SiMe_3)_2]_3$ (**10**).

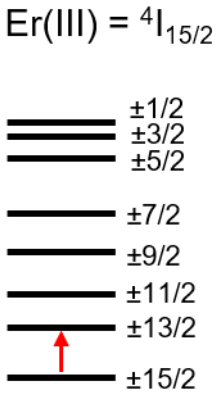

Figure 3.5. Energy and m_J values of the sublevels of the ground multiplet of **10**. The red arrow indicates the transition from $m_J = \pm 15/2 \rightarrow \pm 13/2$.

susceptibility measurement; T = temperature).[114] *Ab initio* calculations in MOLCAS were used to compute $m_J = \pm 15/2 \rightarrow \pm 13/2$ of **10** to be 101 cm^{-1}.[117]

INS in an external magnetic field has been utilized to directly measure the magnetic excitation of this protonated complex with a large magnetic separation.

3.3. Results and Discussion

3.3.1. $(A)_2[Co(NO_3)_4]$ [A = Ph_4P^+ (4), $MePh_3P^+$ (5) and Ph_4As^+ (6)]

3.3.1.1. Static Magnetic Properties

Before discussing the INS data, it is beneficial to understand the static magnetic properties of $(PPh_4)_2[Co(NO_3)_4]\cdot CH_2Cl_2$ (**4**), $(MePPh_3)_2[Co(NO_3)_4]$ (**5**) and $(AsPh_4)_2[Co(NO_3)_4]$ (**6**). Variable-temperature, direct-current (DC) magnetic susceptibilities were measured for polycrystalline samples of **4**-**6** at a field of 2000 Oe in the temperature range of 1.8-300 K. The resulting $\chi_M T$ versus T curves are shown in Figure 3.6. At room temperature, the $\chi_M T$ values are 2.41, 2.16 and 2.31 cm^3 K mol^{-1}, consistent with an S = 3/2 spin center with g = 2.27, 2.15 and 2.22 for **4**-**6**, respectively. These values show a significant decrease below 60, 130 and 50 K for **4**-**6**, reaching values of 1.65, 1.45 and 1.60 cm^3 K mol^{-1} at 1.8 K, respectively. In the absence of intermolecular magnetic interactions judged by the long Co---Co distances and no significant contacts among the ligands, this decline at low temperature is attributed to the intrinsic magnetic anisotropy of the Co(II) ions in **4**-**6** and therefore the presence of ZFS.

The field-dependent magnetizations were measured for **4**-**6** at applied magnetic fields in the range of 1–7 T at 1.8 K (Figure B.8). The magnetizations do not reach

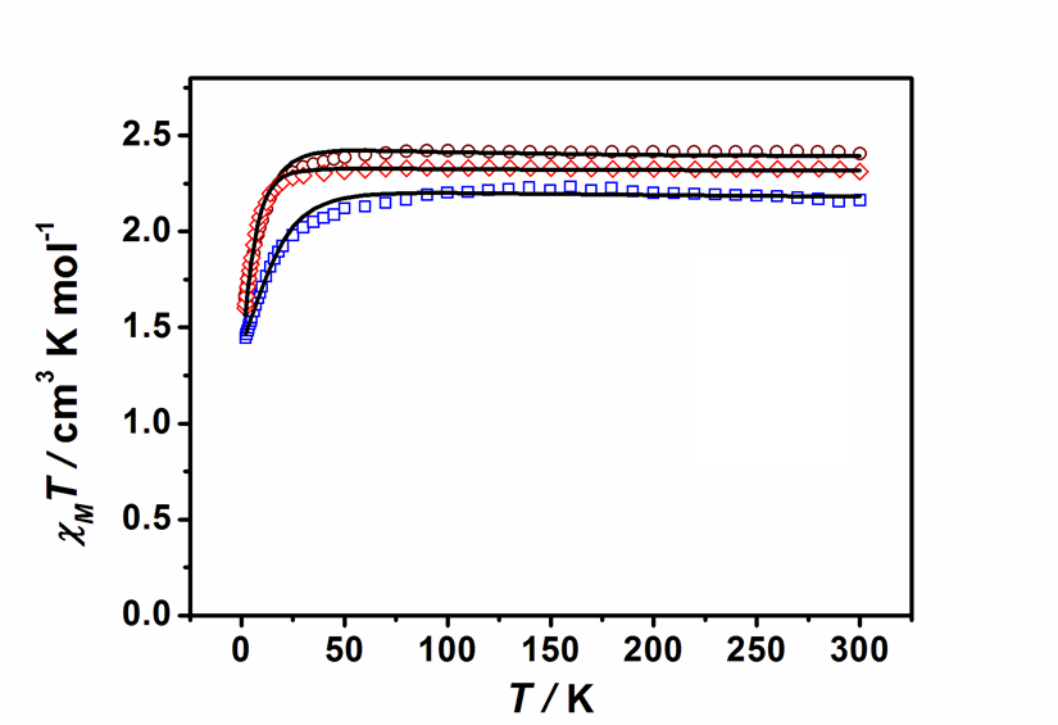

Figure 3.6. Variable-temperature DC susceptibility data under an applied DC field of 2000 Oe **4** (brown circles)**, 5** (blue squares) and **6** (red diamonds). Solid black lines indicate the best fits with the *PHI* program.[36]

saturation at 7 T with 2.44, 2.30 and 2.58 *Nβ* for **4**-**6**, respectively. Low-temperature magnetization data from 1.8 to 5.0 K at various applied DC fields were also measured for **4**-**6** (Figures B.9-B.11). Non-saturation of magnetization at 7 T and the non-superposition of *M* versus *H/T* curves suggest the presence of significant magnetic anisotropies in **4**-**6**. To estimate the zero-field splitting parameters *D* and *E*, the $\chi_M T$ versus *T* and *M* versus *H/T* curves at different temperatures were simultaneously fitted using the *PHI* program[118] by the anisotropic spin Hamiltonian (SH) (with $g_x = g_y$) as given in Eq. 1.1, which includes the axial/rhombic ZFS and Zeeman interactions. The best fits afforded the parameters for **4**-**6** in Table 3.1. The signs of axial ZFS parameters *D* for **4**-**6** are positive. The *D* value for **6** is smaller than those for **4** and **5**, probably due to the different coordination environments of **4** and **5** compared to **6**. It is known that DC magnetic data usually could not yield accurate values for *D* and *E*, especially their signs. Therefore, HF-EPR and INS studies have been performed to further investigate their magnetic anisotropy. It should be noted that the initial fittings of the magnetometry data led to *D* values of -12.5, -9.0, -6.8 cm^{-1} for **4**-**6**, respectively. Upon receiving the INS results, the DC magnetic data were refit to give the *D* values presented in Table 3.1.

3.3.1.2. INS Studies

To further investigate the magnetic anisotropy, the polycrystalline samples of **4**-**6** were studied by INS. Data for **4** were collected at varying temperatures to observe the sole ZFS transition in zero-field for the $S = 3/2$ system. The resulting energy spectrum exhibits a peak associated with transitions from $M_S = \pm 1/2$ to $\pm 3/2$ (Scheme 3.2a). The

splitting between the two Kramers doublets is $U = 2(D^2 + 3E^2)^{1/2}$. (It is $2D$ for the axial symmetrical system when $E = 0$.) In the INS spectra of **4**, a peak at 22.5(2) cm^{-1} is observed with an incident energy of 53.7 cm^{-1} (Figures 3.7; B.1, Table B.1 in Appendix B). As the temperature is increased from 1.7 to 100 K, the population in the ground state is decreased leading to a less intense transition. At 50 K, a peak at –22.5(2) cm^{-1} is observed, indicating that the incident neurons gain energy from the sample in the INS process. During the scattering process, those molecules return to the ground state transferring the energy to the neutrons. Therefore, the zero-field splitting value of $U = 2(D^2 + 3E^2)^{1/2}$ was determined to be 22.5(2) cm^{-1} for **4** from the sole magnetic transition. Peaks of magnetic excitations fall off with increasing $|Q|$, as a result of the decrease in the distribution of spin and orbital magnetization from unpaired electrons. The opposite is true for peaks of the vibrational origin which increase in intensity with $|Q|$. The decrease in magnetic excitations follows the square of the magnetic form factor $F(Q)$ in is true for peaks of the vibrational origin which increase in intensity with $|Q|$. The decrease in magnetic excitations follows the square of the magnetic form factor $F(Q)$ in Eq. 1.3. Additional information about the magnetic peak in the INS spectra of **4** are provided by 2-D scattering intensities vs. $|Q|$ plots in Figure B.6.

In order to determine the sign of the D in **4**, further INS measurements were performed under a magnetic field, which leads to additional splitting ($\Delta M_S = \pm 1$) of the ground KD transition as shown in Scheme 3.2a. If $D > 0$, an additional magnetic transition, $M_S = -1/2 \rightarrow +1/2$, would be observed at low energy and low temperatures (Scheme 3.2a). However, if $D < 0$ the first magnetic transition, $M_S = -3/2 \rightarrow +3/2$, would be forbidden (Scheme 3.2b). Measurements for **4** were taken at 0.0, 0.5, 1.0, and 2.0 T

Table 3.1. Zero-field splitting parameters obtained experimentally for complexes **4**-**6**

	4	**5**	**6**
Fittings of the DC magnetic data			
D (cm^{-1})	12.85	23.21	7.95
E (cm^{-1})	3.60	0.64	1.88
g_z	2.41	2.29	2.03
$g_{x,y}$	1.89	1.83	2.31
INS			
$U = 2(D^2 + 3E^2)^{1/2}$ (cm^{-1})	22.5(2)	26.6(3)	11.1(5)
INS/HFEPR			
D (cm^{-1})	10.90(2)	12.74(2)	4.50(3)
E (cm^{-1})	1.56(2)	2.20(2)	1.00(2)
g_z	2.39(1)	2.20(1)	2.40(2)
$g_{x,y}$	2.23(1)	2.21(1)	2.30(2)

at 1.7 K. The incident energy of 13.4 cm^{-1} was used to see if the magnetic transition, M_S = -1/2 $\rightarrow$ +1/2, would be observed at low temperatures (Scheme 3.2a). An excitation appeared at 2.0 cm^{-1} when a 2 T magnetic field was applied (Figure 3.8; B.4, Table B.4 in Appendix B). This peak confirms easy-plane anisotropy in **4**. It should be noted that signal to noise ratio in Figure 3.8 is significantly reduced compared to measurements without the magnet in the sample environment.

The INS studies are usually performed to probe the magnetic excitations in molecular magnetism with zero magnetic field. The application of a magnetic field is expected to lead to more information about the compound, as shown in this study. Only limited studies of INS under applied magnetic fields have been reported, which were focused on magnetic clusters Cr_8, Fe_9, $Mo_{72}Fe_{30}$, Cr_7Ni,[119-122] and low-dimensional antiferromagnets.[123-125] To the best of our knowledge, such INS under magnetic fields has not been performed on mononuclear metal complexes including SMMs. Our study here provides the first example using INS with magnetic fields to determine the sign of magnetic anisotropy for a mononuclear metal complex.

In the INS spectrum of **5**, a peak at 26.6 cm^{-1} was observed with an incident energy of 40.3 cm^{-1} (Figures 3.9 and B.2 and Table B.2 in Appendix B). From INS measurements the zero-field splitting $2(D^2 + 3E^2)^{1/2}$ was determined as 26.6(3) cm^{-1}. In the INS spectra of **6**, a peak at 11.1(5) cm^{-1} was observed with an incident energy of 24.2 cm^{-1} representing $2(D^2 + 3E^2)^{1/2}$ (Figures 3.10 and B.3 and Table B.3). The ZFS transitions of **5** and **6** are of magnetic nature due to their temperature dependence and decreasing $|Q|$ dependence as observed in Figures 3.9 and 3.10. An additional plot showing how the magnetic peak in the INS spectrum of **6** at 1.7 K changes in two

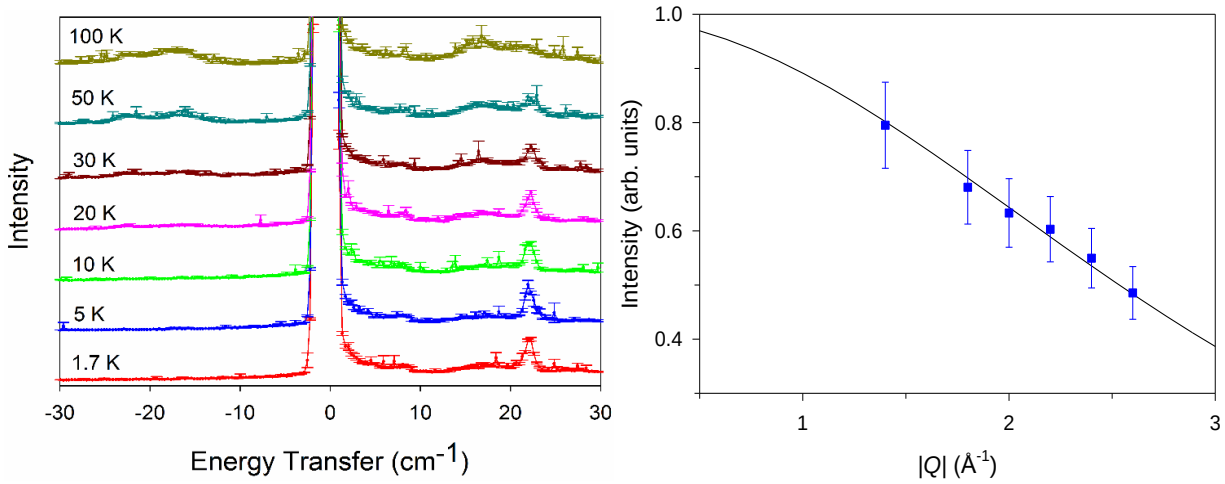

Figure 3.7. (Left) INS spectra of $(PPh_4)_2[Co(NO_3)_4]\cdot CH_2Cl_2$ (**4**) with incident neutron energy E_i = 53.7 cm^{-1}, $|Q|$ = 0.5-1.3 $Å^{-1}$ and a step size of 0.081 cm^{-1}. (Right) Change in intensities of the magnetic peak at 22.5(2) cm^{-1} vs $|Q|$ at 1.7 K. The solid line represents the calculated intensity of the magnetic excitation.

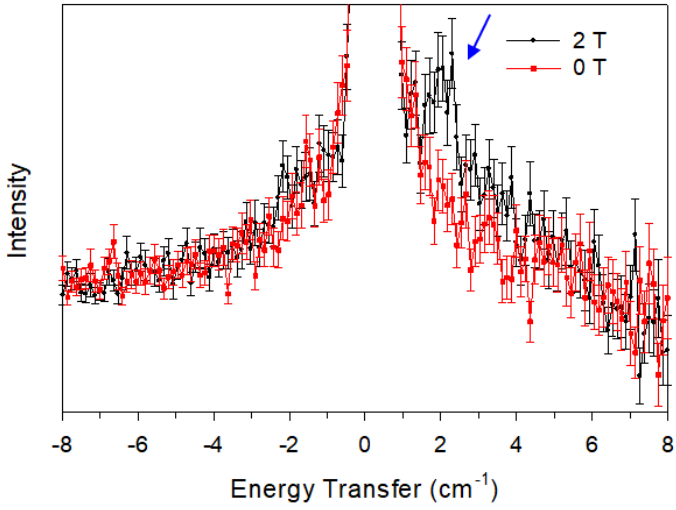

Figure 3.8. INS spectrum of $(PPh_4)_2[Co(NO_3)_4]\cdot CH_2Cl_2$ (**4**) at 1.7 K, showing the M_S = -1/2 → +1/2 transition at 2 T (indicated by the blue arrow) with the incident neutron energy of E_i = 13.4 cm^{-1}, $|Q|$ = 0.4-1.3 $Å^{-1}$. The solid lines are for eye guide.

different |*Q*| ranges are given in Figure B.7.

It is interesting to note that a broad optical phonon peak centered around 18 cm^{-1}, even at 1.7 K, is very close to the ZFS transition of **4** (Figure 3.7). The intensity of this peak increases quadratically with |*Q*| as shown in Figure B.5 in Appendix B, confirming its phonon nature. No such phonon peak near the magnetic peak is obvious in the INS spectra of **5** (Figure 3.9).

3.3.1.3. HF-EPR Studies

The above INS analysis shows that the values of zero-field splitting $U = 2(D^2 + 3E^2)^{1/2}$ are 22.5, 26.6 and 11.1 cm^{-1} for **4**, **5**, and **6**, respectively. However, the *D* and *E* values could not be separately determined from the sole INS transition. In order to determine the sign and values of *D* and *E*, the polycrystalline samples of **4**, **5**, and **6** were investigated by high-frequency and -field electron paramagnetic resonance (HF-EPR)[41,126] in the frequency range of 60-350 GHz (2.0-11.7 cm^{-1}). The HF-EPR spectra of **4** and **5** contain three main features, typical for an $S = 3/2$ system with large and positive *D* values,[11,88,127-131] which are from the intra-Kramers transitions within the $M_S = \pm 1/2$ doublets. By using the constraint imposed by the values of $2(D^2 + 3E^2)^{1/2}$ obtained by INS, the field vs. frequency data were fitted to give the spin-Hamiltonian parameters in Table 3.1.

The combination of INS and HF-EPR studies discussed above clearly demonstrate the easy-plane magnetic anisotropy in the high-coordinate Co(II) complexes **4**-**6**. Similar approach has been used to determine the *D* and *E* values for Re(IV)-SIM by Pedersen *et al*.[109] The *D* values in Table 3.1 from INS and HF-EPR are

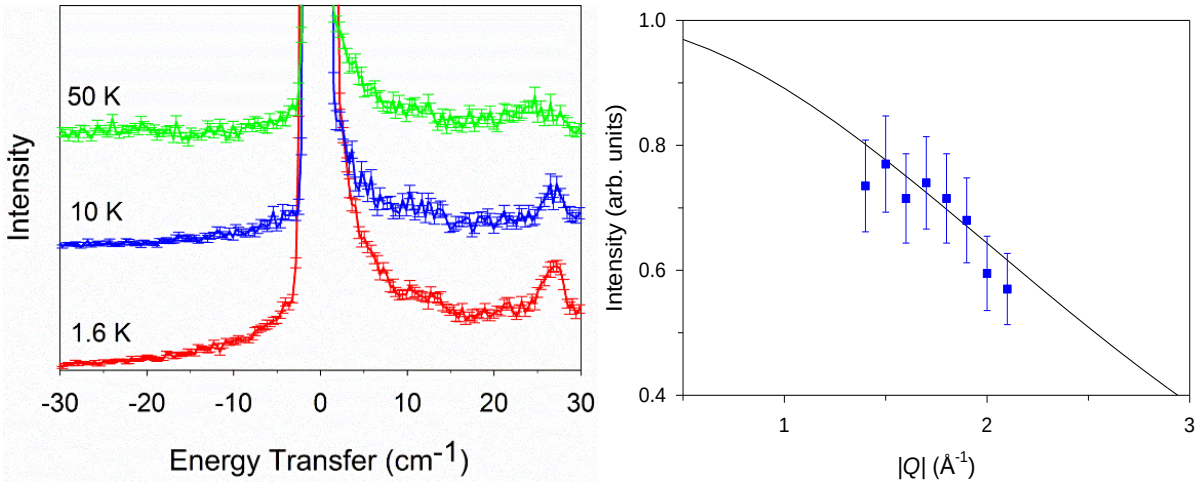

Figure 3.9. (Left) INS spectra of $(MePPh_3)_2[Co(NO_3)_4]$ (**5**) with incident neutron energy E_i = 40.33 cm^{-1}, $|Q|$ = 0.5–1.3 $Å^{-1}$ and a step size of 0.081 cm^{-1}. (Right) Change in intensities of the magnetic peak at 26.6 cm^{-1} vs $|Q|$ at 1.6 K. The solid line represents the expected intensity of the peak calculated from the magnetic form factor.

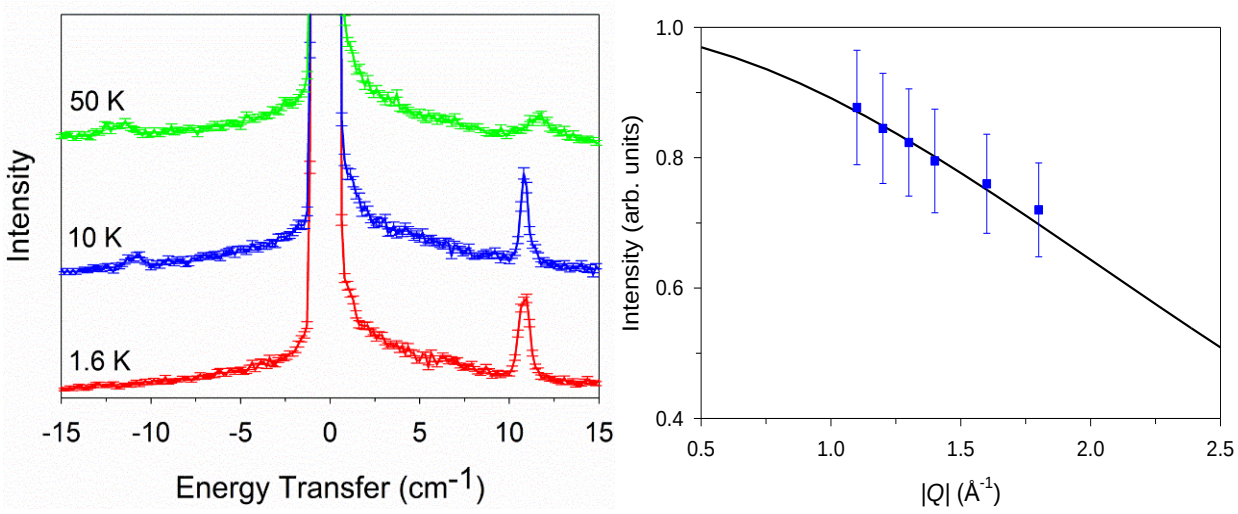

Figure 3.10. (Left) INS spectra of $(AsPh_4)_2[Co(NO_3)_4]$ (**6**) with the incident neutron energy of E_i = 24.2 cm^{-1}, $|Q|$ = 0.5–2.0 $Å^{-1}$ and a step size of 0.081 cm^{-1}. (Right) Change in intensities of the magnetic peak at 11.1(5) cm^{-1} vs $|Q|$ at 1.6 K. The solid line represents the expected intensity of the peak calculated from the magnetic form factor.

smaller than those from the fitting of the DC magnetic data, suggesting that the *D* values were over-estimated by the magnetic data.

3.3.1.4. Dynamic Magnetic Properties

It is generally accepted that a negative zero-field splitting was required for the single-molecule magnetism.[132] In 2012, Long *et al*.[11] firstly observed the slow magnetic relaxation in a four-coordinate Co(II) complex with easy-plane anisotropy. Subsequently several SIMs with $S = 3/2$ ions including Co(II)[11,88,105,127-128,133-138] and Re(IV)[109] have been reported to have positive *D* values. In order to investigate single-molecule magnetism for **4**-**6**, temperature- and frequency-dependent alternative-current (AC) susceptibility measurements were performed. At 1.8 K, no out-of-phase AC susceptibility (χ_M'') signal was observed for **4-5** under zero applied DC field, which is probably due to the occurrence of quantum tunneling of the magnetization (QTM) (Figures B.12-B.13 in Appendix B). The application of an external magnetic field could induce the strong frequency-dependent AC susceptibilities. For **4**, the maximum of χ_M'' appeared at 200 Oe, which shifted to low frequencies with the increase in the applied magnetic field up to 600 Oe and then stayed at the nearly same frequency as the magnetic field increases further (Figures B.12-B.13). Therefore, a magnetic field of 600 Oe was used in temperature- and frequency-dependent AC measurements in the temperature range of 1.8–7.0 K (Figure 3.11). The temperature- and frequency-dependence of AC susceptibility signals indicate that both **4** and **5** exhibit the slow magnetic relaxation processes and thus behave as field-induced SMM. As shown in Figure 3.11, the peaks of χ_M'' signals for **4** and **5** appear at 398 Hz and 35 Hz,

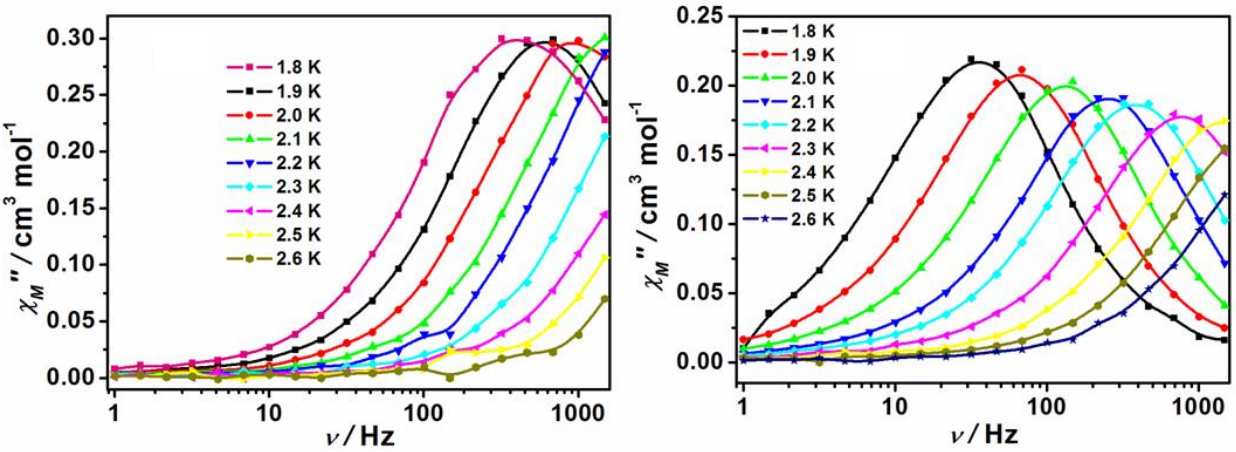

Figure 3.11. Frequency dependence of the AC susceptibility from 1.8 to 2.6 K under 600 Oe DC field for $(PPh_4)_2[Co(NO_3)_4]\cdot CH_2Cl_2$ (**4**) and $(MePPh_3)_2[Co(NO_3)_4]$ (**5**). The solid lines are for eye guide.

respectively, at 1.8 K, suggesting the magnetic relaxation is faster in **4** than in **5** (due to inverse relationship of frequency and time). In contrast with **4** and **5**, no significant out-of-phase signals (χ''_M) were observed for **6** with the frequency of 1-1488.1 Hz at 1.8 K using an applied magnetic field in the range of 0-2500 Oe (Figure B.14 in Appendix B), suggesting that **6** does not exhibit the SMM properties.

The relaxation times extracted from the Debye model were fit by the Arrhenius law $\tau = \tau_0 \exp(U_{eff} / kT)$ to give U_{eff} = 12 cm^{-1} (τ_0 = 4.14 × 10^{-8} s) for **4** and U_{eff} = 20 cm^{-1} (τ_0 = 2.1 × 10^{-9} s) for **5**, respectively (Figure 3.12). Such derivation of the effective energy barrier is based on the assumption that the thermally activated Orbach process is the dominant relaxation mechanism in the studied temperature range. However, these energy barriers obtained by AC susceptibility measurements are much smaller than the ZFS energy difference between the ground and excited states accurately determined from INS studies [22.5(2), 26.6(3) cm^{-1} for **4** and **5**, respectively]. This suggests that the results obtained by AC susceptibility measurements underestimate the energy barriers and other mechanism such as Raman process may occur in the magnetic relaxation of **4** and **5**. Several detailed studies show that Raman mechanism has significant contributions to relaxation process for Co(II)-based SIMs with easy-plane magnetic anisotropy.[10,88,105,129,138]

Our INS spectra showed the presence of a phonon peak around 18 cm^{-1} in **4** (Figure 3.7), which is absent in the INS spectra of **5** (Figure 3.9). In each unit cell [2479.1(8) Å^3] of complex **4**, containing two molecules each of $(PPh_4)_2[Co(NO_3)_4]$ and CH_2Cl_2, there are a total of 224 atoms. In comparison, in each unit cell of **5**, containing two molecules of $(MePPh_3)_2[Co(NO_3)_4]$ (**5**), there are a total of 186 atoms, a reflection of

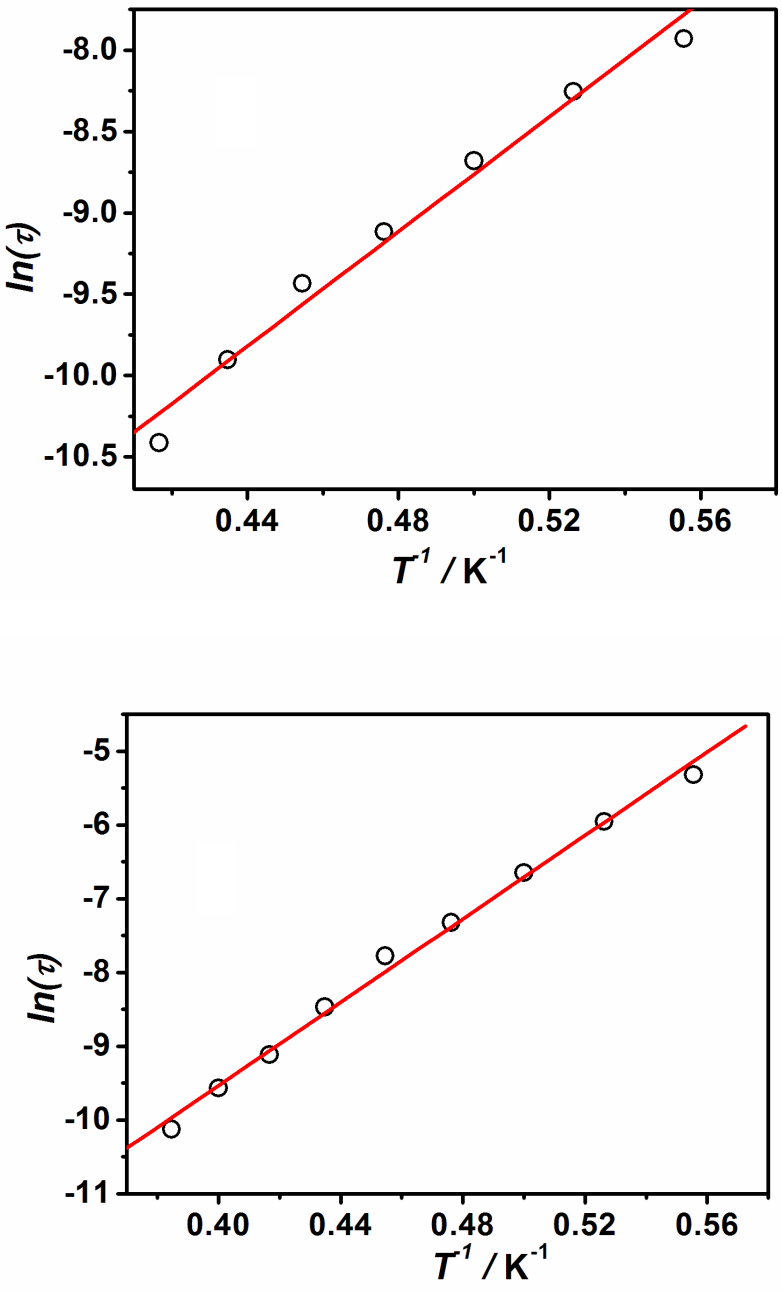

Figure 3.12. Relaxation time of the magnetization *ln(τ)* vs T^{-1} plots for (Top) **4** and (Bottom) **5**. The solid lines represent Arrhenius fits.

the smaller cation and the lack of CH_2Cl_2 in the cell. Since phonon modes are lattice and intramolecular vibrations,[49] the larger number of atoms in the unit cell of **4** is expected to lead to more low-energy delocalized vibrations in its INS spectra.[139]

The absence of phonon peaks in the same region in the INS spectra of **5** (Figure 3.9) is perhaps a result of a smaller number of atoms in its unit cell. There could be few phonons of appropriate frequency to promote a more efficient relaxation in **5**. The phonon peak around 18 cm^{-1} in **4**, which is fairly low in energy, could be involved in the Raman-type relaxation in **4**, leading to its faster magnetic relaxation than **5**, as observed in the AC susceptibility studies. Carretta and co-workers have observed that low-energy optical phonon modes in an Fe_8 complex enhances its magnetic relaxation process.[140]

It is also worth noting that, in addition to giving the ZFS transitions, INS, a spectroscopic method, also directly shows phonon modes in the samples. Unlike electromagnetic IR and Raman spectroscopies with selection rules for vibrational peaks, there is no selection rule for the vibrational peaks in the INS spectroscopy, which is based on the kinetic energy transfer between incident neutrons and the samples. Additional studies linking the INS spectra to the AC susceptibility data to understand relaxation mechanisms are needed.

3.3.2. $[Co(12C4)_2](I_3)_2(12C4)$ (7)

TOPAZ, the single-crystal neutron diffractometer at the ORNL Spallation Neutron Source (SNS) was used to orientate two single crystals of **7** along the molecular *z*-axis, the magnetic anisotropic axis. The molecular *z*-axis is pointed nearly along the crystallographic reciprocal *c** axis, (0 0 -1) (Figure 3.2). With the *c** determined, the

single crystals were aligned parallel to the vertical external magnetic field to observe the Zeeman splitting of the zero-field splitting peak in the B_z orientations.

The two crystals orientated at TOPAZ are shown in Figure 3.13. The first crystal (Figure 3.13-Left) is 100.1 mg and 8 x 3.25 x 2 mm and the second crystal (Figure 3.13-Right) is 80.0 mg and 8 x 2.75 x 1 mm. In addition to the orientations of two single crystals, neutron diffraction data were collected at 100 K to obtain the neutron crystal structure of a third crystal. The single-crystal structure by X-ray diffraction has been previously reported at 293 K. This single-crystal structure by neutron diffraction at 100 K was used for the *Vienna Ab Initio Simulation Package* (VASP) phonon calculations.

The crystals orientated at TOPAZ were then mounted at Cold Neutron Chopper Spectrometer (CNCS) so that the direction of the field would be parallel to the *c** axis, i.e., the molecular *z*-axis (Figure 3.14). An 8 T vertical magnet was placed in the sample environment. Due to its position in the spectrometer, the magnet blocks a sizable portion of the detectors (~70%). An unknown factor was whether the experiment would be technically possible due to the portion of detectors blocked and the large incoherent scattering from hydrogen atoms (48 H atoms/molecule) in the sample.

Measurements were performed at 0, 2, 5 and 8 T at 2.0 K. The spectra are shown in Figures 3.15 and 3.16. The *U* peak is evident at 49.4 cm^{-1} where the magnetic intensity is observed to shift to higher energies, as the field is increased. The leftover intensity around 49.4 cm^{-1} is due to an overlapping phonon that seems unaffected by field. The ZFS intensity eventually overlaps with another phonon at 58 cm^{-1} at 8 T.

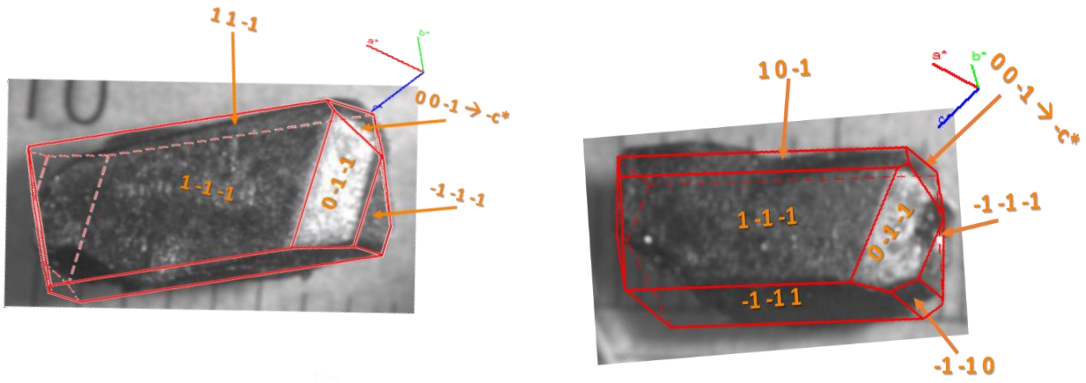

Figure 3.13. Crystals of $[Co(12C4)_2](I_3)_2(12C4)$ (**7**) that were orientated at TOPAZ with miller indices shown. The *c** axis is indicated. The red lines are an overlay of the predicted crystal faces.

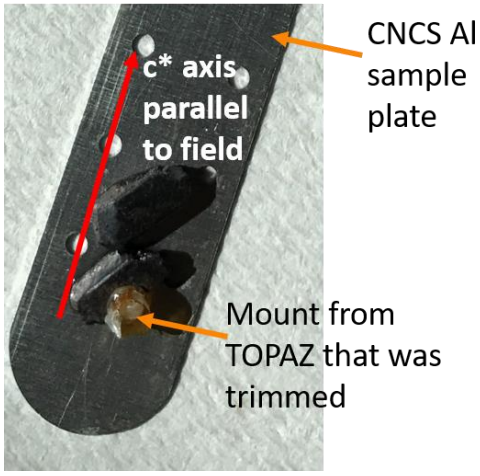

Figure 3.14. Crystals of $[Co(12C4)_2](I_3)_2(12C4)$ (**7**) that were orientated for the CNCS experiment (prior to wrapping the sample plate with Al wires to keep the crystals in position in the magnetic field). Note the mount from the TOPAZ experiment was glued on the crystal and was not able to be removed for the CNCS experiment.

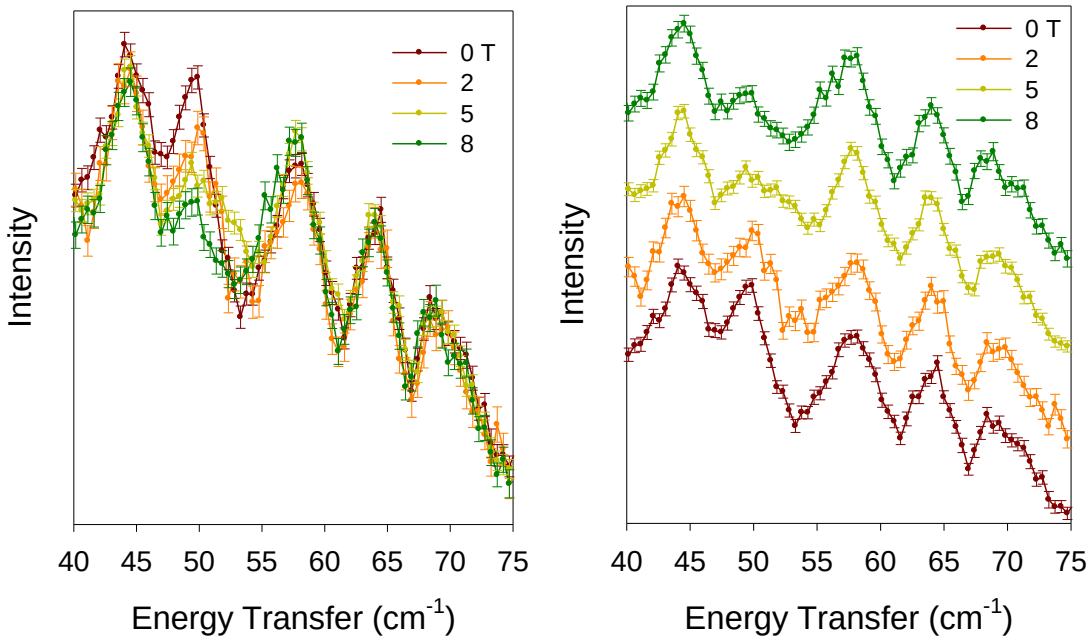

Figure 3.15. INS of $[Co(12C4)_2](I_3)_2(12C4)$ (**7**) at variable magnetic fields showing the ZFS peak at 49.42 cm^{-1}. The $|Q|$ range is summed from 1-3 $Å^{-1}$. The spectrum to the right is offset.

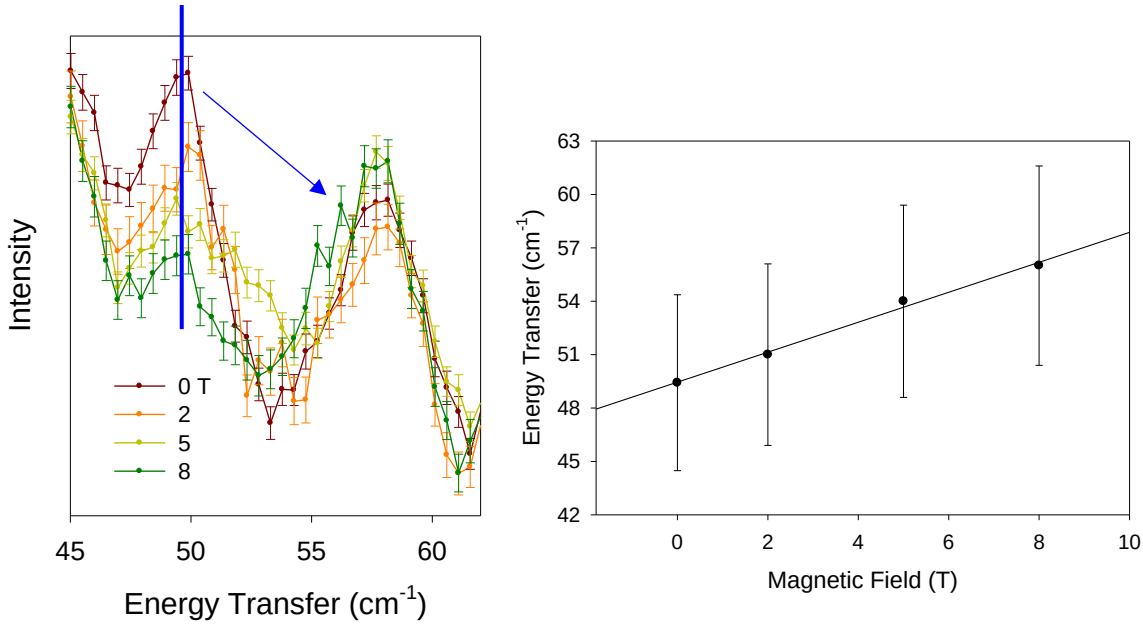

Figure 3.16. (Left) Zoomed-in INS of $[Co(12C4)_2](I_3)_2(12C4)$ (**7**) at variable magnetic fields showing the ZFS peak at 49.42 cm^{-1}. The $|Q|$ range is summed from 1-3 $Å^{-1}$. The solid blue line represents the position of the phonon peak (initially overlapping at 0 and 2 T) and the blue arrow represents the blue shift of the ZFS peak. (Right) Estimated shift of magnetic transition based on intensity changes with field. Error is taken to be 10% of the position.

INS spectra were also recorded at variable temperatures from 10 to 125 K at VISION (Figure 3.17) to see if temperature dependence (with or without the Bose correction) could be used to determine the ZFS peak. The phonon peaks from the CNCS (Figure 3.15) and VISION (Figure 3.17) are consistent with each other. Due to the overlap of *U* with a phonon of similar energy, it is challenging to tell where the *U* peak is in the spectra. A peak with a large intensity change (signifying intensity of magnetic origins) did not stand out in this region. Therefore, variable temperatures and the Bose-corrected data are insufficient to observe the reveal *U* transition by VISION in the case of **7**. In addition, studying temperature dependence in this energy region is challenging as a reduction of the phonon intensity is expected because of the Debye-Waller factor that describes a thermal induced effect caused by coherent scattering of nuclei.

The VASP phonon calculation of the INS spectrum were completed using the structure from single-crystal neutron diffraction at TOPAZ at 100 K. Figure 3.18 shows the comparison of the phonon calculations and the experimental VISION spectra at 5 K. Overall, there is a good match between experimental and calculated INS spectra. Only the database of irreducible representations for a few point group types at the Γ point are implemented in Phonopy.[141] The point group for **7**, 2/m (Space group 15, *C*2/*c*), is not available in Phonopy. Therefore, we were not able to assign the symmetry of the phonon modes. These calculations well reproduce the phonon spectrum. Accurate phonon calculations, such as those by the method used here, are needed as a first step to understand the atomic displacements in SMMs that lead to SPC (Chapter 4).

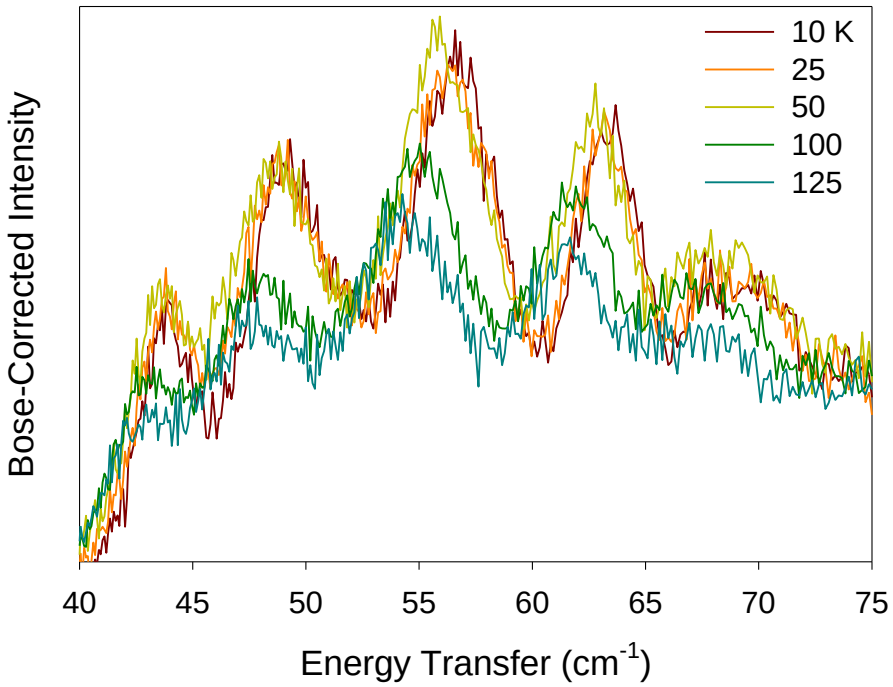

Figure 3.17. Forward scattering INS spectra (VISION) of $[Co(12C4)_2](I_3)_2(12C4)$ (**7**) at variable temperatures. The intensity is Bose-corrected.

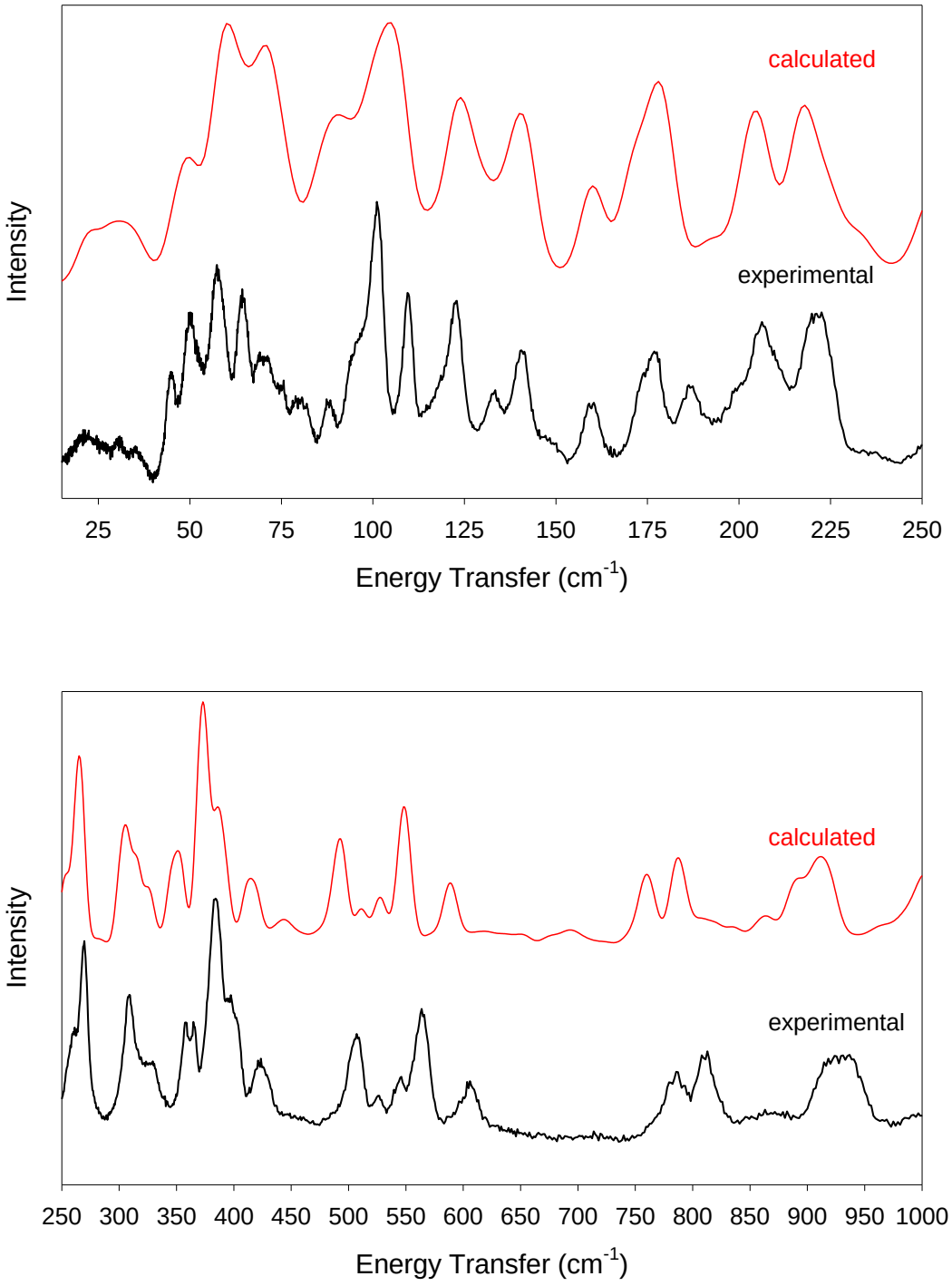

Figure 3.18. Comparison of calculated and experimental phonons of **7** at VISION at 5 K. (Top) The 20-250 cm^{-1} range. (Bottom) The 250-1000 cm^{-1} range.

These studies reveal the following: (1) Magnetometry should not be used as the only confirmation of the *Z*FS magnitude. Indeed the difference in the *U* value from indirect magnetometry and direct INS measurements is 9%. (2) INS and an external magnetic field can be used to probe a protonated SMM (48 H-atoms/molecule). (3) Use of a single crystal sample (180 mg total mass of both orientated crystals) can be utilized to get adequate get orientation dependent splittings. (4) INS can probe low-energy phonons that may play a role in SPC leading to magnetic relaxation.

3.3.3. $Co(acac)_2(D_2O)_2$ (**8-*d*$_4$**) and $Co(acac\text{-}d_7)_2(D_2O)_2$ (**8-*d*$_{18}$**)

INS, unlike optical spectroscopy, is based on kinetic energy transfers between incident neutrons and samples.[8] Since both magnetic and phonon peaks are allowed in INS, both contribute to the observed peaks in $Co(acac)_2(D_2O)_2$ (**8-*d*$_4$**) and $Co(acac\text{-}d_7)_2(D_2O)_2$ (**8-*d*$_{18}$**) in Figures 3.19-3.21. Magnetic scattering is more prominent at small scattering-vector |*Q*|, whereas phonon scattering prevails at high |*Q*|, allowing discrimination of both events.[21] It should be noted that INS experiments using a 10 T magnet at DCS are particularly challenging, as the magnet blocks a large portion of the detectors, leading to low signal/noise ratios of the peaks.

All spectroscopic evidence leads to the assignment of the magnetic excitation in **8-*d*$_{18}$** at ~113 cm^{-1} (Figures 3.19, 3.21). However, this transition is revealed to have a complicated nature not solely reminiscent of pure magnetic origin. Separation of low and high |*Q*| ranges in the INS spectrum of the intensity centered at 113 cm^{-1} (0 T) is consistent with the nature of peaks A and B (Figure 3.19a). At low |*Q*|, B is dominant, indicating it is mostly magnetic. At larger |*Q*|, B mostly disappears and largely phonon A

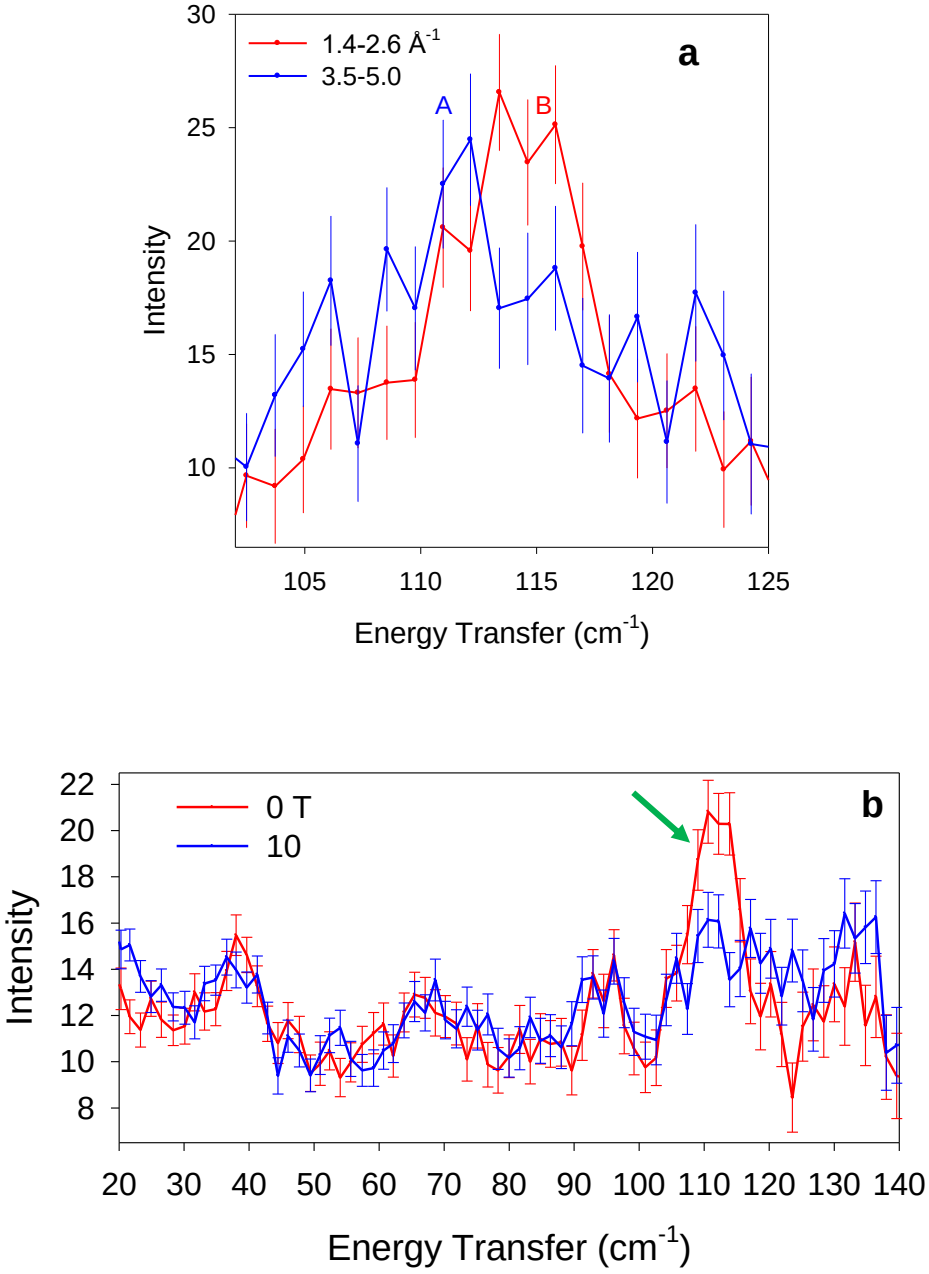

Figure 3.19. (a) 0 T INS spectra at small |*Q*| (1.4–2.6 Å^{-1}) and large |*Q*| (3.5–5.0 Å^{-1}). (b) Variable-field INS spectra of **8-*d*$_{18}$** at 0 and 10 T summed over all |*Q*|. The green arrow represents peaks A and B at 0 T.

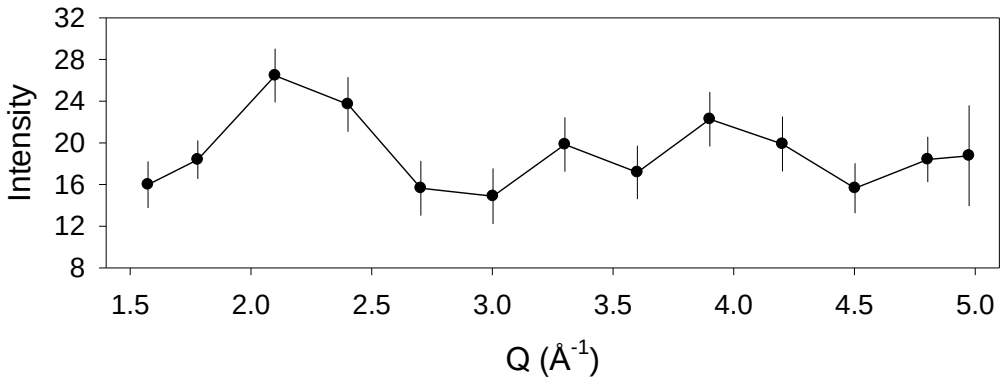

Figure 3.20. |*Q*| dependence of 113 cm^{-1} peak at 0 T.

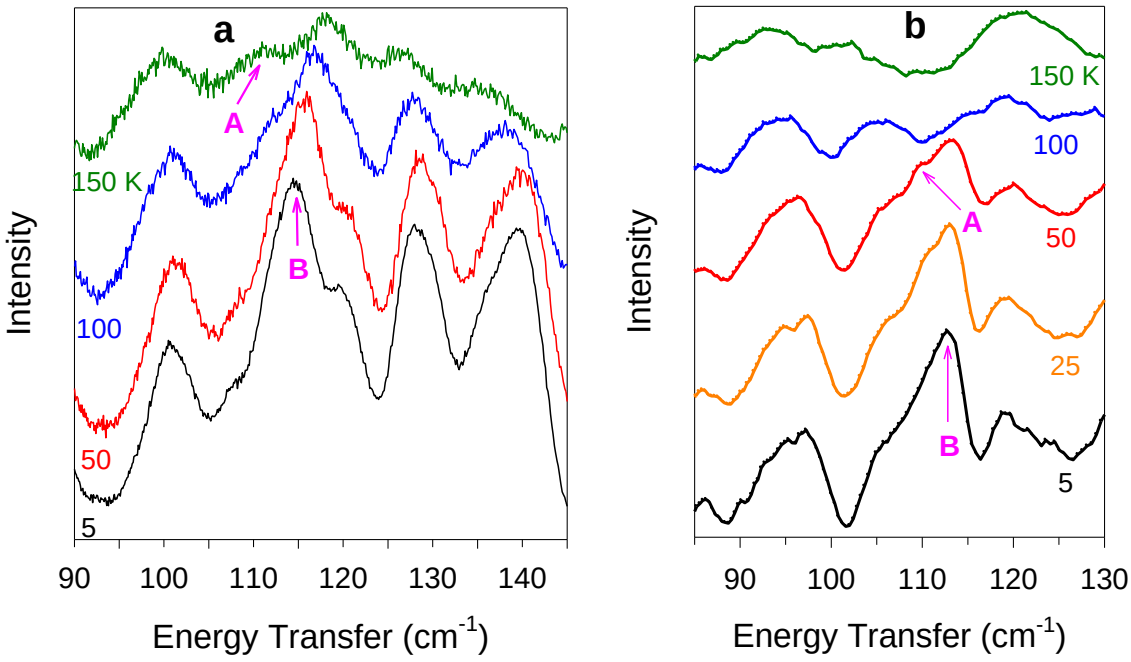

Figure 3.21. INS spectra at variable temperatures without external magnetic fields: (a) **8-*d*$_4$**; (b) **8-*d*$_{18}$**. Peaks A and B are labelled.

is prominent. Other spectroscopic techniques such as far-IR or Raman cannot directly distinguish between magnetic and phonon intensity at 0 T.

At 0 T, the overlapping peaks A and B at 113 cm^{-1} are more intense. The INS spectra for **8-*d*$_{18}$** is from a powder sample. Therefore, it is hard to statistically support where the magnetic peak shifts to at 10 T because of the broadening of the magnetic intensity by different orientations of the powders of the sample inside the field (B_z, B_y, $\underline{B}_x$). However, the change in the intensity at 113 cm^{-1} between 0 and 10 T is clear (Figure 3.19b). At 10 T, there is evidence that B shifts and broadens in the region between 120 and 134 cm^{-1} (Figure 3.19b).

The Zeeman splitting was calculated for **8-*d*$_{18}$** to probe where the orientation-dependent magnetic intensity shifts in the experimental spectra for the powder sample. Based on the increase in energy of the magnetic peak it is expected to stem from the M_S = -1/2 $\rightarrow$ +3/2 transition. The Zeeman splitting calculations shows this transition will shift to the energy region between 127 and 134 cm^{-1} given the three different orientations, B_x, B_y and B_z (Scheme 3.3). This is consistent with the experimental data in Figure 3.19b. The |*Q*| dependence of the 113 cm^{-1} intensity at 0 T is shown in Figure 3.20. The data in Figure 3.19a reveal this peak is composed of two peaks of different |*Q*| dependences: magnetic (B-red line) and phononic (A-blue line). When studied over the entire |*Q*| range range, Figure 3.20 confirms the complex nature of this intensity. This inter-Kramers doublet transition is not purely magnetic, as the intensity does not decrease as |*Q*| increases, following the single-ion form factor for Co(II). This transition is also not purely a phonon either, since it does not increase by $|Q|^2$ as |*Q*| increases. The |*Q*| dependence is relatively constant throughout the studied

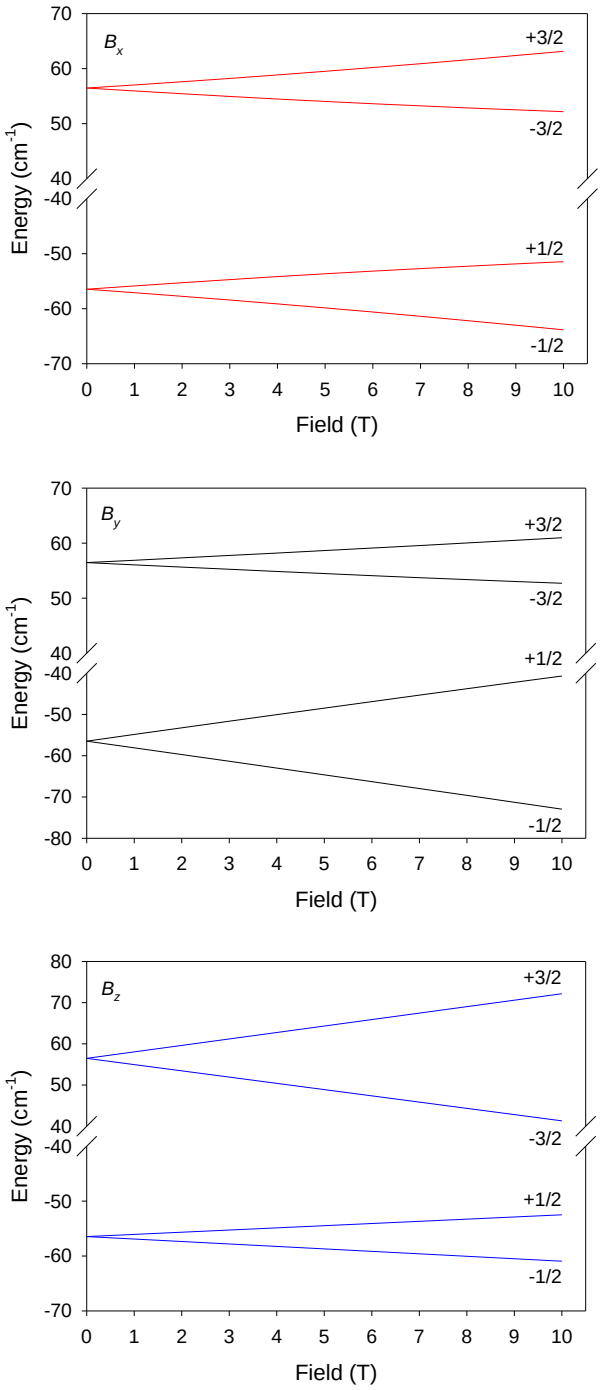

Scheme 3.3. Diagrams of M_S energy levels as a function of external magnetic field in the B_x (top), B_y (middle) and B_z (bottom) orientations. The SH parameters used in this simulation are E/D = 0.31,[10] D = 49.75 cm^{-1}, $g_{x,y,z}$ = 2.50, 2.57, 2.40[10] and S = 3/2.

|*Q*| range. Because it neither consistently increases nor decreases with |*Q*|, this supports the assignment of the 113 cm^{-1} as being composed of both magnetic and phonon contribution entangled together. Due to the complicated nature of the |*Q*| dependence of the spin-phonon coupled peaks A/B, further studies are needed to fully understand its origin.

The spin-phonon coupled peaks A and B in **8-*d*$_4$** and **8-*d*$_{18}$** are present in the variable-temperature INS (without a magnet) on VISION (Figure 3.21). Initially overlapping at 5 K, B (115.4 cm^{-1} for **8-*d*$_4$** and 112.7 cm^{-1} for **8-*d*$_{18}$**) decreases intensity with temperature increase, when the excited ZFS state is gradually populated, confirming its magnetic origin. Phonon A is revealed at 150 K (**8-*d*$_4$**) and 25 K (**8-*d*$_{18}$**). The phonon on the right shoulder of B (~120 cm^{-1}) in **8-*d*$_4$** is an A_u mode (Figure 3.21a) and is therefore not observed in Raman. It should be pointed out that, unlike far-IR and Raman spectra, external magnetic fields are not necessary to determine ZFS peaks in INS in this case. Additional INS spectra from VISION and their discussions are given in Figures B.16 and B.17 in Appendix B.

A comparison of **8-*d*$_4$** with $Zn(acac)_2(D_2O)_2$ (**9-*d*$_4$**) reveals how a diamagnetic control can be used to identify the ZFS transition. The Zn(II) complex was used as a diamagnetic analogue of **8-*d*$_4$**. The effect of substituting the Co(II) ion with the heavier metal Zn(II) ion is apparent as the INS spectrum of **9-*d*$_4$** is red shifted (Figure 3.22). It is evident in Figure 3.22 that there are two phonon peaks that “sandwich” the magnetic intensity in **8-*d*$_4$** at ~114 cm^{-1}, a point to be discussed later in Chapter 4. As the temperature is increased, the magnetic excitation decreases based on Boltzmann statistics (as evidenced at 150 K). At 150 K the magnetic excitation should be weak in

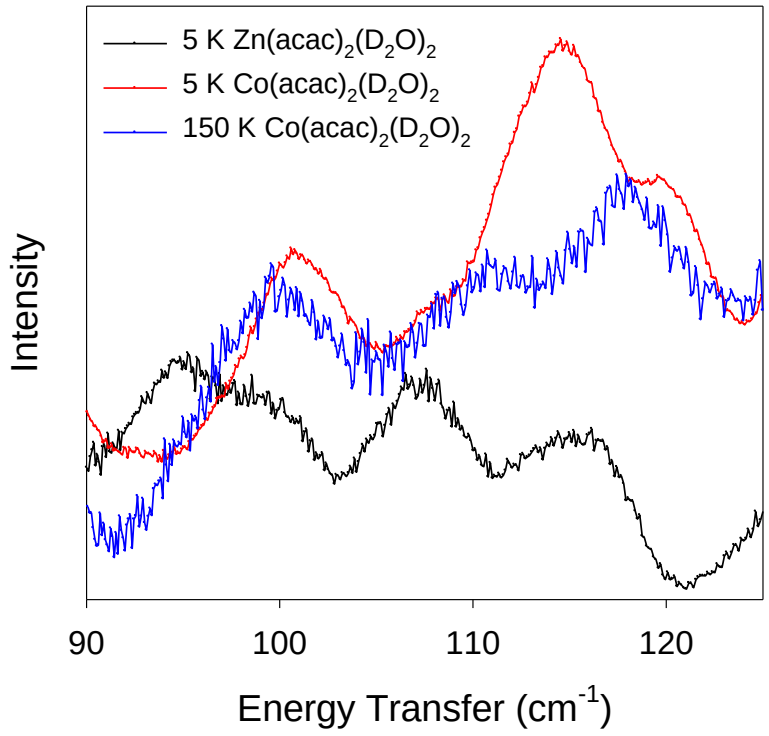

Figure 3.22. Comparison of the INS spectra of $Co(acac)_2(D_2O)_2$ (**8-*d*$_4$**; 5 and 150 K) with diamagnetic $Zn(acac)_2(D_2O)_2$ (**9-*d*$_4$**; 5 K) at VISION.

8-*d*$_4$ while, in **9-*d*$_4$**, it does not exist. The spectrum of **8-*d*$_4$** at 150 K is consistent with the 5 K spectrum of **9-*d*$_4$** confirming the assignment of the ZFS peak.

INS and magnetic fields were used to determine the sign of *D* at 1.7 K. The transitions between the levels ϕ_1 and ϕ_2 of the ground-state Kramers doublet (KD_1, Figure 3.3c) of **8-*d*$_{18}$**, are shown in Figure 3.23. For example, when the field is 2.00(2) T this peak is in the range of ca. 2–6 cm^{-1}. The transition broadens (due to effects of different orientations of the powder sample: B_x, B_y, B_z) and shifts to higher energy with the increasing field up to 10.0(1) T.

To confirm the origin of the low energy transition is in fact magnetic scattering, the |*Q*| dependence of the ground-state intra-Kramers doublet (KD_1) was studied. The experimental |*Q*| dependence was fitted with the single-ion magnetic form factor of Co(II) ion[142] in Figure 3.24 [4.00(4) T data used as a representative data set]. This fitting of the data shows a decrease of the intensity as |*Q*| increases, which reveals its pure magnetic origin.

3.3.4. Er[N(SiMe$_3$)$_2$]$_3$ (10)

The INS experiment on Er[N(SiMe$_3$)$_2$]$_3$ (**10**) were performed at DCS. At 0 T, the transition from ground (m_J = ±15/2) to first excited state (m_J = ±13/2) is at 102 cm^{-1}. When the magnetic field was applied, both Kramers doublets split (Figure 3.25a). Two transitions are possible depending on the temperature: m_J = -15/2 → -13/2 and +15/2 → +13/2. However, since our experiment was conducted at 1.5 K, only the ground state m_J = -15/2 is expected to be populated and m_J = -15/2 → -13/2 transition is expected. In addition, the separation between m_J = -15/2 → -13/2 states increase in magnetic fields

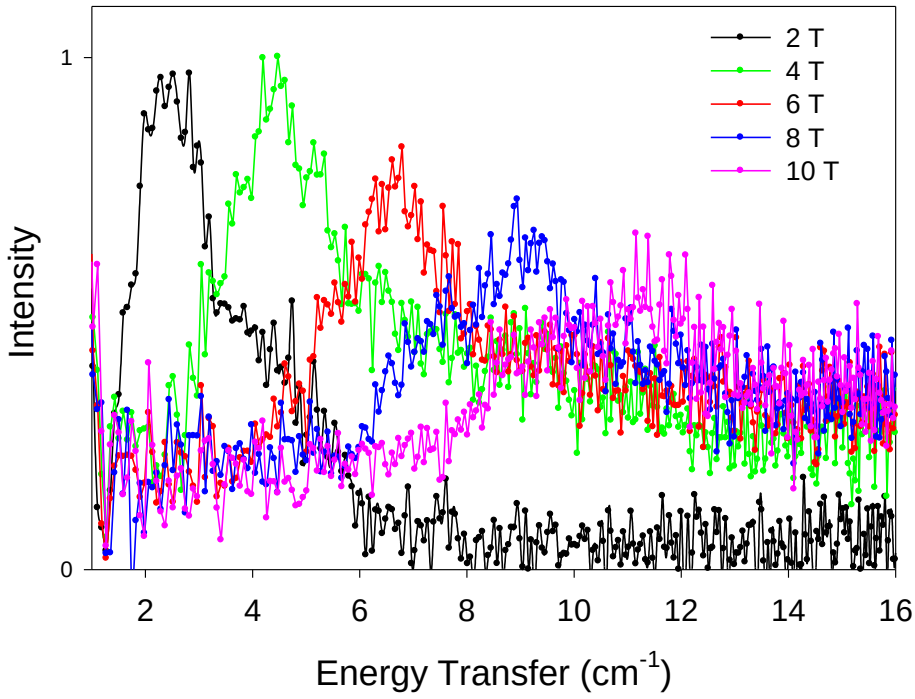

Figure 3.23. Variable-magnetic-field INS of **8-*d*$_{18}$** at DCS, revealing the $\phi_1 \rightarrow \phi_2$ transition (Figure 3.3b) at 1.7 K.

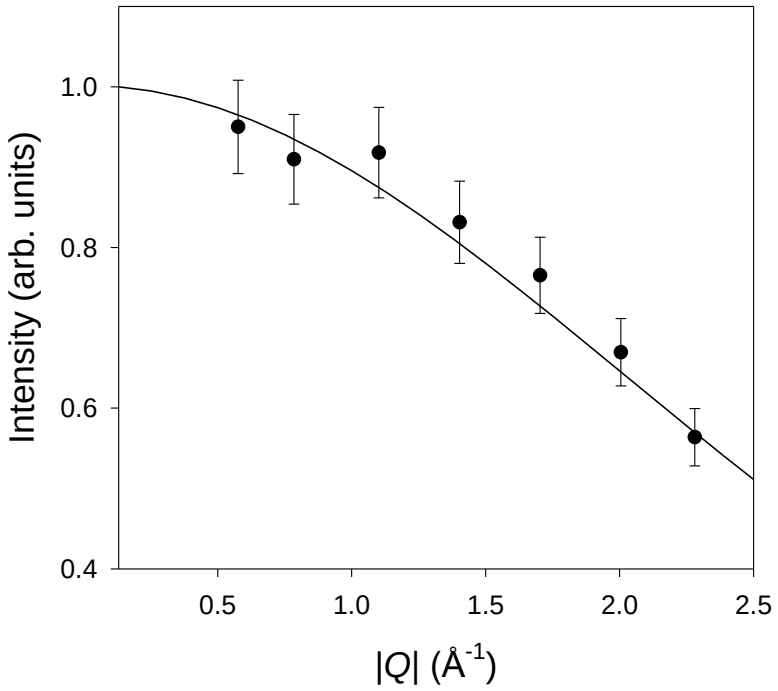

Figure 3.24. Change in intensity of the ground state Kramers doublet at 4.00(4) T vs |*Q*| at 1.7 K. The solid line represents the calculated intensity from the single-ion magnetic form factor of Co(II).

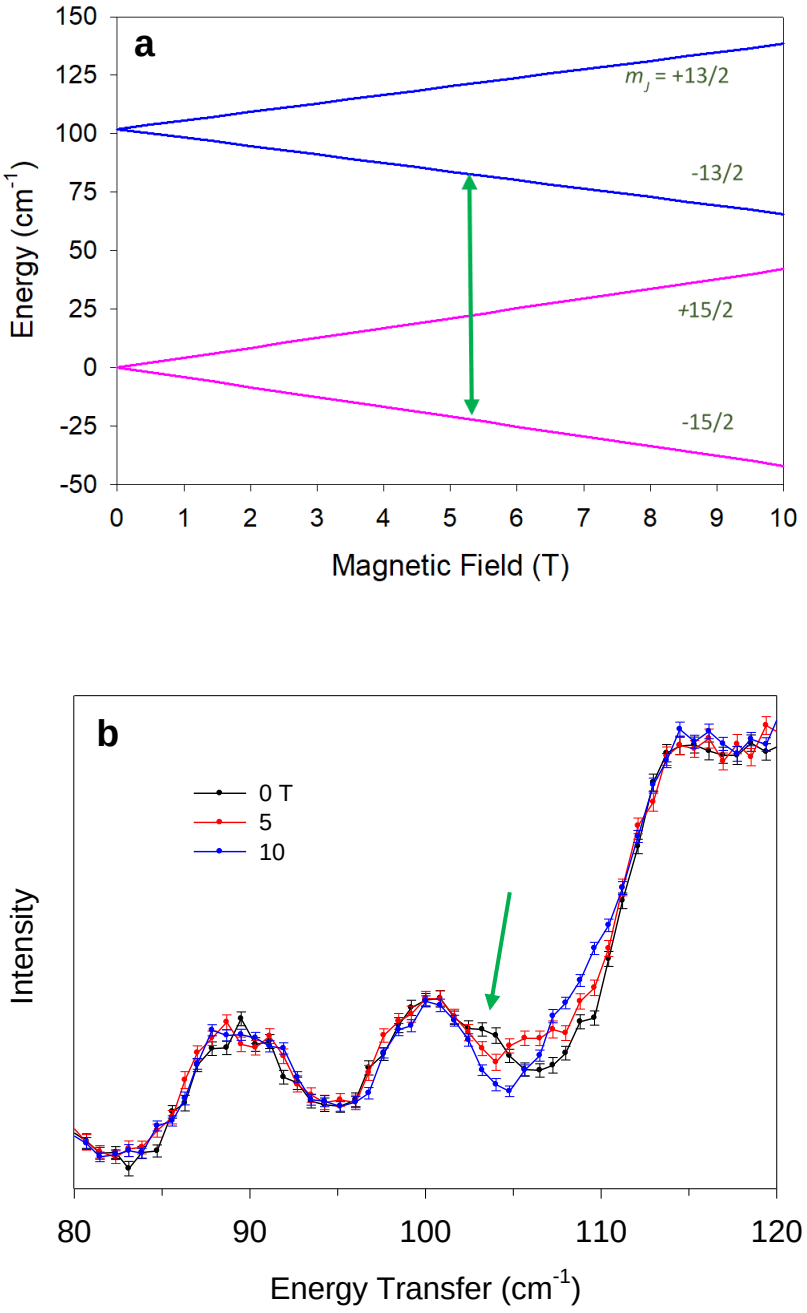

Figure 3.25. (a) Zeeman splitting of the energy levels (m_J = ±13/2 and ±15/2) in response to magnetic field calculated with a *g*-factor = 1.2.[143] (b) INS spectra of **10** at 1.5 K at 0 (black), 5 (red), and 10 T (blue) summed over all *Q*. Green arrow the magnetic transition observed in INS.

(Figure 3.25a). In the INS spectrum, m_J = -15/2 $\rightarrow$ -13/2 transition/peak shifts to higher energies at larger magnetic fields. At 5 T, the magnetic peak shifted to 105.1 cm^{-1} (Figure 3.25b). At 10 T, the magnetic peak further shifted into the shoulder of a phonon peak, and its energy could not be determined. However, both the area and full width at half maximum (FWHM) of the phonon peak increased at 10 T due to the overlap with the magnetic peak (Table 3.2). It is evident from Figure 3.26 that, at 0 T, the magnetic excitation overlaps with a phonon at ~97 cm^{-1}. The difference between INS and the measured U_{eff} and the calculated first excited state via crystal field Hamiltonian is 16.6% and 19.6%, respectively. The excitation is remarkably close to the calculated value by the *ab initio* method with the MOLCAS package at 101 cm^{-1}.[117]

Variable-temperature INS have also been performed at VISION without magnetic field (Figure 3.27). The INS spectra at VISION are similar to the data taken at DCS. The magnetic peak at 103 cm^{-1} is visible on the shoulder of a phonon peak at low temperatures. This peak disappears with increasing temperatures as Boltzmann statistics predicts. However, without the knowledge of the position of the magnetic peak using a magnetic field, this peak would be difficult to locate in the variable-temperature spectra because it is a weak transition on the shoulder to a phonon. The spectra in Figure 3.27 show the magnetic peak disappear by 100 K. At higher momentum and energy transfers, the Debye Waller factor is strong and there are higher energy peaks that survive at 100 K. The observations are supporting evidence that this peak is a magnetic excitation.

Phonon calculations of vibrations in $Er[N(SiMe_3)_2]_3$ (**10**) using VASP[144] show that the experimental and calculated phonon peaks are consistent in Figure 3.28. This

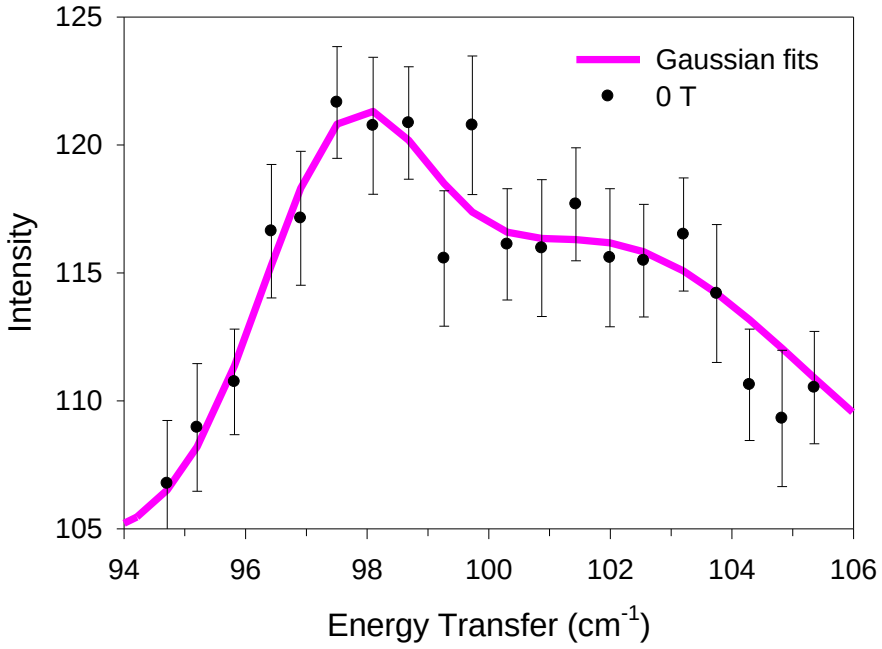

Figure 3.26. Fitting of the phonon and magnetic peaks in $Er[N(SiMe_3)_2]_3$ (**10**) with Gaussian functions at 0 T.

Table 3.2. Area and FWHM of the phonon peak located at 115 cm^{-1} at 10 T for $Er[N(SiMe_3)_2]_3$ (**10**). At this field the magnetic peak is a shoulder off this phonon

	Area	**FWHM (cm^{-1})**
0 T	53.9	7.20
10 T	55.7	8.56
% Difference	3.2%	15.9%

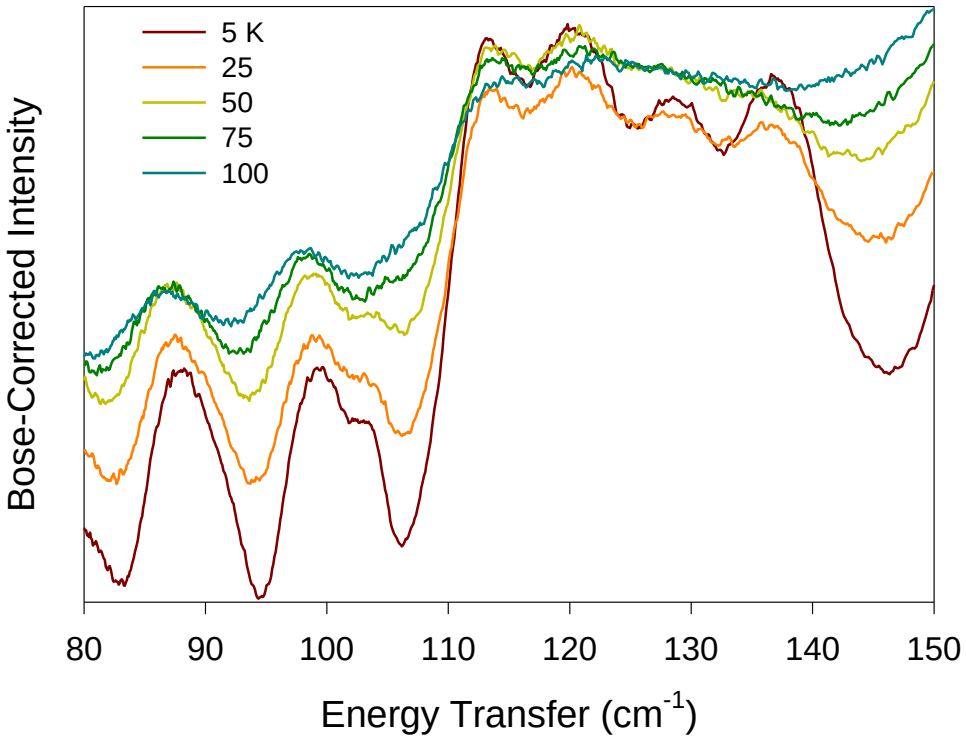

Figure 3.27. Forward scattering INS spectra (VISION) of $Er[N(SiMe_3)_2]_3$ (**10**) at variable temperatures. The intensity was Bose-corrected.

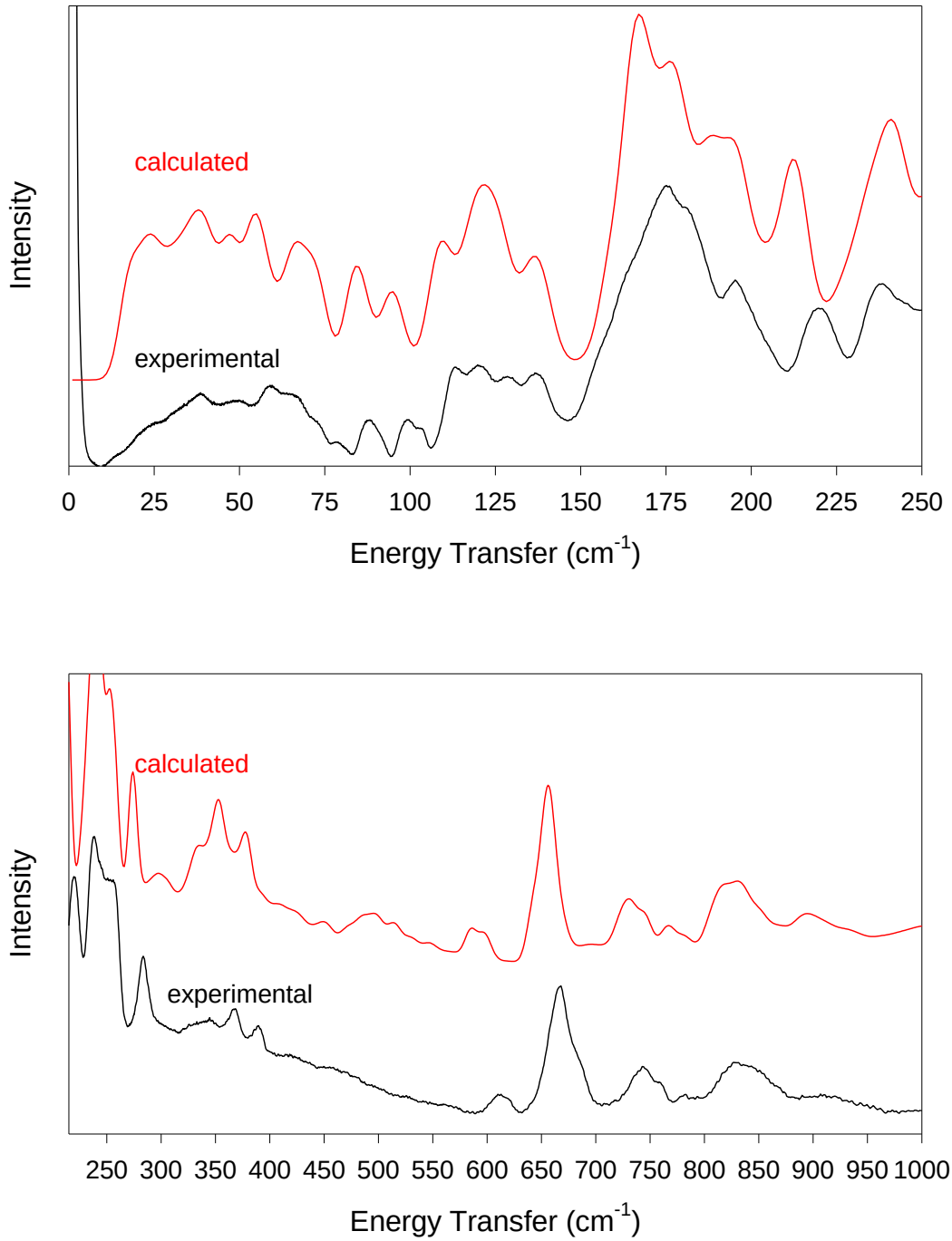

Figure 3.28. Calculated and experimental 5 K INS spectra of **10**. (Top) The 0-250 cm^{-1} range. (Bottom) The 250-1000 cm^{-1} range.

comparison of experimental INS data with high-level phonon calculations is needed to eventually lead to better an understanding of relaxation processes in SMMs.

These results demonstrate that U_{eff} should not be used to estimate the magnetic excitation between the ground and first excited Kramers doublet. This work also shows that a protonated sample with a large energy separation could be used to determine the magnetic excitation. Spectroscopically, we observe phonons of lower energy than the magnetic excitation, which could interact with the unpaired electron spin leading to the relaxation barrier U_{eff} = 85 cm^{-1} obtained from AC susceptibility.

3.4. Conclusions

This chapter has demonstrated the power of directly determining the separations between magnetic energy levels with INS based on the temperature, magnetic field and $|Q|$ dependences. In the case of $(PPh_4)_2[Co(NO_3)_4]\cdot CH_2Cl_2$ (**4**), $MePPh_3)_2[Co(NO_3)_4]$ (**5**) and $(AsPh_4)_2[Co(NO_3)_4]$ (**6**) (Section 3.3.1), INS reveals not only the magnitude of the magnetic separations but also the sign of *D* parameters which previously could not be determined by magnetometry measurements. The measurement of this magnetic separation was crucial to both magnetometry and HF-EPR measurements as both techniques relied on information provided by INS. In addition, the presence of a phonon observed in the INS spectra reveal the importance of spectroscopically examining the vibrational peaks close in energy to the ZFS peak when probing possible spin-phonon coupling mechanisms. This work also provides the first example of using an external field and INS to study a mononuclear SMM. These SMMs reveal one of the benefits of INS, observing the low energy spectra <50 cm^{-1}.

The work on the crystals of $[Co(12C4)_2](I_3)_2(12C4)$ (**7**) (Section 3.3.2) again reveals the power of INS to directly determine *U* when magnetometry measurements over-estimated the ZFS parameters. This experiment also demonstrates that deuterated samples are not required to study $U > 30$ cm^{-1} with a magnet in the sample environment. Another technical challenge was overcome when the small sample of 180 mg of single crystals of **7** was successfully used in INS measurements. A magnet coupled with INS is crucial when the variable-temperature INS alone failed to determine the ZFS peak. The use of single crystals also provided a clear transfer of the magnetic intensity in the spectra, without the broadening typically observed by powder samples, providing the first example of a single crystal mononuclear SMM to be studied with INS and magnetic field. Many low-energy phonons near the *U* peak in **7** are revealed in the INS spectra that the spin could interact with, although detailed spin-phonon couplings from experiments or calculations are needed to see which phonons interact most strongly.

The study of $Co(acac)_2(D_2O)_2$ (**8-*d*$_4$**) and $Co(acac\text{-}d_7)_2(D_2O)_2$ (**8-*d*$_{18}$**) (Section 3.3.3) provides a unique case where the ZFS peak is coupled to a nearly degenerate phonon peak. Both variable–field and variable–temperature spectra show the magnitude of the magnetic separation, demonstrating in this particular case that magnetic fields are not required to extract the *U* peak. This work provides the first example of using temperature-dependent properties of magnetic and phonon peaks above >95 cm^{-1} to confirm the ZFS separation. Variable-field INS is also capable of independently determining the sign of the *D* parameter. The unique momentum transfer (*Q*) properties of neutrons demonstrates the presence of spin-phonon entangled peaks

near 113 cm^{-1}, revealing information about the nature of the peaks that far-IR and Raman spectroscopies could not provide.

Lastly, $Er[N(SiMe_3)_2]_3$ (**10**, Section 3.3.4) was probed with INS inside magnetic field, which allowed for the determination of the magnetic separation of 102 cm^{-1}. This case represents an example of the largest magnetic separation that has been able to be probed with INS and magnetic fields with a *protonated* sample (54 H atoms/molecule).

3.5. Experimental

3.5.1. $(A)_2[Co(NO_3)_4]$ [A = Ph_4P^+ (4), $MePh_3P^+$ (5) and Ph_4As^+ (6)]

The INS measurements were carried out on Cold Neutron Chopper Spectrometer (CNCS)[49] at Spallation Neutron Source, Oak Ridge National Laboratory. CNCS is a direct geometry, time-of-flight spectrometer that receives a beam from a coupled cryogenic H_2 moderator. For energy selection, CNCS employs four chopper assemblies. The speeds and slit widths of the choppers may vary, allowing adjustments in the instrumental resolution and intensity of the incident beam. Approximately 500 mg of each sample was loaded into a ½-inch-thick aluminum tube. For the INS work without a magnet, three tubes, containing $(A)_2[Co(NO_3)_4]$ (**4**-**6**), each were placed in a sample changer. The sample holder was mounted in a standard liquid helium cryostat with a base temperature of T = 1.6 K. An oscillating radial collimator was used to reduce background scattering from the tail of the cryostat. Vanadium was used as a standard for the detector efficiency correction.

The incident neutron energy for every measurement was chosen to cover the anticipated region of interest in both the energy E and scattering-vector $\boldsymbol{Q}$ space. A

small incident energy is especially important to observe excitations near the elastic peak (at energy transfer close to 0 cm^{-1}) as the full-width-at-half-maximum (FWHM) of the elastic peak, which is typically 1.5–2% of the incident energy, would be narrow, giving better energy resolution.

For **4,** zero-field measurements were performed at 1.7, 5, 10, 20, 30, 50, and 100 K with an incident neutron energy of 53.7 cm^{-1}. For **5** and **6**, measurements were performed at 1.6, 10 and 50 K with incident neutron beam energies of 24.2 and 40.3 cm^{-1}. Data were then reduced and analyzed using the MantidPlot[145] and DAVE (Data Analysis and Visualization Environment) program package.[62]

Another INS experiment for the powder sample of **4** was performed at 1.7 K using a 5 T cryomagnet with vertical field at CNCS. Aluminum spacer was added to the headspace of the sample can to prevent the sample reorientation in the applied field. Magnetic fields at 0.5, 1.0 and 2.0 T were used with the incident neutron energy of 13.4 cm^{-1}. The cryomagnet sample room allows only one sample at a given time.

The linewidths of the INS peaks lie within experimental accuracy determined by the instrumental resolution. The effective resolution function $R(Q,E)$ of CNCS is nearly Gaussian in energy.[49] Therefore, the INS intensities were fit assuming Gaussian line shapes with FWHM of the energy resolution for the CNCS spectrometer. Additional details of data processing are provided in Appendix B. The crystal structures of the anions of $[Co(NO_3)_4]^{2-}$ is given in Figure B.15 in Appendix B.

3.5.2. $[Co(12C4)_2](I_3)_2(12C4)$ (7)

The INS experiments were completed at CNCS. The crystals were glued to the sample plate with the fluoropolymer glue, CYTOP (this fluoropolymer glue was used to eliminate scattering from hydrogen). The 8 T magnet, which blocks ~70% of detectors, was placed in the sample environment. Each field measurement (0, 2, 5 and 8 T) was run for approximately 8 hr. The incident energy and temperature for the measurements was 12.07 meV (97.3 cm^{-1}) and 2 K, respectively.

TOPAZ[146] is a neutron time-of-flight single crystal Laue diffractometer. The single crystal samples were mounted on Kapton tubes. The crystals orientated at TOPAZ were 8 x 2.75 x 1 mm (80.0 mg) and 8 x 3.25 x 2 mm (100.1 mg). The goniometer was rotated to varying ω and Φ angles to view different faces of the crystals. Orientation data were collected at 293 K on different faces of the crystals and indexed to assign Miller indices. The data analysis program ISAW (Integrated Scattering Analysis Workbench) provides sample orientation (UB matrix) by auto-indexing. The orientation matrix, UB, describes the sample orientation with respect to the diffractometer angles. Crystal orientations were optimized with CrystalPlan[147] (an experiment planning tool for time-of-flight Laue experiment). CrystalPlan is used to simulate the coverage of reciprocal space of detectors of an instrument, giving a list of sample orientations (peak prediction and placement). This program predicts ω and Φ angles required for the sample orientation that would place a given reflection at a particular spot on a detector.

3.5.3. $Co(acac)_2(D_2O)_2$ (8-d_4) and $Co(acac\text{-}d_7)_2(D_2O)_2$ (8-d_{18})

Two INS studies using different instruments were conducted: (a) Variable-magnetic-field (0-10 T) INS spectra of **8-*d*$_{18}$** at 1.7 K at the time-of-flight DCS[100] at the NIST Center of Neutron Research. This study leads to the identification of the ZFS peak and measurements of the M_S = -1/2 (ϕ_1) $\rightarrow$ +1/2 (ϕ_2) and -1/2 (ϕ_1) $\rightarrow$ +3/2 (ϕ_4) transitions with magnetic fields. (b) Variable-temperature INS spectra of **8-*d*$_4$** and **8-*d*$_{18}$**, without a magnet, at VISION. Both studies used powder samples.

In the variable-magnetic-field INS data at DCS[100], the 10 T vertical magnet with a dilution refrigerator was used in the sample environment. Approximately 2 g of **8-*d*$_{18}$** were put on a piece of aluminum foil, rolled into a cigar shape, and then placed inside an aluminum sample holder. Data were collected at 1.7 K and 4.5 Å (32.6 cm^{-1}) for 0, 2, 4, 6, 8 and 10 T. In addition, the higher energy region was studied at 1.7 K and 1.8 Å (203.6 cm^{-1}) for 0 and 10 T. At DCS, a direct geometry instrument, data were collected up to 196 cm^{-1}. All data processing was completed with DAVE.[62]

For variable-temperature INS at VISION, the samples, approximately 2 g, were sealed in an aluminum container. The INS spectra of **8-*d*$_4$** was measured at 5, 50, 100, 150 K for 1 hr at each temperature. **8-*d*$_{18}$** was measured at 5, 25, 50, 100, 150 K for 2 h at each temperature. VISION,[101] an inverted geometry instrument, provides data up to 4000 cm^{-1}. The inverted geometry design at VISION offers two banks of detectors for both forward (low |*Q*|) and back (high |*Q*|) scattering of neutrons.[101] The phonon population effect was corrected by normalizing the INS intensity at energy transfer ω with $\coth(\frac{\hbar\omega}{2k_BT})$.[19]

With the addition of the 10 T magnet to the sample environment at DCS, there is a degradation by a factor of 2.5 in the incident beam size in comparison to the normal, full beam. In addition, there is background contribution from the small aperture of the magnet and shadowing of detectors by the magnet, giving ~33% detector efficiency. However, even with these limitations, results from INS here are consistent with those from Raman and far-IR spectra.

3.5.4. $Er[N(SiMe_3)_2]_3$ (10)

INS was performed at the DCS on 2.3 g of **10** loaded in an aluminum foil 'cigar' and placed in an aluminum sample can (wedged in place so the field would not move the sample). The incident energy was 1.81 Å (201.6 cm^{-1}). The magnet interfered with energy transfers over 145 cm^{-1}. Thus, only the spectra <145 cm^{-1} are used. Data were collected at 1.5 K at 0, 5 and 10 T magnetic fields to reveal the magnetic excitation. In addition, data at 20 K at 0 T were collected but no significant difference between the spectra at 1.5 and 20 K (0 T) was observed. The variable-temperature VISION was collected at 5, 25, 50, 75 and 100 K.

Chapter 4

Ab Initio Calculations of Phonons in Co(II) Complexes. Understanding Spin-Phonon Couplings in the Complexes

This part is based on the following paper:

Moseley, D.H.; Stavretis, S.E.; Cheng, Y.; Daemen, L.; Thirunavukkuarasu, K.; Ozerov, M.; Ludwig, J.; Lu, Z.; Smirnov, D.; Craig, B.; Atanasov, M.; Bill, E.; Neese, F.; Pandey, A.; Ramirez-Cuesta, A.J.; Lamb, A.; Xue, Z.-L., Spin-phonon couplings in transition metal complexes with slow magnetic relaxation. Spectroscopic and computational studies. *Manuscript in preparation*.

This author performed the phonon calculations and interpretation, including making the phonon animations. The Raman and far-IR experimental spectra are included to give context to her work.

4.1. Abstract

Limited understanding of how spin-phonon coupling leads to magnetic relaxation is recognized as one of the obstacles preventing design of better SMMs with high blocking temperatures. Our Raman spectroscopy data has revealed entangled spin-phonon peaks in $Co(acac)_2(D_2O)_2$ (**8-*d*$_4$**) and $Co(acac\text{-}d_7)_2(D_2O)_2$ (**8-*d*$_{18}$**), allowing experimental determination of spin-phonon coupling constants. (The Raman spectrum is not part of this dissertation.) The phonon modes in the two isotopologues have been calculated through simulated atomic displacements to understand the non-uniform nature of spin-phonon couplings by the vibrations as well as to probe the atomic displacements that are the most detrimental in the energy regions of **8-*d*$_4$** and **8-*d*$_{18}$** near their ZFS transitions.

4.2. Introduction

Spin-phonon coupling is often the mechanism of magnetic relaxation in SMMs.[1,3,115,148-154] The interaction of the magnetic moment with phonons gives accessible pathways for spin reversal at lower energies than those determined from the magnetic anisotropy barrier *U* (Figure 1.1). Indeed, these fast, under-the-barrier, magnetic relaxation processes are a prominent obstacle to the increase in blocking temperature above the boiling point of liquid nitrogen and beyond. One reason for this obstacle is that there is little understanding of how these interactions lead to relaxation in SMMs. Phonons of SMM crystals include both intramolecular (or molecular) and lattice vibrations.[155] Recently, there has been a drive, using theoretical models,[12-13,156] to understand how phonons lead to relaxations in SMMs. Goodwin and co-workers have

reported that $[Dy(Cp^{ttt})_2][B(C_6F_5)_4]$ (Cp^{ttt} = 1,2,4-^{t}Bu$_3$C$_5$H$_2$) displays magnetic hysteresis up to 60 K.[156] The spin-phonon coupling of this SMM reduces the magnetic relaxation rate due to unique, constrained metal-ligand vibrational modes. The magnetic relaxation is attributed to displacements primarily involving the C-H motions on the Cp^{ttt} rings. Experimental studies of phonons in SMMs are needed to directly observe, and thus help understand, how phonons interact with unpaired electron spins. Recent experimental work in this area includes that by Rechkemmer and coworkers to observe spin-phonon couplings of two field-dependent, far-IR absorptions of a Co(II) SMM.[15] However, to our knowledge, there has been no work combining experimental and theoretical studies of phonons. We have obtained INS, Raman and far-IR spectra of $Co(acac)_2(D_2O)_2$ (**8-*d*$_4$**) and $Co(acac\text{-}d_7)_2(D_2O)_2$ (**8-*d*$_{18}$**) which reveal both phonon and spin-phonon coupled modes. In the current chapter, our calculations of the phonon modes in the region near the magnetic excitations of **8-*d*$_4$** and **8-*d*$_{18}$** as well as modelling of important modes are reported. The phonons have been calculated with VASP, an *ab initio* method. The calculated phonons are compared with those from spectroscopies. The work is an attempt to understand what leads to the spin-phonon coupling in **8-*d*$_4$** and **8-*d*$_{18}$**.

It is imperative to understand each vibration to identify ones that would most likely lead to spin relaxation by modulating spin energy levels and modifying magnetic anisotropy of the SMM. The most influencing modes are often those that significantly interfere with the coordination environment of the metal.[12-13] Indeed, most of the unpaired electron spins that the phonons would interact with are localized on the metal center. However, there is evidence that modes only slightly distorting the first coordination sphere are still detrimental.[13]

The chemical structures of SMMs need to be tuned so that slow relaxation at high temperatures is achieved. Currently, most work has focused on modifying SMMs to reach large U_{eff} values.[12,14] How the lattice interacts with the spin to exchange energy, leading to magnetic relaxation, is not understood when only considering U_{eff}. Importantly, spin-phonon coupling is influenced by certain phonon modes to a stronger extent.[12-13] In other words, how the displacements of the atoms (lattice vibrations) affect the unpaired electron spins in the SMMs is vital to understanding spin relaxation. Currently, with AC measurements, only the low temperature region is probed <20 K. Therefore, the vibrational states populated at this temperature (and participate in spin relaxation) are limited to the low energy region of the phonon spectrum.

4.3. Results and Discussion

Ab initio calculations of the phonon modes for C_{2h} **8-*d*$_4$** and **8-*d*$_{18}$** are calculated by VASP, giving both external, internal and acoustic modes. During spin-phonon coupling, the phonon, which is either a molecular vibration (internal mode) or lattice vibration (external mode), modulates the electric field of the magnetic ion, leading to magnetic relaxation in SMMs. In the region of interest around the ZFS excitation (Section 3.3) at ~115 cm^{-1}, vibrations are not localized but involve atomic displacements of the whole molecule. Animations of the vibrations are given as an electronic attachments, Files 1-4.

The phonon calculations are used to understand the nature of the phonon overlapping with the ZFS peak. **8-*d*$_4$** and **8-*d*$_{18}$**, like $Co(acac)_2(H_2O)_2$ (**8**), have a center of symmetry. Therefore, *g* symmetry modes are expected to be observed in the Raman

spectra and the *u* symmetry modes in the IR spectra (Table 4.1). INS is expected to reveal all possible modes of both *g* and *u* symmetries as seen by the presence of overlapping peaks in Figures 3.21 and 4.1.

The very low-energy region is full of intermolecular phonon modes whose frequencies are very sensitive to the accuracy of the crystal structure determined by single-crystal X-ray diffraction and the intermolecular interactions. Frequency calculation of these modes is well known to be challenging. Therefore, it is not surprising that the match of the modes between experiments and calculations is not perfect. However, the full range of the calculated spectra vs. the experimental data matches well (Figure 4.1). The modes and thus atomic displacements of **8** and **8-*d*$_4$** are similar in the region of the ZFS peak (Figure 4.2). Therefore, for simplicity, **8-*d*$_4$** and **8-*d*$_{18}$** are compared.

Deuteration significantly changes the INS spectra (Figures 3.21 and 4.1). With deuteration, modes that involve hydrogen scattering appear weaker or disappear from the spectrum. Since the INS scattering involves a momentum transfer, the spectrum also shows phonons related to wave vectors throughout the Brillouin zone.[157] The Raman scattering involves only the center of the Brillouin zone (Q = 0).[157] IR is also limited to the center of the Brillouin zone.

Table 4.1 demonstrates a good match between calculated and experimental peaks positions, providing an understanding of the phonons near the ZFS peak in the spectroscopic data. The phonon calculations (Table 4.1) confirm the presence of an A_g/B_g phonon (peak A) near the ZFS peak in the INS (Figure 3.21) and Raman (Figure 4.3) spectra of **8**, **8-*d*$_4$** and **8-*d*$_{18}$**. This phonon peak A is entangled with the ZFS peak B as discussed in Section 3.3.3. The calculated peak position suggests there is no A_u or

Table 4.1. Comparisons of peak positions of phonons near the ZFS peak in **8-*d*$_4$** (top) and **8-*d*$_{18}$** (bottom). All units are given in cm^{-1}

8-*d*$_4$; Calculated energy	**Symmetry**	**Peak label**	**Raman**	**Far-IR**
99.1	A_u $(\Gamma^-_{3,4})$	-	-	101.2
103.6	A_g $(\Gamma^+_{3,4})$	-	96.8	-
107.0	B_g $(\Gamma^+_{3,4})$	-	100.2	-
109.2	A_g $(\Gamma^+_{3,4})$	A	115.2	-
120.3	A_u $(\Gamma^-_{3,4})$	-	-	120.0
125.0	B_u $(\Gamma^-_{3,4})$	-	-	123.4
126.0	B_g $(\Gamma^+_{3,4})$	C	124.4	-
129.3	A_g $(\Gamma^+_{3,4})$	D	129.0	-
135.6	B_u $(\Gamma^-_{3,4})$	-	-	131.9
140.1	A_u $(\Gamma^-_{3,4})$	-	-	133.8
142.7	B_g $(\Gamma^+_{3,4})$	E	139.2	-
8-*d*$_{18}$; Calculated energy	**Symmetry**	**Peak label**	**Raman**	**Far-IR**
91.3	B_g $(\Gamma^+_{3,4})$	-	90.9	-
93.5	A_u $(\Gamma^-_{3,4})$	-	-	96.9
95.7	A_g $(\Gamma^+_{3,4})$	-	96.4	-
103.3	A_g $(\Gamma^+_{3,4})$	-	106.2[b]	-

Table 4.1. Continued

8-d_{18}; Calculated energy	Symmetry	Peak label	Raman	Far-IR
109.8	A_g $(\Gamma^{+}_{3,4})$	-	106.2[b]	-
114.3	A_u $(\Gamma^{-}_{3,4})$	-	-	weak
116.3	B_g $(\Gamma^{+}_{3,4})$	A	112.5 (0 T) 115 (6 T)	-
116.6	B_u $(\Gamma^{-}_{3,4})$	-	-	weak

[a] Symmetries of vibrations are listed following Mulliken notations for the C_{2h} group. The vibronic states (in parentheses) are denoted using notations for the C_{2h}' double group as defined in Table 15 of ref. 158.

[b] Either one of those calculated modes could be attributed to the experimental phonon observed at 106.2 cm^{-1}. However, without information on the calculated intensity of these Raman-active peaks, a definitive assignment cannot be made. While there are two calculated peaks in this region, only the one with experimental intensity is observed.

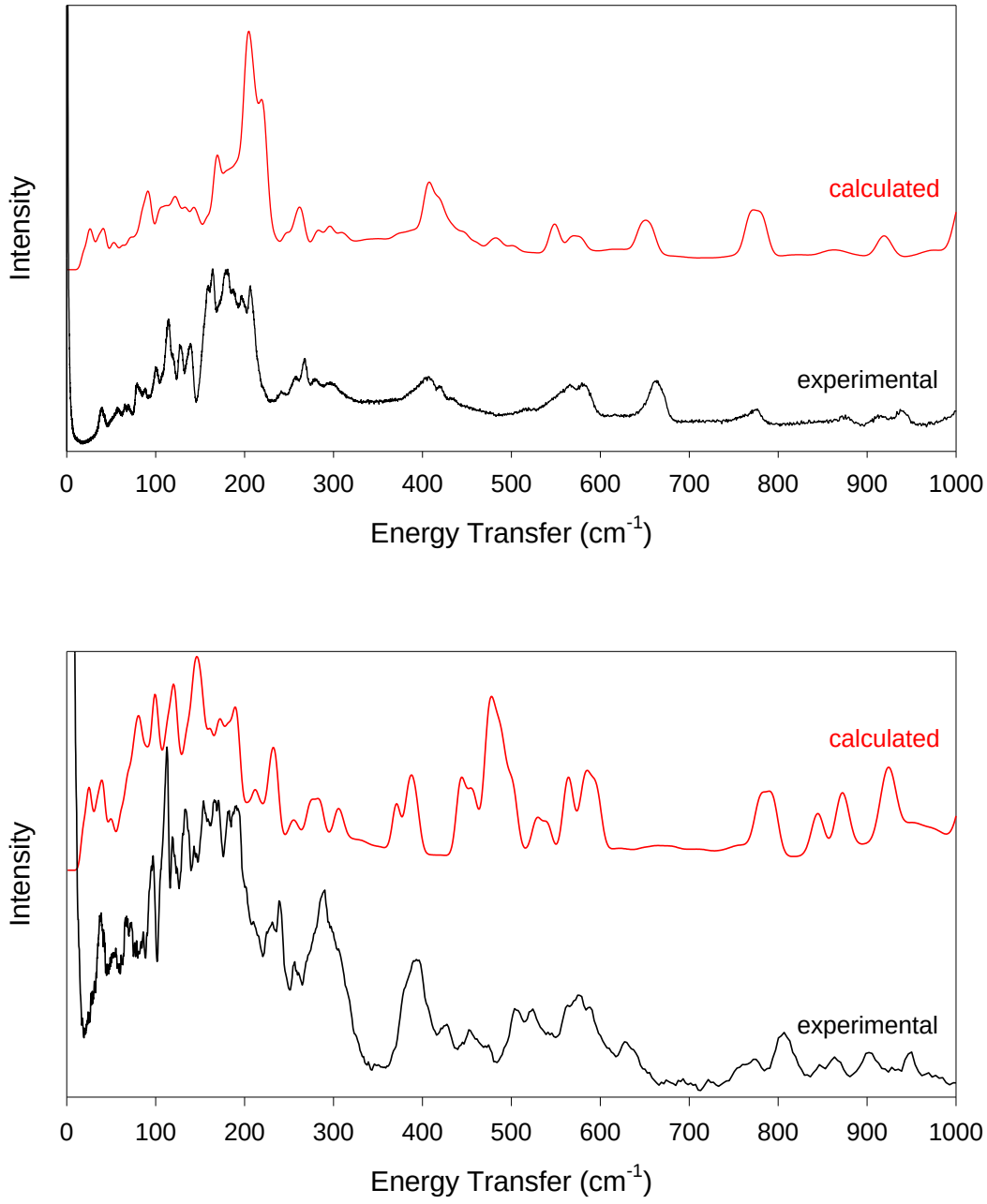

Figure 4.1. Calculated phonons and INS intensities (O'climax) and comparison with the experimental INS data from VISION: (Top) **8-*d*$_4$** and (Bottom) **8-*d*$_{18}$**.

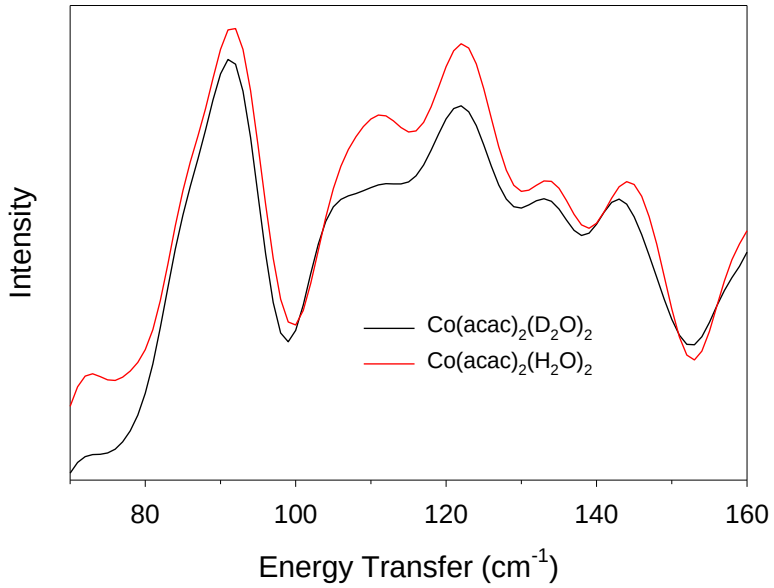

Figure 4.2. Comparison of the calculated phonon spectra of **8** and **8-*d*$_4$**. In the energy region around 100 cm^{-1}, the modes are similar. Therefore, only the calculated modes of **8-*d*$_4$** are discussed.

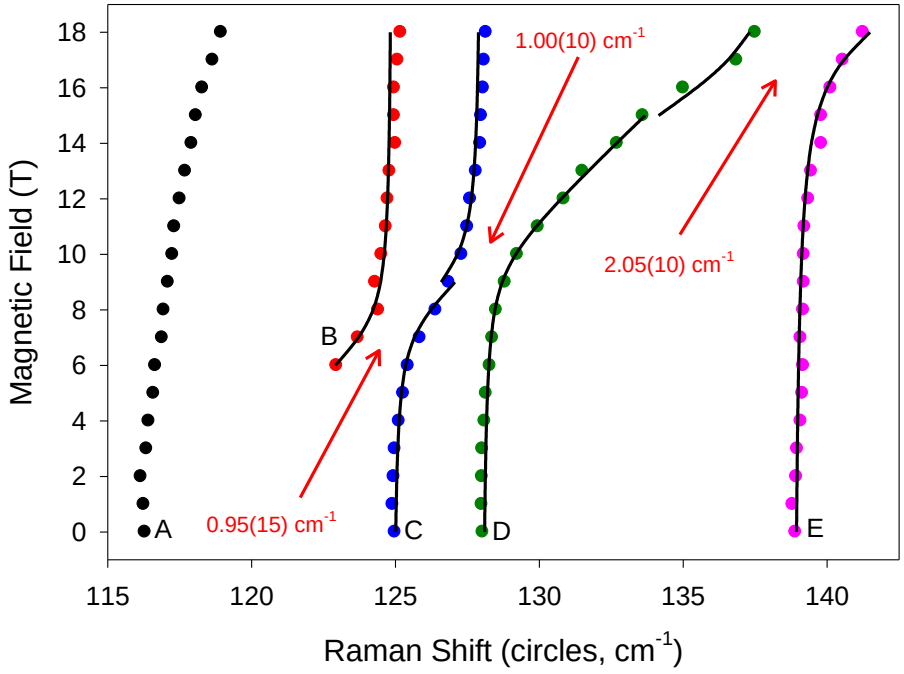

Figure 4.3. ZFS and phonon peak positions vs. magnetic fields in the Raman spectra of **8**. Solid lines represent fittings. Arrows point to corresponding avoided crossings for $|\Lambda|$.[160]

B_u phonon mode directly overlapping with the ZFS peak (~115 cm^{-1} for **8-*d*$_4$** and ~112 cm^{-1} for **8-*d*$_{18}$**) in far-IR. However, the phonon calculations of the peak positions show two phonons of *u* symmetry in the 115 cm^{-1} region (i.e., 114.3 and 116.3 cm^{-1}, Table 4.1) for **8-*d*$_{18}$**. Experimentally, these features are weak (Figure 4.4). In order to show the weakness in intensities of these features, the intensities of the far-IR phonon modes in this region were calculated (Figure 4.4). It is clear there are not quantifiable peak intensities from phonon modes in this region, suggesting that these peaks are very weak in far-IR. Far-IR intensities were derived using the method by Gianozzi and co-workers.[159]

It was determined from the Raman spectroscopy with external magnetic fields that vibrational modes with *g* symmetry couple to the ZFS peak (Table 4.1 and Figure 4.3). The phonon calculations were used to simulate animations of the atomic displacements to understand how the SMM is likely to be altered by vibrations leading to magnetic relaxation. It is clear there is a trend in the magnitude of $|\Lambda|$ and the distortion of the O-Co-O equatorial bond angle. The modes with the largest spin-phonon coupling constant $|\Lambda|$ (Figure 4.3), E in **8/8-*d*$_4$** (File 3) and A in **8-*d*$_{18}$** (File 4), have greatly mismatched vector magnitudes of the equatorial O atoms, leading to a larger net change in this bond angle (Table 4.2 and Figures 4.5-4.6). These vibrations significantly distort the first coordination sphere and perhaps lead to the larger $|\Lambda|$. Therefore, we rationalize that, if these phonons are involved in magnetic relaxation, the O-Co-O equatorial-bond-angle distortion plays a key role in the spin reversal. These spin changes of the excited KD is of prime importance for the magnetic relaxation at elevated temperatures where the excited KD is populated. Likewise, low-energy

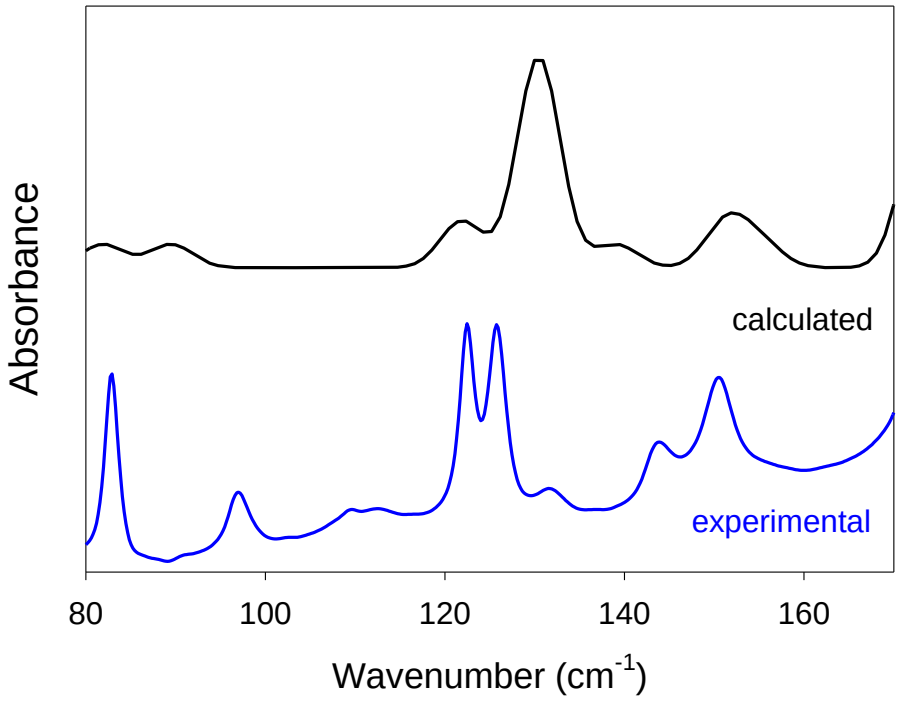

Figure 4.4. Comparison of experimental (0 T) and calculated far-IR spectra of **8-*d*$_{18}$**.

Table 4.2. Distortion of the O-Co-O bond angles in the equatorial plane from the vibrations compared with the spin-phonon coupling constants $|\Lambda|$. These bond angles are determined from the geometry-optimized crystal structure

Complex	Calculated vibration (cm^{-1}) (Peak label)	Equilibrium bond angle (°)	Distorted bond angle (°)	Change in bond angle (°)	Spin-phonon coupling constants $\|\Lambda\|$
8-d_4	126.0 (C)	90.75	90.93	-0.18	0.95(15)
8-d_4	129.3 (D)	90.75	90.85	-0.10	1.00(10)
8-d_4	142.7 (E)	90.75	92.15	-1.4	2.05(10)
8-d_{18}	116.3 (A)	90.75	89.88	0.87	2.15(10)

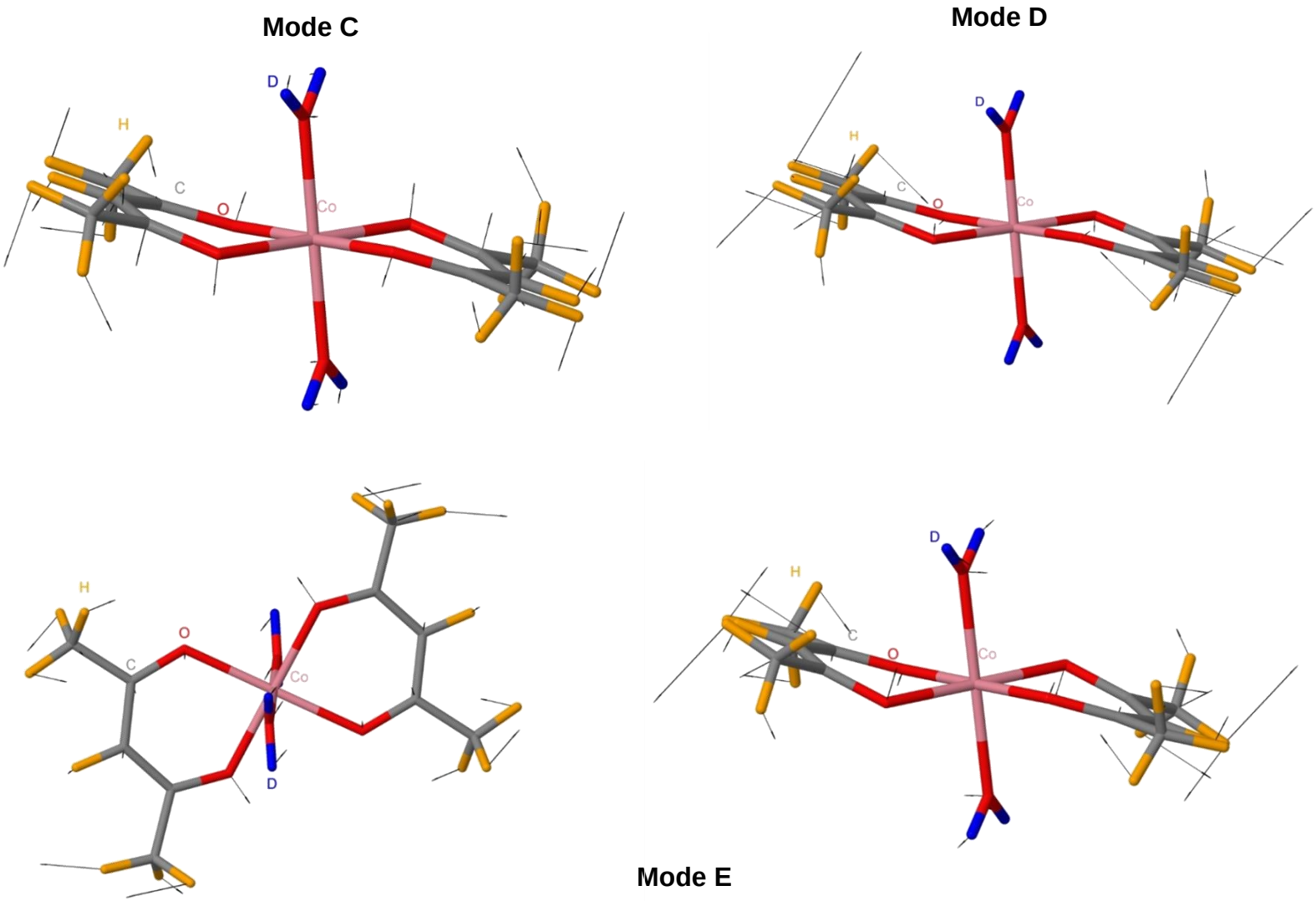

Figure 4.5. Displacement (arrows) of atoms in **8-*d*$_4$** for modes C, D and E (two different orientations of the molecule).

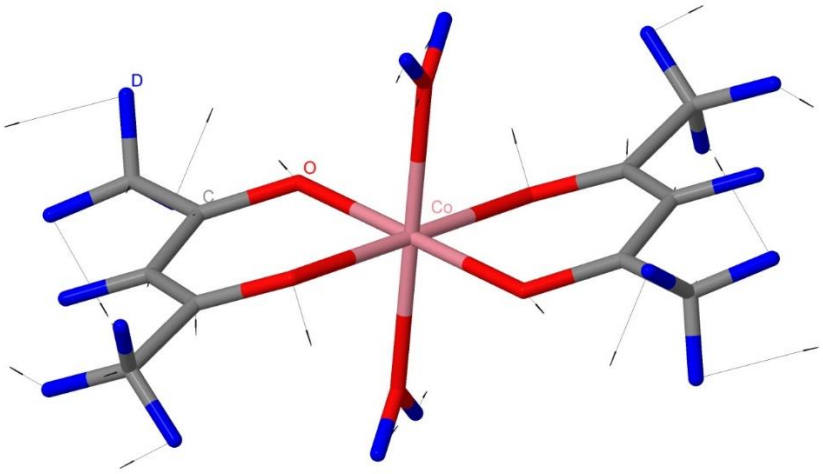

Figure 4.6. Displacement (arrows) of atoms in **8-*d*$_{18}$** for mode A.

phonons (not included in Table 4.2) are responsible for the low-temperature shortcut of the relaxation time. Modes C and D (**8-*d*$_4$**, Files 1 and 2) have less distortion of the O-Co-O equatorial bond angle and therefore, we reason, do not couple as strongly with spin (Figure 4.5). These findings are in line with recent calculations of spin-phonon couplings in $[(tpa^{Ph})Fe]^-$ [H_3tpa^{Ph} = tris((5-phenyl-1*H*-pyrrol-2-yl)methyl)amine] by Lunghi and coworkers demonstrating that the vibrations perturbing the bending angle of the equatorial N atoms coordinated to the Fe(II) ion are strongly coupled to the spin.[12]

The methyl hydrogen (deuterium) atoms have the largest displacements in Figures 4.5-4.6 out of any atoms in the phonons near the ZFS peak, i.e., C, D and E, of **8-*d*$_4$** (A of **8-*d*$_{18}$**). However, due to the distance from these atoms to the Co(II) center (~4.5-5 Å), it is hard to imagine that they have a large role in magnetic relaxation. Therefore, in the case of the aforementioned phonons, these cannot be used to explain the differences in the coupling constants $|\lambda|$ reported here.

4.4. Conclusions

This work demonstrates the necessity of calculating vibrational modes and modeling the atomic displacements to help understand the role chemical structures play in magnetic relaxation. Here, the calculated modes are compared to those observed in the far-IR and Raman spectra. The coupling constants obtained from Raman spectroscopy are non-uniform. To understand why certain modes couple more strongly to the spin, the displacements of the atoms have been studied. It was determined that modes with the largest coupling constant involved the greatly mismatched vector magnitudes of the equatorial O atoms, leading to a larger net change in this bond angle.

This study is the first to use both experimental coupling constants and modeling of the vibrational atomic displacements to understand how these particular could lead to relaxation at higher temperatures.

4.5. Experimental

VASP[144] calculations on **8**, **8-*d*$_4$** and **8-*d*$_{18}$** were conducted. Geometry optimizations were performed on the single-crystal X-ray structure of **1** at 100 K.[160] The optimized structure completed at 0 T was used for the phonon calculations. Spin-polarized, periodic DFT calculations were performed using VASP with the Projector Augmented Wave (PAW)[161-162] method and the local density approximation (GGA)[163] + *U* (*U* = 5.37)[161,164] exchange correlation functional. An energy cut off was 900 eV for the plane-wave basis of the valence electrons. Total energy tolerance for electronic structure minimization was 10^{-8} eV. The optB86b-vdW, a non-local correlation functional that approximately accounts for dispersion interactions, was applied.[165] For the structure relaxation, a $1 \times 3 \times 1$ Monkhorst-Pack mesh was applied. Phonopy,[141] an open source phonon analyzer, was used to create a 140 atom, $1 \times 2 \times 1$ supercell structure. VASP was then employed to calculate the force constants on the supercell in real space using DFT. The crystal structure of **8** was determined to have C_{2h} symmetry.[160] The O'CLIMAX software[166] was used to convert the DFT calculated phonon results to the simulated INS spectra (Figure 4.1). Jmol was used to create the animations (Files 1-4). Since the INS (and far-IR and Raman) peaks of **8** and **8-*d*$_4$** near 115 cm^{-1} are similar, only the calculated phonons of **8-*d*$_4$** are presented.

Chapter 5

Effect of Magnetic Fields on the Methyl Rotation in a Paramagnetic Cobalt(II) Complex. Quasielastic Neutron Scattering Studies

This part is based on the following paper:

Stavretis, S.E.; Mamontov, E.; Moseley, D.H.; Cheng, Y.; Daemen, L.; Ramirez-Cuesta; Xue, Z.-L., Effect of Magnetic Fields on the Methyl Rotation in a Paramagnetic Cobalt(II) Complex. Quasielastic Neutron Scattering Studies. *Submitted for publication*.

This author conducted the QENS experiment and spin density calculations in collaboration with scientists at ORNL. She interpreted all data.

5.1. Abstract

Molecular dynamics is a fundamental property of metal complexes. These dynamic processes, especially for paramagnetic complexes under external magnetic fields, are in general not well understood. Quasielastic neutron scattering (QENS) in 0-4 T magnetic fields has been used to study the dynamics of $Co(acac)_2(D_2O)_2$ (**8-*d*$_4$**, acac = acetylacetonate), a field-induced single-molecule magnet (SMM) at <400 mK. At 80-100 K, rotation of the methyl groups on the acac ligands is the dominant dynamical process. Surprisingly, this rotation is slowed down by the magnetic field increase. Rotation times at 80 K are 5.6(3) x 10^{-10} s at 0 T and 2.04(10) x 10^{-9} s at 4 T. The variable-field QENS studies suggest methyl groups in these paramagnetic Co(II) molecules are not behaving as isolated units. In other words, there are intermolecular interactions between them. We speculate these interactions may originate from the presence of unpaired electron spins dispersed on peripheral hydrogen atoms or from a structure change in the molecules stemming from a magnetic field effect on the paramagnetic Co(II) ions. Methyl torsions in **8-*d*$_4$** have also been observed at 5-100 K in inelastic neutron spectroscopy (INS). Although the temperatures in the current QENS studies are higher than the range in which $Co(acac)_2(H_2O)_2$ (**8**) shows SMM behavior, the QENS and INS results here help understand the dynamics of the compound and may shed light on intermolecular interactions in the solid state.

5.2. Introduction

SMMs are actively studied due to their slow magnetic relaxation, quantum tunneling, and potential applications in, *e.g.*, information storage and quantum

computation.[1] One major focus of SMM research is to increase the blocking temperature T_B above liquid nitrogen of 78 K, and hopefully room temperature in the future, to eliminate the need of the current cryogenic temperatures to observe slow magnetic relaxation. Goodwin and co-workers have recently reported that $[Dy(Cp^{ttt})_2][B(C_6F_5)_4]$ (Cp^{ttt} = 1,2,4-^{t}Bu$_3$C$_5$H$_2$) displays magnetic hysteresis up to 60 K.[156] The magnetic relaxation rate of this dysprosocenium-based SMM is significantly reduced due to improved relaxation dynamics. With increased T_B, more dynamical processes in SMMs would be activated. The dynamics of the ligands/groups of SMMs is believed to play a major role in the relaxation processes, allowing the magnetic moment to re-orientate randomly and thus quenching the magnetic hystersis.[156,167] Studies of the dynamical processes in molecular complexes help understand the properties of the metal complexes at a fundamental level and assist the design of better SMMs.

Gómez-Coca and coworkers have recently reported that, at low temperatures (<400 mK), $Co(acac)_2(H_2O)_2$ (**8**), a Kramers ion, behaves as a field-induced single-molecule magnet (SMM), displaying magnetic hystersis.[10] At higher temperatures, **8** is considered to be a paramagnetic complex with unpaired electrons (S = 3/2) that are not localized but dispersed throughout the molecule, including the ligands.[168]

There have been few direct spectroscopic studies of the dynamics. Although the dynamics of SMMs can be probed by a variety of methods, most often by AC susceptibility for magnetic relaxation, quasielastic neutron scattering (QENS) has been rarely used to study paramagnetic complexes.[169,170] QENS was employed to study a Tb-based SMM.[170] In this work, Kofu *et al*. determined the dynamics (i.e., magnetic relaxation) was activated around 20 K. The dynamics detected by QENS in the Tb-

based SMM is a new relaxation process at the ns and ps timescale, which AC susceptibility studies are not able to reveal. The authors believe that the newly identified relaxation process may stem from either thermally activated tunneling in the higher excited states or unpaired electron spins coupled to the motion of H atoms near the magnetic ions. A paramagnetic oxidized ferrocene complex (not an SMM) was probed with QENS and an external magnetic field.[169] The QENS spectra with the applied field showed that the rotation dynamics of the cyclopentadienyl (Cp) rings was *unaffected* by an external field up to 2.5 T.[169] No further interpretation of the field-independent dynamics was given.

Neutron backscattering spectrometers can be used to obtain high-resolution QENS spectra.[171-172] QENS probes small energy exchanges in a small-energy inelastic process that appears almost elastic. The translational or rotational motion of atoms or molecules cause quasielastic broadening of the elastic peak in comparison to instrument resolution spectrum that has a maximum around $E = 0$ cm^{-1}.[171] At adequately high temperatures, the molecular motions cause measurable energy transfer to or from the neutrons during the scattering event at a given energy resolution of the spectrometer.[173-174] For metal complexes, QENS has been used to probe rotations of methyl and Cp groups[172,175-176] and an exchange between a hydride ligand and peripheral methyl groups in a complex[177] in addition to the studies of the magnetic relaxation in the Tb-based SMM.[170] QENS has also been used to characterize a precursor in spinel $GeCo_2O_4$ that, below its Neel temperature, becomes antiferromagnetically coupled ferromagnetic subunits.[178]

Internal rotations, such as methyl rotation in ethane and ethane-like molecules, have been the subjects of both theoretical and experimental studies since the early years of quantum chemistry.[179-188] Hindered rotations and barriers to internal rotations contribute to the conformations of molecules. The nature of the rotations is of fundamental interest in part as the rotations determine some critical characters of the structures and functions of molecules.[183-184] However, the nature of barrier factors, even for ethane, is still debated.[184,186-187] Electronic origin of the barriers has been considered in terms of steric repulsions, electrostatic models and hyperconjugation, among others.[184,186-187]

We report here our QENS studies of $Co(acac)_2(D_2O)_2$ (**8-*d*$_4$**) with two acac and two deuterated water ligands in the equatorial and axial planes, respectively (Figure 5.1). The acac ligands contain a total of four methyl groups per molecule of **8-*d*$_4$**. QENS has been used in conjugation with an applied magnetic field up to 4 T to probe field-dependent dynamics of **8-*d*$_4$** at 80-100 K, revealing the rotation of the methyl groups. In addition, INS of **8-*d*$_4$** has been investigated at the vibrational spectrometer VISION to examine the methyl torsion peaks and calculate the activation energy of methyl rotation. The methyl groups weakly interact with each other. Thus, the rotations are collective in nature. However, since the interaction/coupling is very weak, the torsion or rotation is nearly independent among molecules and can be considered to be an internal mode. To our knowledge, this is the first time that field-dependent dynamics of the methyl rotation has been observed. Although **8-*d*$_4$** does not behave as an SMM at 80-100 K (the temperature range of the current work), the results here help understand the molecular dynamics and the effect of the magnetic fields on the dynamics.

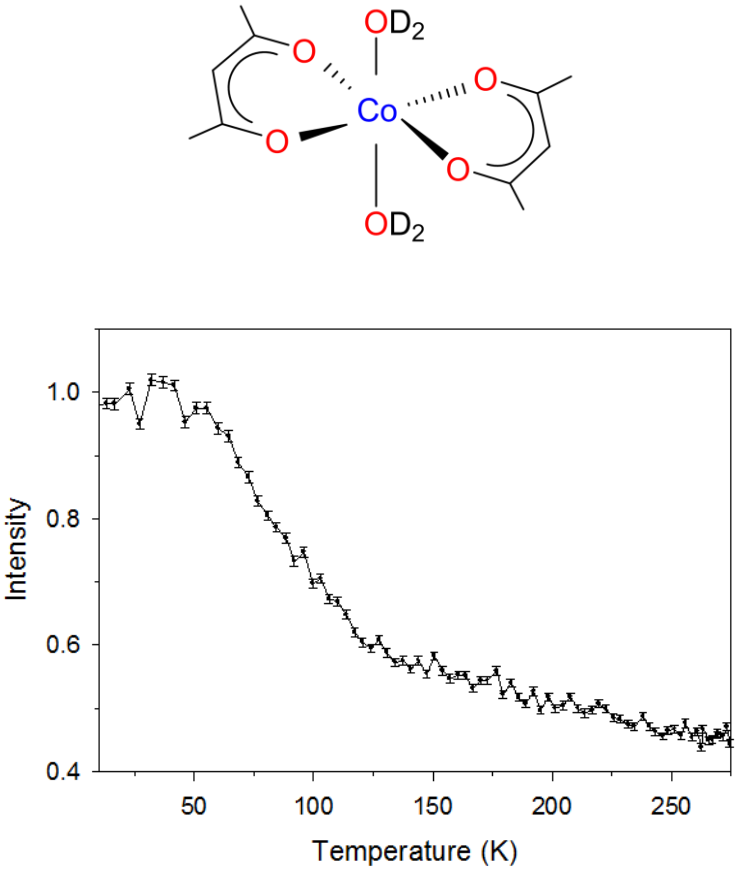

Figure 5.1. (Top) Structure of **8-*d*$_4$**. (Bottom) Fixed window elastic scattering neutron intensity scan at |*Q*| = 0.3 Å^{-1} between 2 and 275 K. |*Q*| dependence of the fixed window scan is shown in Figure C.1.

5.3. Results and Discussion

5.3.1. QENS Data and Calculation of Methyl Rotation Times

To probe the temperature range where the measurable dynamical processes occur, Backscattering Spectrometer (BASIS), a QENS instrument, was utilized. A fixed window scan, where the elastic (within the energy resolution of the spectrometer) intensity is recorded as a function of temperature, was performed on **8-*d*$_4$** as shown in Figure 5.1-Bottom between 2 and 275 K. Based on Figure 5.1, the temperature range where the QENS signal could be probed by BASIS is between 70 and 120 K. Under 70 K, the dynamics is too slow to be detected by BASIS and the elastic intensity shows little temperature dependence aside from the thermal Debye-Waller factor due to the vibrational degrees of freedom that are always present. However, once the temperature is increased to ~70 K, there is a drop in elastic intensity signifying the presence of quasielastic behavior, or broadening of the scattering signal, at the expense of the intensity measured at $\omega = 0$. The dynamics detected in this region is associated with classical stochastic methyl rotations.

QENS data at 80, 90, and 100 K show broadening compared to the resolution function of the sample measured at 2 K. Representative QENS data compared to the resolution function are given in Figures C.2-C.3 in Appendix C. The intensity of the QENS component was found to increase with Q, indicating localized motion (rather than magnetic scattering signal). The QENS spectra were fit with the Cole-Cole model dynamic structure factor (Eqs. 5.1-5.2). Here, E_0, signifies the broadening of the QENS signal. E_0 is analogous to the HWHM (Γ) parameter of a Lorentzian function, which is the limiting case when the "stretching" parameter $\alpha = 0$.[189] E_0 values from these fits are

shown in Tables 5.1 and C.1. It should be noted that initially an attempt was also made to fit the data with the Lorentzian (rather than the Cole-Cole) model dynamic structure factor, but it was not successful. Thus, the data were fit using the following equations:[189]

$$I(Q,E) = \left[x(Q)\delta(E) + \left(1 - x(Q)\right)S(Q,E)\right] \otimes R(Q,E) + B(Q,E) \qquad \text{(Eq. 5.1)}$$

where $\delta(E)$ is a delta function centered at zero energy transfer (E = 0), $x(Q)$ represents the fraction of elastic scattering in the signal, $B(Q,E)$ is a linear background term, $B(Q,E) = C_1(Q)E + C_2(Q)$, $R(Q,E)$ is the resolution function, and $S(Q,E)$ is the Cole-Cole model dynamic structure factor (Eq. 5.2):

$$S(Q,E) = \frac{1}{\pi E_0(Q)} \frac{(E(Q)/E_0(Q))^{-\alpha(Q)} \cos\frac{\pi\alpha(Q)}{2}}{1 + 2(E(Q)/E_0(Q))^{1-\alpha(Q)} \sin\frac{\pi\alpha(Q)}{2} + (E(Q)/E_0(Q))^{2(1-\alpha(Q))}} \qquad \text{(Eq. 5.2)}$$

The Cole-Cole scattering function has been previously used in dielectric measurements to interpret the “stretched” relaxation character in the frequency space, but has also been demonstrated as a function to fit QENS data.[189] A representative fit of the data is given in Figure C.4. From E_0 extracted from data fitting, it is evident that the signal becomes narrower as field increases (Table 5.1). For example, E_0 are 1.19(6) and 0.323(17) μeV at 0 and 4 T, respectively. Methyl rotation time τ is defined to be the time needed to complete one 120° rotation[176] around the C-CH_3 bonds in the acac ligand. 1/τ is thus the frequency of the methyl rotation. The τ and E_0 parameters have an

Table 5.1. E_0 and τ values of **8-*d*$_4$** at different temperatures and 0 and 4 T from QENS

Field	Temp (K)[a]	E_0 (μeV)[b]	τ (s)[c]
0 T	80	1.19(6)	$5.6(3) \times 10^{-10}$
	90	2.43(12)	$2.71(13) \times 10^{-10}$
	100	4.5(2)	$1.48(7) \times 10^{-10}$
4 T	80	0.323(17)[d]	$2.04(10) \times 10^{-9}$
	90	1.14(6)	$5.8(3) \times 10^{-10}$
	100	2.61(13)	$2.53(12) \times 10^{-10}$

[a] Uncertainty in temperature (σT = 0.1 K)

[b] Total uncertainties σ_{total} in E_0 are given in Table 5.1 here:[190] $\sigma_{total}^2 = \sigma_{ran}^2 + \sigma_{sys}^2$. Random uncertainty σ_{ran} for each E_0 value is obtained from the fitting of the QENS data using Eq. 5.1. Systematic uncertainty σ_{sys} in E_0 from the QENS studies here is estimated to be 5% of E_0.

[c] The largest uncertainties in τ at 0 and 4 T are 2.8×10^{-11} s and 10×10^{-10} s, respectively. These are used to calculate uncertainties in E_a and τ_0 by Eqs. 5.7-5.8, respectively.

[d] QENS signals as narrow as the one presented here have been measured in the past on BASIS[191-193] and backscattering spectrometers elsewhere.[194]

inverse relationship, $\tau = \hbar/E_0$ ($\hbar = h/2\pi$; h: Planck constant). An increase in E_0 indicates a decrease in τ. τ values at different temperatures and 0 and 4 T fields, calculated from the E_0 values, are given in Table 5.1.

5.3.2. Activation Energies E_a of the Methyl Rotation at 0 and 4 T

Thermal dependence of rotation times τ vs. temperature is found to follow the Arrhenius equation (Eq. 5.3):

$$\tau = \tau_0 e^{E_a/k_B T} \qquad \text{(Eq. 5.3)}$$

where E_a is the activation energy or barrier of the methyl rotation, τ_0 is the pre-exponential factor and, in the current case, attempt frequency Γ_0 for 120° rotation ($\Gamma_0 = 1/\tau_0$), and k_B is Boltzmann constant.

The Arrhenius plots ln τ vs. 1000/T at 0 and 4 T are given in Figure 5.2. The slopes of the fit lines give E_a for the rotation of the methyl groups in **8-*d*$_4$** at the two magnetic fields. The y-axis intercepts give τ_0. We have derived error propagation formulas (Section 5.5) to estimate the uncertainties in E_a and τ_0 from such fits based on the Arrhenius equation in Eq. 5.3. The approach to derive the formulas is analogous to those used to derive error propagation formulas for the Eyring equation by Girolami and coworkers[195] and for the Van't Hoff equation (changes in equilibrium constant, K_{eq}, of a chemical reaction vs. temperature) by us.[196-197]

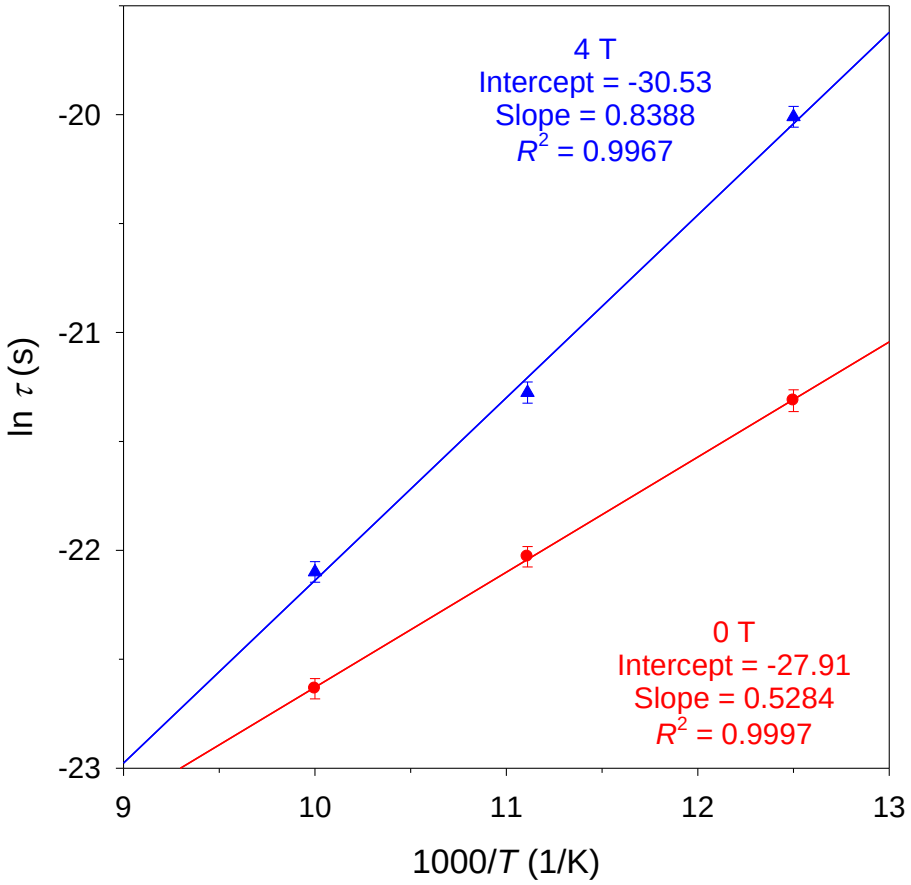

Figure 5.2. Arrhenius plots of ln τ vs. 1000/T at 0 (red points and the fit line) and 4 Tesla (blue points and the fit line).

Fittings of the Arrhenius plots in Figure 5.2 give activation energies at 0 [$E_{a(H=0)}$] and 4 T [$E_{a(H=4T)}$]: $E_{a(H=0)}$ = 46(4) meV [3.7(3) x 10^2 cm^{-1}; 1.05(0.10) kcal/mol] and $E_{a(H=4T)}$ = 72(5) meV [5.8(4) x 10^2 cm^{-1}; 1.67(0.12) kcal/mol]. As expected, the rotation becomes faster (with smaller τ) when temperature is increased (Table 5.1). Notably, the rotation slows down at 4 T (with larger τ) and the activation energy $E_{a(H=4T)}$ for the methyl rotation inside the external magnetic field is larger than $E_{a(H=0)}$ at 0 T. In other words, methyl rotation time τ, as measured by QENS, becomes larger under the applied field.

Energies of the attempt frequency Γ_0 determined are 0.86 (6.9 cm^{-1}, 0 T) and 11.8 meV (95.1 cm^{-1}, 4 T). Γ_0 from methyl rotations are typically between 2 (16 cm^{-1}) and 5 meV (40 cm^{-1}).[198] Γ_0 at 0 and 4 T are found to be field-dependent and are outside the typical range. The magnetic field effect on methyl rotations could indicate interactions between magnetic moments of the methyl groups or Co(II) ions on neighboring molecules at 0 and 4 T, which is discussed below.

The activation energy E_a may also be deduced from neutron vibrational spectroscopy. The torsions of a methyl group refer to the motions within a single potential well (or oscillations about the minimum) (Figure 5.3).[183] That is, the H atoms of the CH_3 groups do *not* traverse the saddle point of the potential barrier (Figure 5.3). Torsions are typically in the meV range (1 meV = 8.065 cm^{-1}) and are measurable at as low as 5 K by vibrational spectroscopies, including inelastic neutron scattering (INS). When the thermal energy in the system becomes sufficient for H atoms to overcome the potential barrier to perform a 120° jump (that is, at finite temperatures), the process is referred to as rotation or stochastic reorientation (Figure 5.3).

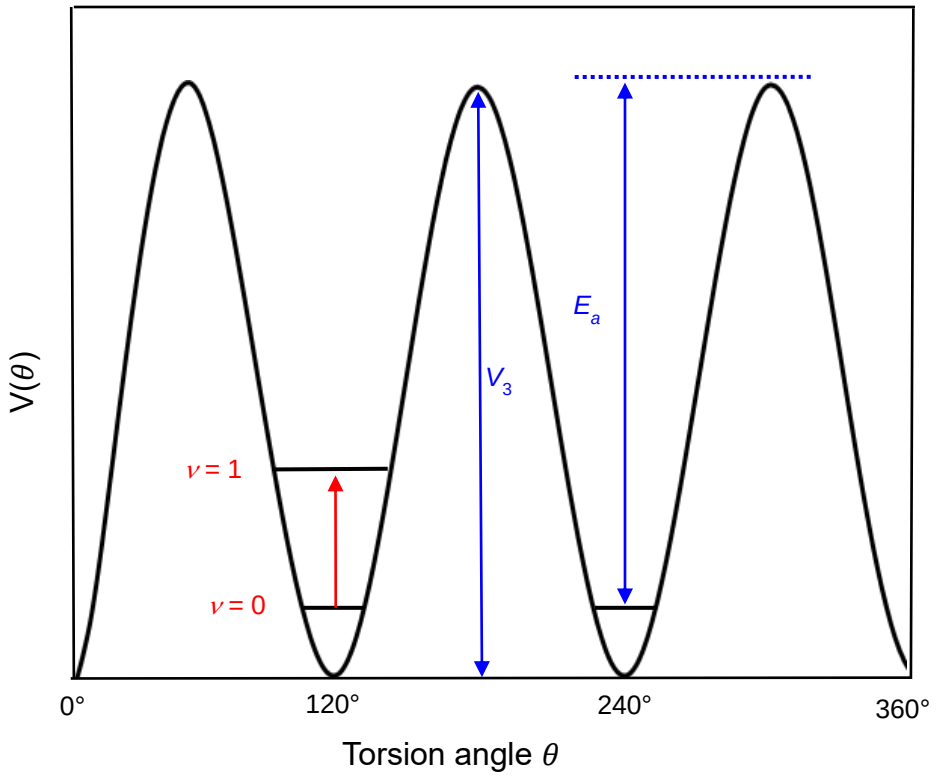

Figure 5.3. Torsion and rotation of a methyl group. E_a is the activation energy of the methyl rotations; v = 0 is the ground torsional level; V_3 is the 3-fold barrier height.

Peaks of methyl torsion (e.g., $\nu = 0 \rightarrow 1$ transition in Figure 5.3) are observed at VISION without external magnetic field. (Currently no external magnetic field can be applied at VISION.) These peaks should be intense in the VISION spectrum since they stem from large displacements of hydrogen atoms which have a large cross section for neutron scattering.[199] At BASIS, the *effective* activation barrier is observed. No particular vibrational mode was activated in the QENS process. In other words, the temperature probed at BASIS (70-100 K) causes many modes to be activated. In comparison, using the VISION data, we are able to calculate E_a for *a particular methyl torsional mode* based on its energy. The most intense vibrational mode (methyl torsion) in the VISION spectrum is at 20.3 meV (164 cm^{-1}, Figure C.5 in Appendix C) which can be considered a mostly internal mode. This mode shows strong torsions of the methyl groups. The 20.3 meV mode is used as a representative methyl torsion in the VISION data. Using the hindered methyl rotor dynamics program in DAVE[62] [methyl rotational constant = 0.65 meV (5.2 cm^{-1})], the Schrodinger equation was solved for various V_3 (height of the potential barrier). From this equation, if the ground state of 10.6 meV (85.5 cm^{-1}), V_3 is 82.0 meV (661 cm^{-1}). Then, the E_a value from the VISION data is 71.4 meV (576 cm^{-1}; 1.65 kcal/mol). Considering the two different approaches in determining E_a, the VISION data are comparable to the E_a value (~50 meV at 0 T) from the Arrhenius fitting of the BASIS data in Figure 5.2. Since E_a from the BASIS data is extracted from the Arrhenius plot, the differences from the E_a extracted from the VISION data could be attributed to processes that are not described by the Arrhenius model such as quantum tunneling.[198]

5.3.3. Effect of the External Magnetic Fields on the Rotation Times τ

The effect has been studied at 100 K (Figure 5.4). Rotation times from QENS were collected for a total of 10 different fields between 0 and 4 T, providing enough data points to see a trend of τ vs. the magnetic field *H* (Table C.1 in Appendix C). Figure C.6 shows an exponential trend in the rate of the methyl rotation. From 0 to 1.5 T, there is little change in τ. However, as the field is increased >1.5 T, the pace of change in τ is faster, suggesting that the observed methyl rotation time is more hindered as the magnetic field is raised.

To our knowledge, how external magnetic fields affect molecular dynamics such as methyl rotation in $Co(acac)_2(D_2O)_2$ (**8-*d*$_4$**) has not been investigated. The experimental data (Table C.1 in Appendix C) show the following exponential relationship in Eq. 5.4:

$$\tau_{(H)} - \tau_{(H=0)} = ae^{bH} \qquad (a \text{ and } b\text{: fitting constants}) \qquad \text{(Eq. 5.4)}$$

or the linear relationship between ln ($\tau_{(H)} - \tau_{(H=0)}$) and *H* in Eq. 5.5, as demonstrated in Figure 5.4:

$$\ln (\tau_{(H)} - \tau_{(H=0)}) = \ln a + bH \qquad \text{(Eq. 5.5)}$$

If the partial electron spin on an H atom (discussed below) behaves similarly as an electron, the partial spin is expected to have two degenerate, spin-up and spin-down states. When a molecule of **8-*d*$_4$** is placed inside the external magnetic fields, Zeeman

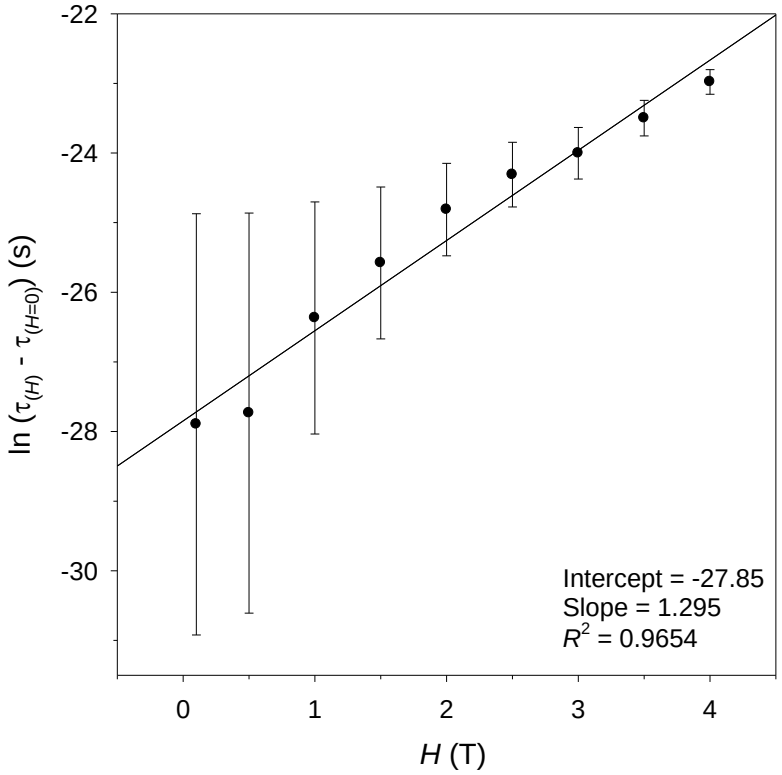

Figure 5.4. Plot of ln ($\tau_{(H)}$ - $\tau_{(H=0)}$) vs H at 100 K. The larger uncertainties at smaller fields H in the plot reflect the fact that the differences between $\tau_{(H)}$ and $\tau_{(H=0)}$ (or the numbers $\tau_{(H)}$ - $\tau_{(H=0)}$) are small. The plot ln($\tau_{(H)}$ – 0.9843 $\tau_{(H=0)}$) vs H gives a better fit (Figures C.6-C.7 in Appendix C) with R^2 = 0.9932.

effect leads to the splitting of the spin-up and spin-down states, as is the case for an unpaired electron inside the field. Why the data in Figure 5.4 give the linear relationship between ln ($\tau_{(H)}$ - $\tau_{(H=0)}$) and H in Eq. 5.5 deserves theoretical studies which are beyond the scope of the current work.

5.3.4. Calculations of Spin Densities

Considering the lack of calculated spin densities for $Co(acac)_2(H_2O)_2$ (**8**), its spin densities have been calculated with the *Vienna Ab Initio Simulation Package* (VASP) to understand how the spin in the molecule of $Co(acac)_2(D_2O)_2$ (**8-*d*$_4$**) is dispersed onto the peripheral methyl H-atoms. It should be pointed out that the current work focuses on using QENS to probe molecular dynamics. The VASP calculations are not designed to be of high-level but were conducted to provide a quantitative scale to show the presence of spin densities on peripheral H atoms of **8**. VASP partitions electrons according to the Wigner Seitz radius a_e in Eq. 5.6:[200]

$$a_e = (3/4\pi n_e)^{1/3} \qquad \text{(Eq. 5.6)}$$

where n_e is electron density. Each atom is considered as a sphere and a_e defines the radius “occupied” by one atom in a sample.

This method leads to the absence of densities between atoms, i.e., densities of bonds. Therefore, the sum of the magnetic moment on all atoms combined, 2.97, is slightly smaller than the total, 3 (= 3 unpaired electrons), on the complex. The spin densities ρ_s

for the atoms of **8** are given in Table 5.2.

The results of spin density calculations, although not at a high level, show that the unpaired electron spin density is transferred from the central Co(II) ion to the atoms on both acac and H_2O ligands. In other words, the unpaired electrons are not localized on a single point, such as the Co(II) ion, but dispersed over the entire molecule. The results are consistent with NMR studies of such paramagnetic compounds,[201-203] and an earlier report by Lohr, Miller and Sharp.[111] It is well known that NMR resonances of ligands in paramagnetic complexes are typically shifted as a result of the electron spin densities on the ligand atoms.[201-203] Lohr and coworkers reported spin densities in $Mn(acac)_2(H_2O)_2$ (S = 5/2) that were calculated using the unrestricted Hartree-Fock method.[111] The spin densities on the H atoms of the methine and methyl groups have an average value of -1.5×10^{-5} and 7.2×10^{-5}, respectively. The value for the water protons is much higher at 4.3×10^{-3}. Lohr and coworkers also attempted to do the same calculations for $Co(acac)_2(H_2O)_2$ (**8**, S = 3/2) but indicated they could not obtain computationally significant values using their method.[111]

The transfer of spin density is probably through both spin delocalization and polarization mechanisms, as shown by the sign of ρ_s in Table 5.2. Such a model has been used to explain spin delocalization in paramagnetic molecules.[201-202] It should be pointed out, however, a majority of the unpaired electron spin density (~95%) is localized on the Co(II) ion. Only 0.03% unpaired electron spin is localized on the 12 H atoms of four methyl groups in the two acac ligands, while 0.3% is localized on the carbon atoms of the methyl groups. On average, each methyl group carries 7.16×10^{-5} (Table C.2 in Appendix C).

Table 5.2. Spin densities ρ_s of the atoms in one molecule of **8**[a]

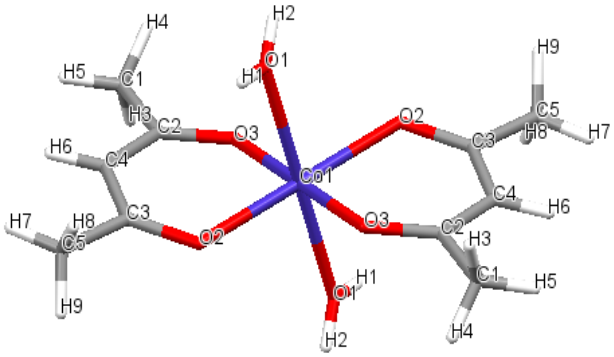

Atom	ρ_s
H6	-2.57×10^{-5}
H3-5 + H7-9	8.60×10^{-4}
H1-2	3.60×10^{-3}
C6	6.80×10^{-3}
C2-3	-3.74×10^{-3}
C1,5	8.20×10^{-3}
O2-3	1.08×10^{-1}
O1	3.81×10^{-2}
Co1	2.81
Total	2.97

[a] There are two molecules in a unit cell of **8**. The total spin density for the unit cell is twice of the total density in this table.

It is not clear why the methyl rotation is slower when magnetic field is applied. It is possible that this is due to the presence of electron spin density on the methyl hydrogen atoms. If the spin density on each H atom is considered as a tiny magnet, the three magnets on the three H atoms of a methyl group will align in the direction of the external magnetic field when the field is applied. In this simple, classic picture, rotating of the three magnets inside the external field is expected to be more difficult. An earlier QENS study of an exchange between the $H_{hydride}$ ligand and $H_{o\text{-methyl}}$ atoms of the mesityl group in *trans*-W(≡Cmesityl)$(dmpe)_2H$ [mesityl = 2,4,6-trimethylphenyl; dmpe = 1,2-bis(dimethylphosphino)ethane] showed that $H_{hydride}$ and $H_{o\text{-methyl}}$ atoms, which are 4.25 Å apart, undergo jump diffusion.[177] Analyses of the crystal structure of $Co(acac)_2(H_2O)_2$ (**8**) at 298 K[10] show that the H-H distances between methyl groups of neighboring molecules are as close as 2.734, 2.836 and 2.907 Å. It would not be surprising that the H atoms of these methyl groups with electron spin densities have magnetic interactions among them, contributing to the intermolecular interactions between the neighboring molecules of **8**. We note the calculated unpaired electron densities on the methyl H atoms are small and temperatures of 80-100 K required for this study provide large thermal energy to the H atoms.

Another possible factor is the intermolecular interactions stemming from the paramagnetic metal of the complex. Gómez-Coca *et al*. have shown that there are intermolecular interactions in the solids of $Co(acac)_2(H_2O)_2$ (**8**).[10] The interactions are significantly reduced in magnetically diluted solids of $Co_{0.05}Zn_{0.95}(acac)_2(H_2O)_2$ containing 95% diamagnetic Zn(II) ions. Such intermolecular interactions between metal centers have also been observed in other SMMs.[10,204] Inside external magnetic fields,

such interactions perhaps alter the structure of two neighboring molecules, possibly making it more difficult for the methyl groups to rotate due to changes in distances between the peripheral methyl groups. However, powder neutron diffraction of Co(acac-d_7)$_2$(D_2O)$_2$ (**8-*d*$_{18}$**) at 0 and 7 T and 4 K using the High Resolution Powder Diffractometer (BT-1) at U.S. NIST Center for Neutron Research showed no observable structure changes beyond errors of the method.[160] Thus, there is no experimental data at this time to confirm such a structure change under magnetic field.

5.4. Conclusions

The current work shows that external magnetic fields influence the rotations of the methyl groups in **8-*d*$_4$**. To our knowledge, this is the first report of field-dependent methyl group rotation. The variable-field QENS studies here suggest that the methyl groups on the paramagnetic molecule probably do not behave alone. That is, there are intermolecular interactions among neighboring molecules. While further work is needed to understand the origin of the changes of methyl group rotation with field, it is clear that the rotation of these groups is susceptible to magnetic field changes. Our results are different from those of Kofu *et al*.[170] as the dynamics observed here occurs at higher temperatures and is ascribed to molecular lattice dynamics instead of magnetic relaxation. The work here helps understand the dynamics in the molecules of **8-*d*$_4$** which behave as SMMs at lower temperatures.

5.5. Experimental

QENS experiments were performed at Backscattering Spectrometer (BASIS) at SNS, ORNL.[205] In a QENS experiment, neutron scattering intensity is measured as a function of the neutron energy transfer, defined as the difference between the incident and detected neutron energy. The energy transfer range probed was ±100 μeV, whereas the *Q*-averaged energy resolution was 3.4 μeV, full width at half maximum. This resolution value corresponds to longest measurable relaxation time of about 0.4 ns. The *Q*-averaged (0.3-1.9 $Å^{-1}$) QENS spectra were fit with the Cole-Cole equation at each temperature/field. Approximately 3.8 g of polycrystalline sample was packed into an aluminum sample can. This can were then topped with aluminum foil to prevent the powders from moving in the magnetic field. A 5 T vertical magnetic was used in the sample environment. The QENS data were fit with the Cole-Cole equation in DAVE.[62] VISION data on **8-*d*$_4$** were collected on ~2 g of samples for 1 h at 5 and 100 K. The unpaired electron spin density was calculated simultaneously with the geometry optimization of $Co(acac)_2(H_2O)_2$ (**8**) in the VASP with the MAGMOM tag on. Geometry optimizations were conducted on the single-crystal X-ray structure of **8** at 100 K[160] described in Section 4.5.

The total uncertainties in the rotation time at 0 and 4 T were used in the ln τ vs 1000/*T* plot in Figure 5.2 and error propagation calculations below. The activation energies E_a were calculated from an unweighted nonlinear least-squares procedure contained in the SigmaPlot Scientific Graph System. The uncertainties in E_a and τ_0 were computed from the following error propagation formulas (Eqs. 5.7-5.9), which were derived from the Arrhenius equation (Eq. 5.3).

$$(\sigma E_a)^2 = k_B^2 T_{max}^2 T_{min}^2 (T_{max}^2 + T_{min}^2) [\ln(\tau_{max}/\tau_{min})]^2 (\sigma T/T)^2/\Delta T^4 + 2k_B^2 T_{max}^2 T_{min}^2 (\sigma\tau/\tau)^2/\Delta T^2 \quad \text{(Eq. 5.7)}$$

$$(\sigma\tau_0/\tau_0)^2 = 2T_{max}^2 T_{min}^2 [\ln(\tau_{max}/\tau_{min})]^2 (\sigma T/T)^2 / \Delta T^4 + (T_{max}^2 + T_{min}^2)(\sigma\tau/\tau)^2/\Delta T^2 \quad \text{(Eq. 5.8)}$$

where $\Delta T = (T_{max} - T_{min})$.

For Arrhenius equation in the following form:

$$1/\tau = (1/\tau_0)\, e^{-U/k_B T}$$ (k = Boltzmann constant)

$$(\sigma U)^2 = k^2 T_{max}^2 T_{min}^2 (T_{max}^2 + T_{min}^2) [\ln(\tau_{max}/\tau_{min})]^2 (\sigma T/T)^2 / \Delta T^4 + 2k^2 T_{max}^2 T_{min}^2 (\sigma\tau/\tau)^2 / \Delta T^2 \quad \text{(Eq. 5.9)}$$

Chapter 6

Conclusions and Recommendations

6.1. Conclusions

This dissertation is focused on three main subjects: (1) Determination of magnetic excitations by inelastic neutron scattering (INS) in paramagnetic complexes including single-molecule magnets (SMMs); (2) Probing the origins of spin-phonon coupling in $Co(acac)_2(D_2O)_2$ (**8-*d*$_4$**) and $Co(acac\text{-}d_7)_2(D_2O)_2$ (**8-*d*$_{18}$**); (3) Investigating field-dependent methyl rotation of **8-*d*$_4$** with quasielastic neutron scattering (QENS).

In Chapter 2 INS is utilized to directly determine the zero-field splitting (ZFS) parameters of nondeuterated metalloporphyrins Fe(TPP)X [X = F (**1**), Br (**2**), I (**3**); H_2TPP = tetraphenylporphyrin]. The ZFS values are D = 4.49(9) cm^{-1} for tetragonal polycrystalline Fe(TPP)F (**1**), and D = 8.8(2) cm^{-1}, E = 0.1(2) cm^{-1} and D = 13.4(6) cm^{-1}, E = 0.3(6) cm^{-1} for monoclinic polycrystalline Fe(TPP)Br (**2**) and Fe(TPP)I (**3**), respectively. Along with the previously reported value D = 6.33(8) cm^{-1} for Fe(TPP)Cl, this work reveals D increases from F to I. Ligand field at the *ab initio* level shows that the origin of D stems in part from delocalization of σ d-electrons on the TPP ligand which reduces the Racah parameter and the energy gap between the ground $^6A_1$ ground and the $^4A_2$ excited state.

Chapter 3 demonstrates the strengths of using INS to probe magnetic excitations in multiple Co(II) complexes and an Er(III) SMM. These studies reveal the following: (1) Necessity of determining magnetic excitations *directly* instead of solely relying on estimates obtained magnetometry measurements. Indeed, discrepancies of the values reported from magnetometry measurements have been found to overestimate the size of the separations between ground and first excited magnetic levels. (2) Viability of using an *external magnetic field* in INS to determine the magnetic excitations of

protonated samples with for large separations (40 and 105 cm^{-1}) where phonons are prevalent. The use of single crystal SMMs eliminated peak broadness under the application of field due to different orientations of the powder samples B_x, B_y, B_z. (3) Use of $|Q|$ dependence from the INS data to disentangle spin-phonon coupled peaks at 0 T, revealing the magnetic and vibrational origin of these peaks.

Chapter 4 highlights the utility of calculating vibrational modes and modeling the displacements of atoms in SMMs. Based on experimental spin-phonon coupling constants ($|\Lambda|$) extracted from magneto-Raman spectroscopy, it is determined that some phonon modes have larger $|\Lambda|$ than others. The displacements of the atoms show that the modes with the largest couplings $|\Lambda|$ have the greatest net change in the equatorial O-atom bond angles. This study is unique in that it is the first to use both experimental coupling constants and modeling of the vibrational atomic displacements to understand how phonons near the magnetic excitation could interact with magnetic moments, leading to relaxation.

Chapter 5 provides a unique approach to examine the molecular dynamics in the temperature range where **8-*d*$_4$** behaves as a paramagnet. Our quasielastic neutron scattering results show the primary dynamical process is methyl rotation. With the application of external magnetic field, the methyl rotation is slowed down demonstrating field-dependent behavior. This field-dependent behavior may be from the intermolecular interactions between molecules of **8-*d*$_4$**.

6.2. Recommendations

Several recommendations for future work are made by looking at the total picture obtained from this dissertation. INS shows the full spectrum of vibrational peaks with no selection rules. When using other spectroscopic techniques, such as Raman and IR, some vibrational peaks may be forbidden. The work outlined in Chapter 3 demonstrates the importance of the following determinations: (1) Exact energy of the magnetic excitation; (2) Energies where the phonons are located, especially in relation to the magnetic excitation. For example, low-energy phonons are found to participate in spin relaxation to significantly reduce the observed spectroscopic barrier (i.e., magnetic separation between ground and first excited state). Therefore, it is of critical importance to create desirable SMMs to maximize the magnetic anisotropy and to design the phonon spectrum, reducing spin-phonon coupling especially in the energies close to the magnetic excitation. Spectroscopies including INS can help probe next generation SMMs.

U_{eff} is determined by the phonon energies that are specific to each SMMs. Therefore, finding ways to fine-tune the phonon energies will be important to engineer future SMMs. It could be possible to increase magnetic relaxation by increasing the energies of lowest energy phonon to slow down direct relaxation between *nearly* degenerate magnetic ground states. In the high temperature regime, where the Orbach processes is applicable, it is perhaps desirable to increase the energies of phonons so a mode that strongly couples would be at higher energies. A potential avenue for increasing magnetic relaxation could be with pressure. For example, **8** has been probed under pressures up to 2.0 GPa (Figure 6.1) in a preliminary study. The low energy

phonons sensitive to intermolecular changes are the most affected. However, how this blue-shift in the low energy phonons affects magnetic relaxation is not known. Extensive work with AC susceptibility measurements under pressure is needed to gain a full understanding of the potential for this method.

In addition, as inelastic neutron scattering instrumentation improves, the ability to probe magnetic excitation will become easier, requiring less time per measurement and smaller sample sizes. In the time of this dissertation, the INS with external magnetic field only has about 33% detector efficiency. However, instrumentation advances such as new radial collimator to extend detector coverage acquired for Cold Neutron Chopper Spectrometer (CNCS) will increase detector efficiency to 80%. In essence, the radial collimators can decrease background scattering from the sample environment by collimating the scattered neutron beam, to eliminate beam divergence, giving better signal-to-noise ratios.[206] This advancement will make INS and magnetic fields even more attractive as a spectroscopic technique to probe SMMs.

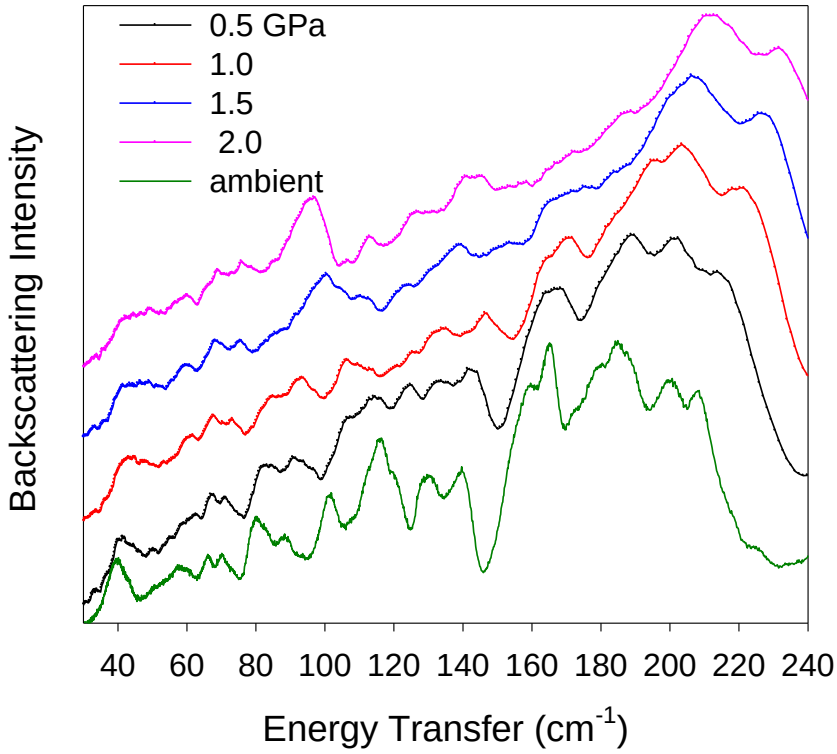

Figure 6.1. INS spectra of $Co(acac)_2(H_2O)_2$ (**8**) at VISION between ambient and 2.0 GPa pressure (5 K).

References

1. Frost, J. M.; Harriman, K. L. M.; Murugesu, M. The Rise of 3-d Single-Ion Magnets in Molecular Magnetism: Towards Materials from Molecules? *Chem. Sci.* **2016,** *7*, 2470.
2. Liddle, S. T.; van Slageren, J. Improving f-Element Single Molecule Magnets. *Chem. Soc. Rev.* **2015,** *44*, 6655.
3. Krzystek, J.; Telser, J. Measuring Giant Anisotropy in Paramagnetic Transition Metal Complexes with Relevance to Single-Ion Magnetism. *Dalton Trans.* **2016,** *45*, 16751.
4. Brackett, G. C. Far-Infrared Magnetic Resonance in Fe(III) and Mn(III) Porphyrins, Myoglobin, Hemoglobin, Ferrichrome A, and Fe(III) Dithiocarbamates. University of California, Berkeley, 1970.
5. Sessoli, R.; Gatteschi, D.; Caneschi, A.; Novak, M. A. Magnetic Bistability in a Metal-Ion Cluster. *Nature* **1993,** *365*, 141.
6. Chen, L.; Cui, H.-H.; Stavretis, S. E.; Hunter, S. C.; Zhang, Y.-Q.; Chen, X.-T.; Sun, Y.-C.; Wang, Z.; Song, Y.; Podlesnyak, A. A.; Ouyang, Z.-W.; Xue, Z.-L. Slow Magnetic Relaxations in Cobalt(II) Tetranitrate Complexes. Studies of Magnetic Anisotropy by Inelastic Neutron Scattering and High-Frequency and High-Field EPR Spectroscopy. *Inorg. Chem.* **2016,** *55*, 12603.
7. Boča, R. Zero-Field Splitting in Metal Complexes. *Coord. Chem. Rev.* **2004,** *248*, 757.
8. Stavretis, S. E.; Atanasov, M.; Podlesnyak, A. A.; Hunter, S. C.; Neese, F.; Xue, Z.-L. Magnetic Transitions in Iron Porphyrin Halides by Inelastic Neutron

Scattering and *Ab Initio* Studies of Zero-Field Splittings. *Inorg. Chem.* **2015,** *54*, 9790.

9. McGarvey, B. R.; Telser, J. Simple Ligand-Field Theory of d_4 and d_6 Transition Metal Complexes with a C_3 Symmetry Axis. *Inorg. Chem.* **2012,** *51*, 6000.
10. Gómez-Coca, S.; Urtizberea, A.; Cremades, E.; Alonso, P. J.; Camón, A.; Ruiz, E.; Luis, F. Origin of Slow Magnetic Relaxation in Kramers Ions with Non-Uniaxial Anisotropy. *Nat. Commun.* **2014,** *5*, 4300.
11. Zadrozny, J. M.; Liu, J.; Piro, N. A.; Chang, C. J.; Hill, S.; Long, J. R. Slow Magnetic Relaxation in a Pseudotetrahedral Cobalt(II) Complex with Easy-Plane Anisotropy. *ChemCommun* **2012,** *48*, 3927.
12. Lunghi, A.; Totti, F.; Sanvito, S.; Sessoli, R. Intra-Molecular Origin of the Spin-Phonon Coupling in Slow-Relaxing Molecular Magnets. *Chem. Sci.* **2017,** *8*, 6051.
13. Escalera-Moreno, L.; Suaud, N.; Gaita-Ariño, A.; Coronado, E. Determining Key Local Vibrations in the Relaxation of Molecular Spin Qubits and Single-Molecule Magnets. *J. Phys. Chem. Lett.* **2017,** *8*, 1695.
14. Lunghi, A.; Totti, F.; Sessoli, R.; Sanvito, S. The Role of Anharmonic Phonons in Under-Barrier Spin Relaxation of Single Molecule Magnets. *Nat. Commun.* **2017,** *8*, 14620.
15. Rechkemmer, Y.; Breitgoff, F. D.; van der Meer, M.; Atanasov, M.; Hakl, M.; Orlita, M.; Neugebauer, P.; Neese, F.; Sarkar, B.; van Slageren, J. A Four-Coordinate Cobalt(II) Single-Ion Magnet with Coercivity and a Very High Energy Barrier. *Nat. Commun.* **2016,** *7*, 10467.

16. Pedersen, K. S.; Dreiser, J.; Weihe, H.; Sibille, R.; Johannesen, H. V.; Sørensen, M. A.; Nielsen, B. E.; Sigrist, M.; Mutka, H.; Rols, S.; Bendix, J.; Piligkos, S. Design of Single-Molecule Magnets: Insufficiency of the Anisotropy Barrier as the Sole Criterion. *Inorg. Chem.* **2015,** *54*, 7600.

17. Chen, L.; Wang, J.; Wei, J.-M.; Wernsdorfer, W.; Chen, X.-T.; Zhang, Y.-Q.; Song, Y.; Xue, Z.-L. Slow Magnetic Relaxation in a Mononuclear Eight-Coordinate Cobalt(II) Complex. *J. Am. Chem. Soc.* **2014,** *136*, 12213.

18. Basler, R.; Boskovic, C.; Chaboussant, G.; Güdel, H. U.; Murrie, M.; Ochsenbein, S. T.; Sieber, A. Molecular Spin Clusters: New Synthetic Approaches and Neutron Scattering Studies. *ChemPhysChem* **2003,** *4*, 910.

19. Mitchell, P. C. H.; Parker, S. F.; Ramirez-Cuesta, A. J.; Tomkinson, J. *Vibrational Spectroscopy with Neutrons: With Applications in Chemistry, Biology, Materials Science and Catalysis*. World Scientific Publishing Company: 2005; Vol. 3.

20. Parker, S. F.; Ramirez-Cuesta, A. J.; Daemen, L. Vibrational Spectroscopy with Neutrons: Recent Developments. *Spectrochim. Acta A* **2018,** *190*, 518.

21. Furrer, A.; Mesot, J.; Strässle, T. *Neutron Scattering in Condensed Matter Physics*. World Scientific: 2009.

22. Andres, H.; Basler, R.; Güdel, H.-U.; Aromí, G.; Christou, G.; Büttner, H.; Rufflé, B. Inelastic Neutron Scattering and Magnetic Susceptibilities of the Single-Molecule Magnets $[Mn_4O_3X(OAc)_3(dbm)_3]$ (X = Br, Cl, OAc, and F): Variation of the Anisotropy along the Series. *J. Am. Chem. Soc.* **2000,** *122*, 12469.

23. Dreiser, J.; Waldmann, O.; Dobe, C.; Carver, G.; Ochsenbein, S. T.; Sieber, A.; Güdel, H. U.; van Duijn, J.; Taylor, J.; Podlesnyak, A. Quantized

Antiferromagnetic Spin Waves in the Molecular Heisenberg Ring $CsFe_8$. *Phys. Rev. B* **2010,** *81*, 024408.

24. (a) Dove, M. T. *Introduction to Lattice Dynamics*. Cambridge University Press: 1993; Vol. Cambridge Topics in Mineral Physics and Chemistry. (b) Schwoerer, M.; Wolf, H. C. *Organic Molecular Solids*, Wiley-VCH, 2007, Ch. 5 (Molecular and Lattice Dynamics in Organic Molecular Crystals), pp. 89-124.
25. Callot, H. J. O., R *The Porphyrin Handbook*. Academic Press: San Diego, CA, 2000; Vol. 1, Chapter 7, pp. 349-398.
26. Hoffman, B. M. Electron-Nuclear Double Resonance Spectroscopy (and Electron Spin-Echo Envelope Modulation Spectroscopy) in Bioinorganic Chemistry. *Proc. Natl. Acad. Sci. U. S. A.* **2003,** *100*, 3575.
27. Yang, F.; Shokhireva, T. K.; Walker, F. A. Linear Correlation between ^{1}H and ^{13}C Chemical Shifts of Ferriheme Proteins and Model Ferrihemes. *Inorg. Chem.* **2011,** *50*, 1176.
28. Scheidt, W. R.; Barabanschikov, A.; Pavlik, J. W.; Silvernail, N. J.; Sage, J. T. Electronic Structure and Dynamics of Nitrosyl Porphyrins. *Inorg. Chem.* **2010,** *49*, 6240.
29. Zhang, P.; Wang, M.; Li, X.; Cui, H.; Dong, J.; Sun, L. Photochemical Hydrogen Production with Molecular Devices Comprising a Zinc Porphyrin and a Cobaloxime Catalyst. *Sci. China Chem.* **2012,** *55*, 1274.
30. Deaton, J. C.; Gebhard, M. S.; Solomon, E. I. Transverse and Longitudinal Zeeman Effect on $[PPh_4][FeCl_4]$: Assignment of the Ligand Field Transitions and

the Origin of the $^6A_1$ Ground-State Zero-Field Splitting. *Inorg. Chem.* **1989,** *28*, 877.

31. Browett, W. R.; Fucaloro, A. F.; Morgan, T. V.; Stephens, P. J. Magnetic Circular Dichroism Determination of Zero-Field Splitting in Chloro(meso-tetraphenylporphinato)iron(III). *J. Am. Chem. Soc.* **1983,** *105*, 1868.
32. Brackett, G. C., Richards, P. L., Caughey, W. S. Far-Infrared Magnetic Resonance in Fe(III) and Mn(III) Porphyrins, Myoglobin, Hemoglobin, Ferrichrome A, and Fe(III) Dithioncarbamates. *J. Chem. Phys.* **1971,** *54*.
33. Uenoyama, H. Far-Infrared Studies on Hemin and Hemin-Like Complexes. *Biochim. Biophys. Acta* **1971,** *230*, 479.
34. Hunter, S. C.; Podlesnyak, A. A.; Xue, Z.-L. Magnetic Excitations in Metalloporphyrins by Inelastic Neutron Scattering: Determination of Zero-Field Splittings in Iron, Manganese, and Chromium Complexes. *Inorg. Chem.* **2014,** *53*, 1955.
35. Maricondi, C.; Swift, W.; Straub, D. K. Thermomagnetic Analysis of Hemin and Related Compounds. *J. Am. Chem. Soc.* **1969,** *91*, 5205.
36. Behere, D. V.; Date, S. K.; Mitra, S. Magnetic Susceptibility, Anisotropy, Low Temperature Magnetisation and Zero Field Splitting in Tetraphenylporphynato Iron(III) Bromide. *Chem. Phys. Lett.* **1979,** *68*, 544.
37. Behere, D. V.; Birdy, R.; Mitra, S. Effect of Axial Interaction in High-Spin Iron(III) Porphyrins. Paramagnetic Anisotropy and Zero-Field Splitting in (Tetraphenylporphyrin)iron(III) Thiocyanate and Iodide. *Inorg. Chem.* **1981,** *20*, 2786.

38. Gatteschi, D.; Sessoli, R. Quantum Tunneling of Magnetization and Related Phenomena in Molecular Materials. *Angew. Chem. Int. Ed.* **2003,** *42*, 268.

39. Nehrkorn, J.; Telser, J.; Holldack, K.; Stoll, S.; Schnegg, A. Simulating Frequency-Domain Electron Paramagnetic Resonance: Bridging the Gap between Experiment and Magnetic Parameters for High-Spin Transition-Metal Ion Complexes. *J. Phys. Chem. B* **2015,** *119*, 13816.

40. Gatteschi, D. Physical Techniques for the Investigation of Molecular Magnetic Clusters. *J. Phys. Chem. B* **2000,** *104*, 9780.

41. Krzystek, J.; Ozarowski, A.; Telser, J. Multi-Frequency, High-Field EPR as a Powerful Tool to Accurately Determine Zero-Field Splitting in High-Spin Transition Metal Coordination Complexes. *Coord. Chem. Rev.* **2006,** *250*, 2308.

42. Goff, H. M.; Shimomura, E. T.; Phillippi, M. A. Correlations of Axial Ligand Field Strength and Zero-Field Splittings in the Carbon-13 NMR Spectra of Five- and Six-Coordinate High-Spin Iron(III) Porphyrin Complexes. *Inorg. Chem.* **1983,** *22*, 66.

43. Ohya, T.; Sato, M. Comparative Study of Mossbauer Spectra of Iron(III) Complexes of Para-Substituted Tetraphenylporphyrins. Electronic Effects of Substituents and Axial Ligands. *J. Chem. Soc., Dalton Trans.* **1996**, 1519.

44. Furrer, A. Magnetic Cluster Excitations. *Int. J. Mod. Phys. B* **2010,** *24*, 3653.

45. Basler, R.; Sieber, A.; Chaboussant, G.; Güdel, H. U.; Chakov, N. E.; Soler, M.; Christou, G.; Desmedt, A.; Lechner, R. Inelastic Neutron Scattering Study of Electron Reduction in Mn12 Derivatives. *Inorg. Chem.* **2005,** *44*, 649.

46. Wang, C. H.; Lumsden, M. D.; Fishman, R. S.; Ehlers, G.; Hong, T.; Tian, W.; Cao, H.; Podlesnyak, A.; Dunmars, C.; Schlueter, J. A.; Manson, J. L.; Christianson, A. D. Magnetic Properties of the *S* = 1/2 Quasisquare Lattice Antiferromagnet $CuF_2(H_2O)_2(pyz)$ (pyz = pyrazine) Investigated by Neutron Scattering. *Phys. Rev. B* **2012,** *86*, 064439.

47. Carver, G.; Tregenna-Piggott, P. L. W.; Barra, A.-L.; Neels, A.; Stride, J. A. Spectroscopic and Structural Characterization of the $[Fe(imidazole)_6]^{2+}$ Cation. *Inorg. Chem.* **2003,** *42*, 5771.

48. Kittilstved, K. R.; Sorgho, L. A.; Amstutz, N.; Tregenna-Piggott, P. L. W.; Hauser, A. Ground-State Electronic Structure of Vanadium(III) Trisoxalate in Hydrated Compounds. *Inorg. Chem.* **2009,** *48*, 7750.

49. Ehlers, G.; Podlesnyak, A. A.; Niedziela, J. L.; Iverson, E. B.; Sokol, P. E. The New Cold Neutron Chopper Spectrometer at the Spallation Neutron Source: Design and Performance. *Rev. Sci. Instrum.* **2011,** *82*, 085108.

50. Hunter, S. C.; Smith, B. A.; Hoffmann, C. M.; Wang, X.; Chen, Y.-S.; McIntyre, G. J.; Xue, Z.-L. Intermolecular Interactions in Solid-State Metalloporphyrins and Their Impacts on Crystal and Molecular Structures. *Inorg. Chem.* **2014,** *53*, 11552.

51. Skelton, B.; White, A. Crystal Structure of Bromo(tetraphenylporphyrin)iron(III). *Aust. J. Chem.* **1977,** *30*, 2655.

52. Hatano, K.; Scheidt, W. R. Molecular Stereochemistry of Iodo(meso-tetraphenylporphinato)iron(III). *Inorg. Chem.* **1979,** *18*, 877.

53. Gatteschi, D.; Sorace, L. Hints for the Control of Magnetic Anisotropy in Molecular Materials. *J. Solid State Chem.* **2001,** *159*, 253.

54. Desrochers, P. J.; Telser, J.; Zvyagin, S. A.; Ozarowski, A.; Krzystek, J.; Vicic, D. A. Electronic Structure of Four-Coordinate C_3v Nickel(II) Scorpionate Complexes: Investigation by High-Frequency and -Field Electron Paramagnetic Resonance and Electronic Absorption Spectroscopies. *Inorg. Chem.* **2006,** *45*, 8930.

55. Ye, S.; Neese, F. How Do Heavier Halide Ligands Affect the Signs and Magnitudes of the Zero-Field Splittings in Halogenonickel(II) Scorpionate Complexes? A Theoretical Investigation Coupled to Ligand-Field Analysis. *J. Chem. Theory Comput.* **2012,** *8*, 2344.

56. Atanasov, M.; Rauzy, C.; Baettig, P.; Daul, C. Calculation of Spin-Orbit Coupling within the LFDFT: Applications to $[NiX_4]^{2-}$ (X = F^-, Cl^-, Br^-, I^-). *Int. J. Quantum Chem.* **2005,** *102*, 119.

57. Sun, Z.-C. S., Y.-B.; Zhou, Y.; Song, X.-F.; Li, K. Synthesis, Characterization and Spectral Properties of Substituted Tetraphenylporphyrin Iron Chloride Complexes. *Molecules* **2011,** *16*, 2960.

58. Adler, A. D.; Longo, F. R.; Kampas, F.; Kim, J. On the Preparation of Metalloporphyrins. *J. Inorg. Nucl. Chem.* **1970,** *32*, 2443.

59. Anzai, K.; Hatano, K.; Lee, Y. J.; Scheidt, W. R. Preparation and Molecular Stereochemistry of Fluoro(meso-tetraphenylporphinato)iron(III). *Inorg. Chem.* **1981,** *20*, 2337.

60. Le Bail, A. Monte Carlo Indexing with McMaille. *Powder Diff.* **2012,** *19*, 249.

61. Feast, G. C. H., J.; Page, L. W.; Robertson, J.; Thompson, A. L.; Watkin, D. J. An Unusual Methylene Aziridine Refined in P21/c and the Nonstandard Setting P21/n. *Acta Cryst.* **2009,** *C65*, o635.

62. Azuah, R. T.; Kneller, L. R.; Qiu, Y.; Tregenna-Piggott, P. L. W.; Brown, C. M.; Copley, J. R. D.; Dimeo, R. M. DAVE: A Comprehensive Software Suite for the Reduction, Visualization, and Analysis of Low Energy Neutron Spectroscopic Data. *J. Res. Natl. Inst. Stan. Technol.* **2009,** *114*, 341.

63. Grimme, S.; Antony, J.; Ehrlich, S.; Krieg, H. A Consistent and Accurate *Ab Initio* Parametrization of Density Functional Dispersion Correction (DFT-D) for the 94 elements H-Pu. *J. Chem. Phys.* **2010,** *132*, 154104.

64. Grimme, S.; Ehrlich, S.; Goerigk, L. Effect of the Damping Function in Dispersion Corrected Density Functional Theory. *J. Comput. Chem.* **2011,** *32*, 1456.

65. Pantazis, D. A.; Chen, X.-Y.; Landis, C. R.; Neese, F. All-Electron Scalar Relativistic Basis Sets for Third-Row Transition Metal Atoms. *J. Chem. Theory and Comput.* **2008,** *4*, 908.

66. Malmqvist, P.-Å.; Roos, B. O. The CASSCF State Interaction Method. *Chem. Phys. Lett.* **1989,** *155*, 189.

67. Angeli, C.; Cimiraglia, R.; Malrieu, J.-P. *n*-Electron Valence State Perturbation Theory: a Fast Implementation of the Strongly Contracted Variant. *Chem. Phys. Lett.* **2001,** *350*, 297.

68. Angeli, C.; Cimiraglia, R.; Malrieu, J.-P. *n*-Electron Valence State Perturbation Theory: A Spinless Formulation and an Efficient Implementation of the Strongly

Contracted and of the Partially Contracted Variants. *J. Chem. Phys.* **2002,** *117*, 9138.

69. Angeli, C.; Cimiraglia, R.; Evangelisti, S.; Leininger, T.; Malrieu, J.-P. Introduction of *n*-Electron Valence States for Multireference Perturbation Theory. *J. Chem. Phys.* **2001,** *114*, 10252.

70. Angeli, C.; Borini, S.; Cestari, M.; Cimiraglia, R. A Quasidegenerate Formulation of the Second Order *n*-Electron Valence State Perturbation Theory Approach. *J. Chem. Phys.* **2004,** *121*, 4043.

71. Angeli, C.; Bories, B.; Cavallini, A.; Cimiraglia, R. Third-Order Multireference Perturbation Theory: The *n*-Electron Valence State Perturbation-Theory Approach. *J. Chem. Phys.* **2006,** *124*, 054108.

72. Neese, F. The ORCA program system. *Wiley Interdisciplinary Reviews: Computational Molecular Science* **2012,** *2*, 73.

73. Atanasov, M.; Ganyushin, D.; Pantazis, D. A.; Sivalingam, K.; Neese, F. Detailed *Ab Initio* First-Principles Study of the Magnetic Anisotropy in a Family of Trigonal Pyramidal Iron(II) Pyrrolide Complexes. *Inorg. Chem.* **2011,** *50*, 7460.

74. Neese, F. Efficient and Accurate Approximations to the Molecular Spin-Orbit Coupling Operator and their Use in Molecular *g*-tensor Calculations. *J. Chem. Phys.* **2005,** *122*, 034107.

75. Ganyushin, D.; Neese, F. First-Principles Calculations of Zero-Field Splitting Parameters. *J. Chem. Phys.* **2006,** *125*, 024103.

76. Schäfer, A.; Horn, H.; Ahlrichs, R. Fully Optimized Contracted Gaussian Basis Sets for Atoms Li to Kr. *J. Chem. Phys.* **1992,** *97*, 2571.

77. Weigend, F.; Ahlrichs, R. Balanced Basis Sets of Split Valence, Triple Zeta Valence and Quadruple Zeta Valence Quality for H to Rn: Design and Assessment of Accuracy. *Phys. Chem. Chem. Phys.* **2005,** *7*, 3297.

78. Jørgensen, C. K.; Pappalardo, R.; Schmidtke, H. H. Do the ``Ligand Field'' Parameters in Lanthanides Represent Weak Covalent Bonding? *J. Chem. Phys.* **1963,** *39*, 1422.

79. Schäffer, C. E.; Jørgensen, C. K. The Angular Overlap Model, an Attempt to Revive the Ligand Field Approaches. *Mol. Phys.* **1965,** *9*, 401.

80. Atanasov, M.; Ganyushin, D.; Sivalingam, K.; Neese, F., A Modern First-Principles View on Ligand Field Theory Through the Eyes of Correlated Multireference Wavefunctions. In *Molecular Electronic Structures of Transition Metal Complexes II*, Mingos, D. M. P.; Day, P.; Dahl, J. P., Eds. Springer Berlin Heidelberg: Berlin, Heidelberg, 2012; pp 149.

81. Zadrozny, J. M.; Atanasov, M.; Bryan, A. M.; Lin, C.-Y.; Rekken, B. D.; Power, P. P.; Neese, F.; Long, J. R. Slow Magnetization Dynamics in a Series of Two-Coordinate Iron(II) Complexes. *Chem. Sci.* **2013,** *4*, 125.

82. Adamsky, H. *AOMX, a FORTRAN Program for the Calculation of d^n Terms within the Angular Overlap Model with Interelectronic Repulsion and Spin-Orbit Coupling*. Institute of Theoretical Chemistry, Heinrich-Heine-University: Düsseldorf, 1995.

83. Pinkowicz, D.; Southerland, H. I.; Avendaño, C.; Prosvirin, A.; Sanders, C.; Wernsdorfer, W.; Pedersen, K. S.; Dreiser, J.; Clérac, R.; Nehrkorn, J.; Simeoni, G. G.; Schnegg, A.; Holldack, K.; Dunbar, K. R. Cyanide Single-Molecule

Magnets Exhibiting Solvent Dependent Reversible “On” and “Off” Exchange Bias Behavior. *J. Am. Chem. Soc.* **2015,** *137*, 14406.

84. Dreiser, J.; Schnegg, A.; Holldack, K.; Pedersen, K. S.; Schau-Magnussen, M.; Nehrkorn, J.; Tregenna-Piggott, P.; Mutka, H.; Weihe, H.; Bendix, J.; Waldmann, O. Frequency-Domain Fourier-Transform Terahertz Spectroscopy of the Single-Molecule Magnet $(NEt_4)[Mn_2(5\text{-Brsalen})_2(MeOH)2Cr(CN)_6]$. *Chem. Eur. J* **2011,** *17*, 7492.

85. Zhong, Y.; Sarachik, M. P.; Friedman, J. R.; Robinson, R. A.; Kelley, T. M.; Nakotte, H.; Christianson, A. C.; Trouw, F.; Aubin, S. M. J.; Hendrickson, D. N. Inelastic Neutron Scattering Study of Mn12–Acetate. *J. Appl. Phys.* **1999,** *85*, 5636.

86. Mirebeau, I.; Hennion, M.; Casalta, H.; Andres, H.; Güdel, H. U.; Irodova, A. V.; Caneschi, A. Low-Energy Magnetic Excitations of the Mn_{12}-Acetate Spin Cluster Observed by Neutron Scattering. *Phys. Rev. Lett.* **1999,** *83*, 628.

87. Basler, R.; Tregenna-Piggott, P. L. W.; Andres, H.; Dobe, C.; Güdel, H.-U.; Janssen, S.; McIntyre, G. J. Magnetic Excitations of $CsMn(SO_4)_2{\cdot}12D_2O$, Measured by Inelastic Neutron Scattering. *J. Am. Chem. Soc.* **2001,** *123*, 3377.

88. Colacio, E.; Ruiz, J.; Ruiz, E.; Cremades, E.; Krzystek, J.; Carretta, S.; Cano, J.; Guidi, T.; Wernsdorfer, W.; Brechin, E. K. Slow Magnetic Relaxation in a Co^{II}–Y^{III} Single-Ion Magnet with Positive Axial Zero-Field Splitting. *Angew. Chem. Int. Ed.* **2013,** *52*, 9130.

89. Sieber, A.; Boskovic, C.; Bircher, R.; Waldmann, O.; Ochsenbein, S. T.; Chaboussant, G.; Güdel, H. U.; Kirchner, N.; van Slageren, J.; Wernsdorfer, W.;

Neels, A.; Stoeckli-Evans, H.; Janssen, S.; Juranyi, F.; Mutka, H. Synthesis and Spectroscopic Characterization of a New Family of Ni_4 Spin Clusters. *Inorg. Chem.* **2005,** *44*, 4315.

90. Sigrist, M.; L. W. Tregenna-Piggott, P.; S. Pedersen, K.; A. Sørensen, M.; Barra, A.-L.; Hauser, J.; Liu, S.-X.; Decurtins, S.; Mutka, H.; Bendix, J. Zero-Field Splitting in $\{Mn^{III}{}_3(\mu_3\text{-}O)\}$ Core Single-Molecule Magnets Investigated by Inelastic Neutron Scattering and High-Field Electron Paramagnetic Resonance Spectroscopy. *Eur. J. Inorg. Chem.* **2015,** *2015*, 2683.

91. Bircher, R.; Chaboussant, G.; Ochsenbein, S. T.; Fernandez-Alonso, F.; Güdel, H. U.; Brechin, E. K. Inelastic Neutron Scattering Study of Undeuterated $[Mn_9O_7(OAc)_{11}(thme)(py)_3(H_2O)_2]$. *Polyhedron* **2005,** *24*, 2455.

92. Giansiracusa, M. J.; Vonci, M.; Van den Heuvel, W.; Gable, R. W.; Moubaraki, B.; Murray, K. S.; Yu, D.; Mole, R. A.; Soncini, A.; Boskovic, C. Carbonate-Bridged Lanthanoid Triangles: Single-Molecule Magnet Behavior, Inelastic Neutron Scattering, and *Ab Initio* Studies. *Inorg. Chem.* **2016,** *55*, 5201.

93. Kofu, M.; Yamamuro, O.; Kajiwara, T.; Yoshimura, Y.; Nakano, M.; Nakajima, K.; Ohira-Kawamura, S.; Kikuchi, T.; Inamura, Y. Hyperfine Structure of Magnetic Excitations in a Tb-Based Single-Molecule Magnet Studied by High-Resolution Neutron Spectroscopy. *Phys. Rev. B* **2013,** *88*, 064405.

94. Vonci, M.; Giansiracusa, M. J.; Van den Heuvel, W.; Gable, R. W.; Moubaraki, B.; Murray, K. S.; Yu, D.; Mole, R. A.; Soncini, A.; Boskovic, C. Magnetic Excitations in Polyoxotungstate-Supported Lanthanoid Single-Molecule Magnets: An Inelastic Neutron Scattering and *Ab Initio* Study. *Inorg. Chem.* **2017,** *56*, 378.

95. Pedersen, K. S.; Ungur, L.; Sigrist, M.; Sundt, A.; Schau-Magnussen, M.; Vieru, V.; Mutka, H.; Rols, S.; Weihe, H.; Waldmann, O.; Chibotaru, L. F.; Bendix, J.; Dreiser, J. Modifying the Properties of 4f Single-Ion Magnets by Peripheral Ligand Functionalisation. *Chem. Sci.* **2014,** *5*, 1650.

96. Prša, K.; Nehrkorn, J.; Corbey, J.; Evans, W.; Demir, S.; Long, J.; Guidi, T.; Waldmann, O. Perspectives on Neutron Scattering in Lanthanide-Based Single-Molecule Magnets and a Case Study of the $Tb_2(\mu\text{-}N_2)$ System. *Magnetochemistry* **2016,** *2*, 45.

97. Marx, R.; Moro, F.; Dorfel, M.; Ungur, L.; Waters, M.; Jiang, S. D.; Orlita, M.; Taylor, J.; Frey, W.; Chibotaru, L. F.; van Slageren, J. Spectroscopic Determination of Crystal Field Splittings in Lanthanide Double Deckers. *Chem. Sci.* **2014,** *5*, 3287.

98. Baker, M. L.; Tanaka, T.; Murakami, R.; Ohira-Kawamura, S.; Nakajima, K.; Ishida, T.; Nojiri, H. Relationship between Torsion and Anisotropic Exchange Coupling in a Tb^{III}-Radical-Based Single-Molecule Magnet. *Inorg. Chem.* **2015,** *54*, 5732.

99. Waldmann, O.; Carver, G.; Dobe, C.; Biner, D.; Sieber, A.; Güdel, H. U.; Mutka, H.; Ollivier, J.; Chakov, N. E. Magnetic Relaxation Studies on a Single-Molecule Magnet by Time-Resolved Inelastic Neutron Scattering. *Appl. Phys. Lett.* **2006,** *88*, 042507.

100. Copley, J. R. D.; Cook, J. C. The Disk Chopper Spectrometer at NIST: a New Instrument for Quasielastic Neutron Scattering Studies. *Chem. Phys.* **2003,** *292*, 477.

101. Seeger, P. A.; Daemen, L. L.; Larese, J. Z. Resolution of VISION, a Crystal-Analyzer Spectrometer. *Nucl. Instr. Meth. Phys. Res. A* **2009,** *604*, 719.

102. Eccleston, R., Time-of-Flight Inelastic Scattering. In *Neutron and X-ray Spectroscopy*, Hippert, F.; Geissler, E.; Hodeau, J. L.; Lelièvre-Berna, E.; Regnard, J.-R., Eds. Springer Netherlands: Dordrecht, 2006; pp 457.

103. Stone, M. B.; Niedziela, J. L.; Abernathy, D. L.; DeBeer-Schmitt, L.; Ehlers, G.; Garlea, O.; Granroth, G. E.; Graves-Brook, M.; Kolesnikov, A. I.; Podlesnyak, A.; Winn, B. A Comparison of Four Direct Geometry Time-of-Flight Spectrometers at the Spallation Neutron Source. *Rev. Sci. Instrum.* **2014,** *85*, 045113.

104. Ehlers, G.; Podlesnyak, A. A.; Kolesnikov, A. I. The Cold Neutron Chopper Spectrometer at the Spallation Neutron Source—A Review of the First 8 Years of Operation. *Rev. Sci. Instrum.* **2016,** *87*, 093902.

105. Huang, X.-C.; Zhou, C.; Shao, D.; Wang, X.-Y. Field-Induced Slow Magnetic Relaxation in Cobalt(II) Compounds with Pentagonal Bipyramid Geometry. *Inorg. Chem.* **2014,** *53*, 12671.

106. Amoretti, G.; Caciuffo, R.; Carretta, S.; Guidi, T.; Magnani, N.; Santini, P. Inelastic Neutron Scattering Investigations of Molecular Nanomagnets. *Inorganica Chimi. Acta* **2008,** *361*, 3771.

107. Baker, M. L.; Mutka, H. Neutron Spectroscopy of Molecular Nanomagnets. *Eur. Phys. J. Spec. Top.* **2012,** *213*, 53.

108. Dobe, C.; Noble, C.; Carver, G.; Tregenna-Piggott, P. L.; McIntyre, G. J.; Barra, A. L.; Neels, A.; Janssen, S.; Juranyi, F. Electronic and Molecular Structure of

High-Spin d_4 Complexes: Experimental and Theoretical Study of the $[Cr(D_2O)_6]^{2+}$ Cation in Tutton's Salts. *J. Am. Chem. Soc.* **2004,** *126*, 16639.

109. Pedersen, K. S.; Sigrist, M.; Sørensen, M. A.; Barra, A.-L.; Weyhermüller, T.; Piligkos, S.; Thuesen, C. A.; Vinum, M. G.; Mutka, H.; Weihe, H.; Clérac, R.; Bendix, J. $[ReF_6]^{2-}$: A Robust Module for the Design of Molecule-Based Magnetic Materials. *Angew. Chem. Int. Ed.* **2014,** *53*, 1351.

110. Zadrozny, J. M.; Xiao, D. J.; Long, J. R.; Atanasov, M.; Neese, F.; Grandjean, F.; Long, G. J. Mössbauer Spectroscopy as a Probe of Magnetization Dynamics in the Linear Iron(I) and Iron(II) Complexes $[Fe(C(SiMe_3)_3)_2]^{1-/0}$. *Inorg. Chem.* **2013,** *52*, 13123.

111. Lohr, L. L.; Miller, J. C.; Sharp, R. R. Electronic structure and magnetic properties of high-spin octahedral Co(II) complexes: $Co(II)(acac)_2(H_2O)_2$. *J. Chem. Phys.* **1999,** *111*, 10148.

112. Pilbrow, J. R. Effective *g* Values for *S* = 3/2 and *S* = 5/2. *J. Magn. Reson.* **1978,** *31*, 479.

113. Gast, P.; Groenen, E. J. J. EPR Interactions – *g*-Anisotropy. *eMagRes* **2016,** *5*, 1435.

114. Zhang, P.; Zhang, L.; Wang, C.; Xue, S.; Lin, S.-Y.; Tang, J. Equatorially Coordinated Lanthanide Single Ion Magnets. *J. Am. Chem. Soc.* **2014,** *136*, 4484.

115. Zhang, P.; Zhang, L.; Tang, J. Lanthanide Single Molecule Magnets: Progress and Perspective. *Dalton Trans.* **2015,** *44*, 3923.

116. Jank, S.; Amberger, H. D.; Edelstein, N. M. Electronic Structures of Highly-Symmetrical Compounds of f Elements: Part 30. Simulation of the Crystal Field Splitting Pattern of Tris(bis(trimethylsilyl)amido)erbium (III). *Spectrochim. Acta A* **1998,** *54*, 1645.

117. Singh, S. K.; Gupta, T.; Shanmugam, M.; Rajaraman, G. Unprecedented Magnetic Relaxation via the Fourth Excited State in Low-Coordinate Lanthanide Single-Ion Magnets: a Theoretical Perspective. *ChemComm* **2014,** *50*, 15513.

118. Chilton, N. F.; Anderson, R. P.; Turner, L. D.; Soncini, A.; Murray, K. S. PHI: A Powerful New Program for the Analysis of Anisotropic Monomeric and Exchange-Coupled Polynuclear d- and f-block Complexes. *J. Comput. Chem.* **2013,** *34*, 1164.

119. Vaknin, D.; Garlea, V. O.; Demmel, F.; Mamontov, E.; Nojiri, H.; Martin, C.; Chiorescu, I.; Qiu, Y.; Kögerler, P.; Fielden, J.; Engelhardt, L.; Rainey, C.; Luban, M. Level Crossings and Zero-Field Splitting in the $\{Cr_8\}$-Cubane Spin Cluster Studied Using Inelastic Neutron Scattering and Magnetization. *J. Phys. Condens. Matter* **2010,** *22*, 466001.

120. Vaknin, D.; Demmel, F. Magnetic Spectra in the Tridiminished-Icosahedron $\{Fe_9\}$ Nanocluster by Inelastic Neutron Scattering. *Phys. Rev. B* **2014,** *89*, 180411.

121. Garlea, V. O.; Nagler, S. E.; Zarestky, J. L.; Stassis, C.; Vaknin, D.; Kögerler, P.; McMorrow, D. F.; Niedermayer, C.; Tennant, D. A.; Lake, B.; Qiu, Y.; Exler, M.; Schnack, J.; Luban, M. Probing Spin Frustration in High-Symmetry Magnetic Nanomolecules by Inelastic Neutron Scattering. *Phys. Rev. B* **2006,** *73*, 024414.

122. Carretta, S.; Santini, P.; Amoretti, G.; Guidi, T.; Copley, J. R. D.; Qiu, Y.; Caciuffo, R.; Timco, G.; Winpenny, R. E. P. Quantum Oscillations of the Total Spin in a Heterometallic Antiferromagnetic Ring: Evidence from Neutron Spectroscopy. *Phys. Rev. Lett.* **2007,** *98*, 167401.

123. Hagiwara, M.; Regnault, L. P.; Zheludev, A.; Stunault, A.; Metoki, N.; Suzuki, T.; Suga, S.; Kakurai, K.; Koike, Y.; Vorderwisch, P.; Chung, J. H. Spin Excitations in an Anisotropic Bond-Alternating Quantum $S=1$ Chain in a Magnetic Field: Contrast to Haldane Spin Chains. *Phys. Rev. Lett.* **2005,** *94*, 177202.

124. Kim, J. H.; Ji, S.; Lee, S. H.; Lake, B.; Yildirim, T.; Nojiri, H.; Kikuchi, H.; Habicht, K.; Qiu, Y.; Kiefer, K. External Magnetic Field Effects on a Distorted Kagome Antiferromagnet. *Phys. Rev. Lett.* **2008,** *101*, 107201.

125. Tsyrulin, N.; Pardini, T.; Singh, R. R. P.; Xiao, F.; Link, P.; Schneidewind, A.; Hiess, A.; Landee, C. P.; Turnbull, M. M.; Kenzelmann, M. Quantum Effects in a Weakly Frustrated *S* =1/2 Two-Dimensional Heisenberg Antiferromagnet in an Applied Magnetic Field. *Phys. Rev. Lett.* **2009,** *102*, 197201.

126. Krzystek, J.; Zvyagin, S. A.; Ozarowski, A.; Trofimenko, S.; Telser, J. Tunable-Frequency High-Field Electron Paramagnetic Resonance. *J. Magn. Reson.* **2006,** *178*, 174.

127. Huang, W.; Liu, T.; Wu, D.; Cheng, J.; Ouyang, Z. W.; Duan, C. Field-Induced Slow Relaxation of Magnetization in a Tetrahedral Co(II) Complex with Easy Plane Anisotropy. *Dalton Trans.* **2013,** *42*, 15326.

128. Wu, D.; Zhang, X.; Huang, P.; Huang, W.; Ruan, M.; Ouyang, Z. W. Tuning Transverse Anisotropy in Co^{III}–Co^{II}–Co^{III} Mixed-Valence Complex toward Slow Magnetic Relaxation. *Inorg. Chem.* **2013,** *52*, 10976.

129. Chen, L.; Chen, S.-Y.; Sun, Y.-C.; Guo, Y.-M.; Yu, L.; Chen, X.-T.; Wang, Z.; Ouyang, Z. W.; Song, Y.; Xue, Z.-L. Slow Magnetic Relaxation in Mononuclear Seven-Coordinate Cobalt(II) Complexes with Easy Plane Anisotropy. *Dalton Trans.* **2015,** *44*, 11482.

130. Xavier, F. R.; Neves, A.; Casellato, A.; Peralta, R. A.; Bortoluzzi, A. J.; Szpoganicz, B.; Severino, P. C.; Terenzi, H.; Tomkowicz, Z.; Ostrovsky, S.; Haase, W.; Ozarowski, A.; Krzystek, J.; Telser, J.; Schenk, G.; Gahan, L. R. Unsymmetrical $Fe^{III}Co^{II}$ and $Ga^{III}Co^{II}$ Complexes as Chemical Hydrolases: Biomimetic Models for Purple Acid Phosphatases (PAPs). *Inorg. Chem.* **2009,** *48*, 7905.

131. Ruamps, R.; Batchelor, L. J.; Guillot, R.; Zakhia, G.; Barra, A.-L.; Wernsdorfer, W.; Guihery, N.; Mallah, T. Ising-Type Magnetic Anisotropy and Single Molecule Magnet Behaviour in Mononuclear Trigonal Bipyramidal Co(II) Complexes. *Chem. Sci.* **2014,** *5*, 3418.

132. Gatteschi, D. S., R.; Villain, J. *Molecular Nanomagnets*. Oxford University Press: Oxford, U.K., 2006.

133. Gomez-Coca, S.; Cremades, E.; Aliaga-Alcalde, N.; Ruiz, E. Mononuclear Single-Molecule Magnets: Tailoring the Magnetic Anisotropy of First-Row Transition-Metal Complexes. *J. Am. Chem. Soc.* **2013,** *135*, 7010.

134. Vaidya, S.; Upadhyay, A.; Singh, S. K.; Gupta, T.; Tewary, S.; Langley, S. K.; Walsh, J. P. S.; Murray, K. S.; Rajaraman, G.; Shanmugam, M. A Synthetic Strategy for Switching the Single Ion Anisotropy in Tetrahedral Co(II) Complexes. *ChemComm* **2015,** *51*, 3739.

135. Smolko, L.; Cernak, J.; Dusek, M.; Miklovic, J.; Titis, J.; Boča, R. Three Tetracoordinate Co(II) Complexes [Co(biq)X_2] (X = Cl, Br, I) with Easy-Plane Magnetic Anisotropy as Field-Induced Single-Molecule Magnets. *Dalton Trans.* **2015,** *44*, 17565.

136. Rajnák, C.; Titiš, J.; Fuhr, O.; Ruben, M.; Boča, R. Single-Molecule Magnetism in a Pentacoordinate Cobalt(II) Complex Supported by an Antenna Ligand. *Inorg. Chem.* **2014,** *53*, 8200.

137. Vallejo, J.; Castro, I.; Ruiz-García, R.; Cano, J.; Julve, M.; Lloret, F.; De Munno, G.; Wernsdorfer, W.; Pardo, E. Field-Induced Slow Magnetic Relaxation in a Six-Coordinate Mononuclear Cobalt(II) Complex with a Positive Anisotropy. *J. Am. Chem. Soc.* **2012,** *134*, 15704.

138. Ishikawa, R.; Horii, Y.; Nakanishi, R.; Ueno, S.; Breedlove, B. K.; Yamashita, M.; Kawata, S. Field-Induced Single-Ion Magnetism Based on Spin-Phonon Relaxation in a Distorted Octahedral High-Spin Cobalt(II) Complex. *Eur. J. Inorg. Chem.* **2016,** *2016*, 3233.

139. Tesi, L.; Lunghi, A.; Atzori, M.; Lucaccini, E.; Sorace, L.; Totti, F.; Sessoli, R. Giant Spin-Phonon Bottleneck Effects in Evaporable Vanadyl-Based Molecules with Long Spin Coherence. *Dalton Trans.* **2016**.

140. Carretta, S.; Santini, P.; Amoretti, G.; Guidi, T.; Dyson, J.; Caciuffo, R.; Stride, J. A.; Caneschi, A.; Copley, J. R. D. Inelastic-Neutron-Scattering Study of Excited Spin Multiplets and Low-Energy Phonons in the $\{Fe_8\}$ Nanomagnet: Implications for Relaxation. *Phys. Rev. B* **2006,** *73*, 144425.

141. Togo, A.; Tanaka, I. First Principles Phonon Calculations in Materials Science. *Scr. Mater.* **2015,** *108*, 1.

142. Magnetic Form Factors. https://www.ill.eu/sites/ccsl/ffacts/ffachtml.html (accessed February 20).

143. Köbler, U. H., Andreas *Renormalization Group Theory: Impact on Experimental Magnetism*. Springer Berlin Heidelberg: Berlin, Heidelberg, 2010.

144. Kresse, G.; Furthmüller, J. Efficient Iterative Schemes for *Ab Initio* Total-Energy Calculations Using a Plane-Wave Basis Set. *Phys. Rev. B* **1996,** *54*, 11169.

145. Arnold, O.; Bilheux, J. C.; Borreguero, J. M.; Buts, A.; Campbell, S. I.; Chapon, L.; Doucet, M.; Draper, N.; Ferraz Leal, R.; Gigg, M. A.; Lynch, V. E.; Markvardsen, A.; Mikkelson, D. J.; Mikkelson, R. L.; Miller, R.; Palmen, K.; Parker, P.; Passos, G.; Perring, T. G.; Peterson, P. F.; Ren, S.; Reuter, M. A.; Savici, A. T.; Taylor, J. W.; Taylor, R. J.; Tolchenov, R.; Zhou, W.; Zikovsky, J. Mantid—Data Analysis and Visualization Package for Neutron Scattering and μ SR Experiments. *Nucl. Instr. Meth. Phys. Res.* **2014,** *764*, 156.

146. Matthew, F.; Christina, H.; Jack, T.; Mark, O.; Michael, A.; Peter, C.; Robert, V.; Echo, M.; Lisa, M. Initial testing of a Compact Crystal Positioning System for the TOPAZ Single-Crystal Diffractometer at the Spallation Neutron Source. *J. Phys. Conf. Ser.* **2010,** *251*, 012084.

147. Zikovsky, J.; Peterson, P. F.; Wang, X. P.; Frost, M.; Hoffmann, C. CrystalPlan: an Experiment-Planning Tool for Crystallography. *J. Appl. Crystallogr.* **2011,** *44*, 418.

148. Benelli, C.; Gatteschi, D. *Introduction to Molecular Magnetism: From Transition Metals to Lanthanides*. Wiley: Somerset, Germany, 2015.

149. Layfield, R. A. Organometallic Single-Molecule Magnets. *Organometallics* **2014,** *33*, 1084.

150. McInnes, E. J. L.; Winpenny, R. E. P., Molecular Magnets. In *Comprehensive Inorganic Chemistry II*, Poeppelmeier, K., Ed. Elsevier: Amsterdam, 2013; pp 371.

151. Neese, F.; Pantazis, D. A. What is Not Required to Make a Single Molecule Magnet. *Faraday Discuss.* **2011,** *148*, 229.

152. Gao, S., Ed. *Molecular Nanomagnets and Related Phenomena*. Springer: 2015.

153. Demir, S.; Jeon, I.-R.; Long, J. R.; Harris, T. D. Radical Ligand-Containing Single-Molecule Magnets. *Coord. Chem. Rev.* **2015,** *289*, 149.

154. Orbach, R.; Stapleton, H. J., Electron Spin-Lattice Relaxation. In *Electron Paramagnetic Resonance*, Geschwind, S., Ed. Plenum Press: New York, 1972; pp 121.

155. Schwoerer, M.; Wolf, H. C., Molecular and Lattice Dynamics in Organic Molecular Crystals. In *Organic Molecular Solids*, Wiley-VCH: 2008; pp 89.

156. Goodwin, C. A. P.; Ortu, F.; Reta, D.; Chilton, N. F.; Mills, D. P. Molecular Magnetic Hysteresis at 60 Kelvin in Dysprosocenium. *Nature* **2017,** *548*, 439.

157. Sherwood, P. M. A. *Vibrational Spectroscopy of Solids*. Cambridge University Press: 1972.

158. Koster, G. F.; Dimmock, J. O.; Wheeler, R. G.; Statz, H. *Properties of the Thirty-Two Point Groups*. MIT Press: 1963; p 104.

159. Giannozzi, P.; Baroni, S. Vibrational and Dielectric Properties of C_{60} from Density-Functional Perturbation Theory. *J. Chem. Phys.* **1994,** *100*, 8537.

160. Unpublished Result. Manuscript in Preparation.

161. Kresse, G.; Joubert, D. From Ultrasoft Pseudopotentials to the Projector Augmented-Wave Method. *Phys. Rev. B* **1999,** *59*, 1758.

162. Blöchl, P. E. Projector Augmented-Wave Method. *Phys. Rev. B* **1994,** *50*, 17953.

163. Perdew, J. P.; Burke, K.; Ernzerhof, M. Generalized Gradient Approximation Made Simple. *Phys. Rev. Lett.* **1996,** *77*, 3865.

164. Zhou, F.; Cococcioni, M.; Marianetti, C. A.; Morgan, D.; Ceder, G. First-Principles Prediction of Redox Potentials in Transition-Metal Compounds with LDA + U. *Phys. Rev. B* **2004,** *70*, 235121.

165. Klimeš, J.; Bowler, D. R.; Michaelides, A. Chemical Accuracy for the van der Waals Density Functional. *J. Phys. Condens. Matter* **2010,** *22*, 022201.

166. Ramirez-Cuesta, A. J. aCLIMAX 4.0.1, The New Version of the Software for Analyzing and Interpreting INS Spectra. *Comput. Phys. Comm.* **2004,** *157*, 226.

167. Escalera-Moreno, L.; Suaud, N.; Gaita-Ariño, A.; Coronado, E. Determining Key Local Vibrations in the Relaxation of Molecular Spin Qubits and Single-Molecule Magnets. *J. Phys. Chem. Lett.* **2017,** *8*, 1695.

168. Ruiz, E.; Cirera, J.; Alvarez, S. Spin Density Distribution in Transition Metal Complexes. *Coord. Chem. Rev.* **2005,** *249*, 2649.

169. Appel, M.; Frick, B.; Elbert, J.; Gallei, M.; Stühn, B. Direct Observation of Electronic and Nuclear Ground State Splitting in External Magnetic Field by Inelastic Neutron Scattering on Oxidized Ferrocene and Ferrocene Containing Polymers. *EPJ Web of Conf.* **2015,** *83*, 02001.

170. Kofu, M.; Kajiwara, T.; Gardner, J. S.; Simeoni, G. G.; Tyagi, M.; Faraone, A.; Nakajima, K.; Ohira-Kawamura, S.; Nakano, M.; Yamamuro, O. Magnetic Relaxations in a Tb-based Single Molecule Magnet Studied by Quasielastic Neutron Scattering. *Chem. Phys.* **2013,** *427*, 147.

171. Frick, B., Neutron Backscattering Spectroscopy. In *Neutron and X-ray Spectroscopy*, Hippert, F.; Geissler, E.; Hodeau, J. L.; Lelièvre-Berna, E.; Regnard, J.-R., Eds. Springer: Dordrecht, 2006; pp 483.

172. Bée, M. *Quasielastic Neutron Scattering. Principles and Applications in Solid State Chemistry, Biology and Materials Science*. Adam Hilger: Bristol, U.K., 1988.

173. Hempelmann, R. *Quasielastic Neutron Scattering and Solid State Diffusion*. Oxford University Press: Oxford, 2000.

174. Trouw, F. R.; Price, D. L. Chemical Applications of Neutron Scattering. *Annu. Rev. Phys. Chem.* **1999,** *50*, 571.

175. Raison, P.; Lander, G. H.; Delapalme, A.; Williams, J. H.; Kahn, R.; Carlile, C. J.; Kanellakopulos, B. Studies of $U(C_5H_5)_3Cl$: Reorientational Motions of Cyclopentadienyl Rings. *Mol. Phys.* **1994,** *81*, 369.

176. Prager, M.; Grimm, H.; Desmedt, A.; Lechner, R. E. Methyl Rotational Potentials of Trimethyl Metal Compounds Studied by Inelastic and Quasielastic Neutron Scattering. *Chem. Phys.* **2003,** *292*, 161.

177. Zou, F.; Furno, F.; Fox, T.; Schmalle, H. W.; Berke, H.; Eckert, J.; Chowdhury, Z.; Burger, P. *trans*-W(Cmesityl)(dmpe)$_2$H: Revealing a Highly Polar W−H Bond and H-Mobility in Liquid and Solid State. *J. Am. Chem. Soc.* **2007,** *129*, 7195.

178. Tomiyasu, K.; Crawford, M. K.; Adroja, D. T.; Manuel, P.; Tominaga, A.; Hara, S.; Sato, H.; Watanabe, T.; Ikeda, S. I.; Lynn, J. W.; Iwasa, K.; Yamada, K. Molecular Spin-Orbit Excitations in the J_{eff} = 1/2 Frustrated Spinel $GeCo_2O_4$. *Phys. Rev. B* **2011,** *84*, 054405.

179. Nielsen, H. H. The Torsion Oscillator-Rotator in the Quantum Mechanics. *Phys. Rev.* **1932,** *40*, 445.

180. Pitzer, K. S. Thermodynamic Functions for Molecules Having Restricted Internal Rotations. *J. Chem. Phys.* **1937,** *5*, 469.

181. Kemp, J. D.; Pitzer, K. S. The Entropy of Ethane and the Third Law of Thermodynamics. Hindered Rotation of Methyl Groups. *J. Am. Chem. Soc.* **1937,** *59*, 276.

182. Mulliken, R. S. Intensities of Electronic Transitions in Molecular Spectra IV. Cyclic Dienes and Hyperconjugation. *J. Chem. Phys.* **1939,** *7*, 339.

183. Lister, D. G.; MacDonald, J. D.; Owen, N. L. *Internal Rotation and Inversion: Introduction to Large Amplitude Motion in Molecules*. 1978.

184. Goodman, L.; Pophristic, V.; Weinhold, F. Origin of Methyl Internal Rotation Barriers. *Acc. Chem. Res.* **1999,** *32*, 983.

185. Spangler, L. H. Structural Information from Methyl Internal Rotation Spectroscopy. *Ann. Rev. Phys. Chem.* **1997,** *48*, 481.

186. Mo, Y.; Gao, J. Theoretical Analysis of the Rotational Barrier of Ethane. *Acc. Chem. Res.* **2007,** *40*, 113.

187. Mo, Y. Rotational Barriers in Alkanes. *Wiley Interdiscip. Rev. Comput. Mol. Sci.* **2011,** *1*, 164.

188. Dorigo, A. E.; Pratt, D. W.; Houk, K. N. Origin of Methyl Conformational Preferences and Rotational Barriers in the Ground States, Excited Triplet States, Radical Cations, and Radical Anions of Molecules Having CH_3-C:X Functionalities. *J. Am. Chem. Soc.* **1987,** *109*, 6591.

189. Mamontov, E.; O'Neill, H. Microscopic Relaxations in a Protein Sustained Down to 160K in a Non-glass Forming Organic Solvent. *Biochim. Biophys. Acta* **2017,** *1861*, 3513.

190. Taylor, J. R. *An Introduction to Error Analysis: The Study of Uncertainties in Physical Measurements*. University Science Books: Mill Valley, CA, 1982.

191. Anunciado, D. B.; Nyugen, V. P.; Hurst, G. B.; Doktycz, M. J.; Urban, V.; Langan, P.; Mamontov, E.; O'Neill, H. In Vivo Protein Dynamics on the Nanometer Length Scale and Nanosecond Time Scale. *J. Phys. Chem. Lett.* **2017,** *8*, 1899.

192. Grimaldo, M.; Roosen-Runge, F.; Hennig, M.; Zanini, F.; Zhang, F.; Zamponi, M.; Jalarvo, N.; Schreiber, F.; Seydel, T. Salt-Induced Universal Slowing Down of the Short-Time Self-Diffusion of a Globular Protein in Aqueous Solution. *J. Phys. Chem. Lett.* **2015,** *6*, 2577.

193. Sharma, V. K.; Mamontov, E.; Ohl, M.; Tyagi, M. Incorporation of Aspirin Modulates the Dynamical and Phase Behavior of the Phospholipid Membrane. *Phys. Chem. Chem. Phys.* **2017,** *19*, 2514.

194. Roosen-Runge, F.; Hennig, M.; Zhang, F.; Jacobs, R. M. J.; Sztucki, M.; Schober, H.; Seydel, T.; Schreiber, F. Protein Self-Diffusion in Crowded Solutions. *Proc. Natl. Acad. Sci.* **2011,** *108*, 11815.

195. Morse, P. M.; Spencer, M. D.; Wilson, S. R.; Girolami, G. S. A Static Agostic a-CH...M Interaction Observable by NMR Spectroscopy: Synthesis of the Chromium(II) Alkyl $[Cr_2(CH_2SiMe_3)_6]^{2-}$ and Its Conversion to the Unusual "Windowpane" Bis(metallacycle) Complex $[Cr(\kappa^2\text{-}C,C'\text{-}CH_2SiMe_2CH_2)_2]_2$. *Organometallics* **1994,** *13*, 1646.

196. Chen, T.; Zhang, X.-H.; Wang, C.; Chen, S.; Wu, Z.; Li, L.; Sorasaenee, K. R.; Diminnie, J. B.; Pan, H.; Guzei, I. A.; Rheingold, A. L.; Wu, Y.-D.; Xue, Z.-L. A Tungsten Silyl Alkylidyne Complex and Its Bis(alkylidene) Tautomer. Their Interconversion and an Unusual Silyl Migration in Their Reaction with Dioxygen. *Organometallics* **2005,** *24*, 1214.

197. Chen, T.; Wu, Z.; Li, L.; Sorasaenee, K. R.; Diminnie, J. B.; Pan, H.; Guzei, I. A.; Rheingold, A. L.; Xue, Z. Direct Observation of an Equilibrium between $(Bu^tCH_2)_2W(CBu^t)(SiBu^tPh_2)$ and $(Bu^tCH_2)W(=CHBu^t)_2(SiBu^tPh_2)$ and an Unusual Silyl Migration. *J. Am. Chem. Soc.* **1998,** *120*, 13519.

198. Jalarvo, N.; Gourdon, O.; Ehlers, G.; Tyagi, M.; Kumar, S. K.; Dobbs, K. D.; Smalley, R. J.; Guise, W. E.; Ramirez-Cuesta, A.; Wildgruber, C.; Crawford, M.

K. Structure and Dynamics of Octamethyl-POSS Nanoparticles. *J. Phys. Chem. C* **2014,** *118*, 5579.

199. Hudson, B. S., Vibrational Spectroscopy via Inelastic Neutron Scattering. In *Frontiers of Molecular Spectroscopy*, Laane, J., Ed. Elsevier: Amsterdam, 2009; pp 597.

200. Reinhard, P.-G.; Suraud, E., Gross Properties and Trends. In *Introduction to Cluster Dynamics*, Wiley-VCH Verlag GmbH: 2008; pp 133.

201. La Mar, G. N. *NMR of Paramagnetic Molecules. Principles and Applications*. Academic Press: New York, 1973.

202. Bertini, I.; Luchinat, C.; Parigi, G.; Ravera, E. *NMR of Paramagnetic Molecules: Applications to Metallobiomolecules and Models*. 2nd Ed. ed.; Elsevier: 2016.

203. Walker, F. A., NMR and EPR Spectroscopy of Paramagnetic Metalloporphyrins and Heme Proteins. In *Handbook of Porphyrin Science*, Kadish, K. M.; Smith, K. M.; Guilard, R., Eds. World Scientific: 2010; Vol. 6, pp 1.

204. Habib, F.; Korobkov, I.; Murugesu, M. Exposing the Intermolecular Nature of the Second Relaxation Pathway in a Mononuclear Cobalt(II) Single-Molecule Magnet with Positive Anisotropy. *Dalton Trans.* **2015,** *44*, 6368.

205. Mamontov, E.; Herwig, K. W. A Time-of-flight Backscattering Spectrometer at the Spallation Neutron Source, BASIS. *Rev. Sci. Instrum.* **2011,** *82*, 085109.

206. Stone, M. B.; Niedziela, J. L.; Overbay, M. A.; Abernathy, D. L. The ARCS Radial Collimator. *EPJ Web Conf.* **2015,** *83*, 03014.

Appendices

Appendix A

Supporting Information for Chapter 2

Synthesis of Fe(TPP)X [X = F (1), Br (2), I (3)]

Iron halide (FeI_2•hydrate, $FeBr_2$•hydrate, FeF_3•$3H_2O$; 1.5 equiv) was added to 1 equiv of H_2TPP refluxing in 100 mL of DMF. Solution was checked periodically by UV-visible spectroscopy in toluene to see if the reaction was completed. Once product was confirmed, the solution was iced and crystals were collected via filtration and recrystallized in methylene chloride. It should be noted that column chromatography was used in attempts to purify the product. However, degradation of the product on the column was observed and column chromatography was thus not used to purify the product.

3 was the most difficult to prepare and purify as the reaction to prepare **3** also gave the μ-oxo dimer derivative $Fe(TPP)_2O$. In order to eliminate the oxo dimer, the product mixture was dissolved in chloroform and HI (57 wt%) was added dropwise, as to not demetallate the compound, until the color changed from green to brown/red solution.[35] Recrystallization in methylene chloride yielded **3**.

Conversion of Fe(TPP)X [X = Br (**2**), I (**3**)] to $Fe(TPP)_2O$ and Fe(TPP)F (**1**), to Fe(TPP)OH was observed by UV-visible spectroscopy when water was added to the reaction mixtures after reflux to crystalize the products.[58] Therefore after several unsuccessful attempts, the procedures for the metalloporphyrin preparation were revised to eliminate water addition after the reflux to prevent undesired products.

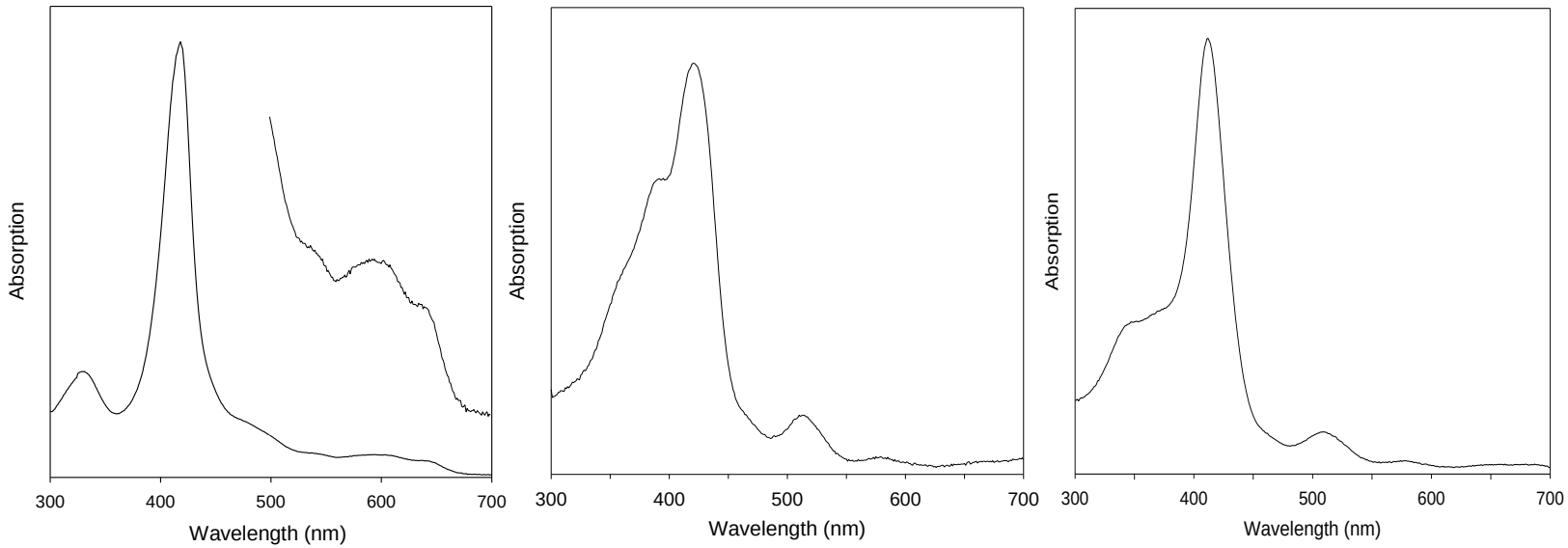

Figure A.1. UV-visible spectra of Fe(TPP)F (**1**, Left),[A1] Fe(TPP)Br (**2**, Middle),[43] and Fe(TPP)I (**3**, Right)[43] in toluene. The spectra are consistent with those reported in the literature.

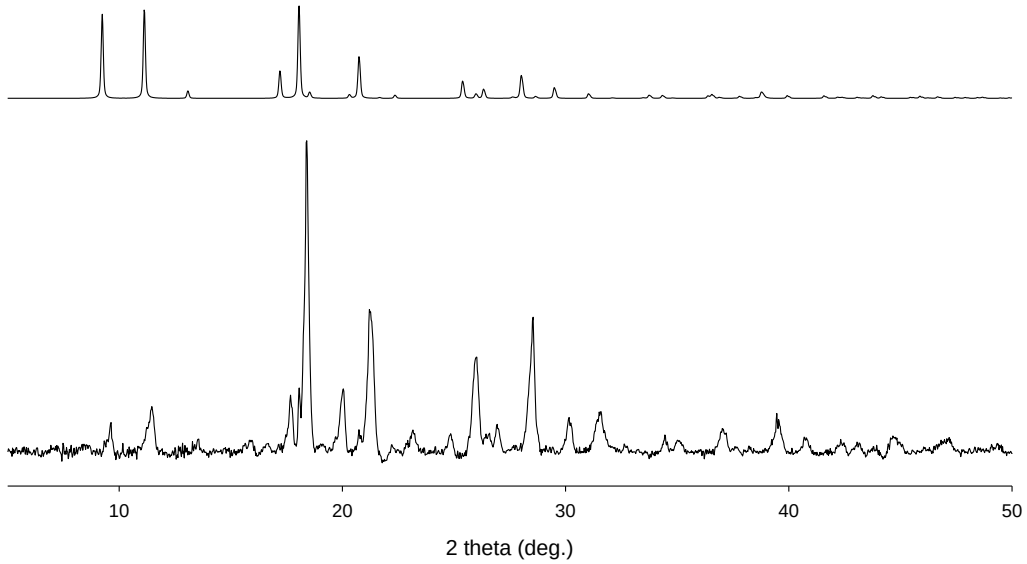

Figure A.2. (Top) Simulated diffraction pattern of Fe(TPP)Cl single crystal data. (Bottom) Diffraction pattern of **1** obtained from a sample used for INS. Crystal structure of Fe(TPP)F reported gave the following: tetragonal space group, T = 293(1) K, a = 13.381(2) Δ, c = 9.767(2) Δ, V = 1748.79 Δ^3. However, details of the structure needed for the simulation of powder diffraction were not provided. The structure is, however, similar to that of Fe(TPP)Cl[59] [T = 293(2) K, $I4$, a = 13.5374(2) Δ, c = 9.8247(2), V = 1800.49(5) Δ^3]. Thus, the simulation of powder diffraction from single-crystal diffraction of Fe(TPP)Cl[59] is used here for comparison.

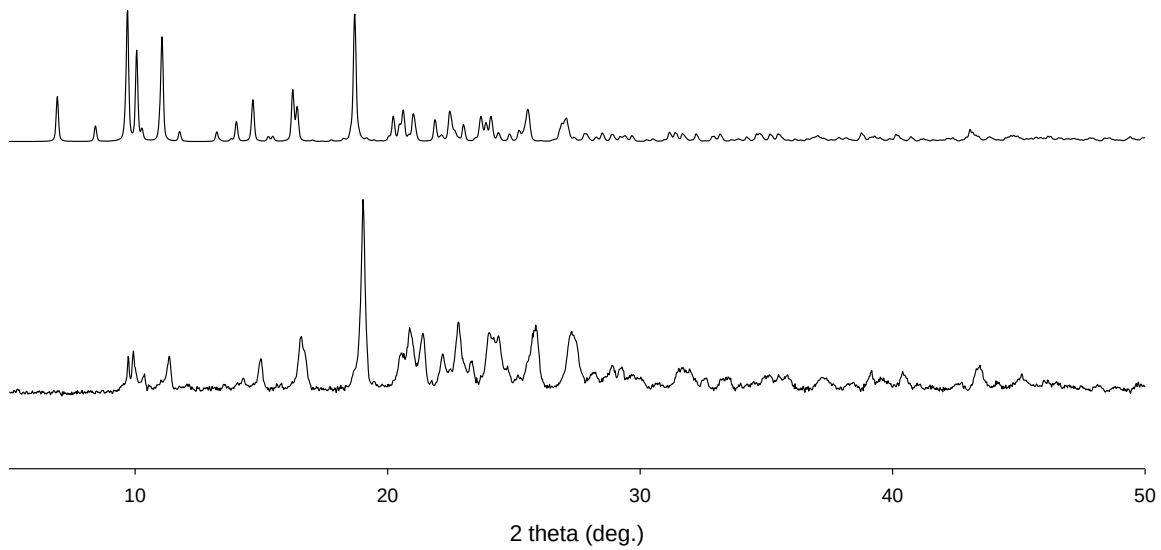

Figure A.3. (Top) Simulated diffraction pattern of **2** from single crystal data. (Bottom) Diffraction pattern of Fe(TPP)Br obtained from a sample used for INS.

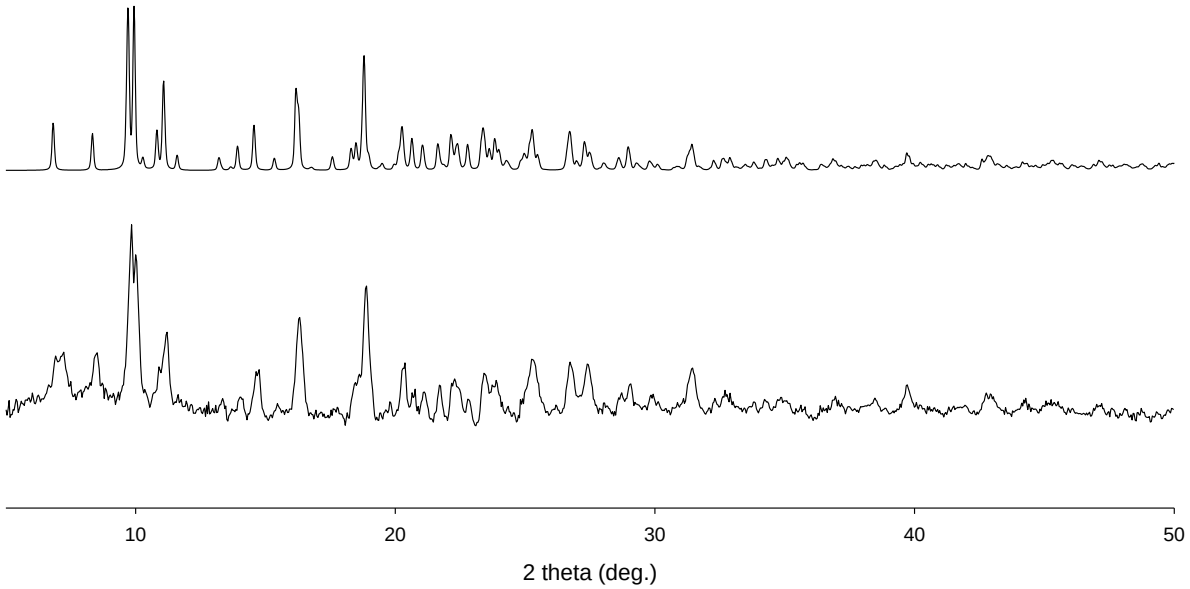

Figure A.4. (Top) Simulated diffraction pattern of **3** from single crystal data. (Bottom) Diffraction pattern of **3** obtained from a sample used for INS.

Elemental analyses were thus performed on **2** and **3** to rule out the presence of impurities that may contribute to these peaks. The analyses gave satisfactory results.

Anal Calcd for $FeC_{44}H_{28}N_4Br$: C, 70.61; H, 3.77; N, 7.44. Found: C, 70.49; H, 3.64; N, 7.65. Anal Calcd for $FeC_{44}H_{28}N_4I$: C, 66.44; H, 3.55; N, 7.04. Found: C, 66.52; H, 3.66; N, 7.19. The nonmagnetic INS peaks were shown to be from phonons as discussed in the text and below.

Mass spectroscopy was performed on all compounds using an ABI (Foster City, CA) Voyager-DETM PRO matrix assisted laser desorption ionization time-of-flight (MALDI/TOF) mass spectrometer. However, the parent peak for all samples was $Fe(TPP)^+$, showing the dissociation of the Fe-X bonds. Thus, MALDI was not capable of determining the identity of the axial ligand.

Additional INS Plots and Error Analysis

INS spectra are functions of the incident neutron energy E_i, scattering vector $\boldsymbol{Q}$, and temperature of the sample. Sufficient E_i is needed to excite the sample to the first and second magnetic excited states in the current samples. In Fe(TPP)I (**3**), e.g., E_i = 97.35 cm^{-1} was required to observe the second magnetic peak, as indicated below. However, larger E_i often leads to a larger elastic peak and lower resolution of the magnetic peaks. Thus, whenever possible, INS spectra with small E_i were used to locate the magnetic peaks.

Variable-temperature INS spectra were used to analyze the change of the magnetic peaks vs. temperatures in part to support the assignment of the peaks as magnetic. The negative peaks were used to make the assignment as well. The positions of the negative peaks were also used to calibrate the elastic peak at Energy Transfer = 0 cm^{-1}. Magnetic peaks at each available temperature were verified by using a baseline

correction on experimental data and then fitting the data with a Gaussian function to find the maximum intensity. Experimental values were then compared with calculated values. The experimental and calculated intensities were scaled using the most intense peak.

The intensity of the magnetic peaks decreases with the increase in the scattering vector ***Q***, while phonon peaks increase with the increase in *Q*.[A2] However, as described in the text, various factors can limit the *Q* dependence of magnetic intensities. Therefore, in the experimental data we looked for consistent intensities in the magnetic peaks. The data were plotted at different *Q* ranges, with low to high *Q* values, to confirm the presence of phonon peaks.

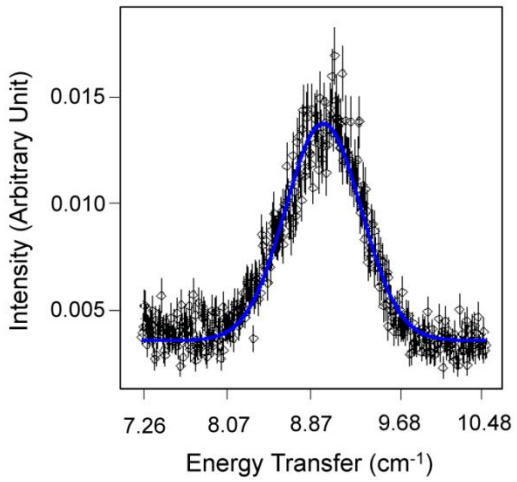

Area	0.0090(1)
Center	8.960(5) cm^{-1}
FWHM	0.83(1) cm^{-1}
Background	0.00347(5)

Figure A.5. Typical first magnetic peaks of for Fe(TPP)F (**1**) used for calibration of the elastic peak and calculation of the *D* value (E_i = 24.17 cm^{-1}, 10 K). FWHM = Full width at half maximum.

For the spectrum at 1.6 K (Figure 2.1), there is no negative magnetic peak to calibrate the elastic peak. Therefore, the spectrum at 1.6 K was not used to locate the first magnetic peak. Only the spectra at 10 K, 50 K, and 100 K were used. The INS spectra at these temperatures using E_i = 24.20 cm^{-1}, |Q| = 0.5-1.3 $Å^{-1}$ give the best resolution and were thus used to locate the first magnetic peaks. These peaks, their average and standard deviation are listed in Table A.1.

Table A.1. Analysis of the first magnetic peaks and random errror in the peak position in Fe(TPP)F

Temperature	**First magnetic peak (cm^{-1})**
100 K	8.961
50 K	9.005
10 K	8.993
	Average = 8.986; σ_{n-1} = 0.0227; Typical 10% FWHM = 0.0832 from Figure A.5

Step size in Figure A.5 is 0.00866 cm^{-1}. Since usually the error associated with a peak position is ca. 10% of FWHM (= 0.0832 cm^{-1} in the current case), 0.0832 cm^{-1} is treated as systematic error.

$$\sigma_{total}^2 = (0.0832)^2 + (0.0227)^2;\ \sigma_{total} = 0.0862 \approx 0.09\ cm^{-1}$$

$2D$ = 8.986 cm^{-1}; D = 4.49(9) cm^{-1}.

The exact peak location of $4D$ for Fe(TPP)F (**1**) was not critical for the determination of the ZFS parameters as there was no E parameter to cause shifting of

this peak. However, the center and FWHM with corresponding errors are listed in table below to compare how close the 4*D* peak location is to 2*D*.

Table A.2. Position and FWHM of the 4*D* peak in Fe(TPP)F (**1**)

Temperature (K)	Center (cm^{-1})	FWHM (cm^{-1})
10	18.15	1.8
50	18.01	1.7
100	17.99	1.1
	Ave. = 18.05 σ_{n-1} = 0.09	

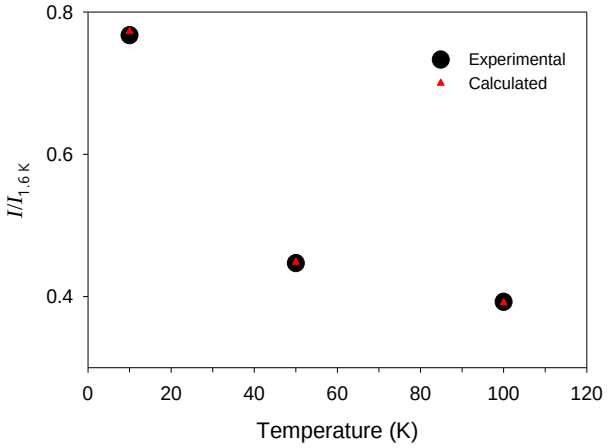

Temp (K)	Expt.	Calc.	% Error
1.6	1.0000	1.0000	N/A
10	0.7673	0.7729	0.725%
50	0.4469	0.4483	0.290%
100	0.3925	0.3912	0.332%

Figure A.6: (Left) Experimental and calculated intensities vs. temperature for the 2*D* peak in INS spectra of **1**. At 1.6 K, the peak is most intense. Therefore, it was used to scale the rest of the temperatures. (Right) Table of error calculations comparing the intensities.

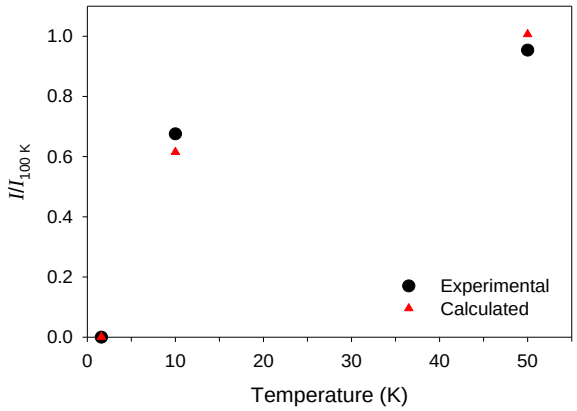

Temp (K)	Expt.	Calc.	% Error
1.6	0.0000	8.799e-4	N/A
10	0.6756	0.6151	9.75%
50	0.9536	1.0064	5.25%
100	1.0000	1.0000	N/A

Figure A.7: (Left) Experimental and calculated intensities vs. temperature for the 4*D* peak in INS spectra of Fe(TPP)F (**1**). At 100 K the peak is most intense. Therefore, it was used to scale the rest of the temperatures. (Right) Table of error calculations comparing the intensities.

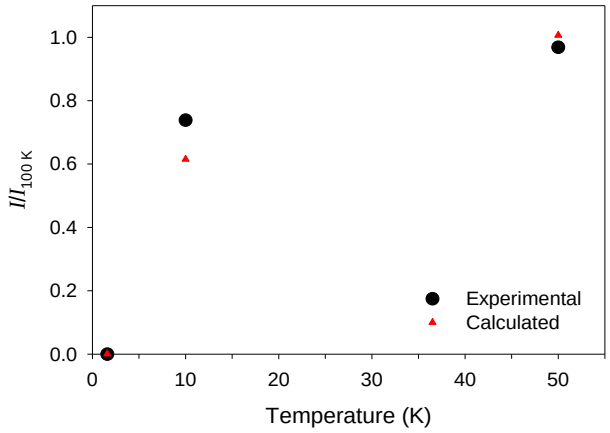

Temp (K)	Expt.	Calc.	% Error
1.6	0.0000	8.801e-4	N/A
10	0.7385	0.6151	20.1%
50	0.9684	1.0064	3.77%
100	1.0000	1.0000	N/A

Figure A.8: (Left) Experimental and calculated intensities vs. temperature for the -2*D* peak in INS spectra of Fe(TPP)F (**1**). At 100 K the peak is most intense. Therefore, it was used to scale the rest of the temperatures. (Right) Table of error calculations comparing the intensities.

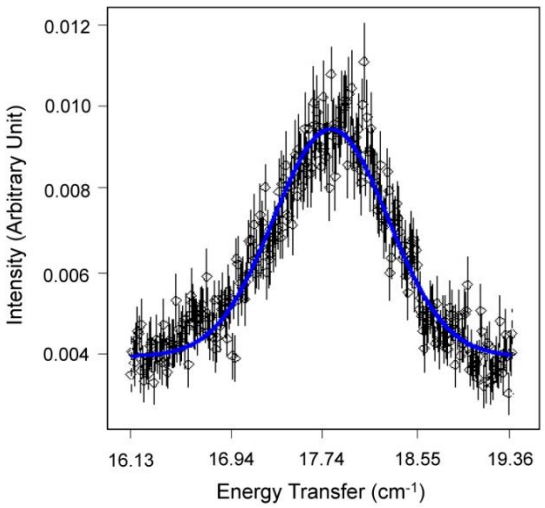

Area	0.0066(2)
Center	17.824(9) cm^{-1}
FWHM	1.13(1) cm^{-1}
Background	0.00395(6)

Figure A.9. Typical first magnetic peak of Fe(TPP)Br (**2**) used for the calibration of the elastic peak and calculation of the *D* and *E* values (E_i = 40.89 cm^{-1}, 50 K). This peak also has the largest error associated with the standard deviation and FWHM. It was used to estimate the total error.

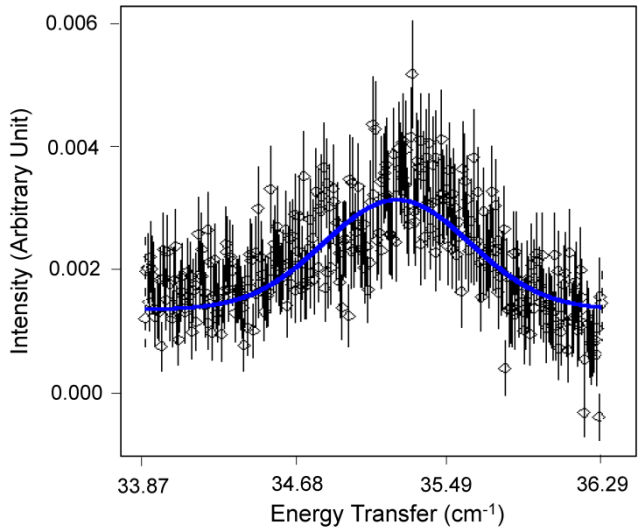

Area	0.0017(2)
Center	35.21(2) cm^{-1}
FWHM	0.90(7) cm^{-1}
Background	0.00136(7)

Figure A.10. Typical second magnetic peak of Fe(TPP)Br (**2**) used for the calculation of the *D* and *E* values (E_i = 40.89 cm^{-1}, 50 K).

For the spectrum at 1.6 K (Figure 2.2), there is no negative magnetic peak to calibrate the elastic peak. Therefore the spectrum at 1.6 K was not used to locate the first magnetic peak. Only the spectra at 10 K and 50 K were used. INS peaks using the larger incident energy E_i = 97.35 cm^{-1} show much larger errors than those using E_i = 40.89 cm^{-1}. Therefore the INS spectra from E_i = 97.35 cm^{-1} were not used in the location of the magnetic peaks.

The INS spectra (Figure 2.2) at these temperatures using E_i = 40.89 cm^{-1}, $|Q|$ = 0.5-1.0 $Å^{-1}$ give the best resolution and were thus used to locate the first magnetic peaks. These peaks, their average and standard deviation are listed in Table A.3.

The second magnetic peaks (both positive and negative) are more prominent in the spectra at 50 K (Figure 2.2). In order to obtain an average for the position of the positive, second magnetic peak, spectra at three different $\boldsymbol{Q}$ ranges were obtained. After calibration of the elastic peak using the first magnetic peaks, the positions of these second magnetic peaks are given in Table A.3.

Table A.3. Analysis of the magnetic peaks and random error in the peak positions (E_i = 40.89 cm^{-1}) in Fe(TPP)Br (**2**)

Temperatures, scattering vectors |*Q*|	**First magnetic peak (cm^{-1})**	**Second magnetic peak (cm^{-1})**
10 K, 0.5-1.0 $Å^{-1}$	17.40	-
50 K, 0.5-1.0 $Å^{-1}$	17.66	-
50 K, 0.48-1.8 $Å^{-1}$	-	35.02
50 K, 0.5-1.3 $Å^{-1}$	-	35.11
50 K, 0.5-2 $Å^{-1}$	-	34.99
	Average = 17.53 σ_{n-1} = 0.184	Average = 35.04 σ_{n-1} = 0.0624
	Typical 10% FWHM = 0.113 from Figure A.9	Typical 10% FWHM = 0.0908 from Figure A.10

The step size in Figures A.9-A.10 is 0.008066 cm^{-1}. For systematic error, 10% of FWHM (= 0.113 cm^{-1} for the first magnetic peak which is larger than that for the second magnetic peak) is used. σ_{n-1} = 0.184 for the first magnetic peak is also larger than that for the second magnetic peak. It is used as random error.

$$\sigma_{total}^2 = (0.113)^2 + (0.184)^2; \sigma_{total} = 0.216 \approx 0.22 \text{ cm}^{-1}$$

The first and second magnetic peaks are 17.5(2) cm^{-1} and 35.0(2) cm^{-1}, respectively. Using the spin-Hamiltonian in Eq. 1.1 gives D = 8.8(2) cm^{-1}; E = 0.1(2) cm^{-1}. χ^2 of the calculated vs. observed peak positions = 0.00005146.

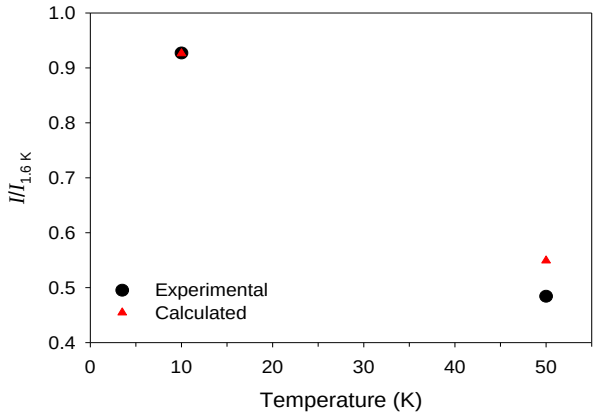

Temp (K)	Expt.	Calc.	% Error
1.6	1.0000	1.0000	N/A
10	0.9270	0.9264	0.065%
50	0.4843	0.5492	11.82%

Figure A11: (Left) Experimental and calculated intensities vs. temperature for the 2*D* peak in INS spectra of Fe(TPP)Br (**2**). At 1.6 K the peak is most intense, therefore it was used to scale the rest of the temperatures. (Right) Table of error calculations comparing the intensities.

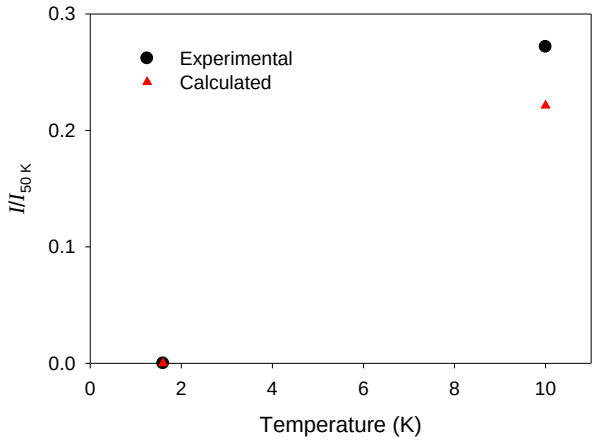

Temp (K)	Expt.	Calc.	% Error
1.6	0.0000	3.881e-7	N/A
10	0.2719	0.2214	22.81%
50	1.0000	1.0000	N/A

Figure A12: (Left) Experimental and calculated intensities vs. temperature for the 4*D* peak in INS spectra of Fe(TPP)Br (**2**). At 50 K, the peak is most intense. Therefore, it was used to scale the rest of the temperatures. (Right) Table of error calculations comparing the intensities.

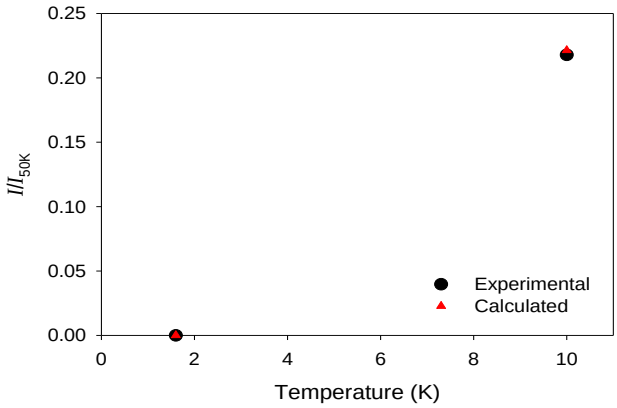

Temp (K)	Expt.	Calc.	% Error
1.6	0.0000	2.461e-7	N/A
10	0.2178	0.2214	1.63%
50	1.0000	1.0000	N/A

Figure A.13: (Left) Experimental and calculated intensities vs. temperature for the -2*D* peak in INS spectra of Fe(TPP)Br (**2**). At 50 K the peak is most intense. Therefore, it was used to scale the rest of the temperatures. (Right) Table of error calculations comparing the intensities.

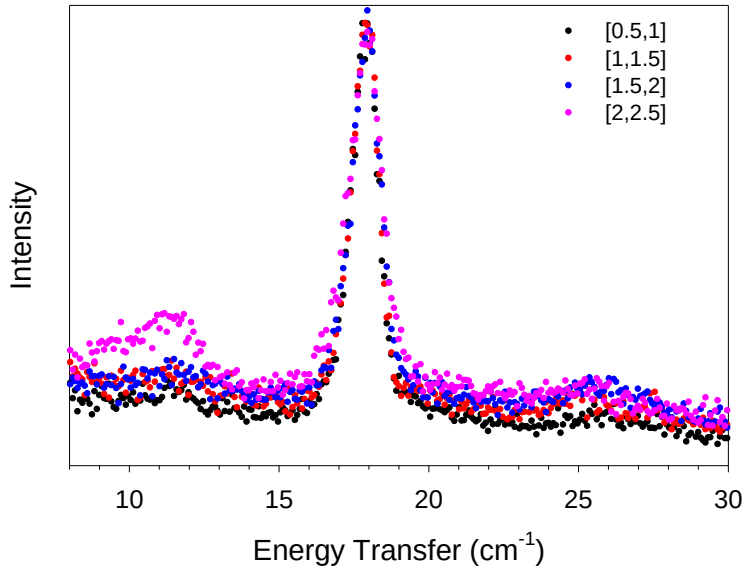

Figure A.14. *Q* dependence of the peaks in the INS spectra of Fe(TPP)Br (**2**) at 40.89 cm^{-1} comparing different *Q* ranges. *Q* ranges of [0.5, 1], [1, 1.5], [1.5, 2], and [2, 2.5] are represented by the black, red, blue, and pink points respectively. It is observed that as *Q* increases, the phonon peaks at ~11.5 and 26 cm^{-1} increase while the magnetic peak at 17.5 cm^{-1} stays constant or decreases with increasing *Q*.

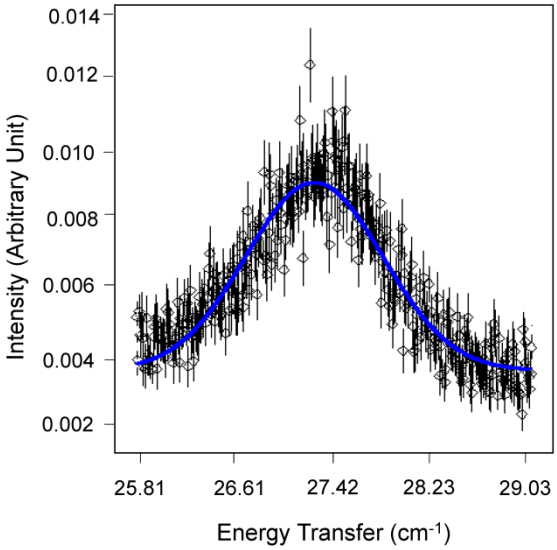

Area	0.0065(3)
Center	27.26(1) cm^{-1}
FWHM	1.40(5) cm^{-1}
Background	0.00289(1)

Figure A.15. Typical first magnetic peak of Fe(TPP)I (**3**) used for calibration of the elastic peak and calculation of the *D* and *E* values (E_i = 40.89 cm^{-1}, 50 K).

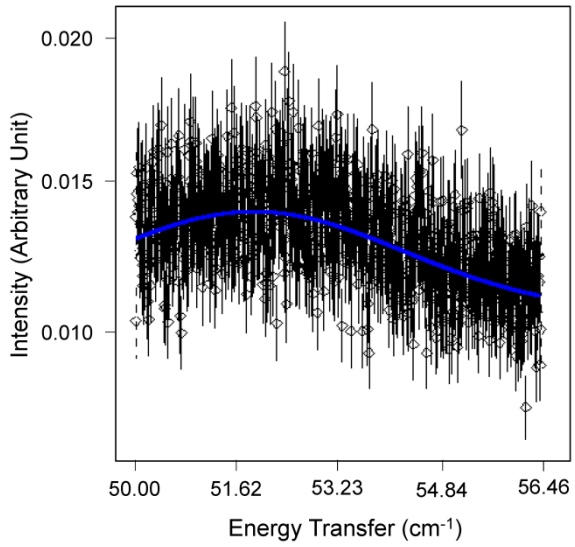

Area	0.0206(7)
Center	51.9(1) cm^{-1}
FWHM	5.6(8) cm^{-1}
Background	0.0106(5)

Figure A.16. Typical second magnetic peak of Fe(TPP)I (**3**) used for the calculation of the *D* and *E* values (E_i = 97.35 cm^{-1}, 50 K). This peak also has the largest error associated with the standard deviation and FWHM. It was used to estimate the total error.

As shown in Figures 2.3, only the INS spectrum at 50 K with E_i = 40.89 cm^{-1} (Figure 2.3a) gives the negative, first magnetic peak. The positive and negative peaks at 50 K here were used to calibrate the elastic peak. In order to obtain an average for the position of the positive, first magnetic peak, spectra at four different *Q* ranges were obtained, as listed in Table A.4.

E_i = 40.89 cm^{-1} is not sufficient to excite the molecules to the second excited state. E_i = 97.35 cm^{-1} is needed to give make the excitation (to show the second magnetic peak). However, at this high incident energy, the negative magnetic peaks in Figure 2.3b could not be located. Without those negative peaks, we could not directly calibrate the elastic peak. Thus, we used a different approach to calibrate. The position of the first magnetic peak, 26.82 cm^{-1}, from the spectrum at E_i = 40.89 cm^{-1} (Figure 2.3a, 50 K; Table A.4) was used so the first magnetic peak of the spectrum in Figure 2.3b (E_i = 97.35 cm^{-1}) is fixed at this value, yielding the position of the second magnetic peak. Again only the 50 K spectrum in Figure 2.3b (E_i = 97.35 cm^{-1}) was used to locate the second magnetic peak, as the peak is more visible and also because the calibration for the first magnetic peak involves the 50 K spectrum in Figure 2.3 (E_i = 40.89 cm^{-1}). In order to obtain an average for the position of the positive, second magnetic peak, spectra at three different, low ranges were obtained, as listed in Table A.4.

Table A.4. Analysis of the magnetic peaks and random error in the peak positions in Fe(TPP)I (**3**)

Scattering vectors |*Q*|	**First magnetic peak (cm^{-1})** E_i **= 40.89** cm^{-1}	**Second magnetic peak (cm^{-1})** E_i **= 97.35** cm^{-1}
0.5-1.0 $Å^{-1}$	26.88	N/A
0.8-2.0 $Å^{-1}$	26.77	53.10
1.0-2.5 $Å^{-1}$	26.75	53.35
0.48-1.8 $Å^{-1}$	26.89	53.41
	Average = 26.82 σ_{n-1} = 0.0727	Average = 53.29 σ_{n-1} = 0.164
	Typical 10% FWHM = 0.14 from Figure A.15	Typical 10% FWHM = 0.56 from Figure A.16

As shown in Table A.4, the error from the weaker, second magnetic peak dominates in both 10% FWHM and standard deviation. Therefore it was used to calculate the total error. The step size in Figures A.15-A.16 is 0.008066 cm^{-1}. As in the studies of Fe(TPP)F (**1**) and Fe(TPP)Br (**2**), 10% of FWHM (= 0.56 cm^{-1} for the second magnetic peak which is larger than that for the first magnetic peak) is treated as systematic error. σ_{n-1} = 0.164 for the second magnetic peak is also larger than that for the first magnetic peak. It is used as random error.

$$\sigma_{total}^2 = (0.164)^2 + (0.56)^2;\ \sigma_{total} = 0.5835 \approx 0.6\ cm^{-1}$$

The first and second magnetic peaks are 26.8(6) cm^{-1}; 53.3(6) cm^{-1}, respectively. Using the spin-Hamiltonian in Eq. 1.1 gives D = 13.4(6) cm^{-1}, E = 0.3(6) cm^{-1}. The chi-square test yields χ^2 of the calculated vs. observed peak positions = 0.001951.

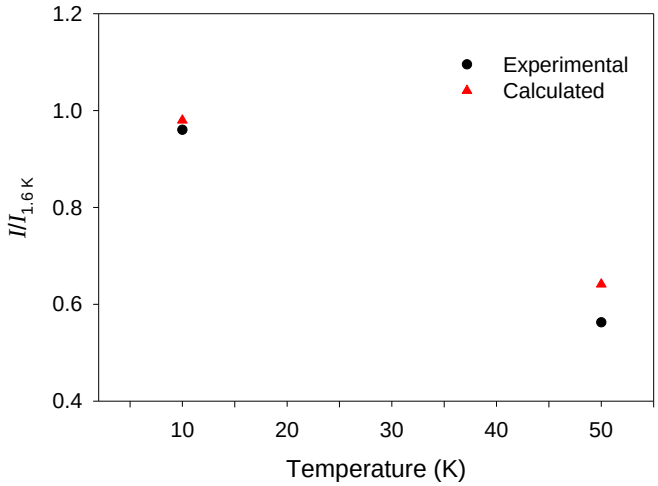

Temp (K)	Expt.	Calc.	% Error
1.6	1.0000	1.0000	N/A
10	0.9601	0.9797	2.00%
50	0.5626	0.6413	12.27%

Figure A.17: (Left) Experimental and calculated intensities vs. temperature for the 2*D* peak in INS spectra of Fe(TPP)I (**3**). At 1.6 K the peak is most intense. Therefore, it was used to scale the rest of the temperatures. (Right) Table of error calculations comparing the intensities.

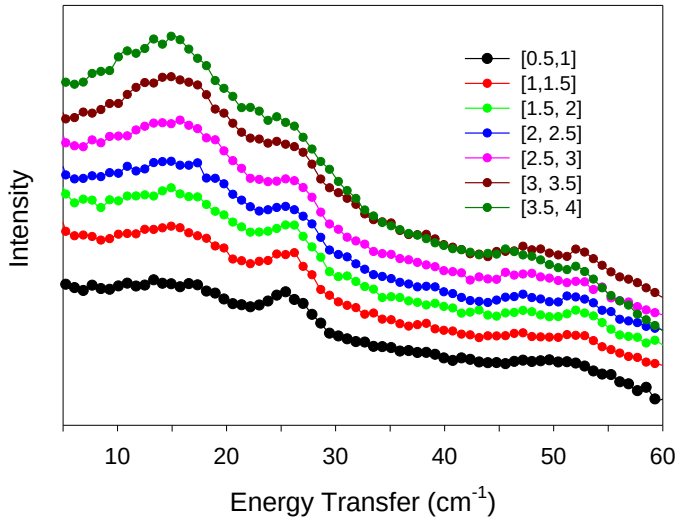

Figure A.18: *Q* dependence plot of **3** at E_i = 97.35 cm^{-1} showing an increase of intensity of the phonon peak ~15 cm^{-1}. This peak grows in intensity as *Q* increases. The *Q* ranges of [0.5, 1.0], [1.0, 1.5], [1.5, 2], [2, 2.5], [2.5, 3], [3, 3.5], and [3.5, 4] are represented as black, red, light green, blue, pink, brown, and dark green, respectively.

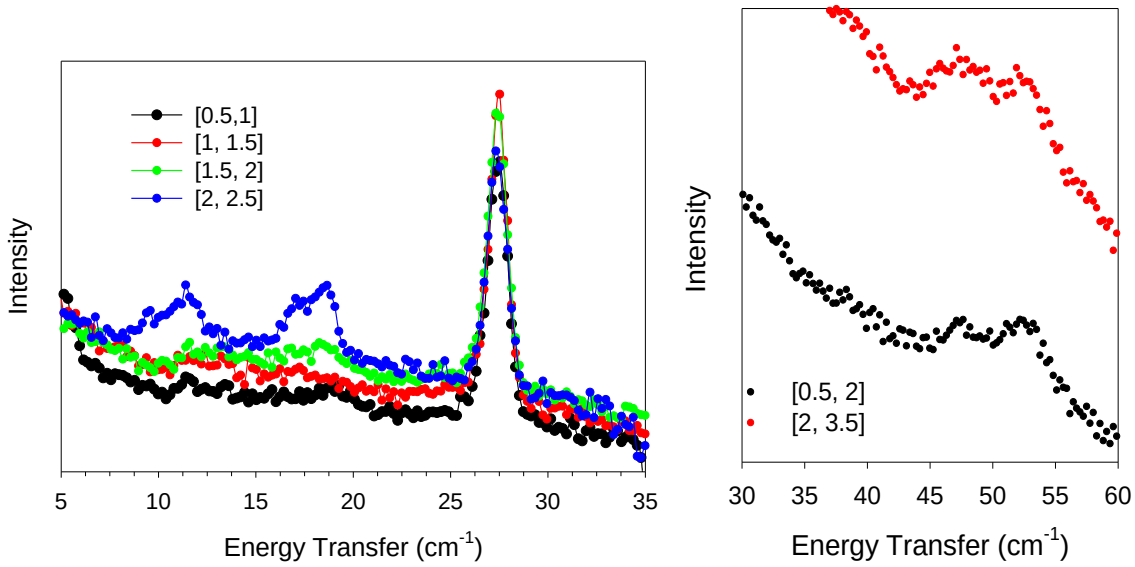

Figure A.19: (Left) *Q* dependence plot of INS spectra of Fe(TPP)I (**3**) with E_i = 40.89 cm^{-1} showing the difference between a phonon and a magnetic peak. *Q* = [0.5, 1], [1, 1.5], [1.5, 2], and [2, 2.5] are represented by black, red and green, and blue, respectively. (Right) *Q* dependence plot of INS spectra of **3** with E_i = 97.35 cm^{-1} comparing a peak at ~47 and 53 cm^{-1}. *Q* = [0.5, 2] and [2, 3.5] are represented by black and red points, respectively.

The peaks between 10 and 20 cm^{-1} in Fe(TPP)I (**3**) are indicative of phonon peaks, becoming more prominent at higher *Q*. It was also observed that the magnetic peak at 26.8 cm^{-1} drops in intensity at high *Q* [2, 2.5].

Q dependence of the INS peaks of Fe(TPP)I (**3**) at ~47 and 53 cm^{-1} with E_i = 97.35 cm^{-1} is given in Figure A.19, Right. Since these peaks are close together it was necessary to distinguish the phonon peak from the magnetic 4*D* peak. It was observed that the peak at 47 cm^{-1} becomes broader and more intense at high *Q*, while the peak at 53 cm^{-1} linewidth and intensity is consistent.

Computational Details

Table A.5. Quartet excited state energies (cm^{-1}) from CASSCF calculations with an active space of five d-electrons distributed of the five 3d MOs [CAS(5,5)] for Fe(TPP)X [X = F (**1**), Cl, Br (**2**), I (**3**)][a]

O_h	C_{4v}	X = F (**1**)	X = Cl	X = Br (**2**)	X = I (**3**)
$^4T_1$	$^4A_2$	21026(1.75)	20425(1.80)	20024(1.87)	19592(1.95)
	^4E	26930(-0.97)	25826(-0.88)	25264(-0.80)	24616(-0.70)
$^4T_2$	$^4B_2$	31123(0)	30900(0)	30228(0)	29554(0)
	^4E	31439(-0.02)	31130(-0.04)	31070(-0.04)	30832(-0.03)
^4E, $^4A_1$	$^4A_1$	32419(0)	31487(0)	31631(0)	31417(0)
	$^4B_1$	32535(0)	31907(0)	31725(0)	31612(0)
	$^4A_1$	32854(0)	32350(0)	32240(0)	32068(0)
$^4T_2$	^4E	38368(-0.06)	38164(-0.04)	38133(-0.03)	38011(-0.01)
	$^4B_2$	39122(0)	38596(0)	38202(0)	37843(0)
^4E	$^4A_1$	39985(0)	39004(0)	39067(0)	38984(0)
	$^4B_1$	40765(0)	40214(0)	40083(0)	39843(0)
$^4T_1$	^4E	43312(-1.40)	42086(-1.42)	41826(-1.28)	41661(-1.02)
	$^4A_2$	47964(1.17)	47641(1.16)	47721(1.22)	47735(1.31)

[a] Ground state $^6A_1$ was taken as energy reference.

Table A.6. Quartet excited state energies (in cm^{-1}) from NEVPT2/CASSCF calculations with an active space of five d-electrons distributed of the five 3d MOs [CAS(5,5)] for Fe(TPP)X [X = F (**1**), Cl, Br (**2**), I (**3**)][a]

O_h	C_{4v}	X = F (**1**)	X = Cl	X = Br (**2**)	X = I (**3**)
$^4T_1$	$^4A_2$	11335(3.24)	10182(3.61)	9574(3.91)	8960(4.26)
	^4E	20006(-1.31)	17987(-1.26)	17056(-1.18)	16089(-1.06)
$^4T_2$	$^4B_2$	24903	26509	25618	24866
	^4E	26354	25618	25328	24580
^4E, $^4A_1$	$^4A_1$	28554	25554	25782	25593
	$^4B_1$	29257	28579	28361	27974
	$^4A_1$	29556	28969	28843	28661
$^4T_2$	^4E	31031	30989	31088	31110
	$^4B_2$	32453	32772	32513	32308
^4E	$^4A_1$	34019	31731	31577	31244
	$^4B_1$	35195	34611	34471	34224
$^4T_1$	^4E	40581(-1.50)	39532(-1.52)	39324(-1.36)	39362(-1.08)
	$^4A_2$	45274(1.24)	44857(1.23)	4847(1.30)	44770(1.39)

[a]The energy of the ground state $^6A_1$ was taken as energy reference.

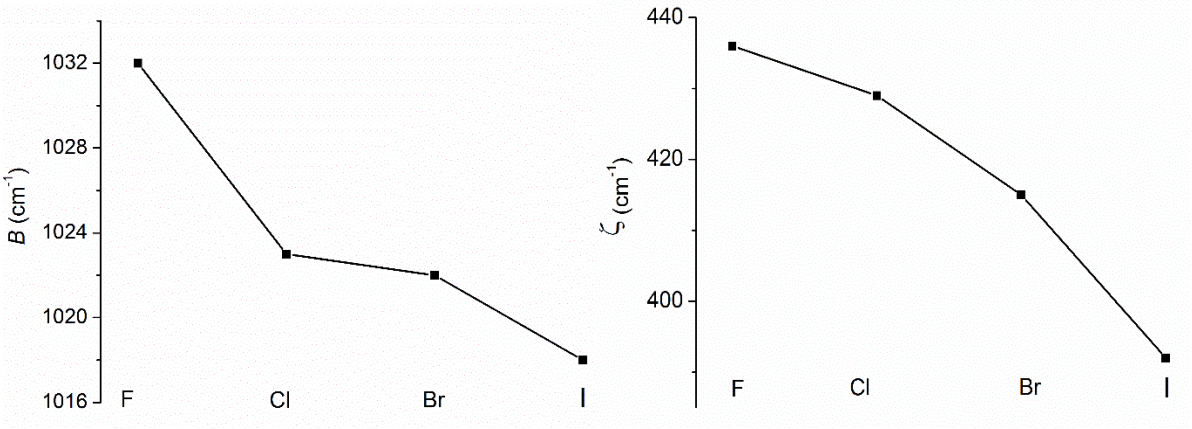

Figure A.20. Non-relativistic (left) and relativistic (right) covalence reduction of the parameters *B* and ζ, respectively, from CASSCF/NEVPT2 calculations of the Fe(TPP)X [X = F (**1**), Cl, Br (**2**), I(**3**)] series. Parameters for the plot are taken from Table 2.3.

Table A.7. Comparison of calculated zero-field splitting parameters (cm^{-1}) of Fe(TPP)X [X = Cl, Br (**2**), I (**3**)] using the reported crystal structures with those using the DFT-optimized geometries

X	**Cl**		**Br** (**2**)		**I** (**3**)	
	CASSCF	NEVPT2	CASSCF	NEVPT2	CASSCF	NEVPT2
D	0.575	1.894	0.929	2.311	1.471	3.155
E	0.000	0.000	0.006	0.003	0.004	0.002
(using reported crystal structures)						
D	0.590	1.980	0.960	2.600	1.480	3.450
E	000	0.000	0.000	0.000	0.000	0.000
(using DFT-optimized structures)						

Cartesian Coordinates Resulting from DFT-Geometry Optimizations of the Fe(TPP)X Series

X = F (**1**)

Fe	0.00000246182137	0.00000216827730	0.62380361087049
F	0.00000685316155	0.00000513764469	2.43910172862482
N	1.94890590248471	0.49957235711009	0.16750408128732
N	-0.49957214501006	1.94890641922755	0.16750839821146
N	0.49957145365003	-1.94890379399719	0.16751079321731
N	-1.94890296413300	-0.49957142063433	0.16751294268320
C	3.02272965828615	-0.36151075511782	0.14073802380082
C	4.24668491035397	0.38624056990997	0.10522290997586
C	3.90946054649493	1.70405059126765	0.10533580434278
C	2.47640756089305	1.77071260589555	0.14077258984378
C	1.74174813869489	2.94080021167935	0.12987469877018
C	2.49337673749366	4.21846512955844	0.10340010964384
C	2.85941796279152	4.84434544401435	1.29421884765235
C	3.55734423480112	6.04834582159698	1.27554916003375
C	3.89605103368324	6.63889935458462	0.06063352347899
C	0.36150862671476	3.02273241840167	0.14074278161926
C	-0.38624784087698	4.24668524845783	0.10521998734937
C	-1.70405683732934	3.90945678158107	0.10535420902467
C	-1.77071514650083	2.47640442176219	0.14077726592995

C	-2.94079632722263	1.74174522947728	0.12987867093139
C	-4.21846070725419	2.49336928622330	0.10340794094757
C	-4.84433883731842	2.85940551343680	1.29422862340271
C	-6.04834237155214	3.55732643230029	1.27556325644867
C	-6.63890098581172	3.89603140445272	0.06064936117667
C	-0.36151393375429	-3.02272837710311	0.14074826743902
C	0.38623900147649	-4.24668121771078	0.10522279599256
C	1.70404912965330	-3.90945768632923	0.10535745716961
C	1.77071358237962	-2.47640494963039	0.14077674116672
C	2.94079762773150	-1.74174729063155	0.12987638883495
C	4.21846028645741	-2.49337606412133	0.10340717935480
C	4.84433729810292	-2.85941165172246	1.29422902730061
C	6.04834015492983	-3.55733396825856	1.27556536522613
C	6.63889425108300	-3.89605001089098	0.06065238731551
C	4.81349534531343	-2.83923505112484	-1.10911491337238
C	6.01750707768571	-3.53718350062475	-1.13286465886199
C	2.83923126373491	4.81349774101364	-1.10912481439725
C	3.53717910653817	6.01750958493330	-1.13288034122527
C	-4.81349686097711	2.83922244606815	-1.10911484891913
C	-6.01751298867147	3.53716294288877	-1.13286667244093
C	-3.02272876810222	0.36151262528606	0.14074507891900
C	-4.24668049433850	-0.38624412329985	0.10523453476879
C	-3.90945333594507	-1.70405314842459	0.10534571667836

C	-2.47640199469269	-1.77071566014090	0.14078299214312
C	-1.74174474639186	-2.94079400058804	0.12987699043677
C	-2.49337209716052	-4.21845500395825	0.10339907827615
C	-2.85941488459940	-4.84433546160024	1.29421612680228
C	-3.55734155700194	-6.04833550399499	1.27554410625637
C	-3.89604718663234	-6.63888704694586	0.06062698613535
C	-2.83922614019265	-4.81348352706238	-1.10912692244704
C	-3.53717572491766	-6.01749422276450	-1.13288561737294
H	5.23574308457377	-0.05834564744794	0.08198053894105
H	4.56236149334262	2.56955364209428	0.08229750853017
H	2.59047130759780	4.37837237447527	2.24278650205872
H	3.83884216819691	6.53156743842250	2.21134484914576
H	4.43936092637652	7.58423591358131	0.04374111142043
H	0.05833432570903	5.23574508270039	0.08197305216342
H	-2.56956267159365	4.56235523490979	0.08232154769759
H	-4.37836071433410	2.59046013633874	2.24279463859432
H	-6.53156238464667	3.83882129011261	2.21136077111022
H	-7.58424024440724	4.43933664174392	0.04375999437907
H	-0.05834719821509	-5.23573991888592	0.08197708101269
H	2.56955191490956	-4.56236003698402	0.08232442870969
H	4.37836219506687	-2.59045856823680	2.24279411296972
H	6.53155905318719	-3.83882831156488	2.21136361950926
H	7.58423140554935	-4.43935904214613	0.04376451357235

H	4.32462833950519	-2.55504011068147	-2.04158719927853
H	6.47645082039213	-3.80299654626302	-2.08539245697827
H	2.55503124187484	4.32462968460897	-2.04159474350169
H	3.80298707143216	6.47645165369875	-2.08541031859208
H	-4.32462925834951	2.55502540604839	-2.04158645347600
H	-6.47645882204982	3.80296970624743	-2.08539527207888
H	-5.23574091970997	0.05833844222777	0.08199305128995
H	-4.56235435332039	-2.56955722890040	0.08230788235435
H	-2.59046777300141	-4.37836318232799	2.24278465341137
H	-3.83884042649614	-6.53155865601822	2.21133886627830
H	-4.43935783840632	-7.58422317750939	0.04373237054068
H	-2.55502522639141	-4.32461228054830	-2.04159554103564
H	-3.80298284681641	-6.47643439006834	-2.08541685919443

X = Cl

Fe	0.00000136295732	-0.00000258576970	0.50831273212566
Cl	0.00000354656166	-0.00001164427704	2.71857146673799
N	1.94636670670710	0.49862563866408	0.04860190253751
N	-0.49862516614840	1.94636529396365	0.04860912568423
N	0.49862456793678	-1.94636683830713	0.04859090979055
N	-1.94636615059530	-0.49862437712500	0.04860335314802
C	3.02112056161443	-0.36192843568771	0.02838306912768
C	4.24525416000744	0.38528985425758	-0.00012519265880

C	3.90820050921457	1.70310444713176	-0.00028089577537
C	2.47523579735168	1.76953893829786	0.02824985793374
C	1.74148659057326	2.93940952753536	0.01891261050488
C	2.49307366539846	4.21694128634635	0.00104233784862
C	2.85499571397289	4.83617521747579	1.19657754249790
C	3.55243890610139	6.04052796197261	1.18643998134443
C	3.89460363569239	6.63769595313717	-0.02427483057213
C	0.36192866408084	3.02111888011221	0.02839241791243
C	-0.38528974146224	4.24525282910310	-0.00012203719256
C	-1.70310480835745	3.90819875292015	-0.00026753044147
C	-1.76953876992594	2.47523314214731	0.02823440894051
C	-2.93941085539997	1.74148565753413	0.01891619747231
C	-4.21693952794752	2.49307772207134	0.00106612203255
C	-4.83614006203372	2.85502007711128	1.19661205871396
C	-6.04048640678318	3.55247480939788	1.18649598323803
C	-6.63768088530940	3.89463126249276	-0.02420814261185
C	-0.36192838304179	-3.02112103216256	0.02839248525376
C	0.38528965479547	-4.24525506336852	-0.00012679116515
C	1.70310416378982	-3.90820055695898	-0.00028699793701
C	1.76953826970361	-2.47523505566352	0.02821682804818
C	2.93941053676767	-1.74148645227039	0.01894938901298
C	4.21694083806091	-2.49307812934286	0.00108845008446
C	4.83615120061524	-2.85502348379753	1.19662851781000

C	6.04049945236276	-3.55247493984681	1.18650096125595
C	6.63768472148363	-3.89462745090699	-0.02420884437028
C	4.81831507358175	-2.84220405399332	-1.20721908958639
C	6.02269240022689	-3.53979887858768	-1.22222473687212
C	2.84221461235894	4.81829694038219	-1.20727012858254
C	3.53979913205963	6.02268002540291	-1.22228558946529
C	-4.81832204286236	2.84220896026816	-1.20723583730110
C	-6.02269824165463	3.53980587736006	-1.22222996031355
C	-3.02112088876653	0.36192863649106	0.02841673191394
C	-4.24525480743360	-0.38528991092578	-0.00007253364074
C	-3.90819808414771	-1.70310409288265	-0.00032735159807
C	-2.47523373572746	-1.76953848264003	0.02821684494273
C	-1.74148609411252	-2.93941104719684	0.01893544358932
C	-2.49307504003946	-4.21694194182887	0.00105744523368
C	-2.85500569615758	-4.83617871252971	1.19658875028814
C	-3.55244929284641	-6.04053128519423	1.18644365170741
C	-3.89461013975810	-6.63769429459943	-0.02427481077563
C	-2.84220960895080	-4.81829402652373	-1.20725865488101
C	-3.53979655321321	-6.02267570620496	-1.22228158001247
H	5.23430769381145	-0.05951374188280	-0.01756197648630
H	4.56114230953150	2.56867157250467	-0.01769755433420
H	2.58297315785481	4.36474115491025	2.14153726279636
H	3.83085792084700	6.51879034735912	2.12567500338388

H	4.43754748999589	7.58333271642013	-0.03433843621351
H	0.05951381877962	5.23430621289591	-0.01756239967412
H	-2.56867251603917	4.56113993249904	-0.01768087276642
H	-4.36468591534769	2.58300340517856	2.14156348097120
H	-6.51872258778251	3.83090983459145	2.12573961475682
H	-7.58331308841375	4.43758330242782	-0.03425470676005
H	-0.05951373841782	-5.23430881806428	-0.01755527205559
H	2.56867154208021	-4.56114243775569	-0.01769490260120
H	4.36470377175168	-2.58301070482789	2.14158447187720
H	6.51874310439493	-3.83091225105523	2.12574012773310
H	7.58331790341079	-4.43757764295189	-0.03426439833068
H	4.33440348051133	-2.56107330722025	-2.14319077263226
H	6.48700297615936	-3.80834413913629	-2.17135759370127
H	2.56110150066730	4.33436706659689	-2.14323757258370
H	3.80835619574709	6.48697566244129	-2.17142242468568
H	-4.33441765274728	2.56108051430077	-2.14321187584949
H	-6.48701571491340	3.80835461198340	-2.17135848280763
H	-5.23430889628039	0.05951312505328	-0.01748779371441
H	-4.56113876349175	-2.56867160520865	-0.01776742068997
H	-2.58298661449546	-4.36474866715451	2.14155150854363
H	-3.83087550769650	-6.51879498825084	2.12567587194828
H	-4.43755537347681	-7.58333018139869	-0.03434423939948
H	-2.56109081846450	-4.33436216419957	-2.14322339658246

H	-3.80834913927721	-6.48696802304078	-2.17142129112014

X = Br (**2**)

Fe	-0.00000316867818	0.00000227702380	0.40320184648818
Br	-0.00001709558646	0.00001782458914	2.76344832605701
N	1.94649982793378	0.49862473161341	-0.03738211463020
N	-0.49862595381543	1.94649920366908	-0.03740489843291
N	0.49862838200409	-1.94649996057861	-0.03737567298970
N	-1.94650033640449	-0.49862777637333	-0.03739919916098
C	3.02121577018340	-0.36202146220201	-0.05510379689720
C	4.24529650249591	0.38523148489797	-0.07927169106021
C	3.90824563609157	1.70311738260672	-0.07918132086285
C	2.47528094146859	1.76959660433752	-0.05507184355408
C	1.74143248237568	2.93925332662984	-0.06371599219786
C	2.49294918773024	4.21671183714118	-0.07730023053698
C	2.85290108524921	4.83272458149813	1.12050462169871
C	3.55037942449173	6.03706666372725	1.11455396937556
C	3.89446701046939	6.63731731807811	-0.09408643746626
C	0.36202017330204	3.02121498726231	-0.05512617184002
C	-0.38523071764827	4.24529654939002	-0.07930640239937
C	-1.70311702062436	3.90824806782764	-0.07917049922612
C	-1.76959710061442	2.47528302003611	-0.05506231717068
C	-2.93925533648921	1.74143423879656	-0.06367294957130

C	-4.21671515078164	2.49295110374120	-0.07726202663603
C	-4.83273344826889	2.85290315996837	1.12054017333991
C	-6.03707794138747	3.55037745329796	1.11458441110079
C	-6.63732386390428	3.89446395035780	-0.09405876661030
C	-0.36202038752196	-3.02121398314141	-0.05515775742989
C	0.38523159408293	-4.24529417227075	-0.07937807947531
C	1.70311865592967	-3.90824922450460	-0.07907648595953
C	1.76959957127847	-2.47528371931548	-0.05501537074695
C	2.93925473907606	-1.74143371675979	-0.06377959982859
C	4.21671341859010	-2.49294962460358	-0.07733217231306
C	4.83270284007474	-2.85288426178252	1.12048951442656
C	6.03704816264255	-3.55035695066960	1.11457216888619
C	6.63732302480591	-3.89446030749029	-0.09405163137428
C	4.82108953174104	-2.84396909268119	-1.28351965870467
C	6.02555206871636	-3.54147033626726	-1.29424300592826
C	2.84395006787993	4.82106557209202	-1.28350433602778
C	3.54145484513304	6.02552586668075	-1.29426083833379
C	-4.82106341939171	2.84395281948778	-1.28346871059786
C	-6.02552440007637	3.54145647649023	-1.29423058785854
C	-3.02121552007662	0.36201948077863	-0.05516372701381
C	-4.24529574528545	-0.38523262715822	-0.07939484179847
C	-3.90824978647955	-1.70311907737071	-0.07907501536923
C	-2.47528431802280	-1.76959896149291	-0.05502286174299

C	-1.74143312795573	-2.93925331233447	-0.06373733882341
C	-2.49294794328348	-4.21671400142281	-0.07731434741527
C	-2.85289354780420	-4.83272249605699	1.12049438649399
C	-3.55036817691638	-6.03706673446759	1.11455181530735
C	-3.89446274254375	-6.63732127768107	-0.09408472110886
C	-2.84395267150533	-4.82107347787568	-1.28351452010891
C	-3.54145600643800	-6.02553469937125	-1.29426330433754
H	5.23450069136433	-0.05944002013312	-0.09369445510689
H	4.56136375657247	2.56865270474539	-0.09347239953120
H	2.57930296809112	4.35862698315387	2.06371997530782
H	3.82730291263385	6.51286252591929	2.05553011248662
H	4.43738630181010	7.58305270240194	-0.10081391879000
H	0.05944233782658	5.23450013581532	-0.09372148696726
H	-2.56865178053971	4.56136780120024	-0.09343102905580
H	-4.35864126418267	2.57930274340839	2.06375758494804
H	-6.51287857861664	3.82729973604173	2.05555855514598
H	-7.58305959720668	4.43738263058532	-0.10079033829171
H	-0.05944137811584	-5.23449717447222	-0.09384858697301
H	2.56865296395942	-4.56137005213068	-0.09332126555095
H	4.35858872143590	-2.57927053291309	2.06369202834496
H	6.51282710552216	-3.82726535669644	2.05556132121358
H	7.58305965631463	-4.43737781870289	-0.10075313783982
H	4.33963881955680	-2.56432162508465	-2.22125754728419

H	6.49247892955618	-3.81158304857528	-2.24169167128535
H	2.56429184077026	4.33959563560826	-2.22122914291083
H	3.81155515998634	6.49243415066094	-2.24172215488084
H	-4.33959101300694	2.56429211028879	-2.22119154589953
H	-6.49242929528470	3.81155562921981	-2.24169392131253
H	-5.23449903801975	0.05943975689463	-0.09385083269837
H	-4.56137012429173	-2.56865395043606	-0.09330372179872
H	-2.57929299469651	-4.35862016704567	2.06370677335327
H	-3.82728750293726	-6.51285911628981	2.05553097983600
H	-4.43737962836787	-7.58305810865159	-0.10080604243231
H	-2.56429917552874	-4.33960660239063	-2.22124242905426
H	-3.81156081084710	-6.49244640056918	-2.24172169260690

X = I (**3**)

Fe	0.00000006430380	0.00000126463843	0.27193013762943
I	-0.00000389692371	0.00001054855809	2.83755727250520
N	1.94717030000237	0.49785070763535	-0.15022716459143
N	-0.49783475211577	1.94717198231133	-0.15024024398393
N	0.49783660483165	-1.94717329828871	-0.15022223729194
N	-1.94716875728831	-0.49785274885555	-0.15022888268392
C	3.02156217175209	-0.36360337740759	-0.16525525690642
C	4.24606716230713	0.38319595961542	-0.18713336219619
C	3.90966257158817	1.70135510394246	-0.18712062462238

C	2.47681494109229	1.76880151736693	-0.16522433787604
C	1.74313853590395	2.93855828425443	-0.17288573092954
C	2.49464728565475	4.21620272531193	-0.18134324833873
C	2.85172493789169	4.82857255136945	1.01925314959977
C	3.54768050052343	6.03378565336185	1.01877181213988
C	3.89263443118525	6.63893363910337	-0.18723458198382
C	0.36361285651193	3.02157317093025	-0.16505801584141
C	-0.38319280011754	4.24607674625801	-0.18674256377001
C	-1.70134647340416	3.90965358723620	-0.18749272695374
C	-1.76878707320255	2.47680790333417	-0.16541930740649
C	-2.93855006896392	1.74313399495772	-0.17245937614380
C	-4.21619393826269	2.49464347948348	-0.18104238812309
C	-4.82866079053485	2.85177942944404	1.01948846957659
C	-6.03387389098335	3.54773549016931	1.01887652704165
C	-6.63892684614449	3.89262618394304	-0.18719585269044
C	-0.36361015599827	-3.02157368819988	-0.16505792848661
C	0.38319489667701	-4.24607799077235	-0.18674000478867
C	1.70134885227823	-3.90965432808780	-0.18748008550071
C	1.76878821759897	-2.47680841911246	-0.16540859341815
C	2.93855214332857	-1.74313453238037	-0.17251052856316
C	4.21619688219166	-2.49464402388561	-0.18107528207343
C	4.82865134375984	-2.85177013831610	1.01946487370170
C	6.03386502378241	-3.54772534282960	1.01887141753676

C	6.63892761125911	-3.89263154570354	-0.18719164069548
C	4.82529431753407	-2.84673475511942	-1.38463273030186
C	6.03068455253113	-3.54269081092427	-1.39013283085395
C	2.84678577606398	4.82538473787020	-1.38484456240454
C	3.54274127094849	6.03077591790242	-1.39023276161672
C	-4.82527826204307	2.84672401574299	-1.38460910707673
C	-6.03066789681211	3.54268099544187	-1.39012774626561
C	-3.02155861818583	0.36360327743876	-0.16529869122696
C	-4.24606414112289	-0.38319396687885	-0.18722049867074
C	-3.90966475336157	-1.70135451804030	-0.18704102583487
C	-2.47681602142728	-1.76880184195812	-0.16518346097527
C	-1.74313812558661	-2.93855927188550	-0.17293356855563
C	-2.49464821857580	-4.21620375639220	-0.18137453078249
C	-2.85171560047623	-4.82856217730944	1.01923101483694
C	-3.54767575188237	-6.03377265509420	1.01876698370083
C	-3.89263916193493	-6.63893295632909	-0.18723043045726
C	-2.84679974327683	-4.82539628559959	-1.38486724644916
C	-3.54276044853811	-6.03078458957327	-1.39023743210985
H	5.23477082642255	-0.06219713472530	-0.19886219766676
H	4.56295026192136	2.56660225272236	-0.19885375552512
H	2.57706472040588	4.35026653396453	1.95987608104059
H	3.82248537546709	6.50663915898136	1.96163559538820
H	4.43410723881311	7.58529359683142	-0.18971242178792

H	0.06219420080557	5.23478519496526	-0.19831537259514
H	-2.56659650022852	4.56293467243568	-0.19936388781168
H	-4.35042952686008	2.57716350011627	1.96016233970334
H	-6.50680384893874	3.82258246234759	1.96168977788480
H	-7.58528618147438	4.43409966947054	-0.18977601818095
H	-0.06219195843722	-5.23478603312154	-0.19832958029258
H	2.56659884420994	-4.56293491654987	-0.19936293587502
H	4.35041110613888	-2.57714574551071	1.96013156814877
H	6.50678374737582	-3.82256708538398	1.96169178606556
H	7.58528711786972	-4.43410479616517	-0.18975730038653
H	4.34618386172560	-2.56926224978971	-2.32404559638565
H	6.50118048034521	-3.81363267646773	-2.33536756026129
H	2.56934983036408	4.34633875870912	-2.32430128302215
H	3.81371998128979	6.50133744981826	-2.33542438325851
H	-4.34615758031063	2.56924395470449	-2.32401466214350
H	-6.50115549391093	3.81361268634979	-2.33536955755127
H	-5.23476641981067	0.06220127927276	-0.19898428987883
H	-4.56295448728228	-2.56660035324337	-0.19873846831974
H	-2.57704598817296	-4.35024852943176	1.95984710066493
H	-3.82247101160886	-6.50661804581710	1.96163758613950
H	-4.43411542618460	-7.58529097574483	-0.18969440858621
H	-2.56937224743082	-4.34635970808387	-2.32433102867690
H	-3.81374798684270	-6.50135476933222	-2.33542219565747

Additional References for Appendix A

A1. Meininger, D. J.; Muzquiz, N.; Arman, H. D.; Tonzetich, Z. J. A Convenient Procedure for the Synthesis of Fluoro-Iron(III) Complexes of Common Synthetic Porphyrinates. *J. Porphyrins Phthalocyanines* **2014**, *18*, 416.

A2. Gurevich, I. I.; Tarasov, L. V. *Low-Energy Neutron Physics*, North-Holland Publishing Company, Amsterdam, 1968.

Appendix B

Supporting Information for Chapter 3

Error Analysis of Variable-Temperature INS Data for $(PPh_4)_2[Co(NO_3)_4]\cdot CH_2Cl_2$ (4), $(MePPh_3)_2[Co(NO_3)_4]$ (5) and $(AsPh_4)_2[Co(NO_3)_4]$ (6)

INS spectra are functions of the incident neutron energy E_i, scattering vector $\boldsymbol{Q}$, and temperature of the sample. Sufficient E_i is needed to excite the sample to the magnetic excited state. However, larger E_i often leads to a larger elastic peak and lower resolution of the magnetic peaks. Thus, whenever possible, INS spectra with small E_i were used to locate the magnetic peak for the S = 3/2 systems.

In general, the intensity of the magnetic peaks decreases with the increase in $|Q|$, while phonon peaks increase with the increase in $|Q|$. We have looked at INS spectra at different $|Q|$ to select the best for presentation in Figures 3.7 and 3.9-3.10.

Variable-temperature INS spectra were used to analyze the change of the magnetic peak vs. temperatures in part to support the assignment of the peaks as magnetic. When possible the negative magnetic peaks were used to calibrate the elastic peak at Energy Transfer = 0 cm^{-1}. If there was no transition present indicating that the incident neutrons *gain* energy from the sample in the INS process, the elastic peak was fit using a Gaussian function and its position was used to correct the magnetic transition position. For example, if the elastic band was fitted and displayed a slight shift towards a positive energy transfer, the magnetic transition was corrected for the amount the elastic peak had shifted by subtracting the elastic peak's difference from 0 cm^{-1}.

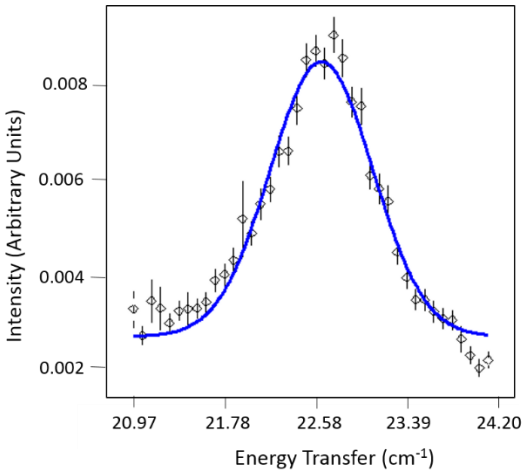

Area	0.00076(3)
Center	22.68(1) cm^{-1}
FWHM	1.07(3) cm^{-1}
Background	0.00285(7)

Figure B.1. Typical magnetic peak of $(PPh_4)_2[Co(NO_3)_4]\cdot CH_2Cl_2$ (**4**) used for determination of magnetic transition and calculation of the $2(D^2 + 3E^2)^{1/2}$ value (E_i = 53.7 cm^{-1}, 1.7 K). FWHM = Full width at half maximum.

Most of the temperatures with the exception of 50 K do not have negative energy transfer peaks that were possible to be fit with Gaussians (Figure 3.7). Therefore, fitting of the elastic peak was used to correct for the shifting of the elastic peak from 0 cm^{-1} during the experiment and applied to the magnetic transition. The 50 K data were calibrated with the negative energy transfer peak since it was available.

The INS spectra at these temperatures using E_i = 53.7 cm^{-1}, $|Q|$ = 0.5-1.3 $Å^{-1}$ give the best resolution and were thus used to locate the magnetic peaks. These peaks, their average and standard deviation are listed in Table B.1.

Table B.1. Analysis of the magnetic peak and random error in the peak position in $(PPh_4)_2[Co(NO_3)_4]\cdot CH_2Cl_2$ (**4**)

Temperature	Magnetic peak (cm^{-1})
100 K	22.18
50 K	22.42*
30 K	22.65
20 K	22.53
10 K	22.48
5 K	22.44
1.7 K	22.46
	Average = 22.45 σ_{n-1} = 0.142 Typical 10% FWHM = 0.107 from Figure B.1

*Negative magnetic peak was used to calibrate the elastic band.

Step size in Figure B.1 is 0.0801 cm^{-1}. Since usually the error associated with a peak position is ca. 10% of FWHM (= 0.107 cm^{-1} in the current case), 0.107 cm^{-1} is treated as systematic error.

$$\sigma_{total}^2 = (0.107)^2 + (0.142)^2;\ \sigma_{total} = 0.177 \approx 0.18\ cm^{-1}$$

$$2(D^2 + 3E^2)^{1/2} = 22.5(2)\ cm^{-1};\ (D^2 + 3E^2)^{1/2} = 11.2(2)\ cm^{-1}$$

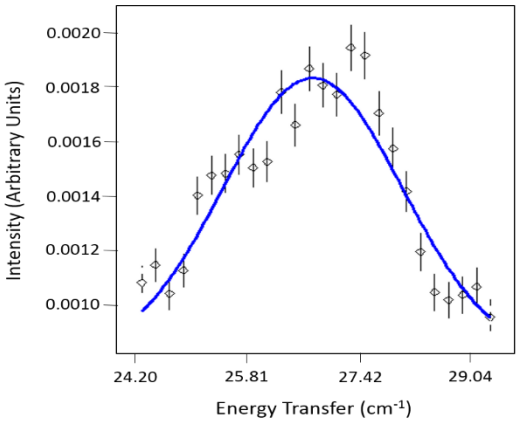

Area	0.00041(9)
Center	26.77(4) cm^{-1}
FWHM	3.0(4) cm^{-1}
Background	0.0008(1)

Figure B.2. Typical magnetic peak of $(MePPh_3)_2[Co(NO_3)_4]$ (**5**) used for determination of magnetic transition and calculation of the $2(D^2 + 3E^2)^{1/2}$ value (E_i = 40.3 cm^{-1}, 1.6 K).

There is no negative magnetic peak to calibrate the elastic peak (Figure 3.9). Therefore, fitting of the elastic peak was used to correct for the shifting of the elastic peak from 0 cm^{-1} during the experiment and applied to the magnetic transition for all temperatures.

The INS spectra at these temperatures using E_i = 40.3 cm^{-1}, $|Q|$ = 0.5-1.3 $Å^{-1}$ give the best resolution and were thus used to locate the magnetic peaks. These peaks, their average and standard deviation are listed in Table B.2.

Table B.2. Analysis of the magnetic peak and random error in the peak position in $(MePPh_3)_2[Co(NO_3)_4]$ (**5**)

Temperature	**Magnetic peak (cm^{-1})**
50 K	Could not be fit
10 K	26.54
1.6 K	26.66
	Average = 26.60 σ_{n-1} = 0.0849 Typical 10% FWHM = 0.30 from Figure B.2

Step size in Figure B.2 is 0.0807 cm^{-1}. Since usually the error associated with a peak position is ca. 10% of FWHM (= 0.30 cm^{-1} in the current case), 0.30 cm^{-1} is treated as systematic error.

$$\sigma_{total}^2 = (0.30)^2 + (0.0849)^2;\ \sigma_{total} = 0.312 \approx 0.31\ cm^{-1}$$

$$2(D^2 + 3E^2)^{1/2} = 26.6(3)\ cm^{-1};\ (D^2 + 3E^2)^{1/2} = 13.3(3)\ cm^{-1}$$

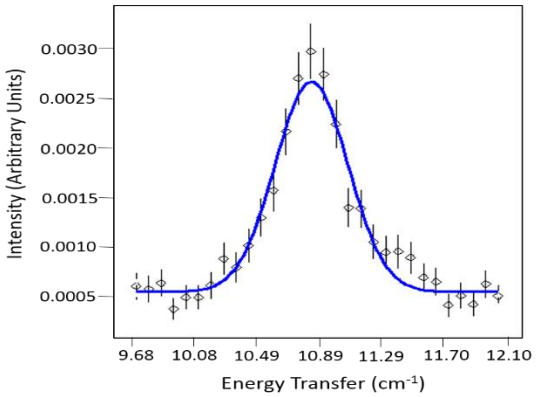

Area	0.000154(9)
Center	10.85(1) cm^{-1}
FWHM	0.55(3) cm^{-1}
Background	0.00056(3)

Figure B.3. Typical magnetic peak of $(AsPh_4)_2[Co(NO_3)_4]$ (**6**) used for determination of magnetic transition and calculation of the $2(D^2 + 3E^2)^{1/2}$ value (E_i = 24.2 cm^{-1}, 10 K).

For the spectrum at 1.6 K (Figure 3.10), there is no negative magnetic peak to calibrate the elastic peak. Therefore, fitting of the elastic peak was used to correct for the shifting of the elastic peak from 0 cm^{-1} during the experiment and applied to the magnetic transition. The 10 and 50 K data was calibrated with the negative energy transfer peak since it was available.

The INS spectra at these temperatures using E_i = 24.2 cm^{-1}, $|Q|$ = 0.5-2.0 $Å^{-1}$ give the best resolution and were thus used to locate the magnetic peaks. These peaks, their average and standard deviation are listed in Table B.3.

Table B.3. Analysis of the magnetic peak and random error in the peak position in $(AsPh_4)_2[Co(NO_3)_4]$ (**6**)

Temperature	**Magnetic peak (cm^{-1})**
50 K	11.65*
10 K	10.85*
1.6 K	10.74
	Average = 11.08 σ_{n-1} = 0.497 Typical 10% FWHM = 0.055 from Figure B.3

*Negative magnetic peak was used to calibrate the elastic band.

Step size in Figure B.3 is 0.0807 cm^{-1}. Since usually the error associated with a peak position is ca. 10% of FWHM (= 0.055 cm^{-1} in the current case), 0.055 cm^{-1} is treated as systematic error.

$$\sigma_{total}^2 = (0.055)^2 + (0.497)^2;\ \sigma_{total} = 0.500 \approx 0.50\ cm^{-1}$$

$$2(D^2 + 3E^2)^{1/2} = 11.1(5)\ cm^{-1};\ (D^2 + 3E^2)^{1/2} = 5.5(5)\ cm^{-1}$$

INS in Variable Magnetic Fields for $(PPh_4)_2[Co(NO_3)_4]\cdot CH_2Cl_2$ (4), $(MePPh_3)_2[Co(NO_3)_4]$ (5) and $(AsPh_4)_2[Co(NO_3)_4]$ (6)

Table B.4 shows a new magnetic peak present in the INS spectra after the application of magnetic fields in $(PPh_4)_2[Co(NO_3)_4]\cdot CH_2Cl_2$ (**4**) (Figure 3.8). As the field increases from 0.5 to 2.0 T, the peak position is more certain as the error and FWHM become smaller. At higher magnetic fields, the peak is shifted further away from the elastic band. Even though the data at 0.5 T have a large error, the presence of this peak at higher fields confirms that $D > 0$.

Table B.4. Analysis of the -1/2 $\rightarrow$ +1/2 magnetic peak and random error in the peak position in $(PPh_4)_2[Co(NO_3)_4]\cdot CH_2Cl_2$ (**4**)

Field Strength (T)	Magnetic Transition (cm^{-1})	FWHM (cm^{-1})
0.0	Not present	-
0.5	0.73(1.0)	4.96(29.0)
1.0	1.25(9)	0.8(5)
2.0	2.19(6)	0.4(4)

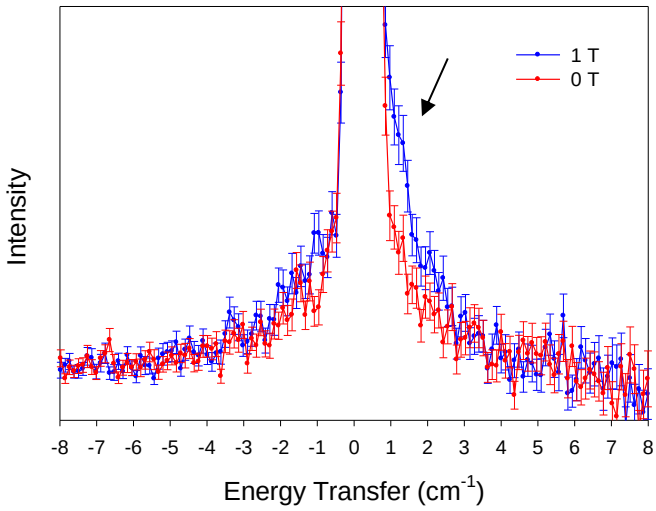

Figure B.4. INS spectrum of $(PPh_4)_2[Co(NO_3)_4]\cdot CH_2Cl_2$ (**4**) at 1.7 K, showing the M_S = -1/2 $\rightarrow$ +1/2 transition at 1 T (indicated by the black arrow) with the incident neutron energy of E_i = 13.4 cm^{-1}, $|Q|$ = 0.4-1.3 $Å^{-1}$. The solid lines are for eye guide.

|*Q*| vs. Intensity Plots for $(PPh_4)_2[Co(NO_3)_4]\cdot CH_2Cl_2$ (4), $(MePPh_3)_2[Co(NO_3)_4]$ (5) and $(AsPh_4)_2[Co(NO_3)_4]$ (6)

For the plots in Figures 3.7 (Right), 3.9-3.10 (Right), and B.5 (below), 2-dimensional peak intensity vs |*Q*| plots were used to guide the selection of the magnetic and phonon peaks. The baselines of the peaks were corrected and the peaks were fitted with a Gaussian function to obtain their intensities. The error was estimated to be the 10% of the intensity. Figures 3.7 (Right) and 3.9-3.10 (Right) confirm the presence of a magnetic excitation. Figure B.5 shows that the peak at 17.8 cm^{-1} in Figure 3.7 (left) is phonon.

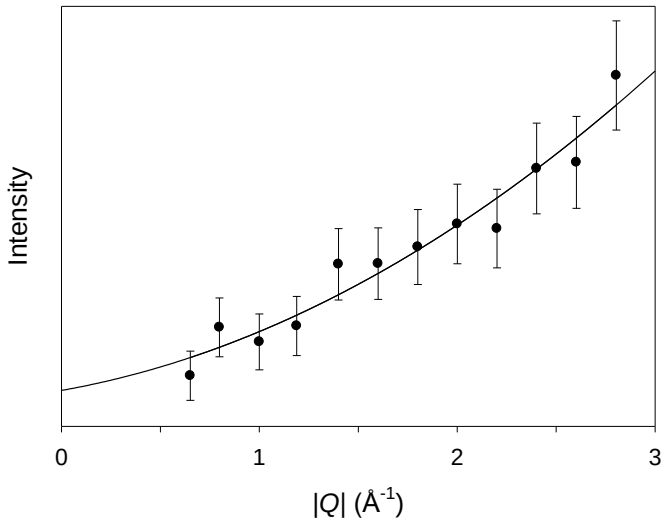

Figure B.5. Change in the intensity of the phonon peak at 17.8 cm^{-1} vs |*Q*| at 1.7 K in $(PPh_4)_2[Co(NO_3)_4]\cdot CH_2Cl_2$ (**4**). The data are fitted with the quadratic formula.

In INS spectra, peaks of magnetic excitations *decrease* in intensity with increased scattering-vector |*Q*|, while those from vibrations *increase* in intensity with increased |*Q*|. Thus, the 2-D plots of scattering intensities vs. |*Q*| may be used to identify the magnetic peaks. However, if the magnetic peak and phonon overlap, the peak intensity may not change with increased |*Q*|.

Hydrogen atoms in samples **4-6** contribute strongly incoherent scattering to the background. However, for the current studies at CNCS, SNS, deuteration of the samples was not necessary in order to reveal the magnetic peaks in **4-6**. As discussed in the manuscript, both temperature dependence and |*Q*| dependence of the magnetic peaks were used to distinguish the ZFS transitions. A straightforward way to look at how peaks change in intensities vs. |*Q*| is to examine the plots in Figure B.6. The left plot shows a sharp magnetic band (pointed out by a yellow arrow) at 1.7 K. The intensity is roughly constant through the observable |*Q*| range due to partial overlap with the nearby phonon and the high background from hydrogen in the sample. A phonon peak is observable at high |*Q*| around 18 cm^{-1}. As the sample is warmed up to 30 K (Figure B.6, right) the ZFS peak loses intensity and the phonon peak at 18 cm^{-1} is more visible at high |*Q*|.

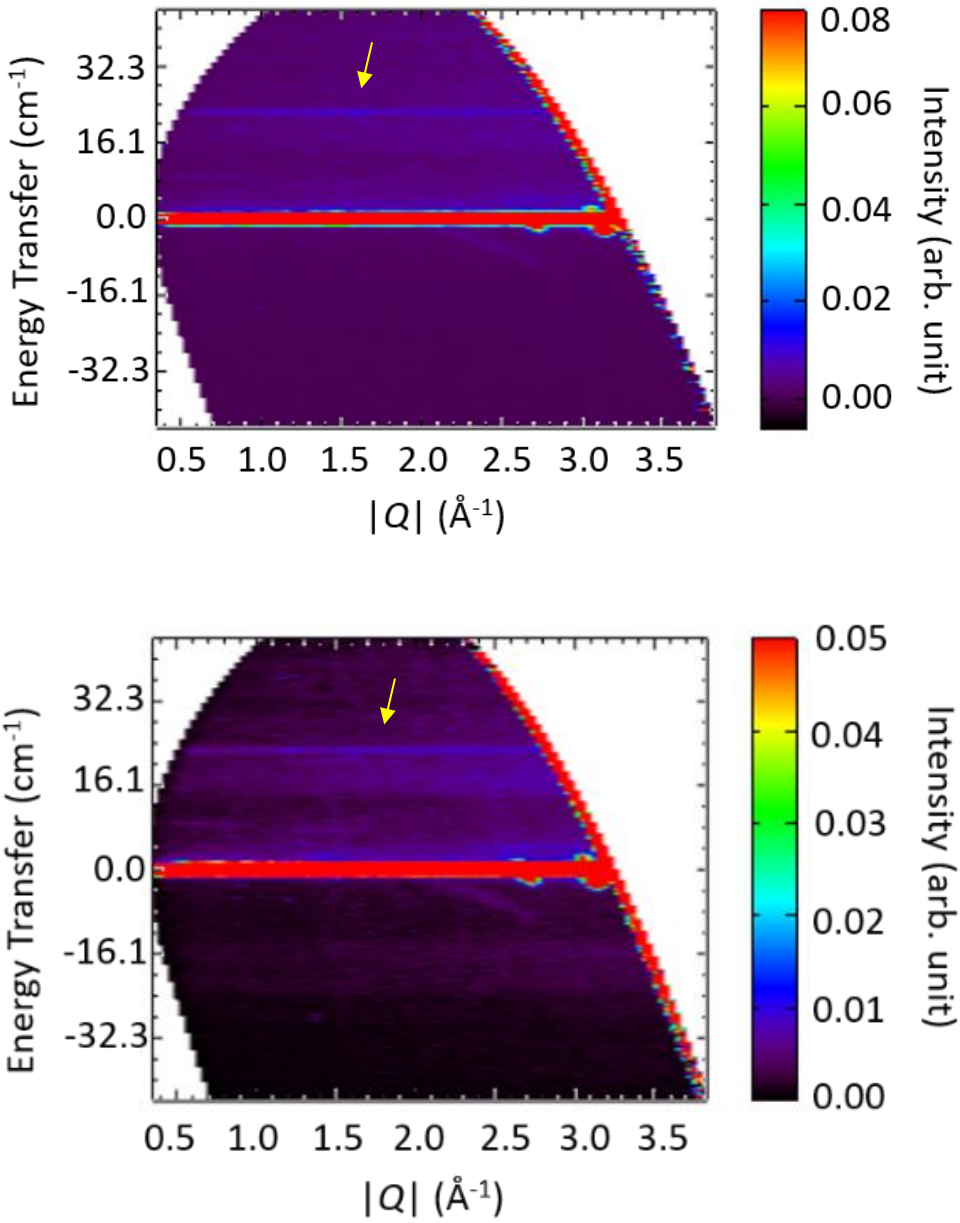

Figure B.6. (Left) Change in the peak intensities in $(PPh_4)_2[Co(NO_3)_4]\cdot CH_2Cl_2$ (**4**) vs $|Q|$ a 1.7 K. Incident neutron energy: 53.7 cm^{-1}. (Right) Change in the peak intensities in **4** vs $|Q|$ a 30 K. Incident neutron energy: 53.7 cm^{-1}. The yellow arrows represent the ZFS transition.

Figure B.7 shows the change in peak intensity for the ZFS peak of $(AsPh_4)_2[Co(NO_3)_4]$ (**6**) summed over two |*Q*| ranges. At a higher |*Q*| range (red line), the peak is less intense.

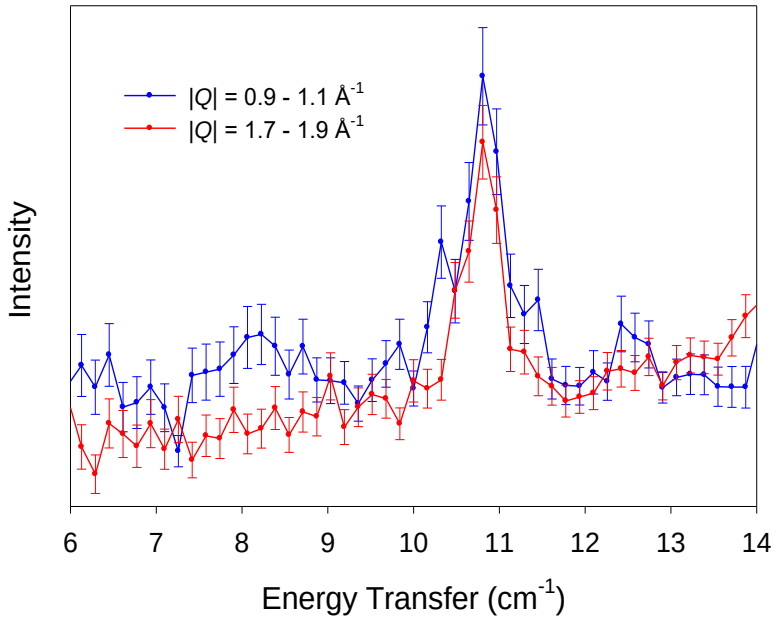

Figure B.7. INS spectra of $(AsPh_4)_2[Co(NO_3)_4]$ (**6**) at 1.6 K showing a comparison of the ZFS transition at different |*Q*| ranges. The baseline of the peak has been corrected.

Additional Magnetic Susceptibility Plots for $(PPh_4)_2[Co(NO_3)_4]\cdot CH_2Cl_2$ (4), and $(MePPh_3)_2[Co(NO_3)_4]$ (5) and $(AsPh_4)_2[Co(NO_3)_4]$ (6)

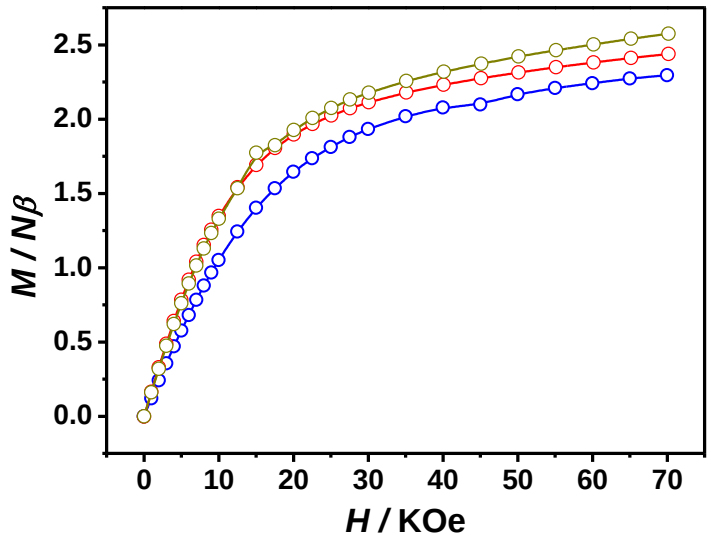

Figure B.8. The isothermal field dependence of magnetization at 1.8 K for $(PPh_4)_2[Co(NO_3)_4]\cdot CH_2Cl_2$ (**4**, green line), $(MePPh_3)_2[Co(NO_3)_4]$ (**5**, blue line) and $(AsPh_4)_2[Co(NO_3)_4]$ (**6**, red line).

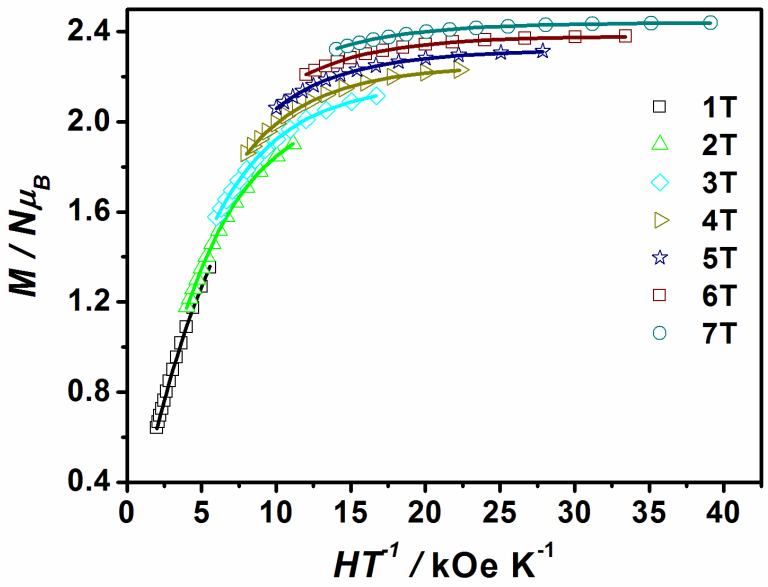

Figure B.9. Variable-temperature, variable-field DC magnetization data collected on a polycrystalline sample of for $(PPh_4)_2[Co(NO_3)_4]\cdot CH_2Cl_2$ (**4**). Fields of 1-7 T were used at temperatures from 1.8 to 5 K. Solid black lines indicate the best fits with *PHI* program, as discussed in the main text.

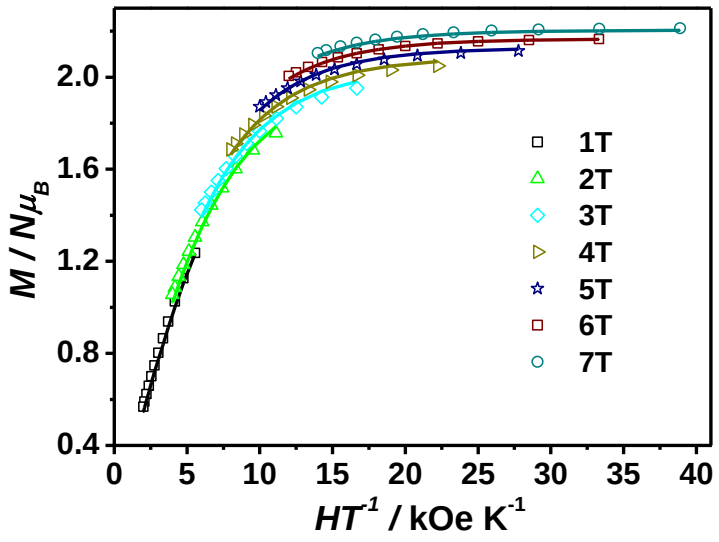

Figure B.10. Variable-temperature, variable-field DC magnetization data collected on a polycrystalline sample of $(MePPh_3)_2[Co(NO_3)_4]$ (**5**). Fields of 1-7 T were used at temperatures from 1.8 to 5 K. Solid black lines indicate the best fits with *PHI* program as discussed in Section 3.3.1.

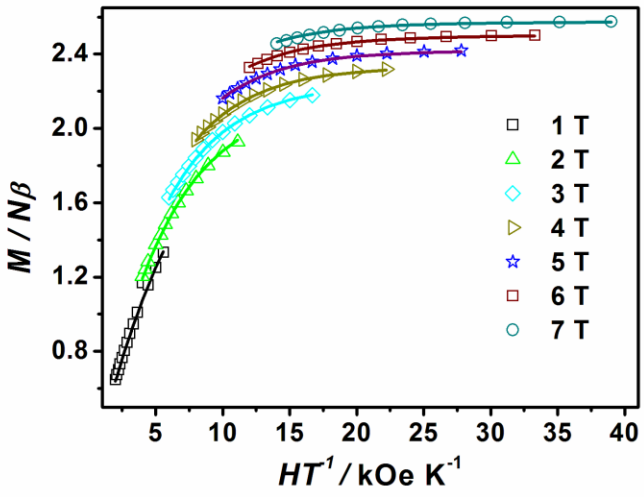

Figure B.11. Variable-temperature, variable-field DC magnetization data collected on a polycrystalline sample of $(AsPh_4)_2[Co(NO_3)_4]$ (**6**). Fields of 1-7 T were used at temperatures from 1.8 to 5 K. Solid black lines indicate the best fits with *PHI* program, as discussed in the main text.

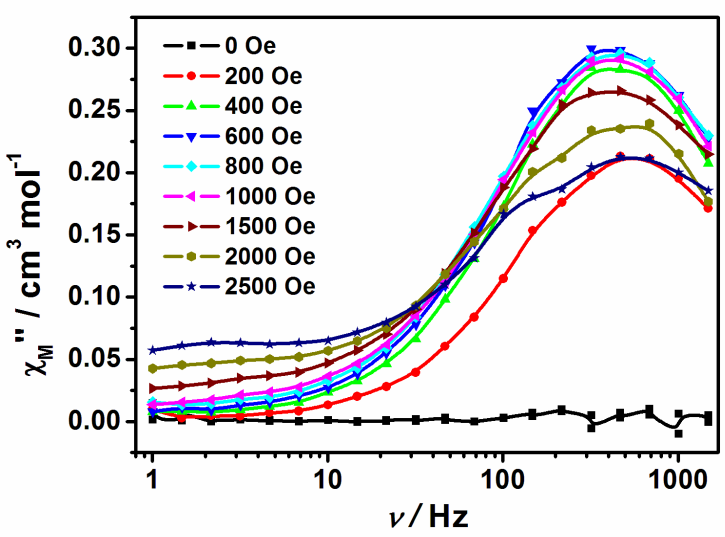

Figure B.12. Frequency dependence of out-of-phase (χ_M'') AC susceptibility at 1.8 K under the different applied static fields from 0 to 2500 Oe for $(PPh_4)_2[Co(NO_3)_4]\cdot CH_2Cl_2$ (**4**). The solid lines are for eye guide.

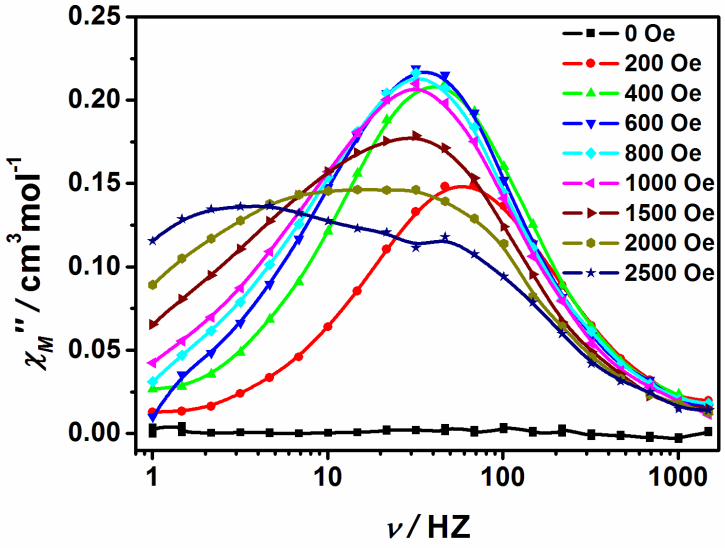

Figure B.13. Frequency dependence of out-of-phase (χ_M'') AC susceptibility at 1.8 K under the different applied static fields from 0 to 2500 Oe for $(MePPh_3)_2[Co(NO_3)_4]$ (**5**). The solid lines are for eye guide.

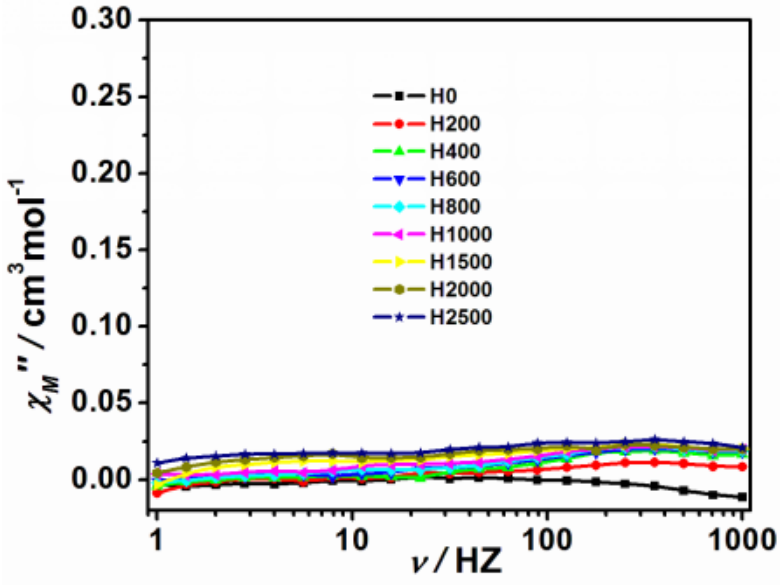

Figure B.14. Frequency dependence of out-of-phase (χ_M'') AC susceptibility at 1.8 K under the different applied static fields from 0 to 2500 Oe for $(AsPh_4)_2[Co(NO_3)_4]$ (**6**). The solid lines are for eye guide.

Crystal Structures of 4-6

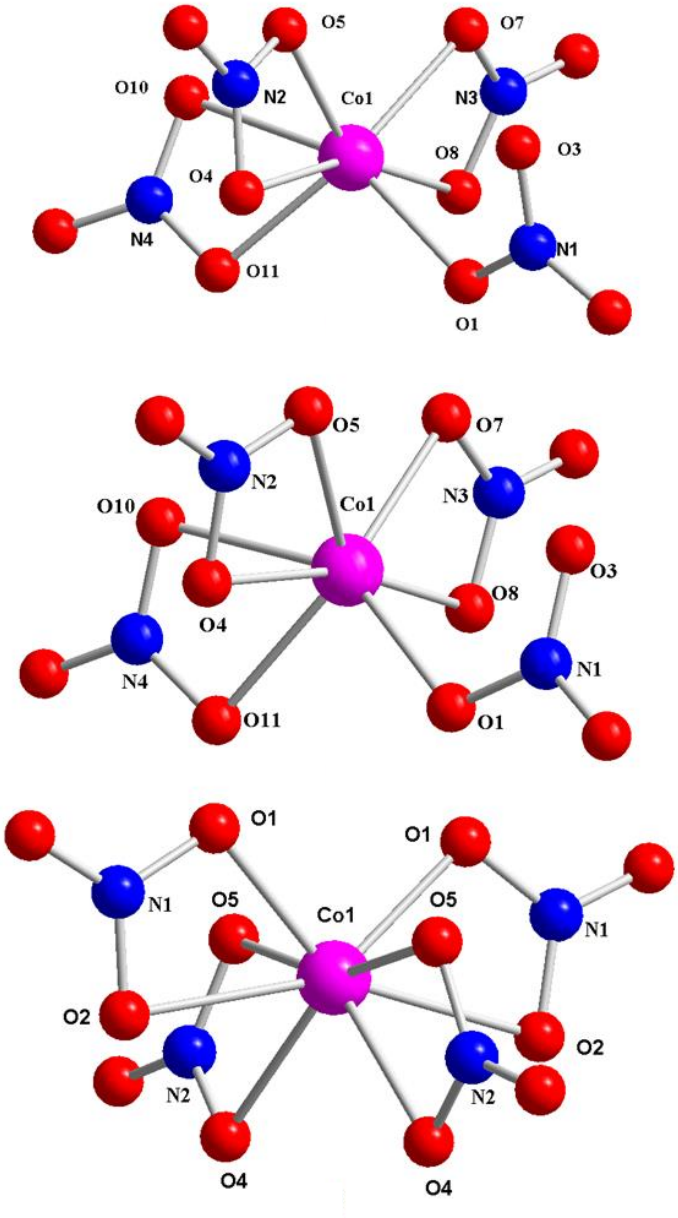

Figure B.15. Structures of the anions $[Co(NO_3)_4]^{2-}$ in **4**-**6**. Pink, red, and blue spheres represent Co, O, and N atoms, respectively. H atoms are omitted for clarity. Only one set of the two disordered nitrate groups centered around N(2) atom is shown for clarity.

Additional VISION Spectra for $Co(acac)_2(D_2O)_2$ (8-d_4) and $Co(acac\text{-}d_7)_2(D_2O)_2$ (8-d_{18})

Most phonons observed in Figure 3.21 seem to soften, or decrease in energy, with increasing temperature. The softening is generally attributed to thermal expansion.[24] It should be noted that even after applying the Bose correction, reduction of the phonon intensity is still expected because of the Debye-Waller factor, especially at high energy transfers (with relatively high $|Q|$ determined by the instrument geometry; Figures B.1610-B.17). We note that in $Co(acac)_2(D_2O)_2$ (**8-d_4**) and $Co(acac\text{-}d_7)_2(D_2O)_2$ (**8-d_{18}**), the magnetic peaks are strong. Thus, it is easy to distinguish the temperature dependences between magnetic and phonon peaks. However, if the magnetic peak is weak and/or overlapping with a phonon, it would be very difficult to use the temperature-dependence method.

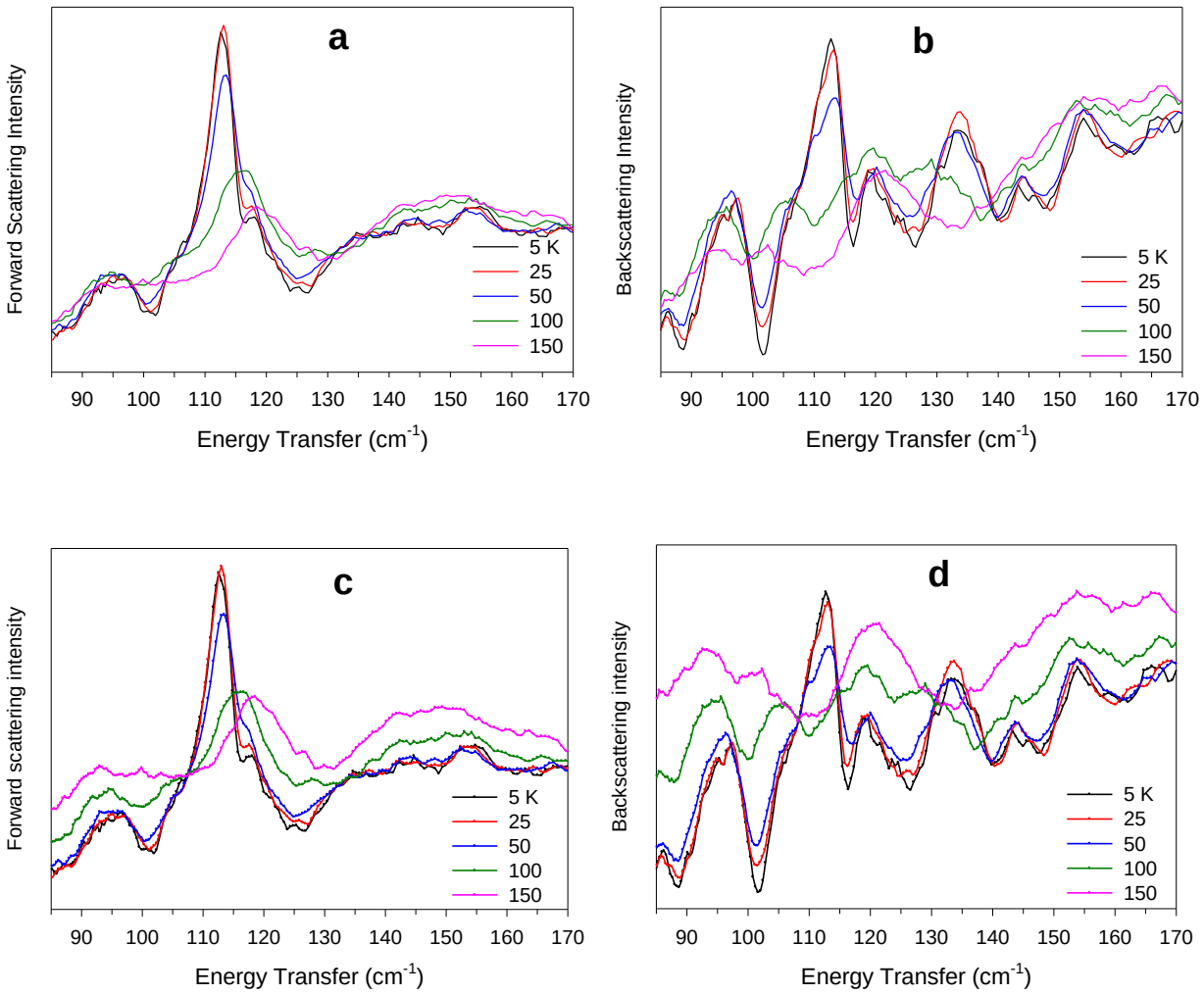

Figure B.16. (a) Forward scattering (low |*Q*|), Bose-corrected spectra of Co(acac-d_7)$_2$(D$_2$O)$_2$ **8-*d*$_{18}$**. (b) Backscattering intensity (high |*Q*|), Bose-corrected spectra of **8-*d*$_{18}$**. (c) Forward scattering, non-Bose-corrected spectra of **8-*d*$_{18}$**. (d) Backscattering, non-Bose-corrected spectra of **8-*d*$_{18}$**. Spectra collected at VISION.

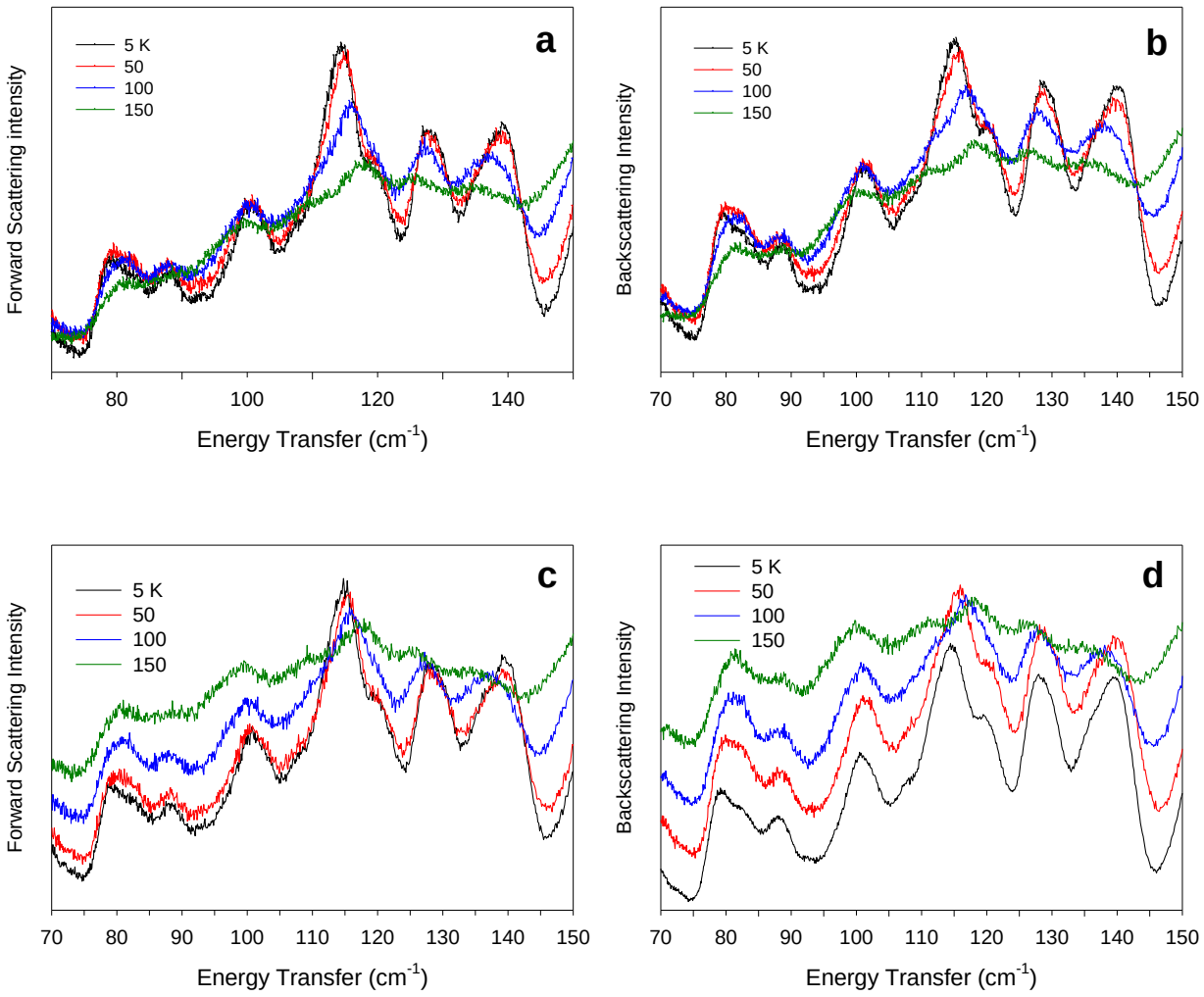

Figure B.17. (a) Forward scattering (low $|Q|$), Bose-corrected spectra of $Co(acac)_2(D_2O)_2$ **8-*d*$_4$**. (b) Backscattering intensity (high $|Q|$), Bose-corrected spectra of **8-*d*$_4$**. (c) Forward scattering, non-Bose-corrected spectra of **8-*d*$_4$**. (d) Backscattering, non-Bose-corrected spectra of **8-*d*$_4$**. Spectra collected at VISION.

Appendix C

Supporting Information for Chapter 5

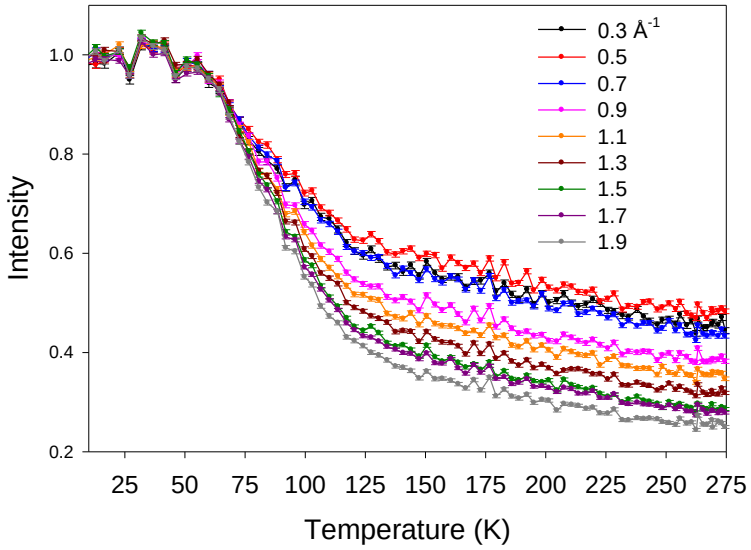

Figure C.1. Fixed window elastic scattering neutron intensity scan at variable |*Q*| in $Co(acac)_2(D_2O)_2$ (**8-*d*$_4$**).

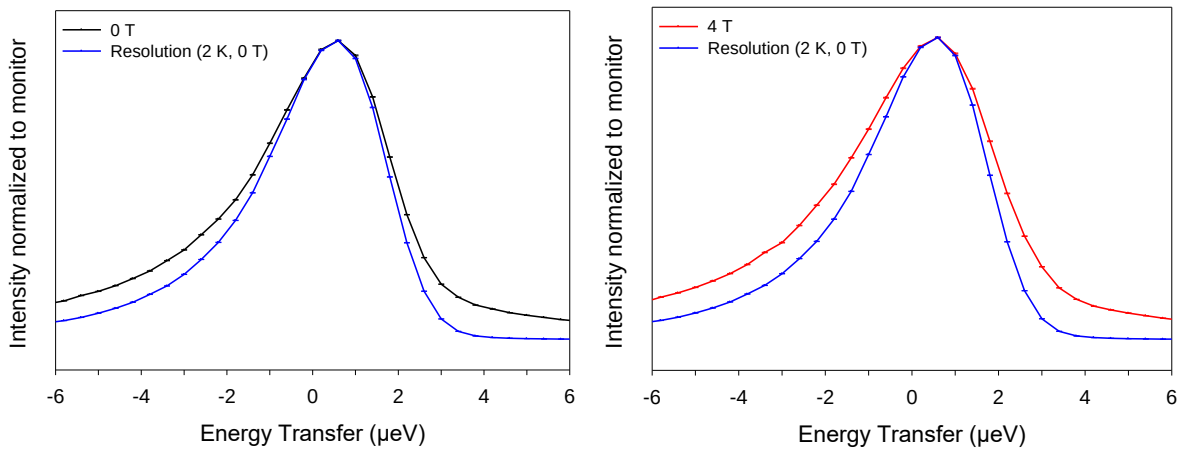

Figure C.2. Comparison of resolution function at 2 K with QENS data of $Co(acac)_2(D_2O)_2$ (**8-*d*$_4$**) at 100 K (Left, 0 T; Right, 4 T).

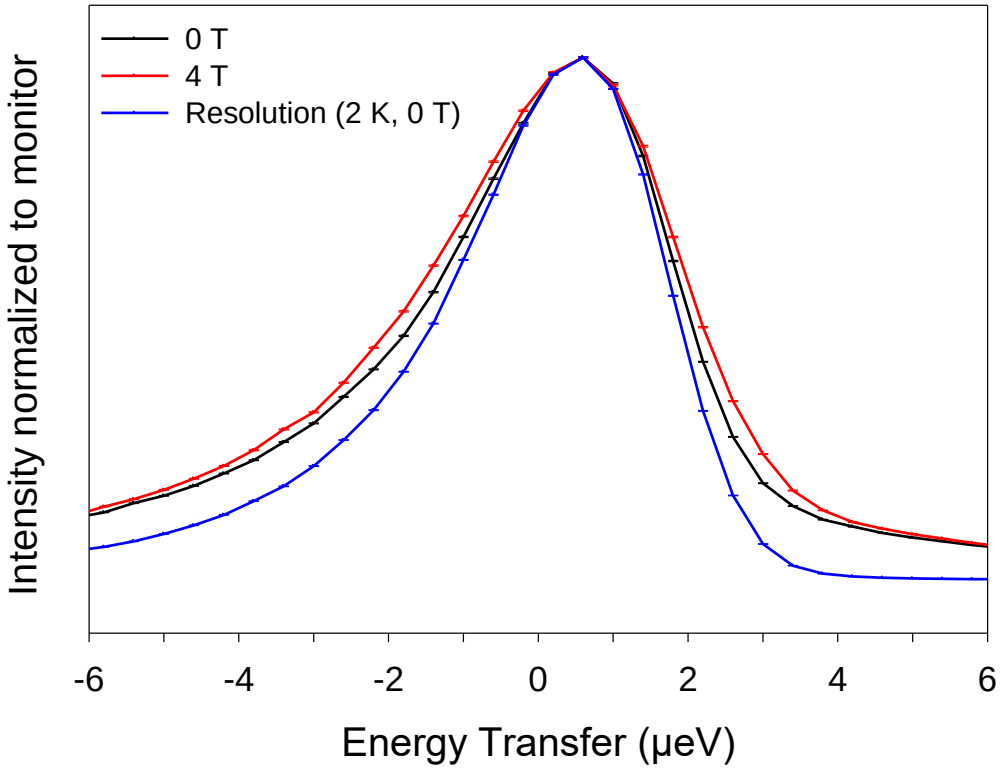

Figure C.3. Comparison of resolution function at 2 K with QENS data of $Co(acac)_2(D_2O)_2$ (**8-*d*$_4$**) at 0 and 4 T and 100 K.

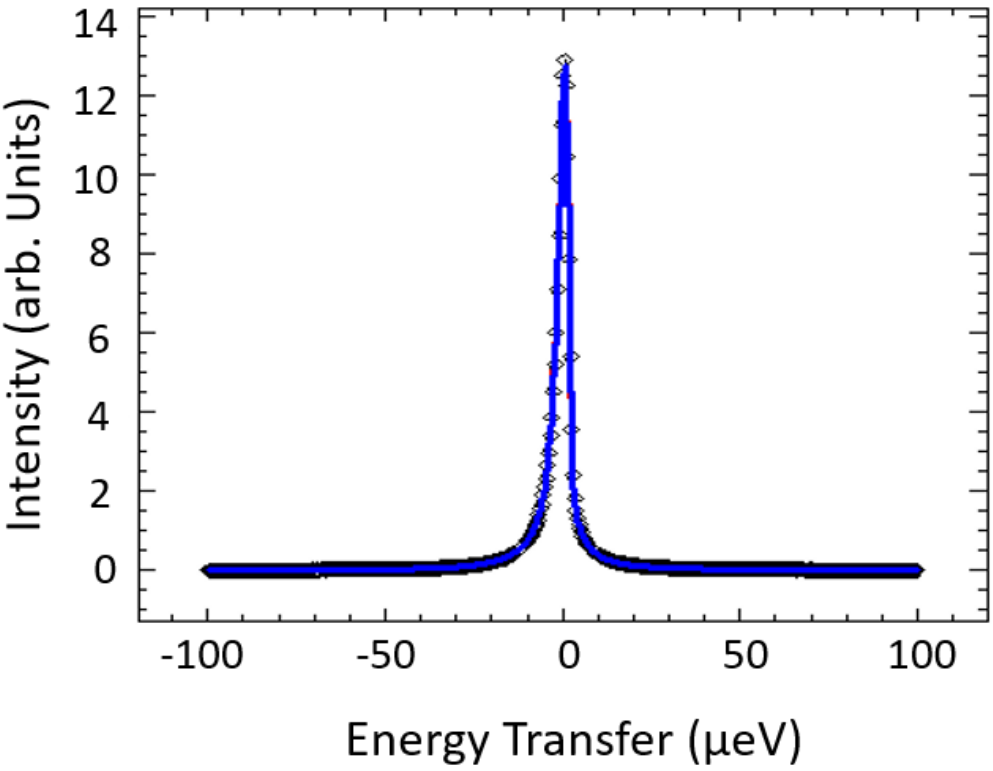

Figure C.4. The use of the Cole-Cole equation to fit a representative data set of $Co(acac)_2(D_2O)_2$ (**8-*d*$_4$**) at 100 K and 0 T.

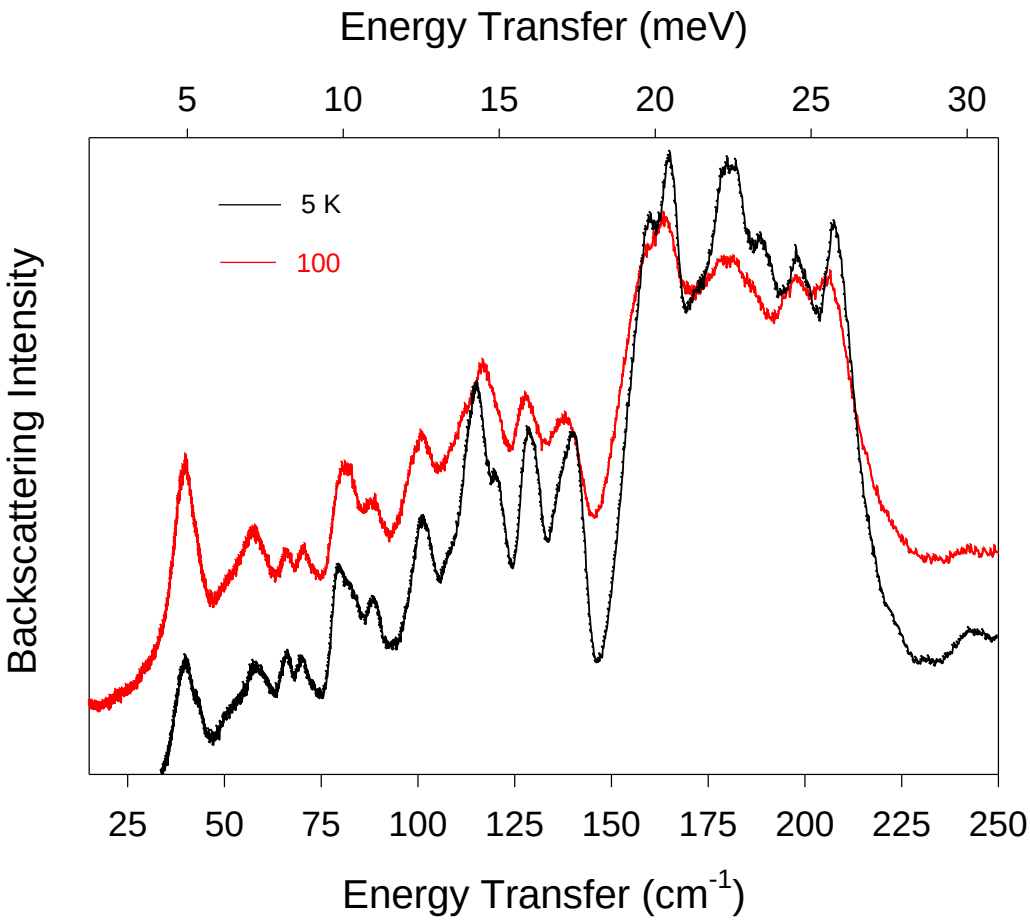

Figure C.5. VISION spectra at 5 and 100 K showing the strongest methyl torsion peak at 164 cm^{-1} (20.3 meV) in $Co(acac)_2(D_2O)_2$ (**8-*d*$_4$**)..

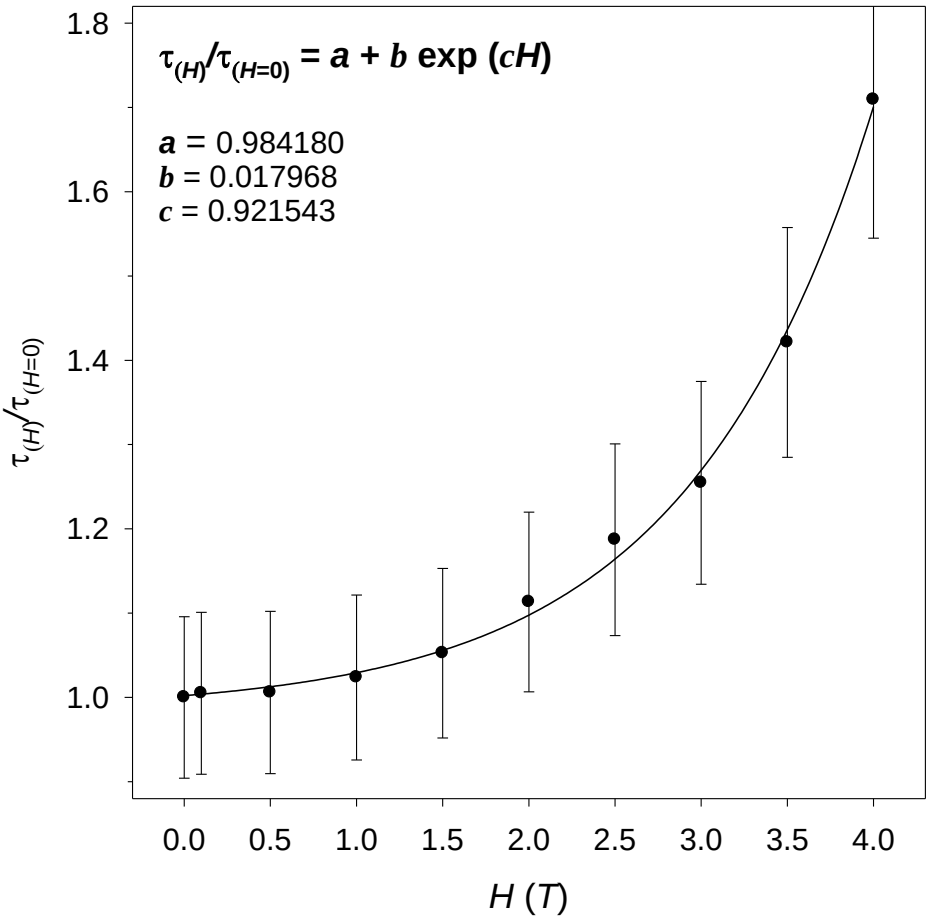

Figure C.6. Plot of $\tau_{(H)}/\tau_{(H=0)}$ vs. H at 100 K. a, b and c are fitting constants.

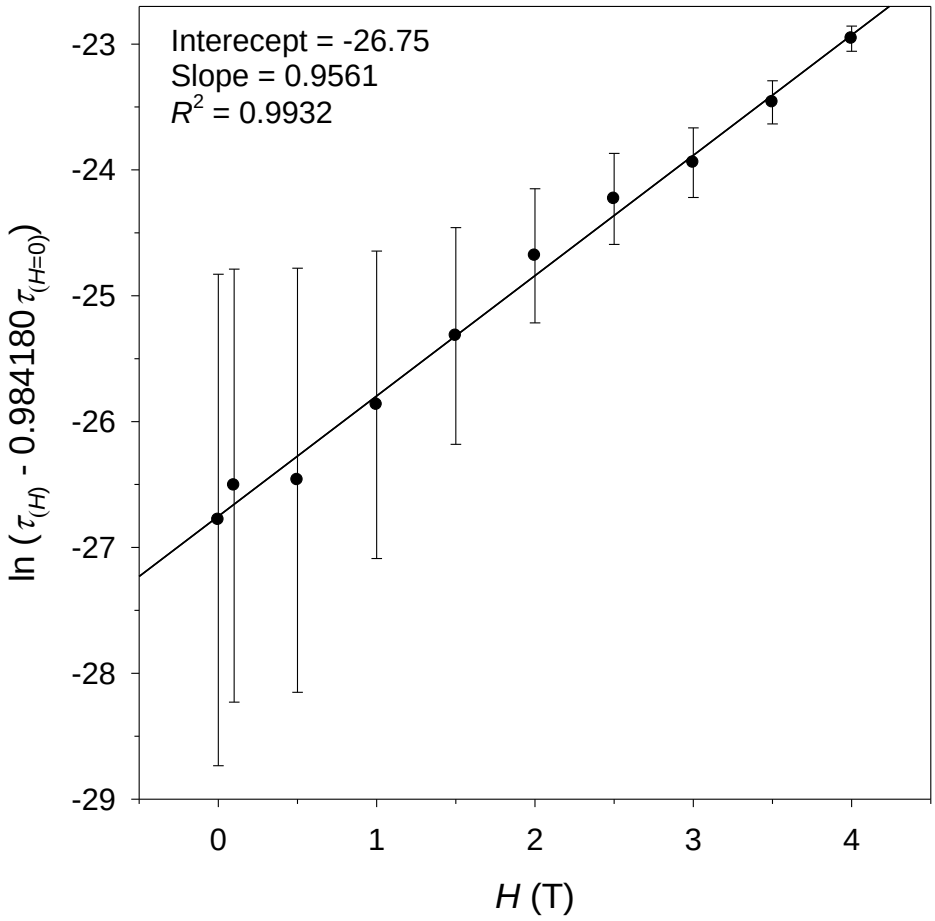

Figure C.7. Plot of ln ($\tau_{(H)}$ – 0.984180 $\tau_{(H=0)}$) vs H. The number a = 0.984180 is from the fitting of Figure C.6.

Table C.1. Comparison of the broadening and elastic parameters of the QENS peak at different fields in (**8-*d*$_4$**). The error in the E_0 and elastic parameters are in parentheses

80 K, summed over all *Q*			
Field (T)	**E_0, μeV**	**Elastic scattering fraction, *x***	**τ (s)**
0.0	1.19(6)	0.632(4)	5.6(3) x 10^{-10}
4.0	0.323(17)	0(0)	2.04(10) x 10^{-9}
90 K, summed over all *Q*			
Field (T)	**E_0, μeV**	**Elastic scattering fraction, *x***	**τ (s)**
0.0	2.43(12)	0.577(2)	2.71(13) x 10^{-10}
4.0	1.14(6)	0.332(5)	5.8(3) x 10^{-10}
100 K, summed over all *Q*			
Field (T)	**E_0, μeV**	**Elastic scattering fraction, *x***	**τ (s)**
0.0	4.46(22)	0.537(1)	1.48(7) x 10^{-10}
0.1	4.43(22)	0.541(1)	1.49(8) x 10^{-10}
0.5	4.43(22)	0.543(1)	1.49(8) x 10^{-10}
1.0	4.35(22)	0.538(1)	1.51(8) x 10^{-10}
1.5	4.23(21)	0.537(1)	1.55(8) x 10^{-10}
2.0	4.00(20)	0.515(1)	1.64(8) x 10^{-10}
2.5	3.75(19)	0.490(2)	1.75(9) x 10^{-10}
3.0	3.55(18)	0.484(2)	1.85(9) x 10^{-10}
3.5	3.13(16)	0.446(2)	2.10(11) x 10^{-10}
4.0	2.61(13)	0.396(2)	2.53(12) x 10^{-10}

Total uncertainties σ_{total} in E_0 are given in Table C.1 here: $\sigma_{total}^2 = \sigma_{ran}^2 + \sigma_{sys}^2$. Random uncertainty σ_{ran} for each E_0 value is obtained from the fitting of the QENS data using Eqs. 5.1-5.2. Systematic uncertainty σ_{sys} in E_0 from the QENS studies here is estimated to be 5% of E_0.

Table C.2. Average spin density $\rho_{S\text{-average}}$ per atom in $Co(acac)_2(H_2O)_2$ (**8**). See Table 5.2

Atom	$\rho_{S\text{-average}}$
H6	-1.28×10^{-5}
H3-5 or H7-9	7.16×10^{-5}
H1-2	9.00×10^{-4}
C6	3.40×10^{-3}
C2-3	-9.34×10^{-4}
C1,5	2.10×10^{-3}
O2-3	2.70×10^{-2}
O1	1.91×10^{-1}
Co1	2.81

Vita

Shelby Elizabeth Stavretis was born in Fort Wayne, IN to Bill and Susan Stavretis. Her adolescence education was through the Fort Wayne Community school system. She graduated high school in 2009. In the following fall, Shelby enrolled in Butler University (Indianapolis, IN). She graduated in May 2013 with an ACS certified B.S. degree in Chemistry. Shelby conducted undergraduate research with Dr. Luanne McNulty on the synthesis of dihydropyrans. She began her Ph.D. studies in inorganic chemistry at the University of Tennessee (Knoxville) in August 2013.